Jouni Puranen

Protective Spinel Coatings for Solid Oxide Fuel Cell Interconnectors by Thermal Spray Processes
From Conventional Dry Powder to Novel Solution Precursor Thermal Spraying

Tampere 2015

Jouni Puranen

Protective Spinel Coatings for Solid Oxide Fuel Cell Interconnectors by Thermal Spray Processes
From Conventional Dry Powder to Novel Solution Precursor Thermal Spraying

Thesis for the degree of Doctor of Science in Technology to be presented with due permission for public examination and criticism in Festia Building, Auditorium Pieni Sali 1, at Tampere University of Technology, on the 18th of September 2015, at 12 noon.

Abstract

Protective coatings are used on ferritic stainless steel interconnectors to prevent the transport of the harmful $CrO_3(g)$ and $CrO_2(OH)_2(g)$ compounds in solid oxide fuel cells. These compounds are transported on the triple-phase boundary of the cathode, and electrically reduce back to Cr_2O_3 causing degradation of the cell. The most promising materials to be used as protective coatings are $(Mn,Co)_3O_4$ spinels. However, in order to provide good protectiveness in long-term use (5 years or more), these coatings should have a dense microstructure, good adhesion with the substrate and good chemical stability at high temperature in an oxidizing atmosphere. Several deposition techniques have been studied, for example various wet-ceramic processes and thin film techniques. However, the studies have shown that the coatings produced with these methods are not dense, and therefore their long-term protectiveness is questionable.

In this study, protective $(Mn,Co)_3O_4$ and $(Mn,Co,Fe)_3O_4$ spinel coatings were manufactured with conventional atmospheric plasma spraying (APS) and novel high velocity solution precursor flame spraying (HVSPFS). The aim was to obtain a dense microstructure. Since the HVSPFS process is a novel deposition method, the coating build-up mechanism and materials synthesis were studied more closely. The as-sprayed coatings were oxidized in order to obtain more detailed information about the Cr barrier and electrical properties during the oxidation cycles.

The spinel coatings with a dense microstructure were sprayed using the APS and the HVSPFS processes. The deposition methods caused the as-sprayed coatings to sinter during the oxidation cycles. The sintering was a consequence of the metastable phase structure and the small particle and crystallite size. Due to the dense microstructure and fully recovered spinel phases, the coatings provided a good Cr barrier and electrical properties, even in a relatively harsh environment. It can be stated that $Mn_{1.5}Co_{1.5}O_4$ and $MnCo_{1.9}Fe_{0.1}O_4$ spinel coatings, manufactured either by conventional thermal spraying using agglomerated cermet powder, or by solution precursor thermal spraying, are good candidates for use as protective coatings on metallic interconnectors.

Preface

This work was carried out in the Department of Material Science at Tampere University of Technology during the years 2008–2015. The work was supervised by Prof. Petri Vuoristo, to whom I am pleased to express my greatest gratitude for his guidance and for providing financial support.

I would like to express my gratitude to my colleagues Dr. Heli Koivuluoto, Dr. Minna Kotilainen and the rest of the co-workers in the Surface Engineering research group. In addition, I would also like to address my special thanks to my colleagues Mr. Juha-Pekka Nikkanen, Mr. Jarmo Laakso, Mr. Mikko Kylmälahti and Mr. Leo Hyvärinen for many meaningful discussions that helped me to continue and finish my research work.

This quality of research work would never have been accomplished without the help of my co-authors and therefore I would like to give credit to Mr. Juha Largerbom (VTT) for important comments and power material synthesis, Mr. Mikko Pihlatie (VTT) for performing the ageing and electrical tests, Dr. Olli Himanen (VTT) and Dr. Jari Kiviaho (VTT) for coordinating the SOFC-Power project. Special thanks go also to Prof. Erkki Levänen (TUT) and Prof. Tapio Mäntylä (TUT) for important comments and discussions, Mr. Mikko Kylmälahti for coating manufacturing (TUT), Mr. Jarmo Laakso (TUT) for FESEM analysis and Mr. Leo Hyvärinen (TUT) for materials synthesis, Dr. Turkka Salminen (TUT) for performing and analyzing the Raman tests, Ms. Saara Heinonen (TUT) for elemental analysis, Dr. Mari Honkanen (TUT) for TEM analysis and Mrs. Sinikka Pohjonen (TUT) for thermal analysis. High quality research was done and shared at international level and so I would like to express my gratitude to Prof. Thomas Coyle, Prof. Olivera Kesler, Mr. Stan Lugowski, and other researchers working in the Center for Advanced Coating Technologies and Fuel Cell Materials and Manufacturing Laboratories at the University of Toronto, Canada. Many important findings were made in the University of Modena and Reggio Emilia, Italy with the help of Prof. Luca Lusvarghi and Dr. Giovanni Bolelli.

This research work was funded by Tekes - the Finnish Funding Agency for Technology and Innovation through the SOFC-Power Project, the Graduate School of Advanced Materials and Processes, Tutkijat Maailmalle-Osaamista Suomeen Foundation, the City of Tampere and Tampere University of Technology.

Last but not least I wish to thank my parents Sirkka and Seppo for their encouraging support throughout my research career. Some special thanks go to my important friends, especially to Henri Lahtinen and Harri Poikolainen for their endless support.

Jouni Puranen   Tampere 14.7.2015

Contents

List of Symbols and Abbreviations

Symbols

2Θ	Diffraction angle
E_a	Activation energy
G_b	Free energy associated with grain boundaries
G_s	Free energy associated with surface
G_T	Total free energy
G_v	Free energy associated with volume
r	Pore radius
R_a	Surface roughness
T_m	Melting temperature of the ceramic material in degrees Kelvin
γ_s	Material specific surface energy
Δ	Change in variant
σ	Sintering pressure

Abbreviations

°C	Degrees Celsius
$(A,B)_2O_3$	Generic formula of the perovskite structure
$(A,B)_3O_4$	Generic formula of the spinel structure
$(La,Co)_2O_3$	Lanthanum cobalt perovskite oxide
$(La,Mn)_2O_3$	Lanthanum manganese perovskite oxide
$(La,Sr,Co)_2O_3$	Strontium substituted lanthanum cobalt perovskite oxide
$(La,Sr,Co,Fe)_2O_3$	Strontium and iron substituted lanthanum cobalt perovskite oxide
$(La,Sr,Co,Mn)_2O_3$	Strontium and manganese substituted lanthanum cobalt perovskite oxide
$(La,Sr,Fe)_2O_3$	Strontium substituted lanthanum iron perovskite oxide
$(La,Sr,Mn)_2O_3$	Strontium substituted lanthanum manganese perovskite oxide
$(Mn,Co)_3O_4$	Manganese cobalt spinel oxide
$(Mn,Co,Fe)_3O_4$	Iron substituted manganese cobalt spinel oxide
$(Mn,Cr)_3O_4$	Manganese chromium spinel oxide
AFC	Alkaline fuel cell
Al	Aluminium

Al_2O_3	Aluminium oxide
APS	Atmospheric plasma spraying
ASR	Area specific resistance
at%	Atomic percentage
C	Carbon
Ce	Cerium
$Ce_{1-x}Gd_xO_2$	Gadolinium doped cerium oxide
$Ce_{1-x}Sm_xO_2$	Samaria doped cerium oxide
cf.	confer (compare)
CH_3OH	Methanol
CH_4	Methane
cm^2	square centimetre
Co	Cobalt
$Co(NO_3)_2 \cdot 6H_2O$	Cobalt(II) nitrate hexahydrate
CO	Carbon monoxide
CO_2	Carbon dioxide
CO_3^{2-}	Carbonate ion
$CoCO_3$	Cobalt(II) carbonate
CoO	Cobalt oxide
Cr	Chromium
Cr_2O_3	Chromium oxide
$CrO_2(OH)_x(g)$	Chromium oxyhydroxide (gas phase)
$CrO_3(g)$	Chromium trioxide (gas phase)
CTE	Coefficient of thermal expansion
Cu	Copper
DC	Direct current
DMFC	Direct methanol fuel cell
DTA-DSC	Differential thermal analysis combined with differential scanning calorimetry
e.g.	exempli gratia (for example)
EDS	Energy dispersed spectroscopy
et al.	et alia
EU	European Union
eV	Electron volts
Fe	Iron
$Fe(NO_3)_3 \cdot 9H_2O$	Iron(III) nitrate nonahydrate
Fe_2O_3	Iron(III) oxide
FESEM	Field emission scanning electron microscopy
FT-IR	Fourier Transform Infrared spectroscopy
Gd	Gadolinium

h	hour
H^+	Proton
H_2	Hydrogen molecule
H_2O	Water molecule
$HV_{0.025}$	Vickers microhardness (25 gram load)
HVOF	High velocity oxy-fuel spraying
HVSPFS	High velocity solution precursor flame spraying
i.e.	id est (that is)
IC	Interconnector/current collector
ICP – AES	Inductively coupled plasma – atomic emission spectrometry
K/min	Kelvins per minute
kJ/kg K	Kilo joules per kilograms times Kelvin
kJ/mol	Kilojoules per mole
kPa	Kilopascal
kW	Kilowatt
La	Lanthanum
$LaCrO_3$	Lanthanum chromite
LFS	Liquid flame spraying
LSM	Strontium substituted lanthanum manganese perovskite oxide
mA/cm^2	Milliamperes per square centimetre
MCFC	Molten carbonate fuel cell
mm	Millimetre
Mn	Manganese
$Mn(NO_3)_2 \cdot 4H_2O$	Manganese(II) nitrate tetrahydrate
$Mn_{1-x}Y_xCo_2O_4$	Yttria substituted manganese cobalt spinel oxide
$MnCO_3$	Manganese(II) carbonate
MnO	Manganese oxide
Mn^{x+}	Manganese cation
mol/L	molar concentration
MPa	Megapascal
mPas	Millipascal second
N	Newton
NASA	National Aeronautics and Space Administration
Nb	Niobium
Ni	Nickel
nm	nanometre
O_2	Oxygen molecule
OH^-	Hydroxide ion
P	Phosphorus
PAFC	Phosphoric acid fuel cell

PEMFC	Proton exchange membrane fuel cell
ppm	Parts per million
PVA	polyvinyl acetate
RF-GD-OES	Radio frequency glow discharge optical emission spectrometer
S	Sulphur
S/cm	Siemens per centimetre
SE	Secondary electron
SEM	Scanning electron microscope
Si	Silicon
SiO_2	Silicon oxide
Sm	Samarium
SOFC	Solid oxide fuel cell
SPPS	Solution precursor plasma spraying
SPTS	Solution precursor thermal spraying
Sr	Strontium
$SrCrO_4$	Strontium chromate
TEM	Transmission electron microscope
Ti	Titanium
toe	Metric ton of oil equivalent (42 GJ in SI units)
TPB	Triple/three-phase boundary
TUT	Tampere University of Technology
VTT	Technical Research Centre of Finland
vol%	Volume percentage
W/mK	Watts per meter times Kelvin
Wt%	Weight percentage
XRD	X-ray diffraction
XRF	X-ray fluorescence
Y_2O_3	Yttrium oxide
YSZ	Yttria-stabilized zirconium oxide
ZrO_2	Zirconium oxide
Å	Angstrom (10^{-10} m)
µm	Micrometre

List of publications included in the thesis

I.   J. Puranen, J. Lagerbom, L. Hyvärinen, M. Kylmälahti, O. Himanen, M. Pihlatie, J. Kiviaho, and P. Vuoristo, The structure and properties of plasma sprayed iron oxide doped manganese cobalt oxide spinel coatings for SOFC metallic interconnectors, Journal of Thermal Spray Technology, 20, 1–2 (2010) pp. 154–159.

II.   J. Puranen, J. Lagerbom, L. Hyvärinen, T. Mäntylä, E. Levänen, M. Kylmälahti, and P. Vuoristo, Formation and structure of plasma sprayed manganese-cobalt spinel coatings on preheated metallic interconnector plates, Surface and Coatings Technology, 205, 4(2010) pp. 1029–1033.

III.   J. Puranen, M. Pihlatie, J. Lagerbom, G. Bolelli, J. Laakso, L. Hyvärinen, M. Kylmälahti, O. Himanen, J. Kiviaho, L. Lusvarghi and P. Vuoristo, Post-mortem evaluation of oxidized atmospheric plasma sprayed Mn-Co-Fe oxide spinel coatings on SOFC interconnectors, International Journal of Hydrogen Energy, 39, 30(2014) pp. 17284-17294.

IV.   J. Puranen, M. Pihlatie, J. Lagerbom, T. Salminen, J. Laakso, L. Hyvärinen, M. Kylmälahti, O. Himanen, J. Kiviaho and P. Vuoristo, Influence of powder composition and manufacturing method on electrical and chromium barrier properties of atmospheric plasma sprayed spinel coatings prepared from $MnCo_2O_4$ and Mn_2CoO_4+Co powders on Crofer 22 APU interconnectors, International Journal of Hydrogen Energy, 39, 30(2014) pp. 17246-17257.

V.   J. Puranen, J. Laakso, M. Kylmälahti, and P. Vuoristo, Characterization of high-velocity solution precursor flame-sprayed manganese cobalt oxide spinel coatings for metallic SOFC interconnectors," Journal of Thermal Spray Technology, 22, 5(2013), pp. 622–630.

VI.   J. Puranen, J. Laakso, M. Honkanen, S. Heinonen, M. Kylmälahti, S. Lugowski, T. Coyle, O. Kesler and P. Vuoristo, High temperature oxidation tests for the high velocity solution precursor flame sprayed manganese-cobalt oxide spinel protective coatings on SOFC interconnector steel, International Journal of Hydrogen Energy, 40, 18(2015), pp. 6216-6227.

Author's contribution

I.   The author wrote the paper as corresponding author. The author planned and prepared the coating samples with the help of Mr. Kylmälahti. Mr. Lagerbom was responsible for powder synthesis. The author planned and executed the rest of the experimental work.

II.   The author wrote the paper as corresponding author. The author planned and prepared the samples with the help of Mr. Kylmälahti. Mr. Lagerbom was responsible for powder synthesis. The author planned and executed the rest of the experimental work.

III.   The author wrote the paper as corresponding author. The author planned and prepared the samples with the help of Mr. Kylmälahti. Mr. Lagerbom was responsible for powder synthesis and Mr. Pihlatie for the electrical measurements. Dr. Bolelli and Prof. Lusvarghi carried out high temperature XRD analysis, elemental analysis and Raman analysis. The author planned and executed the rest of the experimental work. FESEM analyses were carried out with the help of Mr. Laakso.

IV.   The author wrote the paper as corresponding author. The author planned and prepared the samples with the help of Mr. Kylmälahti. Mr. Lagerbom was responsible for powder synthesis and Mr. Pihlatie for the electrical measurements. Dr. Salminen was responsible for the Raman measurements. FESEM analyses were carried out with the help of Mr. Laakso.

V.   The author wrote the paper as corresponding author. The author prepared the samples with the help of Mr. Kylmälahti. The author planned and executed the experimental work and FESEM analyses were carried out with the help of Mr. Laakso. Dr. Honkanen was responsible for the TEM analyses and Ms. Heinonen carried out the FTIR analyses. Mr. Lugowski was responsible for the RF-GD-OES tests. Prof. Coyle and Prof. Kesler were supervisors during the research exchange at the University of Toronto.

VI.   The author wrote the paper as corresponding author. The author prepared the samples with the help of Mr. Kylmälahti. The author planned and carried out the experimental work and the FESEM analyses were carried out with the help of Mr. Laakso.

1 Introduction

According to the International Energy Agency (IEA), energy consumption has doubled since the 1970s, reaching the value of 8 918 Mtoe in 2011. This sets new challenges for energy production in terms of production and distribution reliability, price, political, health and environmental issues. The main environmental concern has been greenhouse gases and especially carbon dioxide (CO_2) emissions, impact on the environment and radiation wastes that can be harmful for living species. CO_2 emissions totalled 31 342 Mt in 2011. The largest source, accounting for 79.3% of the CO_2 emissions, was non-renewable energy sources, such as coal, peat and oil. Natural gas caused 20.2% of the emissions and 0.5% originated from other sources. [1]

Since environmental issues are becoming more important in energy production, the demand for renewable and clean energy production has increased. This can be seen in different national strategies, for example European Commission EU 2020 objectives are to reduce greenhouse gas emissions by 20%, increase the share of renewable energies to 20% and increase energy efficiency by 20% [2]. The trend can be seen in investments made for non-fossil fuel research, as in 2000 it stood at $65 billion and in 2013 $260 billion [3]. An overall distinction of renewable energies between primary energy harvesting methods can be categorized as biomass, geothermal, hydro, wind, and solar power.

Hydrogen economy is a term that is often linked to the renewable or green energy concept. However, hydrogen is not a primary energy source, similar to for example hydro or wind power. Hydrogen, or hydrogen equivalent gas mixtures, i.e. syngas (H_2 and CO), is the high energy containing products of the primary energy harvesting methods. This means that hydrogen or hydrogen equivalent products are produced with renewable or conventional energy production methods. These products can be stored in the form of compressed gas, liquid gas or stored in chemical storage (metal hybrids), transferred and converted into any basic form of energy that is required. Some of the clear advantages of hydrogen are high specific heat capacity (14.32 kJ/kg K) and non-toxic reaction products.

One of the basics in the hydrogen economy is that energy (electricity or heat) is converted from the primary energy source products near the place of application where it is needed. This can be done either by chemical reactions (combustion reactions) or electrochemical conversion. Ideally, these systems would run for an infinite time if the flow of the fuel were sustained. The best known devices for electrochemical conversion are fuel cells.

1.1.1 Fuel cell

A fuel cell is an electrochemical device or galvanic cell that converts chemical energy into reaction products and energy through oxidation and reduction, as shown in reaction Equation 1. This

equation shows that the combustion reaction is exothermic. It produces water as the reaction product and 286.5 kJ/mol of energy, which is usually in the form of heat.

$$2H_2 + O_2 \rightarrow 2H_2O + energy \tag{1}$$

In general, the fuel cell is a system of electrodes, i.e. an anode where oxidation (de-electronation) and cathode reduction (electronation) take place. The electrodes are separated by a thin, gas-tight electrolyte that conducts ions. This system is called a single cell. Interconnectors are used in the fuel cell to connect single cells into series and provide the fuel and the oxidant gases for the electrodes.

The history of fuel cells starts from 1839 when Sir William Grove built the first gaseous voltaic cell [4]. In the 1960s, NASA started to develop and use fuel cells in space missions to provide electricity during the space flight. Since then, general interest and research and development into different fuel cell models has increased and the fuel cell has been adopted in different applications such as [5]:

1. Stationary applications for an emergency power source or implemented in the power grid to generate electricity for isolated areas

2. Applications related to transport, such as alternatives for the commonly used combustion engines in vehicles

3. Portable applications in areas where a power grid connection is not provided, such as camping areas, or where more user- and environment-friendly power sources are preferred

4. Micro-power applications as chargers for laptops and other telecommunication devices.

A more accurate listing of the available fuel cell models is presented in Table 1. As observed, one of the most obvious differences between the cell models is the operating temperature and efficiency. Low temperature fuel cell models can be categorized as operating below 200ºC, and high temperature models above this. For this reason, low temperature fuel cells are more favourable in portable and transport-related applications, whereas the high temperature fuel cell models are more commonly used in stationary applications.

TABLE 1   Comparison of available fuel cell models [5].

Model	Anode side gas	Electrolyte / Temperature / Efficiency*	Cathode side gas	Advantages	Disadvantages
Proton exchange membrane fuel cell (PEMFC)	H_2	Polymer or composite membrane $\rightarrow 2H^+ \rightarrow$ 60-80ºC 40-45 %	O_2 (air)	+Low operating temperature +Non-corrosive electrolyte +Tolerant to CO_2 +High voltage, current and power density +Low operating pressure +Compact and robust +Simple design +Stable building materials	-Sensitive to impurities in hydrogen -Low tolerance for CO -Humidification units of reactive gases -Platinum as catalyst
Direct methanol fuel cell (DMFC)	$CH_3OH + H_2O$	Polymer electrolyte membrane $\rightarrow 2H^+ \rightarrow$ 130ºC 25-30 %	O_2	+Liquid fuel +No reforming process +Similar type of electrolyte as PEM FC	-Low efficiency -Need for large amount of catalyst for electro-oxidation of methanol
Phosphoric acid fuel cell (PAFC)	H_2	Liquid phosphoric acid with silicon carbide matrix $\rightarrow 2H^+ \rightarrow$ 150-200ºC 40-45 %	O_2 (air)	+Tolerate up to 30 vol% CO_2 +Excess heat for cogeneration +Good stability of electrolyte and low volatility	-Low tolerance for CO -Corrosive electrolyte -No auto-reform of fuel -Operating temperature must be reached

Alkaline fuel cell (AFC)	H_2	Potassium hydroxide $\leftarrow OH^- \leftarrow$ 65-220ºC 50-60 %	O_2	+Work in low temperatures +Fast start time +High efficiency +Small amount of catalyst +Simple operation and design +Low weight and volume	-Low tolerance for CO_2 and CO -Fuel only pure hydrogen -Liquid electrolyte -Relatively short lifetime
Molten carbonate fuel cell (MCFC)	H_2	Lithium carbonate and potassium $\leftarrow CO_3^{2-} \leftarrow$ 650ºC 50-55 %	O_2 and CO_2	+Spontaneous internal fuel reforming +Heat production +High-speed reactions +High efficiency +No noble catalyst metals	-Corrosion-resistant materials at high temperature -Intolerant to sulphur, no more than 1.5 ppm particles in fuel -Liquid electrolyte -Preheating before use
Solid oxide fuel cell (SOFC)	$H_2/CO/CH_4$	Zirconium-lanhanum/yttrium $\leftarrow O^{2-} \leftarrow$ 600-1000ºC 50-55%	O_2 / air	+Spontaneous internal reforming fuel, can be used to oxidize any combustible gas +Heat production +Fast chemical reactions +High efficiency +High current densities +Solid components +No metal catalyst	-Corrosion-resistant and stable materials at high temperature -Intolerant to sulphur, no more than 50 ppm particles in fuel -Not a mature technology -Degradation mechanisms

*) Lower heating value basis

1.1.2 Solid oxide fuel cell

Research into solid oxide fuel cells (SOFCs) started in 1988, when Walter Hermann Nernst described a solid-state conductor with a composition of 85 % zirconium dioxide (ZrO_2) and 15 % diyttrium trioxide (Y_2O_3), known as Nernst mass. Since Nernst mass was capable of conducting oxygen ions, it was the most remarkable stepping-stone for electrolytes used in present-day SOFCs.

There are two different SOFC models available: planar and tubular. This study focuses on the planar version, and its schematic structure and principle of operation are presented in Fig. 1. In its simple form, a planar SOFC is composed of a solid structure of anode, electrolyte and cathode layer, forming a cell. The supporting layer, which can be either the anode or the electrolyte, is usually the thickest in order to give mechanical strength. These cells are connected electrically by interconnects to form a stack.
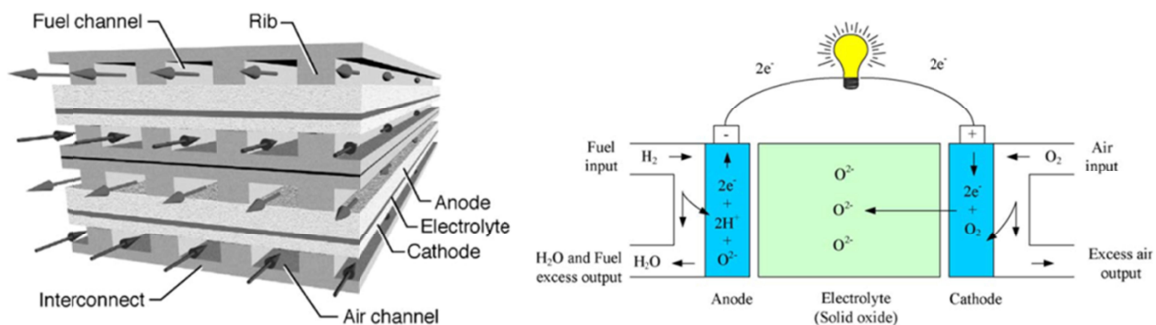

FIGURE 1   Schematic presentation of the planar model of solid oxide fuel cell (left) [6] and principle of operation (right) [5].

The electrolyte is a dense layer that must be stable in oxidizing and reducing atmospheres and achieve high ionic but low electronic conductivity. The purpose of the electrolyte layer is to transport the oxygen ions from the cathode side to the fuel-rich anode side. The most used material is yttria-stabilised zirconia (YSZ), but also doped ceria, e.g. samaria-doped ceria electrolytes, i.e. $Ce_{1-x}Sm_xO_2$ have been studied. A well-established composition for the electrolyte is YSZ with 8 mol% of Y_2O_3. [7]

The cathode is a porous layer which provides a surface for the oxygen reduction reactions. The reaction occurs at the interphase of the cathode, the electrolyte and the gas phase. In general, the cathodes are manufactured by using lanthanum strontium manganite $(La,Sr,Mn)_2O_3$ or alloyed lanthanum-strontium based perovskites, e.g. $(La,Sr,Co)_2O_3$, $(La,Sr,Co,Fe)_2O_3$. [8] Cobalt-alloyed

cathodes are used together with gadolinium-doped ceria, i.e. $Ce_{1-x}Gd_xO_2$, as a diffusion barrier layer in order to prevent undesirable reactions with the YSZ electrolyte at high temperatures [9].

The anode is also a porous layer where the fuel (H_2 or CH_4) oxidation reaction occurs. The anode materials are capable of ionic and electron conduction with good transport and catalytic properties. The most commonly used anode material is a combination of ceramic and metallic material, i.e. cermet, with a composition of nickel (Ni) and Y_2O_3-ZrO_2. The oxidation reactions occur at the interphase of the gas phase, the electrolyte and a Ni catalyst. [10], [11]

Figure 2 shows a schematic presentation of the interconnector (IC) used in the SOFC. The ICs have the same operation principle in every fuel cell model which are: i) to provide gases for the electrodes, ii) act as a gas barrier to oxidant and fuel gases, i.e. prevent mixing of gases, and iii) to form an electrical connection between the cells in planar SOFCs. For the SOFCs operating in high temperatures, at 800⁰C and above, the interconnectors are conventionally manufactured using ceramic materials, e.g. lanthanum chromites ($LaCrO_3$). However, the next generation of SOFC models operates in a temperature range of 600–800⁰C, which means that alternative materials can be used as interconnectors. The materials which have the greatest potential for this purpose are ferritic stainless steels [12]–[14]. By using ferritic stainless steels, the manufacturing costs can be decreased and more complex gas channel profiles can be manufactured.
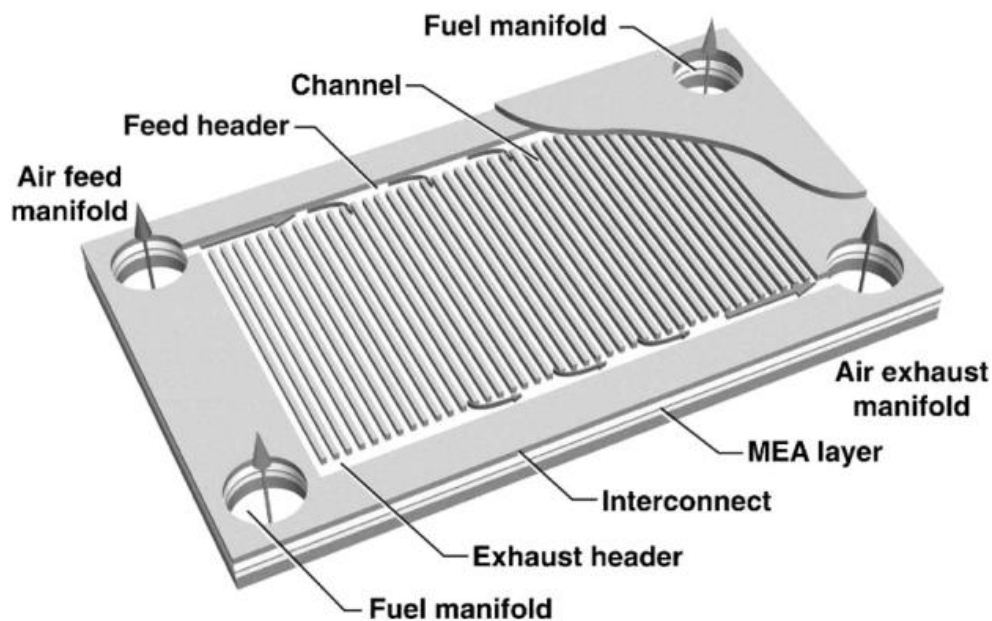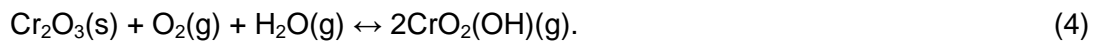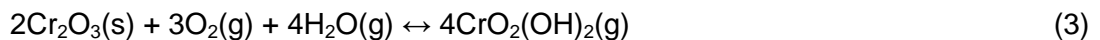

FIGURE 2   Schematic presentation of a planar SOFC interconnector [6].

2 Material issues in long-term use

This chapter introduces the background problem in novel SOFCs. The problem is related to the long-term stability behaviour of the cells when metallic ICs are used, as the ferritic stainless steels react with the atmosphere and form volatile Cr species. These Cr species have a tendency to cause chromium poisoning and degradation of cells.

2.1 Chromium poisoning

The use of ferritic stainless steels is based on acceptable corrosion behaviour, and the formation of chromium oxide scale (Cr_2O_3) at typical SOFC operating temperatures of the order of 600–800°C. This scale forms a protective layer on steels, which should decrease further oxidation in the cathode side atmosphere. However, Cr scale protects only in moderate temperatures and at 850°C there is already a risk of uncontrolled oxidation. In addition, moisture further increases the oxidation rate [15]. Furthermore, under certain conditions Cr_2O_3 reacts with water molecules and forms chromium oxides and oxyhydroxides, i.e., CrO_3, $CrO_2(OH)_2$ and $CrO_2(OH)$ compounds, as shown in reaction equations 2–4 [16], [17]

$$2Cr_2O_3(s) + 3O_2(g) \leftrightarrow 4CrO_3(g) \tag{2}$$

$$2Cr_2O_3(s) + 3O_2(g) + 4H_2O(g) \leftrightarrow 4CrO_2(OH)_2(g) \tag{3}$$

$$Cr_2O_3(s) + O_2(g) + H_2O(g) \leftrightarrow 2CrO_2(OH)(g). \tag{4}$$

The partial pressures of the $CrO_3(g)$ (dominant in dry air) [16], [17] and $CrO_2(OH)_2(g)$ (dominant in humid air) [16]–[18] are the highest over $Cr_2O_3(s)$, meaning that these are the main Cr species in the SOFC cathode side atmosphere, in proportion of moisture content. These Cr species transport to a triple- or three-phase boundary (TPB), which is the shared interface of the electrolyte, the cathode and the gas phase, and through electrochemical reduction they transport back to Cr_2O_3 [18]. Over time, Cr_2O_3 blocks the effective TPB sites and causes a decrease in the electrochemical performance of the cell, i.e. degradation [19]–[21].

In general, it can be stated that Cr_2O_3 is deposited on the TPB, but the actual deposition site is associated to the electrolyte and cathode material employed. For a hole-conductive cathode, e.g. a $(La,Sr,Mn)_2O_3$ cathode, the deposition of Cr_2O_3 is localized on the TPB, also causing delamination of the cathode. For mixed-conductive cathodes, e.g. $(La,Sr,Fe)_2O_3$, $(La,Sr,Co,Fe)_2O_3$ and $(La,Sr,Co)_2O_3$ cathodes, the deposition is less localized to the TPB and more on the surface of the

cathode. [22] In addition, strontium chromate (SrCrO$_4$) nuclei have been observed to form when (La,Sr,Co,Fe)$_2$O$_3$ cathodes are used [18].

By using a special vacuum melting process, ferritic stainless steel with low amount of silicon (Si) can be obtained, such as commercial available Crofer 22 APU. Ferritic stainless steel with low Si obtains more favourable oxidation behaviour including oxidation rate and scale composition in the SOFC cathode side atmosphere. [23] In addition, Crofer 22 APU forms a scale with a dual layered structure due to Mn alloying. Figure 3 shows the scale consisting of sublayer of Cr$_2$O$_3$ and reaction layer of MnCr$_2$O$_4$ due to outward diffused Mn cations which should decrease the degradation and improve the electrical conductivity as reported in [24]. However, as seen in the Fig. 3, MnCr$_2$O$_4$ layer is not evenly formed and therefore protective arrangements are required to prevent chromium evaporation in order to achieve extended lifetime of the single cells and the SOFCs.
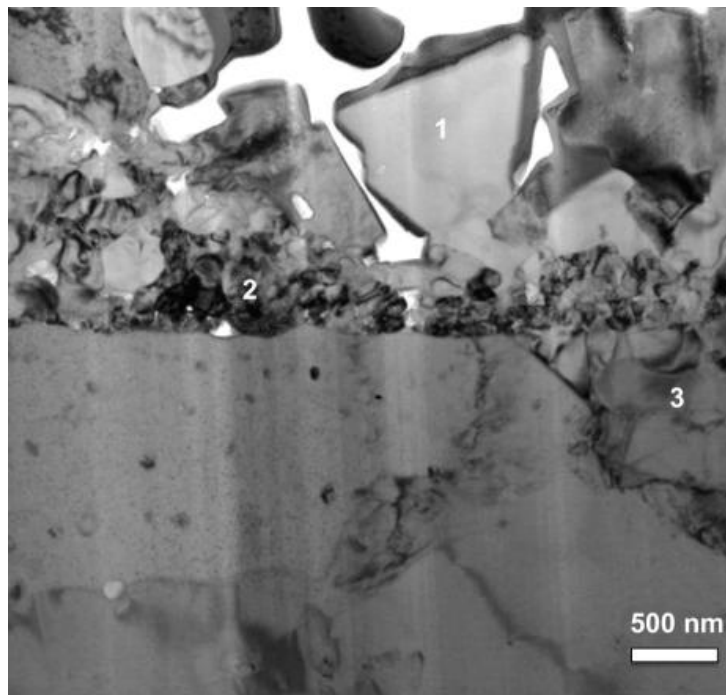

FIGURE 3 TEM cross-section image of Crofer 22 APU oxidized for 750 hours at 800°C, where (1) and (3) represent cubic MnCr$_2$O$_4$ spinel reaction layer and subscale pockets, respectively and (2) Cr$_2$O$_3$ layer [25].

The ferritic stainless steels manufactured with conventional (in normal atmosphere) methods, such as AISI 430, AISI 441 contain Si and niobium (Nb). Niobium is used to form (Fe,Cr)$_2$(Mo,Si,Nb) Laves phase [26] as it reacts with Si and decrease formation of silicon oxide (SiO$_2$) layer on metal/Cr$_2$O$_3$ interface [27]. However, part of Si is diffused to the surface and SiO$_2$ is formed. Silicon oxide can be categorized as an insulator by its electrical properties and hence, the use of this type of steels is questionable in the SOFC interconnectors [14].

2.2 Protective coatings

In order to increase the lifetime of the novel SOFCs and to prevent the degradation phenomena, ferritic stainless steel ICs must be coated prior to use in the SOFCs. The coating prevents Cr transport and thereby protects the cathode from degradation. The technical requirements for the interconnect-coating system are:

- low diffusion coefficient of Cr ions and low transport of Cr compounds [28],
- excellent electrical conductivity, with the objective of 100 % electronic conduction [12],
- chemical, microstructural and phase stability at the stack operating temperature in an oxidizing environment [12], [28],
- coefficient of thermal expansion (CTE) matches the other stack components such as the metallic interconnector and the cathode [12],
- suitable thermal conductivity, at least 5 W/mK, in order to transfer heat generated at the cathode to the anode for endothermic fuel reformation reactions [12],
- the coatings, together with the metallic substrate, should present high temperature strength, creep and spallation resistance and provide structural support when used as a stationary or an auxiliary power unit under external stresses and vibrations [12],
- simple and economical manufacturing process in mass production [12].

Several material compositions have been studied as possible candidates for protective coatings. When degradation was observed to be a consequence of reactions between volatile Cr species and the TPB, the studies were focused on the use of perovskite-type ceramic coatings, as they exhibit similar physical behaviour compared to the cathode layer. However, recently the focus has changed to spinel-type ceramics, as they seem to provide better protection against Cr poisoning as described in the following chapters.

2.2.1 Perovskite ceramics

Perovskites are ceramic materials with the generic formula of $(A,B)_2O_3$, where A and B refer to metallic cations and O for oxygen. The usage is based on the similar mechanical and chemical behaviour as the SOFC cathodes and favourable electrical properties. The studies are associated with doped $(La,Mn)_2O_3$ or $(La,Co)_2O_3$ perovskites. In many cases, the dopant is either Sr, Cr or Fe. [29]–[31]

Perovskite provides excellent electrical properties, and conductivity values of 645 up to 855 S/cm have been measured for Sr- and Sr-Fe-alloyed $(La,Co)_2O_3$ peroskites, whereas Sr-alloyed $(La,Mn)_2O_3$ have more moderate values in the order of 50 to 80 S/cm [30]. The use of $(La,Mn)_2O_3$ and especially Sr-doped $(La,Sr)MnO_3$ is based on the formation of a $Cr_2O_3/(Mn,Cr)_3O_4$ duplex

scale during the oxidation cycles, as the coating facilitates the internal diffusion of Mn in the $(Mn,Cr)_3O_4$ spinel layer [29], [31]–[34].

Although $(La,Sr)MnO_3$ perovskites show good electrical properties and formation of a duplex scale, the problem is a relatively high cation self-diffusion coefficient [34]–[36]. As a result, the Cr cations diffuse through the coatings during oxidation treatment in high temperatures, as reported e.g. in [32], [34], [37], which can cause degradation of the cathode in long-term use.

2.2.2 Spinel ceramics

Spinel is a ceramic material with the generic formula of $(A,B)_3O_4$, where A and B are metallic cations. The greatest interest in SOFC use is focused on $(Mn,Co)_3O_4$-based spinels. These have both cubic and tetragonal crystal structures, as shown in Fig. 4. According to Kurokawa et al. [37], Mn-Co spinels have a low Cr transport rate, providing even better Cr-barrier properties than perovskites. In addition, migrated Cr forms stable Cr-containing spinel compounds [38], [39], indicating that coating thickness may provide a buffer function in long-term use. Another advantage is the compatibility of CTE with ferritic stainless steel and perovskite-type cathodes, as reported in [40].
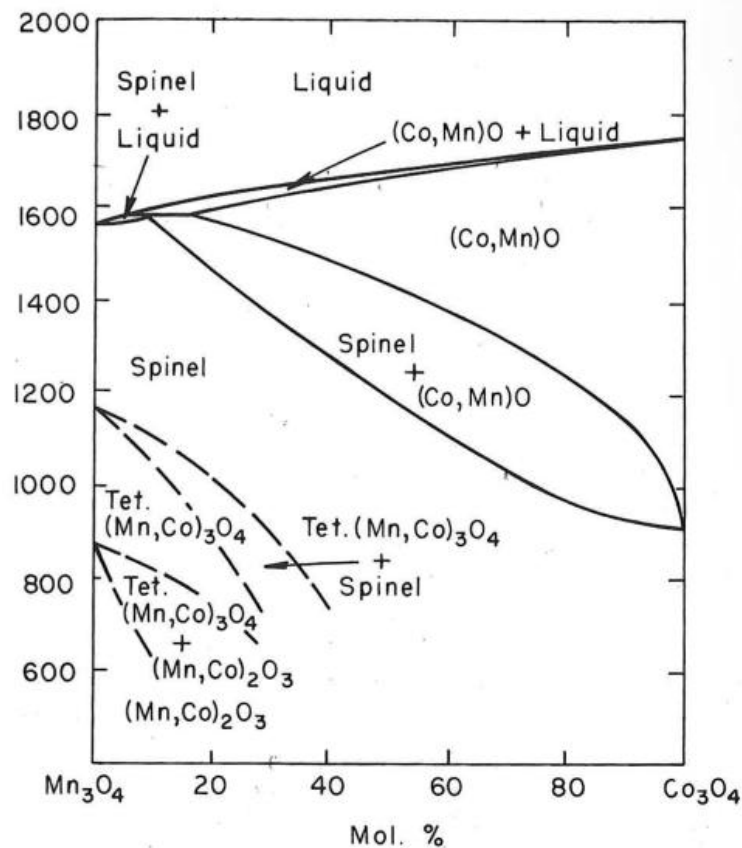

FIGURE 4 Phase diagram of Co_3O_4–Mn_3O_4 system in air [41].

$(Mn,Co)_3O_4$ spinels have acceptable electrical properties with electrical conductivities varying from 15 to 68 S/cm in a temperature range of 700 to 800 ºC [42], [43]. The conduction is caused by small polaron hopping, attributed to hopping between Mn^{3+}/Mn^{4+} on octahedral sites [24], [44]. In other words, the electron is excited across the band gap from the valence band to the conduction band and therefore a hole is formed in the valence band (intrinsic semiconductor) [45]. Although $(Mn,Co)_3O_4$ seems to be promising for protective coatings, it should be noted that perovskites do have significantly better electrical conductivity than $(Mn,Co)_3O_4$ spinels.

Iron doping, by obtaining $MnCo_{2-x}Fe_xO_4$, most likely enhances electronic conduction as studied in [44], [46], [47]. Doping causes the formation of $(Co^{2+},Mn^{2+},Fe^{3+})(Co^{2+},Co^{3+},Mn^{3+},Mn^{4+},Fe^{2+},Fe^{3+})_2O_4$ cation distribution in the spinel system [47], as Co cations have a stronger tendency to occupy tetrahedral sites compared to Mn cations, and Fe cations have a lower tendency to occupy tetrahedral sites than Co and Mn cations [44]. Due to the presence of mixed valence states at octahedral sites in the $(A,B)_3O_4$ spinel system, the activation energy (E_a) for $MnCo_{1.9}Fe_{0.1}O_4$ is 0.38 eV, i.e. lower than the E_a of $MnCo_2O_4$, which is 0.44 eV [47]. As a result, the following electronic conductivities have been reported: 37.5 S/cm for $MnCo_{1.9}Fe_{0.1}O_4$ at 800˚C in air [46], 72 S/cm for $MnCo_{1.9}Fe_{0.1}O_4$ at 800˚C in air [47] and 85 S/cm for $MnCo_{1.85}Fe_{0.15}O_4$ at 800˚C in air [44]. The small variation in electrical properties can be explained by the sintering temperature and remnant porosity. A further increase of iron decreased the electrical conductivity [44], [46] as the distance between the neighbouring octahedral sites increased [44].

2.2.3   Deposition methods

The protectiveness of spinel coatings is based on the chemical reactions with migrated Cr cations as described previously. In addition, Kurokawa et al. [37] have shown that the density of the $(Mn,Co)_3O_4$ spinel coatings, and various perovskites, dominates the suppression of the Cr migration rate. The density of the coatings becomes more important in harsh environments as the study of Persson et al. [31] showed. For example, a porous $(Mn,Co)_3O_4$ coating may suffer a breakaway oxidation effect (uncontrolled oxidation) above 900˚C, as the growing oxide scale causes spallation of the deposited coating.

2.2.3.1   Wet-ceramic processes

In wet-ceramic processes, protective coatings are manufactured by using a paste that is applied on the substrate by spraying [31], [40], [47]–[49], dip-coating [50], [51] or screen printing [29], [52]–[54], followed by calcination in order to obtain a "green-state" solid layer. The layer is then heat-treated, i.e. sintered to obtain dense and well-adhered coatings. The slurry is prepared by manufacturing the desired spinel powder, using either solid state or liquid state material synthesis, which is then mixed with dispersants and additives to obtain the optimal slurry properties required for the deposition process [55].

The properties of spinel coatings deposited by the wet-ceramic process have been widely studied, as reviewed in Table 2. The effective Cr barrier and electrical properties of the coatings are linked to the microstructures of the deposited coatings and achieved if a dense microstructure is obtained. With metallic substrates, conventional sintering temperatures, i.e. $0.5–0.8T_m$, [56] cannot be used directly, and therefore sintering is a two-phased process. First, the paste is heat-treated for several hours in a reducing atmosphere at 800–850°C, which is called reactive sintering. For $(Mn,Co)_3O_4$ coatings, this causes phase segregation and the formation of manganese oxide (MnO) and metallic cobalt (Co) phases [39], [49], [57]–[59]. The reactive sintered coatings have a porous microstructure, as reported in [49]. After reaction sintering, the coating is re-oxidized by heat treatment for several hours in an oxidizing environment, and as a result, the spinel structure and dense microstructure should be formed. However, in many cases, cross-section studies have shown that sintered coatings have porous microstructures with potential remnant porosity.

TABLE 2   Summary of ASR data of the relevant studies of coatings manufactured by wet-ceramic processes.

Material	Thickness (µm)	Substrate	Contact paste / Cathode	Oxidation time (h)	Temperature (°C)	ASR value (mOhm·cm^2)	Ref.
$Mn_{1.5}Co_{1.5}O_4$	20	Ducrolloy alloy	Perovskite/$(La,Sr,Mn)_2O_3$	10000 (prediction)	900	24	[29]
$Mn_{1.5}Co_{1.5}O_4$	10	Crofer 22 APU	$La_{0.8}Sr_{0.2}Co_{0.5}Mn_{0.5}O_3$/ $La_{0.8}Sr_{0.2}FeO_3$	1000	800	11.4	[52]
$Mn_{1.5}Co_{1.5}O_4$	10	Crofer 22 APU	Platinum/$(La,Sr,Co,Fe)_2O_3$	500	800	7.5	[49]
$Mn_{1.5}Co_{1.5}O_4$	20	Crofer 22 APU		1000		18	[50]
$MnCo_2O_4$	15-20	430SS		60/120	800/850	2.3	[40]
$MnCo_2O_4$	15-20	430SS		50000 (prediction)	850	500	[40]
$MnCo_2O_4$	5	232J3	Platinum	1000	850	12	[53]
$Cu_{0.2}Mn_{1.4}Co_{1.4}O_4$	20	Crofer 22 APU		1000	800	14	[50]
$Cu_{0.3}Mn_{1.35}Co_{1.35}O_4$	20	Crofer 22 APU		553	750	16	[51]
$Ni_{0.2}Mn_{1.4}Co_{1.4}O_4$	20	Crofer 22 APU		1000	800	18	[50]
$MnCo_{1.9}Fe_{0.1}O_4$	10	Crofer 22 APU	$(La,Sr,Co,Fe)_2O_3$ / $(La,Sr,Fe)_2O_3$	260	800	36	[54]
$MnCo_{1.9}Fe_{0.1}O_4$	10	Crofer 22 APU	$(La,Sr,Co,Fe)_2O_3$ /-	1000	800	33	[54]
$MnCo_{1.9}Fe_{0.1}O_4$		Crofer 22 APU	$(La,Sr,Fe)_2O_3$/ $Ce_{1-x}Sm_xO_2$ -YSZ	1000	800	800	[47]

Deposition of protective spinel coatings using a sol-gel process are studied in [60]–[63]. In sol-gel processes, the coating microstructure and phase structure are formed during calcination from hydrolysis and condensation reactions [64]. The heat treatment processes are fairly similar to the wet-ceramic processes described above. However, the coating thicknesses are usually less than 1 µm, and therefore the Cr-barrier properties are dubious in long-term (50 000 hours) use.

2.2.3.2 Vapour deposition methods

Vapour deposition methods include processes where the protective spinel layer is formed either by radio-frequency sputtering [49], [65] and magnetron sputtering [38], [66]–[69] or by the atomic layer deposition process [70]. It is characteristic for these methods that the coating thickness can be grown from a few nanometres up to several micrometres and that the microstructures are usually dense, producing good electrical properties, as shown in Table 3. Conversely, the deposition speed can be relatively slow, especially when thick coatings (several micrometres) are required.

TABLE 3   Studies containing ASR data for $(Mn,Co)_3O_4$ spinel coatings manufactured by vapour deposition methods.

Material	Thickness (µm)	Substrate	Contact paste / Cathode	Oxidation time (h)	Temperature (°C)	ASR value (mOhm·cm^2)	Ref.
$Mn_{1.5}Co_{1.5}O_4$	1	Crofer 22 APU	Platinum/ $(La,Sr,Fe)_2O_3$	275	800	19	[49]
$Mn_{1.5}Co_{1.5}O_4$	2	441HP	Platinum	1700	800	5.5	[68]
$Mn_{1.5}Co_{1.5}O_4$	0.3	ZMG232L	Platinum	500	800	59	[65]
$MnCo_2O_4$	15	Fe-21Cr	Platinum/-	1000	750	5	[38]
$MnCo_2O_4$	3	Crofer 22 APU	-/$La_{0.7}Sr_{0.3}MnO_3$	1000	800	9	[66]
$MnCo_2O_4$	3	Crofer 22 APU	-/$La_{0.7}Sr_{0.3}MnO_3$	5000	800	6	[66]

2.2.3.3 Conventional thermal spraying

The thermal spraying technique is well adapted to different industrial fields (wear, corrosion, thermal barrier coatings etc.) due to the large deposition temperature range, which then allows the use of a large variety of spray materials in the form of rod, wire or powder [71]. The basic principle in thermal spray techniques is that the feedstock material melts due to the heat content of the thermal flame. The flame temperature varies from 2500 to 3160ºC when using high velocity oxy-fuel spraying (HVOF) [72], [73] and up to 15 000ºC when employing atmospheric plasma spraying (APS) [71]. As the spray feedstock enters the thermal flame, heat is transferred from the flame to the feedstock material. As a consequence, molten or semi-molten droplet/particles are formed, which are accelerated towards the substrate due to the high velocity gas flow. As a final step, the droplets spread, impacting the substrate, generating a coating with a lamellar microstructure. [71] As-sprayed coatings are fairly dense due to the closely packed molten and solidified droplets, as shown in Fig. 5.
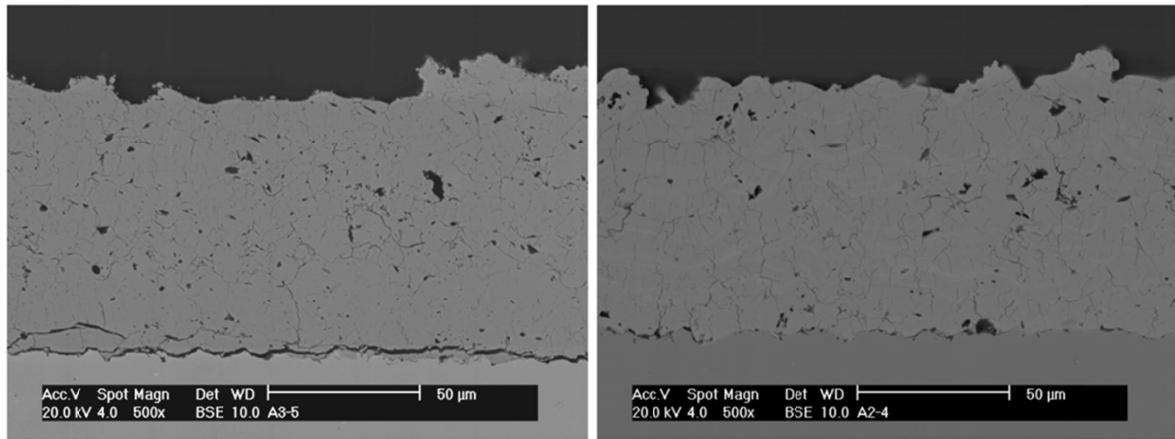
FIGURE 5 Atmospheric plasma sprayed $(Mn,Co,Fe)_3O_4$ spinel (left) and $(La,Sr,Co,Fe)_2O_3$ perovskite (right).

Studies on manufacturing protective coatings for ICs by thermal spraying are related to perovskite [29], [34], [74]–[78] and spinel materials [79]–[82]. Since the coatings are manufactured by a process where the materials are exposed to high temperature and fast transformation of the solid-liquid-solid state, it can cause selective evaporation of some elements and phase decomposition of perovskites [34], [75], [77], [78] and spinels [80], [81]. However, the decomposed phases were recovered during post-deposition heat treatment indicating that as-deposited phases have metastable characteristics. Although some selective evaporation of the metallic elements has been reported and as-sprayed coatings are metastable, the microstructures of as-sprayed coatings are dense and therefore these coatings should provide good protection against volatile Cr compounds, decreasing the growth of oxide scale and obtaining acceptable ohmic resistances, as shown in Table 4.

TABLE 4 Available ASR values for spinel coatings manufactured by thermal spraying processes.

Material	Thickness (µm)	Substrate	Contact paste / Cathode	Oxidation time (h)	Temperature (°C)	ASR value (mOhm·cm^2)	Ref.
$MnCo_2O_4$	20-28	Cfrofer 22 APU	-/$La_{0.85}Sr_{0.15}Mn_{1.1}O_3$	1000	700	20	[81]
$MnCo_2O_4$		F17TNb	-/$(La,Sr,Co,Mn)_2O_3$	575	800	50	[79]
$MnCo_{1.8}Fe_{0.2}O_4$	15-18	Cfrofer 22 APU	-/$La_{0.85}Sr_{0.15}Mn_{1.1}O_3$	1000	700	20	[81]

2.2.3.4 Solution precursor thermal spraying

Solution precursor thermal spraying (SPTS) is a process where the feedstock is in the form of a liquid solution, and not a dry powder as in conventional thermal spraying. The process is a

development of the powder synthesis process called liquid flame spaying (LFS) [83]–[85]. The liquid solution is a mixture of inorganic salts and/or metallo-organic compounds called precursors dissolved in organic or inorganic solvents such as alcohols or water [86]. The solution precursor is fed into the high temperature flame, which can be either plasma, as in APS, or formed by burning combustible gases, as in HVOF or LFS processes.

In order to form a solid coating, the solution precursor must go through a material synthesis phase. As the solution precursor is fed into the thermal flame, the shear stress exerted by the flowing gas atomizes the precursor stream. The heat energy of the thermal flame is then transferred into the droplets. A small droplet size is preferred for more effective heat transfer in order to i) evaporate the solvent, ii) obtain effective precipitation and pyrolysis reactions of the metallic salts, and finally ii) melt the synthesized material, as shown in Fig. 6. [87]–[92]
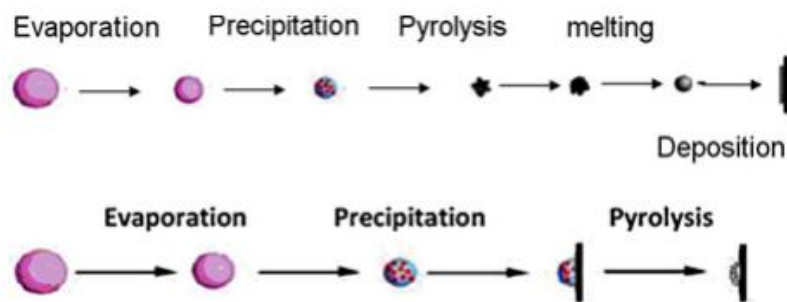

FIGURE 6   Schematic presentation of the solid evolution in the solution precursor thermal spray process [89].

Studies related to applications with a similar approach to SPTS processes are based on solution precursor plasma spraying processes (SPPS), for example, porous yttria-stabilized zirconia (YSZ) as in thermal barrier coatings [91], [93]–[101], a dense YSZ electrolyte layer [102], [103], a porous anode with a YSZ-Nickel composition [104]–[106] and an $(Sm,Sr,Co)_2O_3$ cathode [107] for SOFC applications. In addition, functional titanium dioxide (TiO_2) [108]–[110] and bio active glass-ceramics [111] manufactured by SPPS have shown great potential in their own specific research fields. The SPPS process has been studied for the manufacture of $(Mn,Co)_3O_4$ coatings in [112], [113] obtaining the desired crystallographic structure. However, the microstructures were porous and therefore cannot be used as protective coatings, as shown in Fig. 7.
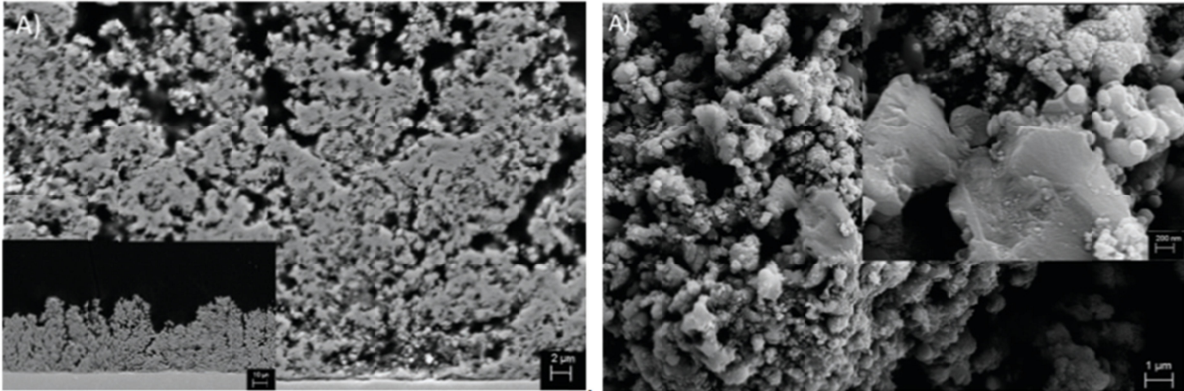
FIGURE 7   Cross section (right) and topography (left) images of SPPS MnCo$_2$O$_4$ coatings [113].

Most of the studies conducted on high velocity solution precursor flame sprayed (HVSPFS) or comparable methods are related to the modelling of droplet behaviour during the spray process [114]–[119]. Chen et al. [120] have studied HVSPFS processes for manufacturing Al$_2$O$_3$-ZrO$_2$ coatings, showing that by employing the process, it is possible to produce coatings with a dense microstructure. Since the crystallographic structure of the (Mn,Co)$_3$O$_4$ spinel was obtained by using the SPPS process, it is most likely that coatings with a dense microstructure and optimal crystal structure can be obtained by employing a deposition process with high particle velocity such as HVSPFS.

In general, it can be stated that various coating methods as listed previously show great potential when used to deposit protective coatings on an IC to prevent harmful cathode degradation. As long as the dense microstructure and desired crystallographic phase structure are obtained, the coatings should prevent the migration of Cr cations, decrease the oxidation rate of the ferritic stainless steel without significantly increasing the ohmic resistance of the IC. However, in order to decrease the manufacturing cost, the coating methods should be economical, meaning that the number of separate process steps should be as low as possible. In addition, the coating method should be scalable to industrial production when the production rates are several million ICs per year. Great added value is obtained by the convertible coating process in depositing other material compositions. When taking into account these aspects, thermal spraying, and especially the SPTS process, should be one of the most promising techniques for adoption to produce coatings for SOFC components.

3 Aim, research questions and scientific contribution of the thesis

The aim of this work was to study the properties of thermally sprayed spinel coatings for ICs used in SOFCs with a planar structure. Thermal spraying is a widely used deposition technique in industrial applications as described previously, and therefore has potential for manufacturing thin and dense ceramic coatings. In addition, a novel thermal spraying technique, i.e. SPTS, was studied as it shows great potential in the thermal spraying field. Figure 8 shows the structure of the thesis and how the journal papers [I–VI], containing the relevant research information, are interlinked.
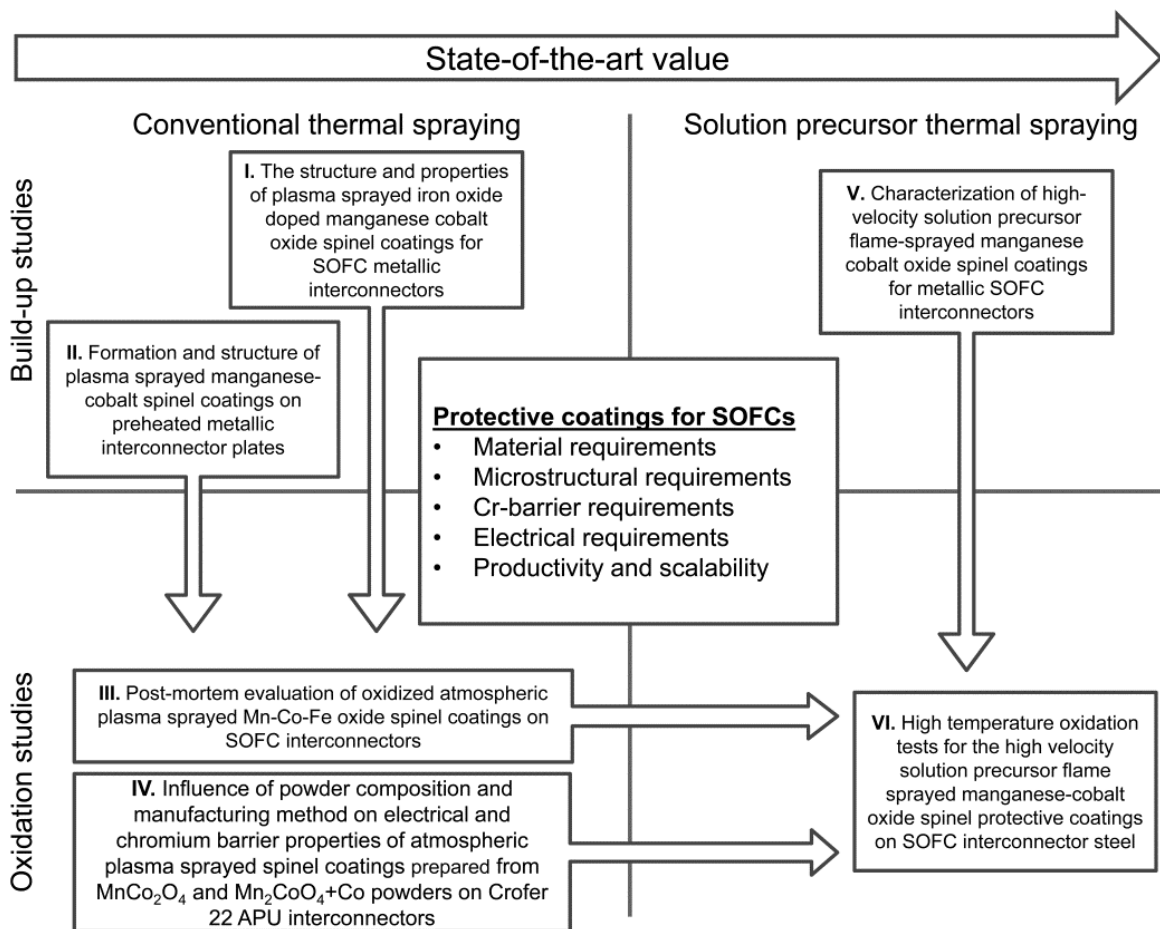

FIGURE 8   The structure of the thesis and relationship of the published papers [I–VI].

The work was executed organized in such a way to answer the following research questions:

1. What benefits can be obtained when protective spinel oxide coatings are manufactured employing the thermal spraying technique?

2. Which material and feedstock characteristic aspects should be taken into account when manufacturing thin and dense protective coatings by thermal spraying?

3. Is HVSPFS a viable deposition technique for producing thin and dense spinel coatings for SOFC applications?

4. What are the properties and the benefits of using HVSPFS compared to conventional thermal spraying methods?

The research is based on studying the coating build-up mechanism and how the microstructures that are characteristic for the various thermal spraying techniques influence coating behaviour in long-term oxidation cycles. The oxidation cycles simulated the SOFC cathode side oxidizing atmosphere in a temperature range of the order of 700 to 850ºC. Journal papers [I and II] are focused on the study of optimizing the parameters for coating build-up mechanisms when $(Mn,Co)_3O_4$ and Fe doped $(Mn,Co,Fe)_3O_4$ spinels are sprayed using the conventional thermal spraying technique. The aim was to obtain as dense coatings as possible with the lowest possible influence on the chemical balance. The findings were used when manufacturing coatings for long-term oxidation, including electrical Cr-barrier studies in journal papers [III and IV], in order to benchmark spinel materials that show the greatest potential for protective coatings. The usability and coating formation mechanisms of solution precursor thermally sprayed coatings were studied in journal papers [V and VI]. The findings according to the material specific behaviour from the studies published in [III and IV] were used in research paper [VI], where the thermally sprayed solution precursor coatings were manufactured and tested in a high-temperature oxidizing environment.

Scientific contribution of the thesis is as follows:

- Material compositions and optimal particle morphology is proposed when employing conventional thermal spray technique, i.e. APS for producing protective $(Mn,Co)_3O_4$ spinel coatings on ICs steels.

- Novel HVSPFS technique is described, i.e. coating formation mechanism and coating microstructures are studied and reported for the first time when manufacturing $(Mn,Co)_3O_4$-based spinels. The results are presented in comparison to the conventional thermal spray technique.

- The root cause for the thermal decomposition of the $(Mn,Co)_3O_4$-based spinel was studied and the temperature depended recovery process is presented for the first time.

- Cr barrier and electrical properties of the APS and HVSPFS $(Mn,Co)_3O_4$-based coatings are studied and high the temperature sintering process is proposed.

4 Materials and methods

This chapter introduces the materials and methods employed in this study. The first part of this chapter briefly explains a commercially available substrate and spray material, followed by a more detailed description of the material synthesis for spray powders made in collaboration with the Technical Research Centre of Finland and solution precursors made in-house. The second part focuses on methods such as spray processes and characterization techniques.

4.1 Materials

Substrate

Crofer 22 APU (ThyssenKrupp VDM GmbH), ferritic stainless steel (Table 5) particularly designed for SOFC applications was used as a substrate. Crofer 22 APU exhibits similar CTE behaviour as the other cell components and acceptable corrosion behaviour at the SOFC running temperature and atmosphere. The surface roughness (R_a) was less than 0.5 µm, representing the surface quality as received from the factory. Two different substrate thicknesses were employed: 0.20 and 0.50 mm. Prior to the spraying process, the substrates were grit-blasted using 240 grit Al_2O_3 sand or cleaned in ethanol to remove surface contamination and to provide a mechanical anchorage for the coatings. Grit blasting was used prior to atmospheric plasma spraying, whereas only ethanol cleaning was used prior to high velocity solution precursor flame spraying.

TABLE 5   Chemical composition of Crofer 22 APU in wt% [121].

	Cr	Fe	C	Mn	Si	Cu	Al	S	P	Ti	La
Min.	20	Bal.		0.3						0.03	0.04
Max.	24		0.03	0.8	0.5	0.5	0.5	0.020	0.050	0.20	0.20

Powder feedstock

In the conventional thermal spraying process, which in this case means the APS process, the spray material was in the form of a dry powder. The $MnCo_{1.8}Fe_{0.2}O_4$ [Publications I and II], $MnCo_{1.7}Fe_{0.3}O_4$ [Publication III] and Mn_2CoO_4+Co [Publication IV] powders were made in collaboration with the Technical Research Centre of Finland, whereas the $MnCo_{1.9}Fe_{0.1}O_4$ [Publication III] and $MnCo_2O_4$ [Publication IV] powders were commercially acquired from H.C. Starck and the Swiss federal laboratories for materials science and technology (EMPA), respectively.

In HVSPFS, which can be stated to be a novel thermal spraying technique, the spray material was in the form of a liquid solution containing metallic salts. The $MnCo_2O_4$ [Publication V], $Mn_{1.5}Co_{1.5}O_4$ [Publication VI] and $MnCo_{1.9}Fe_{0.1}O_4$ [Publication VI] solution precursors were prepared in-house.

The spinel powders with a composition of $MnCo_{2-x}Fe_xO_4$ [Publications I–III] were produced by solid-state synthesis. The synthesized powders were agglomerated by a spray drying process to obtain spherical form in order to have good flowability in the powder feeder equipment employed in thermal spray systems. The powder synthesis process was started by weighing appropriate amounts of manganese(II) carbonate ($MnCO_3$), cobalt(II) carbonate ($CoCO_3$) and iron oxide (Fe_2O_3), so that a stoichiometric factor x in $MnCo_{2-x}Fe_xO_4$ of 0.2 [Publications I and II] or 0.3 [Publication III] was obtained. The powders were mixed together by milling them for 20 hours in a drum ball mill. After the milling phase, the mixture of powders was calcined at 1000°C in air for six hours. The acquired spinel structure was formed during the calcination process. The calcinated spinel powder was then dispersed in water using 1 wt% of Dispex A40 dispersant and mixed in a planetary ball mill for two hours at 300 rpm with ZrO_2 balls (Fritsch pulverisette 5, Fritsch GmbH). The slurry was then mixed with a high shear mixer and 2 wt% of organic bonding agent polyvinyl acetate (PVA) was added to form a suspension for the spray drying process. The suspension was fed into a spray dryer (Niro pilot, GEA Niro) equipped with a high-speed rotation nozzle to obtain fine agglomerate powder. The powder was sintered at 1150°C to improve powder strength, where an isothermal step at 500°C for two hours was used in order to pyrolyse the dispersant and the organic binder without fracturing the agglomerates. After sintering, the powders were sieved to collect the desired particle size range for the thermal spray process.

The Mn_2CoO_4+Co powder [Publication IV] that corresponded to a composition of $Mn_{1.5}Co_{1.5}O_4$ was manufactured by solid-state synthesis by weighing appropriate amounts of $MnCO_3$, $CoCO_3$ and metallic cobalt (Co). The carbonate powders were milled for 20 hours in a drum ball mill and calcined at 800°C in air for 6 hours to obtain the spinel structure. The spinel powder obtained was mixed with metallic Co and dispersed in water using 1 wt% of Dispex A40 dispersant using a planetary ball mill for two hours at 300 rpm with steel balls and vials (Fritsch pulverisette 5, Fritsch GmbH) to form a suspension. The suspension for the spray drying process was prepared by adding 2 wt% of PVA in a high shear mixer. The suspension was then spray-dried and the agglomerated powder was sintered at 1050°C in an argon + 3 % helium atmosphere in order to improve the strength of the powder without oxidizing Co. An isothermal step at 500°C was used for two hours in order to pyrolyse the dispersant and the organic binder without fracturing the spray-dried agglomerates.

The solutions were prepared by dissolving the stoichiometric weights of manganese(II) nitrate tetrahydrate ($Mn(NO_3)_2 \cdot 4H_2O$), cobalt(II) nitrate hexahydrate ($Co(NO_3)_2 \cdot 6H_2O$) and iron(III) nitrate nonahydrate ($Fe(NO_3)_3 \cdot 9H_2O$) into deionised water to form $MnCo_2O_4$ [Publication V], $Mn_{1.5}Co_{1.5}O_4$ [Publication VI] and $MnCo_{1.9}Fe_{0.1}O_4$ [Publication VI] coatings during the HVSPFS process.

Deionised water and a cationic concentration of 3 mol/L were used due to the promising results reported in [112].

4.2 Methods

Two thermal spray techniques were used in this study. The coatings in [Publications I - IV] were manufactured by the APS process, which can be considered a conventional thermal spraying technique. The more novel process method used in [Publications V and VI] is called HVSPFS. This is a modification of the conventional HVOF spraying process.

The characterization was focused on i) the spray material; ii) as-sprayed and iii) oxidized coatings. The spray material characterization studies included qualitative and quantitative and microstructural analysis, in addition to rheological and thermal decomposition studies for the solution precursor feedstock. The as-sprayed and oxidized coatings were mainly studied using qualitative and quantitative analysis methods, including on-line electrical analysis simultaneously during the oxidation cycles.

Atmospheric plasma spraying

The APS coatings were manufactured by using atmospheric plasma spraying equipment (A3000S 4/2 plasma spray system, Sulzer Metco) equipped with a 55 kW plasma gun (F4-MB, Oerlikon Metco), as shown in Fig. 9. The gun enabled the use of argon, nitrogen, helium and hydrogen or a ternary gas composition as plasma gases. In this study, the plasma plume was formed using argon and helium gases. The agglomerated powder was fed radially into the plasma plume. The spraying parameters were optimized to form a dense microstructure with a low coating thickness [Publication I and II]. The movement of the plasma torch was controlled by an x-y manipulator.

FIGURE 9   Sulzer Metco F4-MB plasma gun with a cut-away image on the right.

As described in the introduction, the APS coatings contain pores which may interlink and form an open porosity. Therefore, simultaneous substrate heating was used in the coatings [Publications II–IV] together with the plasma spraying process, in order to obtain a dense microstructure. An induction heater (Minac 18/25, EFD Induction) was used for substrate heating. The temperature of the substrates was increased to the desired level and kept constant during the spraying process. A K-type thermocouple that was attached to the back of the substrates provided temperature information for the induction power controller. The controller monitored the influence of the plasma plume on the substrate temperature and adjusted the heating power appropriately. After spraying, the samples were cooled back to room temperature freely with the fixture. The recorded cooling rate was ~50°C/min.

High velocity solution precursor flame spraying

The HVSPFS coatings were manufactured using a modified high velocity oxy-fuel system (HVOF, TopGun, GTV Verschleiss-Schutz GmbH), as shown in Fig. 10. The torch consisted of a 22 mm combustion chamber, a 135 mm expansion nozzle with a 8 mm hole, and a specially designed liquid injector nozzle system supplied by Fraunhofer IWS. Ethene and oxygen were used as combustion gases. The normalized molar-based oxygen-ethene ratio was adjusted between 1.00-1.05. Two non-atomizing solid stream liquid injector nozzles with diameters of 250 μm and 300 μm were used to inject the liquid precursor into the combustion chamber. A pressurized vessel with a rotometer was used to control the solution flow rate, and exceed the back pressure of the HVOF torch while coating.

FIGURE 10 GTV high velocity oxy-fuel torch with liquid injector nozzle.

Feedstock specific characterization

Particle size distributions prior to the APS processes in [Publications I–IV] were measured by laser diffraction (Helos laser diffraction sensor, Sympatec GmbH) using wet conditions. Ultrasonic and mechanical mixing were used to avoid agglomerations during the measurements.

The rheological properties of the $MnCo_2O_4$ [Publication V] $Mn_{1.5}Co_{1.5}O_4$ [publication VI] and $MnCo_{1.9}Fe_{0.1}O_4$ [publication VI] solution precursors were analysed with a rotational rheometer (Haake RheoStress 150, Thermo Fisher Scientific) at a temperature range of 22–24 ºC.

Microstructural, elemental and phase characterization

Microstructural characterizations for the powders and the as-sprayed coatings in [Publications I, II] were performed using a scanning electron microscope (SEM, Phillips XL 30, Phillips), equipped with energy-dispersed spectroscopy (EDS). Field-emission scanning electron microscopy (FESEM, Carl Zeiss ULTRAplus, ZEISS) combined with energy dispersive X-ray spectroscopy (EDS, INCA Energy 350, Oxford Instruments) was used for the powder, the as-sprayed and the oxidized coating studies in [Publications III–VI]. The microscopes were used in the secondary electron (SE) mode. Before the SEM and FESEM studies, the as-sprayed and oxidized samples were cut and moulded in epoxy in a chamber under reduced pressure to avoid cracking and to give mechanical support while polishing the cross-section surfaces.

An optical profilometer (Wyko NT1100, Veeco) was used for a single splat profile analysis, splat size distribution measurements and the APS coatings build-up studies reported in [Publication II]. The build-up mechanisms and especially the splat adhesion were studied with a micro-hardness tester (MMT-XL, Matsuzawa) using a relatively low 250 mN test load [publication I]. The HVSPFS coating build-up studies were characterized by using higher magnification inspections. These were carried out using an in-lens mode FESEM and transmission electron microscope (TEM, Jeol JEM 2010 analytical, JEOL ltd.) in [Publication VI].

Qualitative phase analyses for the powder, as-sprayed coatings and oxidized coatings were studied using a X-ray diffractometer (XRD, Siemens D-500, Siemens) in [Publications I and II] and X-ray diffractometer (XRD, Empyrean, PANalytical B.V.) in [Publications III-VI] with a Cu-K$_\alpha$ radiation source. The data was background corrected and crystallographic data, such as crystallite size and d-spacing values were calculated using HighScore Plus software.

The elevated temperature phase analysis was perfomed with an X-ray diffractometer equipped with a high temperature stage (XRD, PANalytical X'Pert PRO, PANalytical B.V.). The test was done for the as-sprayed and decomposed APS $MnCo_{1.7}Fe_{0.3}O_4$ coating, in order to study the recovery process of the spinel. The XRD study was conducted by placing a free-standing coating sample of (10*20 mm) onto a resistance-heated Pt strip and controlling its temperature through a thermocouple. Patterns were acquired in isothermal conditions at 25, 400, 600, 800, 1000 and

1200°C. Heating from one temperature to the next took place in 24 minutes in all cases. Acquisition conditions included a step size of 0.020 º, a counting time of 2.70 s/step and an angular range of 28º ≤ 2Θ≤ 47º. [Publication III]

Additional phase analyses were performed using μ-Raman spectroscopy (LabRam, Horiba Jobin-Yvon), with a 632.81 nm-wavelength He:Ne laser focused through a 100x objective [Publication III]. The second Raman study was done using a spectrograph (Andor Shamrock 303, Oxford Instruments) and spectroscopic CCD camera (Andor Newton 940P, Oxford Instruments) The excitation laser (Cobolt Samba) had a 532 nm wavelength with a beam diameter of 0.7 mm [Publication VI].

The selective elemental evaporation studies on the $MnCo_{1.7}Fe_{0.3}O_4$ powder and the APS coating were conducted by X-ray fluorescence (XRF, Advant'X spectrometer, ThermoFisher Scientific). In addition, the evaporation of elements was studied by inductively coupled plasma – atomic emission spectrometry (ICP – AES, Liberty 200, Varian Inc.). Prior to the ICP – AES analysis, the coating was removed from the substrate, manually ground in an agate mortar and dissolved in a hydrochloric acid aqueous solution. [Publication III]

The qualitative compound studies of the nitrate precursors and the HVSPFS as-sprayed coatings were analyzed by Fourier transform infrared spectroscopy (FT-IR, Spectrum One, PerkinElmer) to determine the presence of nitrates after the spraying process. The as-sprayed coatings were removed from the substrates and manually ground in an agate mortar. To obtain reference data, nitrates were dissolved in deionized water and dried at 50ºC. The powder samples were pressed into KBr pellets (sample/KBr ratio being 2/200) and the spectra were measured and presented in the range of 4000–750 cm^{-1}. Thermal decomposition analyses for the nitrate precursors were carried out by differential thermal analysis combined with differential scanning calorimetry (DTA-DSC, PerkinElmer 6000, PerkinElmer). Prior to the DTA-DSC tests, nitrates were dissolved in deionized water and dried at 50ºC to obtain homogenous precursor powder. The heating rate was 10 K/min using oxygen as the atmosphere. [Publication VI]

Quantitative elemental analyses for the oxidized HVSPFS coatings were studied with a radio frequency glow discharge optical emission spectrometer (RF-GD-OES, GD-Profiler HR, HORIBA Jobin Yvon GmbH) in [Publication VI]. The oxidized coatings were sputtered with a 5 mm spot size. The vaporised coating material was analysed in order to obtain a more comprehensive picture of the elemental diffusion during the oxidation cycles.

Oxidation cycle and in-situ electrical measurements

Area specific resistance (ASR) tests were utilised with a four-point method for the coated samples. Three different test set-ups were carried out for measuring the electrical properties of the coated samples. The same samples were used for the post-mortem analysis, including microstructural

and Cr-barrier studies. The measurements were carried out without a contact paste, and therefore the results show only substrate-coating/coating-substrate contact data, including the oxide scale formed between the substrates and the coatings.

The ASR study for the APS-sprayed spinel coatings was carried out at 700°C in air for 1000 hours. The voltage drop was measured over the corrugated and coated 0.2 mm Crofer 22 APU in contact with the coated 1.0 mm flat Crofer 22 APU coupons. The top of the corrugation ridges formed the actual contact area, calculated to be 1.25 cm^2 in total. The samples were arranged as a stack and pressed together by a force of 49 N, whereby the estimated contact pressure was 0.40 MPa. Direct current (DC), estimated as 640 mA/cm^2, was used throughout the test procedure. [Publications III and IV]

The APS-sprayed MnCo$_{1.7}$Fe$_{0.3}$O$_4$-coated Crofer 22 APU was tested together with a La$_{0.85}$Sr$_{0.15}$Mn$_{1.1}$O$_3$ spacer (IRD Fuel Cells A/S) to simulate the contact resistance with the SOFC cathode. Two flat (26*26*0.2 mm) and coated Crofer 22 APU coupons were stacked with the spacer. A load of 20 N was applied, causing a surface pressure of 29.5 kPa. The DC density was 200 mA/cm^2. The samples were heated (15°C/min) up to 850°C and sintered for 12 hours to improve the contact between the samples and the spacer, then cooled to 700°C for the ASR test, which was carried out for 1000 hours. [Publication III]

The ASR study for the HVSPFS spinel-coated Crofer 22 APU substrates was performed at 850°C in air for 500 hours. The coated sample disks with a diameter of 25.4 mm were facing each other and a force of 9.81 N was applied, causing 4.50 kPa surface pressure. The DC density was 500 mA/cm^2. [Publication VI]

5 Results and discussion

In this chapter, the most important results of the six published journal papers are presented and discussed. The chapter is divided into three different sections. The first and second sections describe the coating formation mechanisms of APS and HVSPFS coatings, including the microstructural, chemical and phase analysis. The third section combines the data of the oxidized coatings, including the microstructural analysis, Cr-barrier studies and electrical properties.

5.1 Conventional plasma spraying

The conventional APS process is a common deposition method in different industrial applications and research information is widely available. In this study, the APS process was used to manufacture coatings using fused and crushed or agglomerated and sintered $(Mn,Co,(Fe))_3O_4$ and $(Mn,Co)_3O_4$ spinel-based spray powders.

5.1.1 Powder feedstock

The typical morphology of the spray-dried and sintered $MnCo_{2-x}Fe_xO_4$ powders is presented in Fig. 11. The spray drying process forms spherical agglomerates, which are sintered by a post-heat treatment process. The round morphology is a more favourable form, which enhances flowability during plasma spraying in the powder-feeding equipment. The particle size ranges of the iron-doped spinel powder varied between -36 +13 μm (d_{90}-d_{10}).
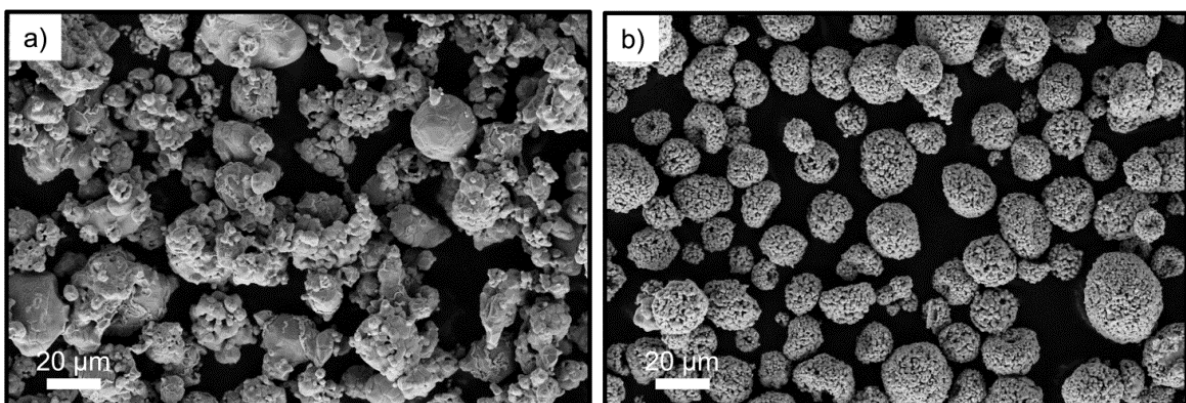

FIGURE 11 Morphologies of a) commercially acquired $MnCo_{1.9}Fe_{0.1}O_4$ and b) agglomerated and sintered $MnCo_{1.8}Fe_{0.2}O_4$ and $MnCo_{1.7}Fe_{0.3}O_4$ powders [Publication III].

The X-ray diffraction pattern in Fig. 12a shows that the $MnCo_{2-x}Fe_xO_4$ powders had corresponded closely to the cubic $MnCo_2O_4$ phase. However, the iron doping caused an increase in the unit cell volume. The XRD pattern shifted to lower Bragg angles as the Co cations were replaced by Fe cations. The d-spacing values were 0.25 nm and 0.26 nm for $MnCo_{1.9}Fe_{0.1}O_4$ and $MnCo_{1.7}Fe_{0.3}O_4$, respectively, measured from the atomic plane (311). The Fe^{3+} cations embraced a higher ionic radius compared to Co^{3+} cations, with radii values of 0.645 Å and 0.61 Å, respectively [122].
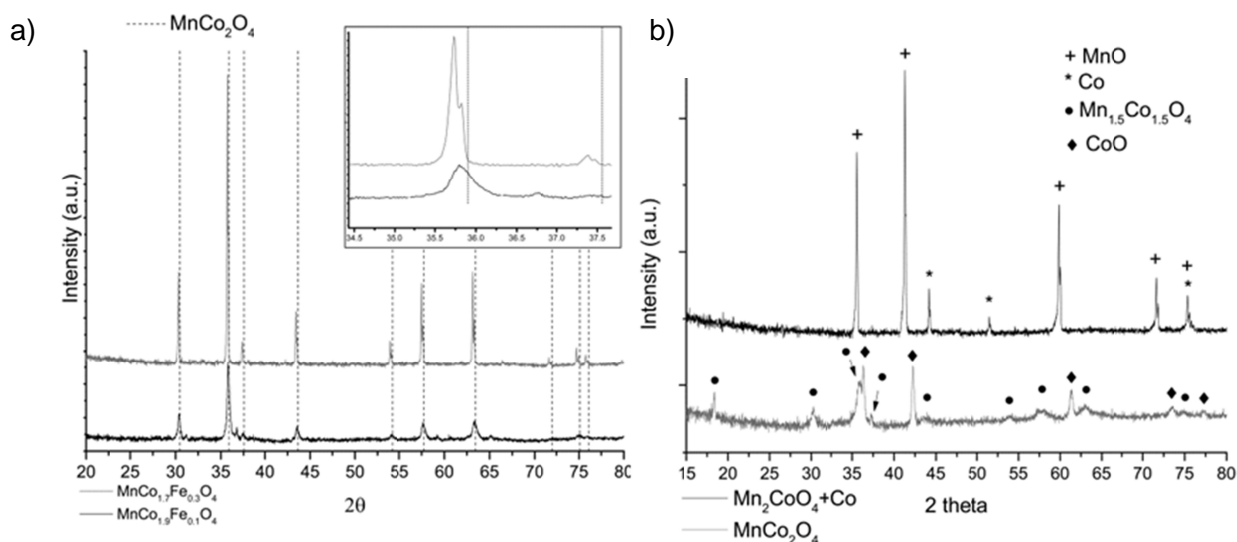
FIGURE 12 Crystallographic phase analysis of a) $MnCo_{2-x}Fe_xO_4$ powders [Publication III], b) $MnCo_2O_4$ [Publication IV] and Mn_2CoO_4 + Co spray powders [Publication IV].

The commercial fused and crushed $MnCo_2O_4$ spinel powder with a particle size range of -33 + 6 µm (d_{90}-d_{10}) contained partially agglomerated and sintered particles, as shown in Fig. 13a. According to the XRD analysis shown in Fig. 12b, the material synthesis was partially completed. The powder contained $Mn_{1.5}Co_{1.5}O_4$ and CoO phases, but should have formed the cubic $MnCo_2O_4$ spinel structure during in-situ oxidation.

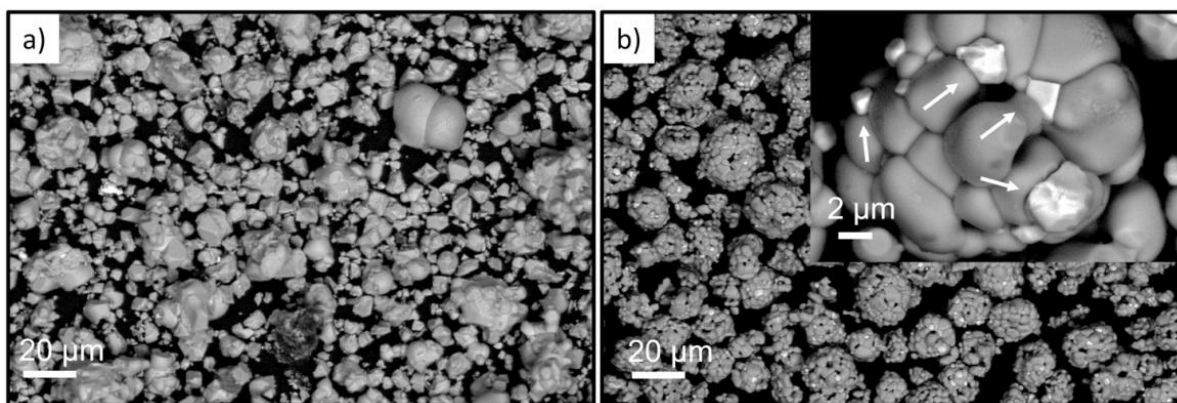FIGURE 13 Morphologies of a) $MnCo_2O_4$ and b) Mn_2CoO_4 + Co spray powders [Publication IV].

Figure 13b presents spray-dried and sintered Mn_2CoO_4+Co powder with a particle size range of -36 +11 µm (d_{90}-d_{10}). The powder contained MnO and Co phases, as shown in Fig 12b. Xianshuang et al. [59] have obtained the same dual-phase structure when post heat-treating $Mn_{0.9}Y_{0.1}Co_2O_4$ spinel powder in an H_2 atmosphere. The aim of using this cermet type of powder is to reduce intersplat cracks and pores as the Co works as a binder during the spraying process because it melts at a lower temperature. Oxidation of the added Co with Mn_2CoO_4 forms $Mn_{1.5}Co_{1.5}O_4$, which should eventually form a dual-phase structure of $[Mn_{1+\delta}Co_{2-\delta}O_4]_{cubic}$ and $[Mn_{2-\delta}Co_{1-\delta}O_4]_{tetragonal}$ phases, and no other undesirable compounds or side products.

5.1.2 As-sprayed coatings

Microstructures

The spinel coatings presented in Fig. 14 have the typical microstructure of an APS coating, containing pores and cracks when deposited on non-heated substrates. The remnant crack and pore distribution is a consequence of the spreading mechanism of the molten or semi-molten material droplets, i.e., splats [71]. The optical profilometer studies presented in Fig. 15 show that the splats have a flower-like pattern when deposited on substrates without heating. This kind of splat pattern is a consequence of the irregular cooling and high quench rate of the spreading splat. Inadequate melting of the particles (either larger particles or low flame temperature) has caused un-molten cores, which are loosely attached to the substrate.
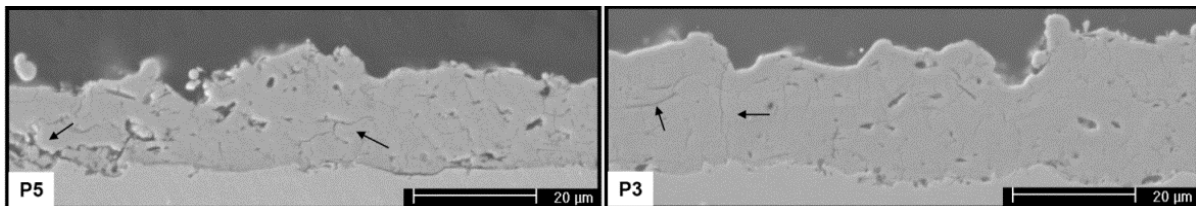

FIGURE 14 Cross-sectional SE-images (SEM) of plasma sprayed spinel coatings deposited with different spraying parameters. The as-sprayed coating with 6.9 vol% porosity (right) and the as-sprayed coating with 3.8 vol% porosity (left) [Publication I].

The microstructure of the as-sprayed coating is a consequence of the spraying parameters used for the specific powder composition and morphology. McPherson and Shafer [123] have studied inter-splat bonding and found that contact may be only 25 % of the total splat area, causing inter-lamellae gaps varying from 0.01 to 0.10 µm. By altering the parameters, the porosity of the as-sprayed coatings varied between 3.8 vol% to 6.9 vol% and the hardness values from 375 $HV_{0.025}$ up to 575 $HV_{0.025}$ [Publication I], specifying how well the deposited splats are adhered to each other. Cold spray conditions caused the droplets to be inefficiently spread on the substrate and particles were only partially molten. It is clear that poor inter-splat bonding increases the ohmic resistance of protective coatings and forms a pathway for volatile Cr compounds. When the gun power was

increased, the single particles were able to achieve a fully molten state and spread more efficiently, due to the increased flame temperature and kinetic energy of the molten droplet.
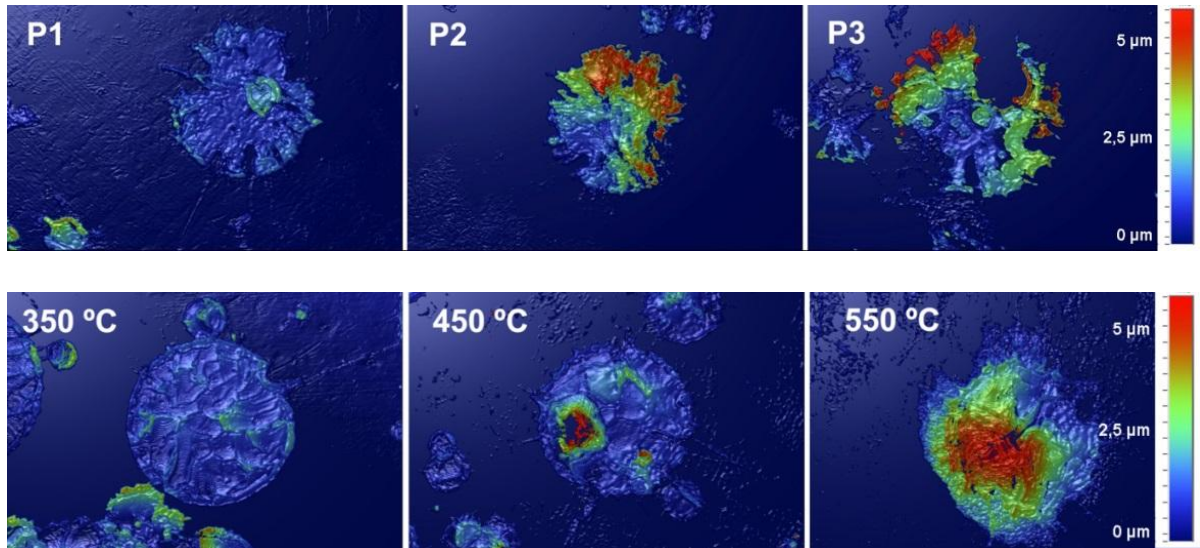

FIGURE 15 Optical profilometer pictures of single splats deposited on cold and hot substrates [Publication II].

Obtaining good inter-splat adhesion is important due to the average splat height, which varied between 1.40–1.50 µm for powder with a particle size range of -36 + 15 µm (d_{90}-d_{10}) [Publication I]. In practice, this means that a coating with a thickness of 10–20 µm is achieved by some tens of overlapping splats. For thin coatings, simultaneous substrate heating was found to be an efficient way of decreasing the number of cracks, in other words, increasing the inter-splat bonding. Cracks, especially segmentation cracks, dominate gas leakage in thin coatings as reported in [124]. According to the splat studies, a substrate temperature of 450°C enhanced the spreading of the molten splat. As a result, optimal splats with the shape of a disc-like structure were deposited, as shown in Fig. 15. Although the temperature of 350°C was enough to achieve well spreading droplets, the main problem was the high quenching rate, which caused many internal cracks inside the splats.

The polished cross-section views of the as-sprayed $(Mn,Co,Fe)_3O_4$ coatings are presented in Fig. 16 and those of the $(Mn,Co)_3O_4$ coatings in Fig. 17. The coating thicknesses were in the range of 10–20 µm, which can be considered a favourable thickness for protective coatings. However, the coatings were not smooth in terms of target coating thickness due to the relatively large agglomerates. As the cross-section images clearly show, the density of the as-sprayed coatings was enhanced by simultaneous substrate heating. Due to the controlled cooling rate of the deposited splats, the amount of inter-splat cracks and segmentation cracks was reduced. The white arrows in Figs. 16 and 17 show favourable inter-splat bonding. In principle, this kind of inter-splat bonding should provide coatings with a lower ohmic resistance and an effective barrier to

volatile Cr compounds. The remnant pores that are still visible in the cross-section images were most likely gas entrapments as the agglomerates enabled plasma gas to be transported inside the particle.

As stated previously, the microstructure of the as-sprayed coatings is a net result of the spraying parameters used, together with powder morphology. By using powders with a well-agglomerated structure, the inter-splat crack network was notably decreased. Porous morphology contributed to the melting process from inside and outside the agglomerate, whereas fused and crushed powders with a blocky structure contributed to melting only from the outside of the particle. In other words, blocky morphology may prevent the heat transfer of the thermal flame into the inner part of the spray particles, resulting in partially molten particles.

Spray drying allows the use of two-component powders, also known as ceramic-metallic, i.e. cermet powders. In this work, the Mn_2CoO_4+Co powder represents powder feedstock with a cermet structure. During the spraying process, the melted Co particles distributed evenly in the inter-splat gaps and decreased the amount of cracks. Since only a few clear areas of metallic Co were observed (Fig. 17e), it can be expected that most of the Co oxidized or mixed with the Mn_2CoO_4 spinel. Using a similar principle, Park et al. [76] clearly demonstrated that a two-component spray powder effectively reduces the amount of cracks in APS coatings, and it is a favourable method when spraying thin coatings for SOFC applications.
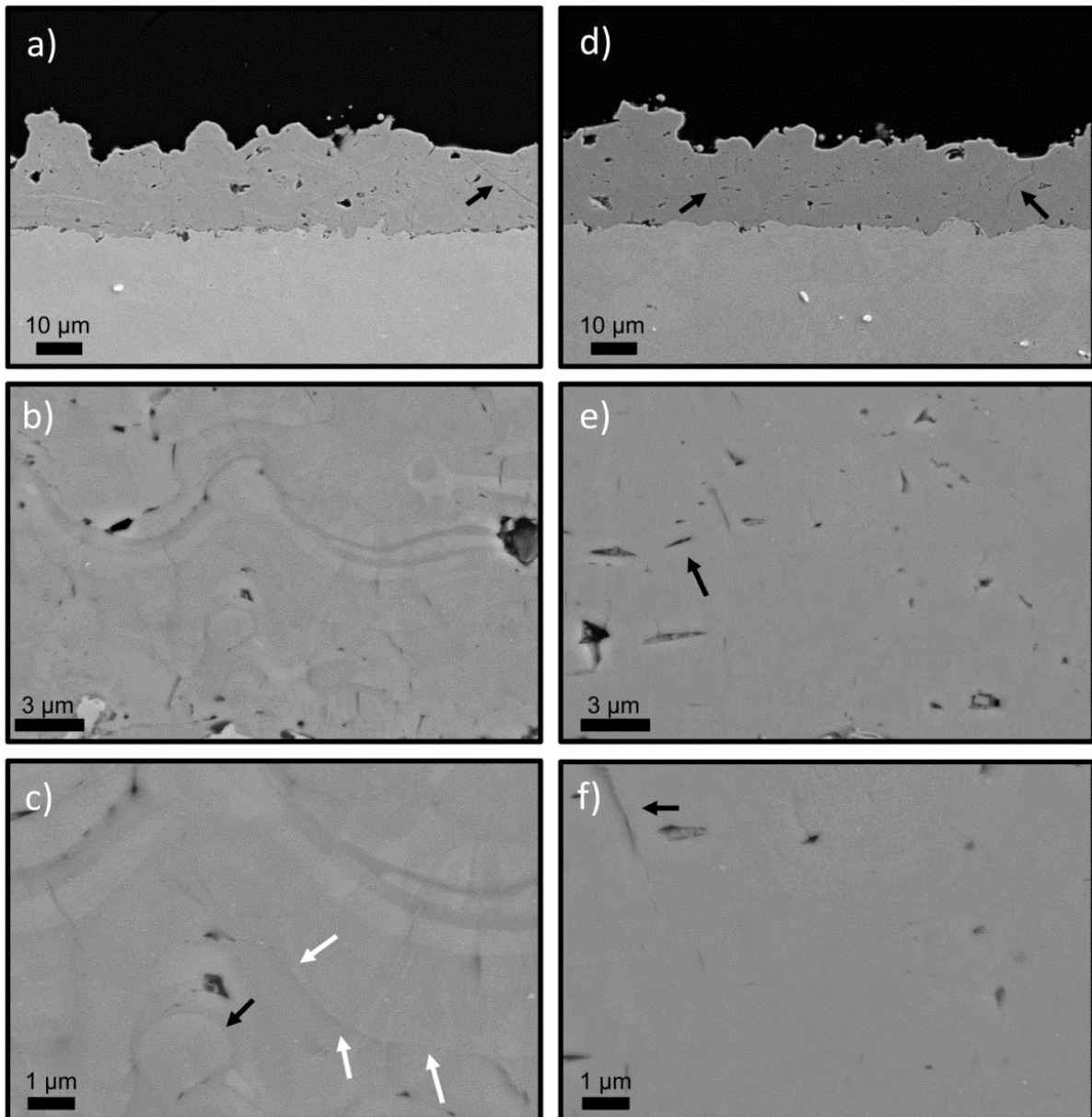
FIGURE 16 Cross-section images of as-sprayed a-c) $MnCo_{1.9}Fe_{0.1}O_4$ d-f) $MnCo_{1.7}Fe_{0.3}O_4$ spinel coatings. The black arrows point to typical coating faults such as segmentation cracks (a, d) un-molten spray particle (c) and lamellar gaps (d-f). The white arrows point to desirable spat-splat interaction (c). FE-SEM (SE) images [Publication III].
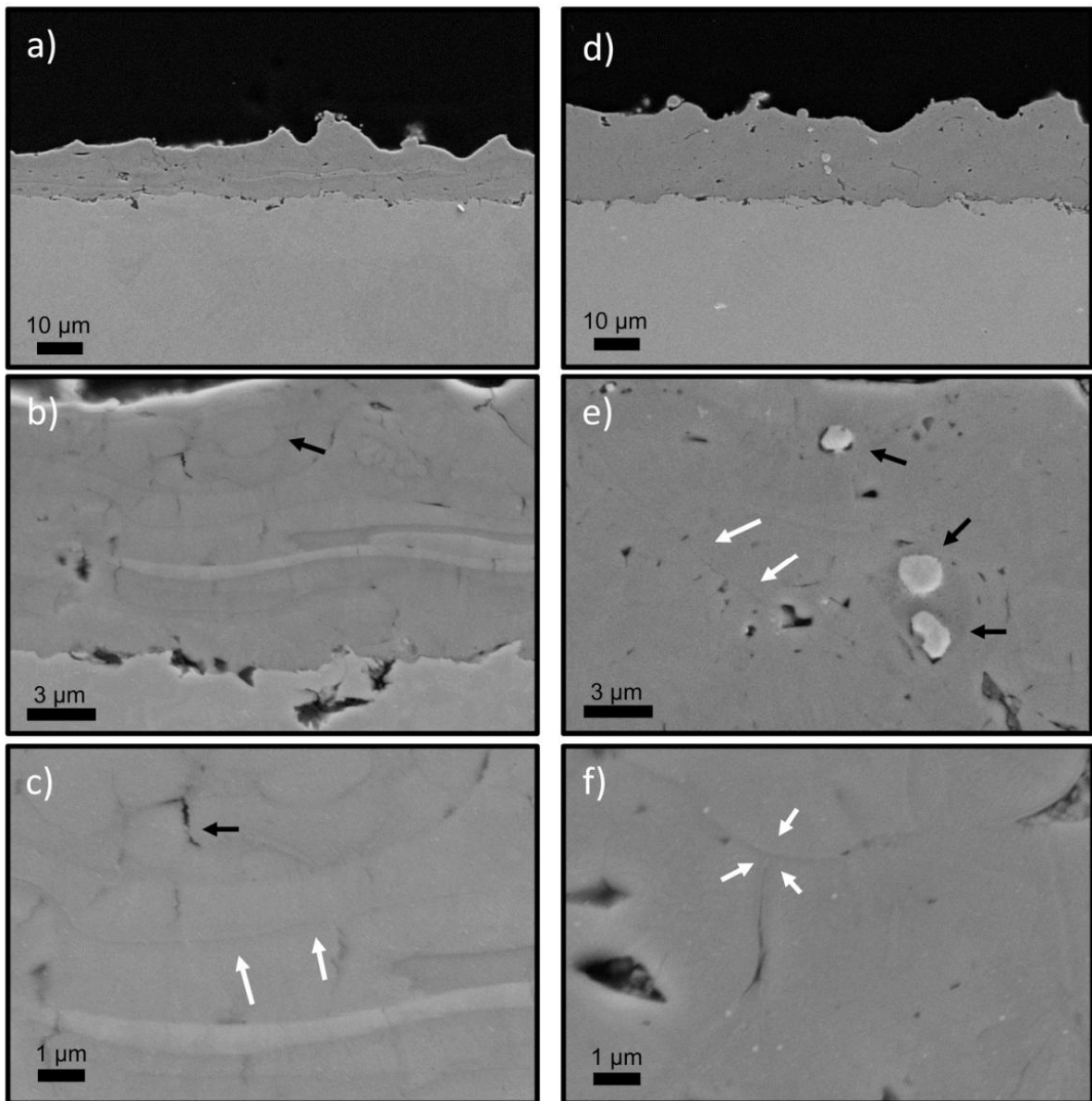
FIGURE 17 Cross-section images of as-sprayed a-c) $MnCo_2O_4$ and d-f) Mn_2CoO_4+Co coatings. The black arrows show an un-molten $MnCo_2O_4$ particle in (b) and partially molten or un-molten Co particles in (e). The white arrows show well-adhered splat boundaries in (c, e, f) FESEM (SE) images [Publication IV].

Chemical and phase analysis

The $MnCo_{2-x}Fe_xO_4$, $MnCo_2O_4$ and Mn_2CoO_4+Co (equivalence with $Mn_{1.5}Co_{1.5}O_4$) spinel structures decomposed during the deposition process, as shown in Fig. 18, meaning that the crystallographic structure did not correspond to the initial phase structure. The phase analysis showed that the deposited coatings had equivalence with a simple cubic metal-oxide phase, where the metallic element was either Fe or Co. Thomann et al. [81] suggested that one possible phase could be

MnO. According to the literature, decomposition of the spinel structure is only observed when the coatings are deposited by employing thermal spray processes. However, the XRD studies showed some traces of the spinel when iron-doped powders were deposited. According to the results, iron doping may favour the formation of spinel during the spraying process.
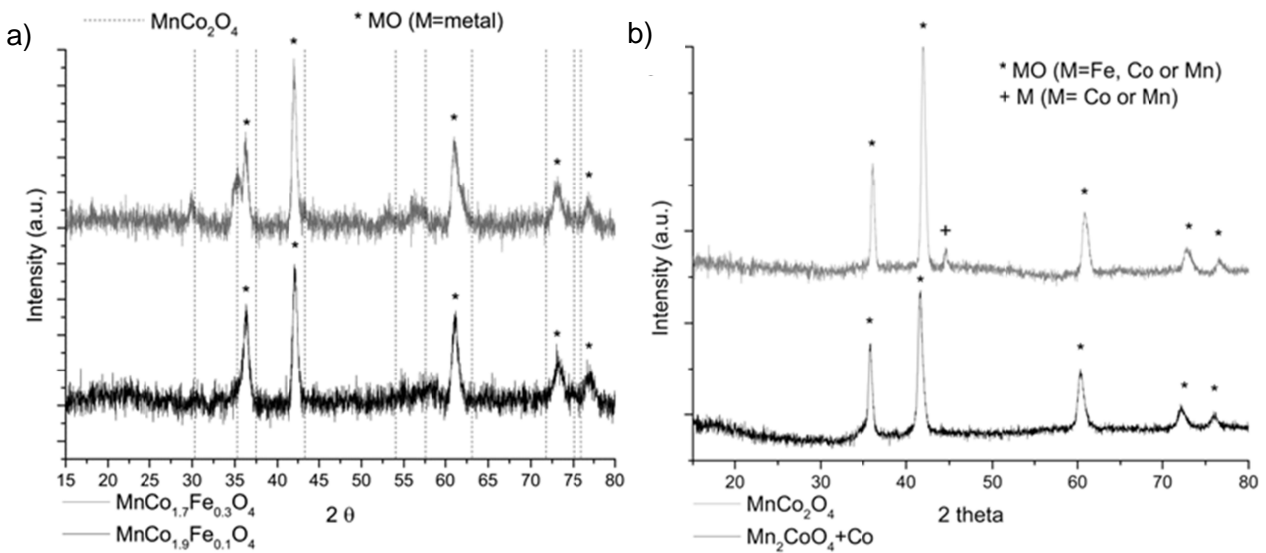

FIGURE 18 Crystallographic phase analysis of the as-sprayed a) $(Mn,Co,Fe)_3O_4$ coatings [Publication III] and b) $(Mn,Co)_3O_4$ coatings [Publication IV].

Figure 19 shows the μ-Raman spectra of the $MnCo_{1.7}Fe_{0.3}O_4$ feedstock powder, as-sprayed and the decomposed $MnCo_{1.7}Fe_{0.3}O_4$ coating, and the oxidized $(Mn,Co)_3O_4$ spinel coatings. The spinels have relatively similar spectra with two main peaks at 491 and 632 cm^{-1}, 586 and 679 cm^{-1} and at 570 and 681 cm^{-1} for crystalline $MnCo_{1.7}Fe_{0.3}O_4$, $MnCo_2O_4$ and Mn_2CoO_4+Co ($Mn_{1.5}Co_{1.5}O_4$), respectively. The Raman spectra of as-sprayed $MnCo_{1.7}Fe_{0.3}O_4$ coatings had three peaks at 543, 623 and 672 cm^{-1}, indicating the same decomposition of the spinel as observed by the XRD studies. In contrast with the XRD studies, the Raman spectra did not exhibit correlation with peaks for CoO, or for other compounds such as $MnFe_2O_4$ or MnO_2 phases. In the case of the CoO phase, the Raman peaks should be located at 484 and 693 cm^{-1} and for Co_3O_4 at 197, 485, 523, 624 and 693 cm^{-1} [125].
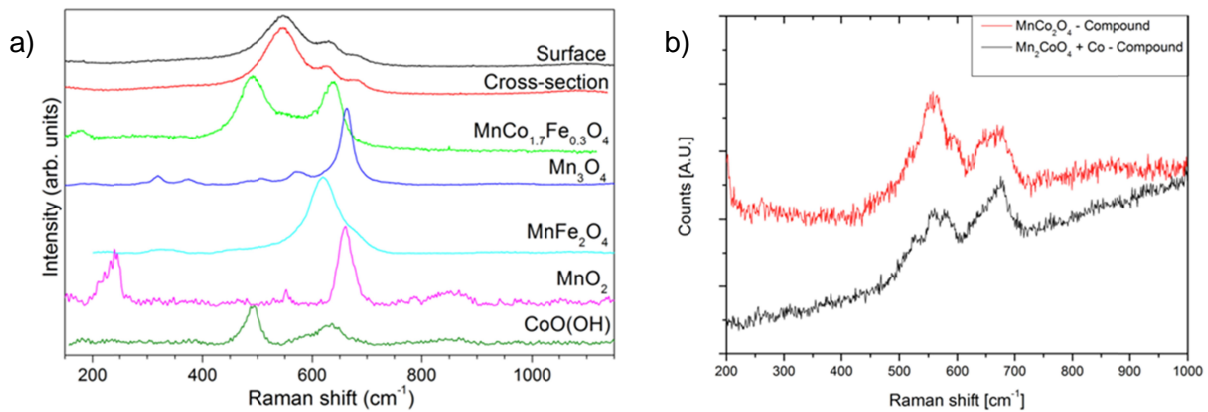
FIGURE 19 Raman spectra of the a) $MnCo_{1.7}Fe_{0.3}O_4$ powder and as-sprayed coatings [Publication III] and b) oxidized $(Mn,Co)_3O_4$ spinel coatings [Publication IV].

Elemental XRF, ICP-AES and EDS studies of the as-sprayed $MnCo_{1.7}Fe_{0.3}O_4$ coating and the $MnCo_{1.7}Fe_{0.3}O_4$ spray powder were carried out to study the possible selective evaporation of metal elements (Table 6). Selective evaporation could be a possible explanation for the decomposition of the spinel, particularly when rather complex material structures are deposited using high temperature deposition methods such as the APS process. According to the results, the difference between the relative amounts of the elements in the powder and in the as-sprayed coatings was insignificant. Therefore, it can be clearly established that the selective evaporation of the metal ions was not a root cause for decomposition of the spinel structure. However, it should be noted that the coatings were sprayed with relatively cold conditions and evaporation is more likely to occur when the torch operating power is increased.

TABLE 6   Elemental concentration analyses of the $MnCo_{1.7}Fe_{0.3}O_4$ spray powder and as-sprayed coating. The results are in wt% [Publication III].

X-ray fluorescence (XRF)	Mn	Co	Fe
$MnCo_{1.7}Fe_{0.3}O_4$ spray powder	27.1	61.9	11.0
As-sprayed $MnCo_{1.7}Fe_{0.3}O_4$ coating	27.1	62.0	10.9
Inductively coupled plasma spectrometry (ICP-AES)	Mn	Co	Fe
$MnCo_{1.7}Fe_{0.3}O_4$ spray powder	27.9	60.8	11.3
As-sprayed $MnCo_{1.7}Fe_{0.3}O_4$ coating	27.6	60.7	11.4
Energy dispersive X-ray spectroscopy (EDS)	Mn	Co	Fe
$MnCo_{1.7}Fe_{0.3}O_4$ spray powder	31.4	56.2	12.4
As-sprayed $MnCo_{1.7}Fe_{0.3}O_4$ coating	31,9	56.3	11.8

According to the results, decomposition is linked to the rapid cooling rate of the deposited molten droplets, in other words a liquid-to-solid phase transformation [80], [81]. Since it is caused by the cooling rate of the material, the spraying parameters do not have an influence on the decomposition phenomena as long as the powder achieves the fully molten state. As stated in the

literature [41], [126], the melting temperature for $(Mn,Co)_3O_4$ spinels varies between 1300–1700°C. When deposited at this temperature range, the ideal $Mn^{2+}(Co^{3+},(Fe^{3+}))_2O_4^{2-}$ spinel structure is not able to form, and due to the multiple oxidation states of the elements [47], coatings with mixed phases of cubic (Mn,Co,Fe)O and partially amorphous character are most likely to be formed.

5.2 Solution precursor thermal spraying

New methods such as suspension and solution precursor thermal spray processes (SPTS) show great potential for coating deposition in the thermal spraying field. The clear advantage of the SPTS techniques is that the number of process steps can be decreased significantly compared to conventional methods, e.g. APS or HVOF. The main difference in this technique compared to conventional dry powder spraying processes is that separate material synthesis and powder preparation phases are no longer needed and therefore fewer process steps are required to obtain a coating, as shown in Fig. 20. If an agglomerated spray powder is manufactured by solid-state synthesis (SSS), the number of process steps can easily be up to six, as implemented in [Publications I–III]. For liquid-state synthesis (LSS), the number of process steps can be up to nine, as described in [127]. Novel spray processes, such as suspension thermal spray techniques, decrease the number of process steps down to five or eight, depending on which type of raw materials are used.

	Diluting	Mixing/ milling	Calcination	Milling	Calcination	Milling	Silting	Spray drying	Spray process
Conventional TS Powder: SSS or (LSS)	(1)	1(2)	2(3)	(4)	(5)	3(6)	4(7)	5(8)	6(9)
Suspension TS Powder: SSS or (LSS)	(1)	1(2)	2(3)	(4)	(5)	3(6)	4(7)		5(8)
Solution precursor TS Feedstock: LP	1								2

TS = thermal spraying   LSS = liquid-state synthesis
SSS = solid-state synthesis   LP = liquid precursors

FIGURE 20 Comparison of the process steps for different thermal spray techniques [Publication V].

5.2.1 Solution feedstock

The water-based $(Mn,Co)_3O_4$ nitrate solutions obtained good flow properties, behaving as Newtonian fluids, with viscosity values of 3.00–3.50 mPas [112]. However, iron doping changed the rheological behaviour in such a way that the $(Mn,Co,Fe)_3O_4$ nitrate solution behaved as a

Newtonian fluid in a shear rate range from 0 to 400 s^{-1}, with a viscosity of 4.0 mPas, but as a dilatant fluid above 400 s^{-1}. Low viscosity enhances the feed and the atomization properties of the precursor. When entering the combustion chamber, the atomized solution precursor droplets follow the same thermal decomposition steps as obtained in the TG-DSC analysis, presented in Fig. 21, to form a $MnCo_{1.9}Fe_{0.1}O_4$ and $Mn_{1.5}Co_{1.5}O_4$ spinel structure. The first endothermic peaks from 50°C to 110°C refer to the evaporation of water. The peaks above 160°C are related to the formation of NO_x, as Nissinen et al. [128] observed when heat treating Mn and Co nitrate powder. The last exothermic peaks at 285°C and 330°C characterize the thermal decomposition of the nitrates and the formation of $MnCo_{1.9}Fe_{0.1}O_4$ and $Mn_{1.5}Co_{1.5}O_4$ spinels, respectively. Crystallite formation is a relatively slow process, which causes broadening of the exothermic peaks. The thermal decomposition and formation of spinels was confirmed by TG analysis, as the mass change reached a plateau even though the temperature was further increased.
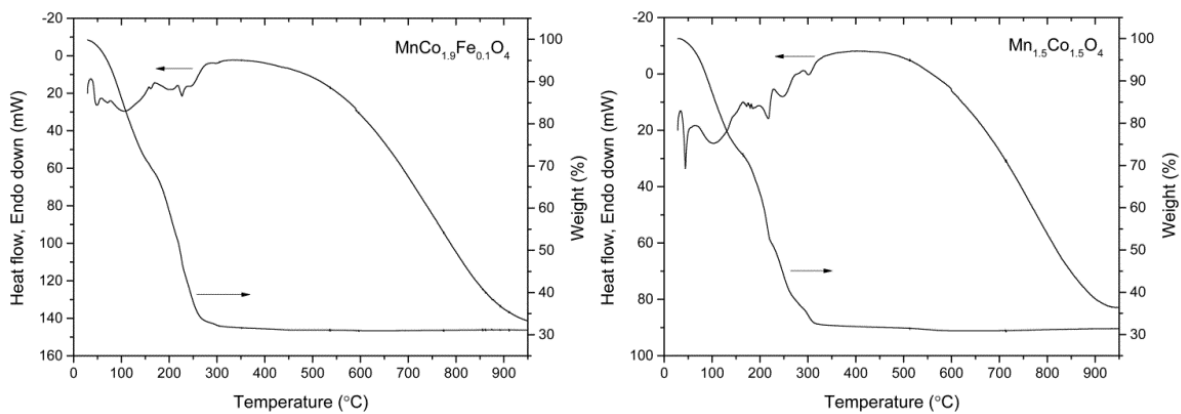

FIGURE 21 TG DSC analysis of the nitrate precursors with nominal composition [Publication VI].

5.2.2 As-sprayed coatings

<u>Microstructure</u>

Figure 22 shows the SE images of an HVSPFS $MnCo_2O_4$ coating and Fig. 23 SE images of HVSPFS $MnCo_{1.9}Fe_{0.1}O_4$ and $Mn_{1.5}Co_{1.5}O_4$ coatings. By optimizing the spraying parameters and the properties of the precursors, coatings were sprayed with dense or relatively low porosity and a closed structure. The clear advantage in the HVSPFS process is that the as-sprayed coatings can be deposited on Crofer 22 APU substrates without using the grit-blasting process. Grit blasting may be problematic as it induces stresses for the substrates, which most likely cause bending of the thin IC structure. Although grit blasting was not carried out, there were no signs of spallation, meaning that the as-sprayed coatings were well adhered to the substrates.
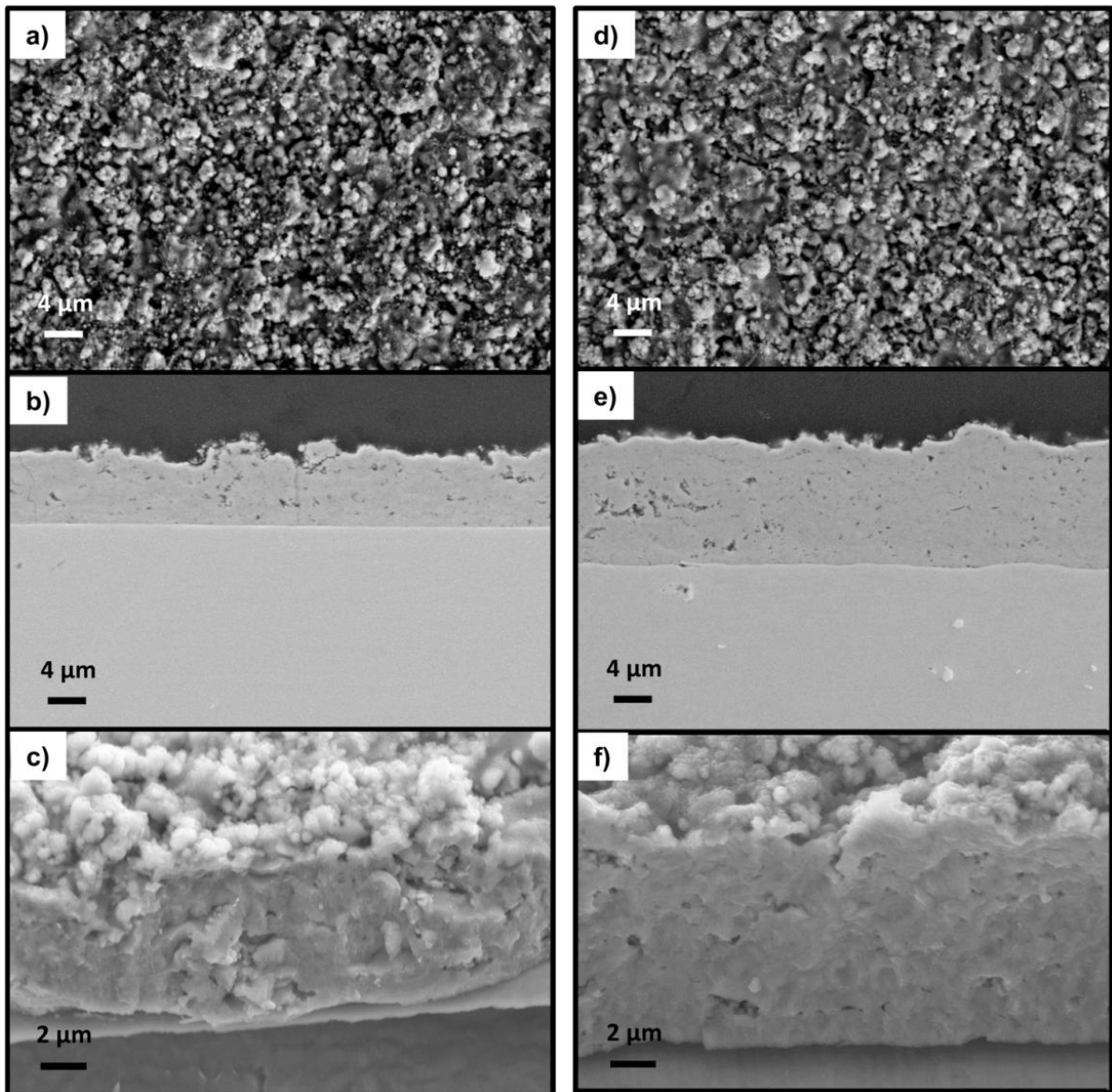
FIGURE 22 Topography, cross-section and fracture surface SE images of $MnCo_2O_4$ coatings [Publication V].
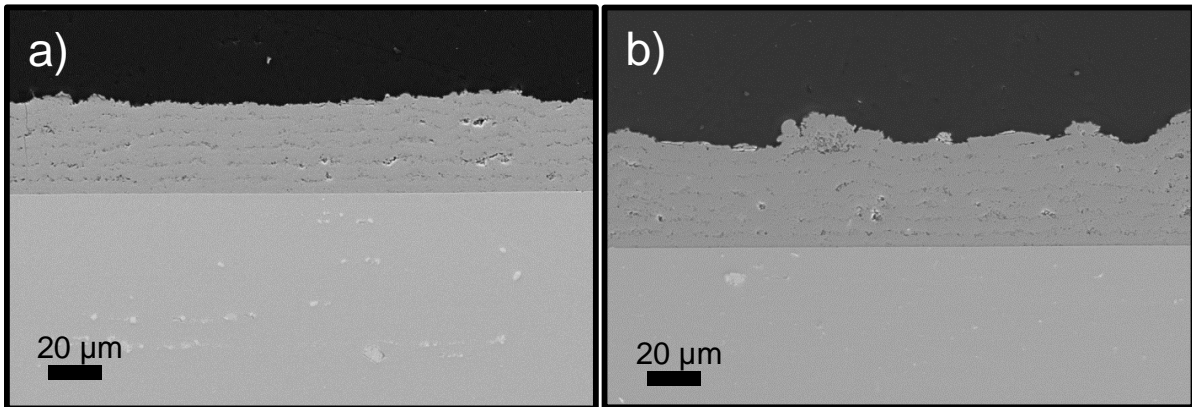
FIGURE 23 Cross-section and fracture surface SE images of a) $MnCo_{1.9}Fe_{0.1}O_4$ and b) $Mn_{1.5}Co_{1.5}O_4$ coatings [Publication VI].

The topography images in Fig. 22, high magnification fracture surface image in Fig. 24 and particles collected from the surface in Fig. 25 revealed that the HVSPFS coatings were mainly formed of micron, sub-micron and nano-sized particles with granular morphology. The sub-micron particles had a size range of 100–500 nm, whereas the nanoparticles were in a size range of 10–20 nm forming larger agglomerates. The sub-micron particles obtained a perfectly round morphology, whereas the nanoparticles were blocky. Some conventional splat-shaped particles were also observed in the fracture surface images with thicknesses of 200–300 nm. Due to the small particle and splat size, mechanical anchorage was achieved even though the R_a value was under 0.5 µm. Baccionichini et al. [129] have stated that substrate roughness should be of the same order of magnitude as the flattened lamellae thickness to provide the required adhesion in thermal spraying, which explains why the HVSPFS coatings were well adhered.
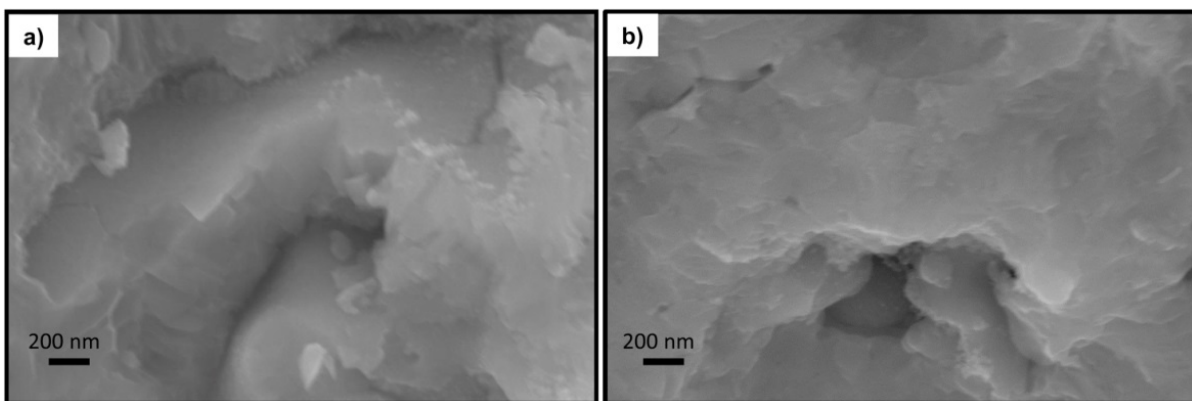

FIGURE 24 High magnification fracture surface SE images of $MnCo_2O_4$ coatings [Publication V].
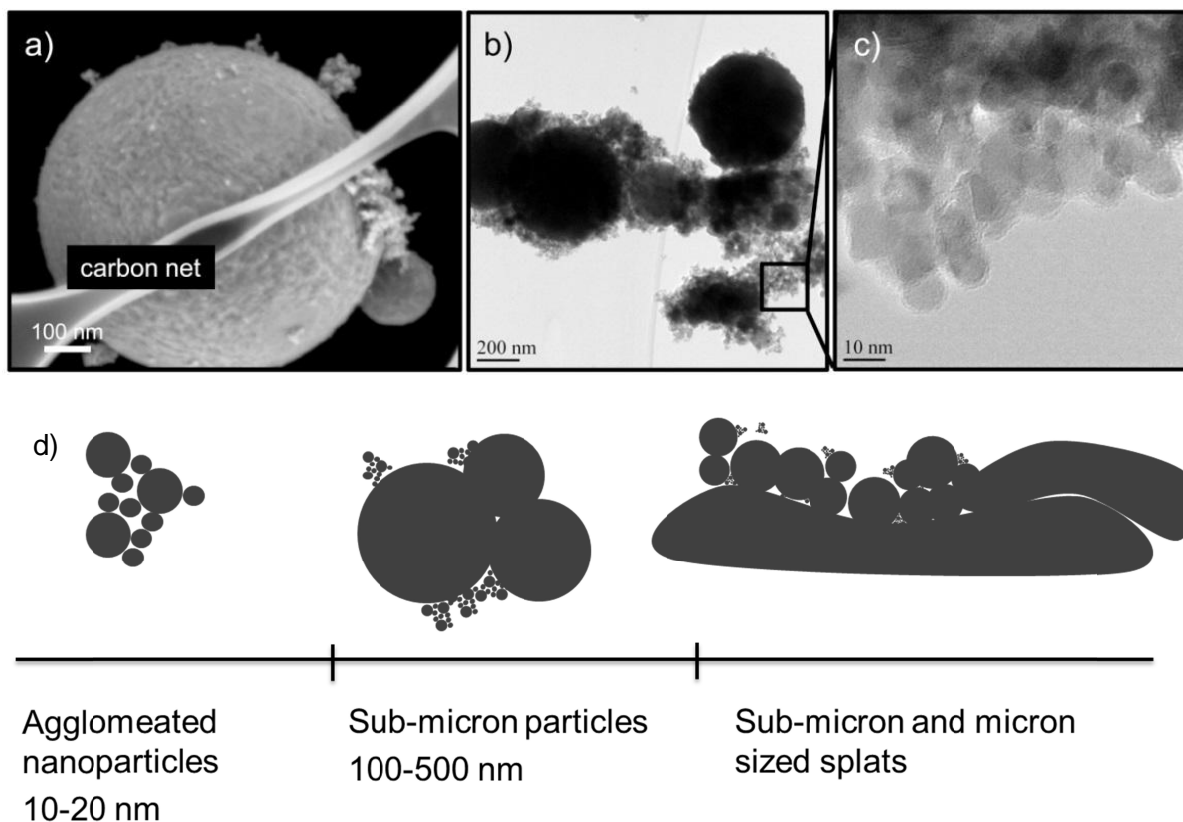
FIGURE 25 Particles collected from the surface of the as-sprayed HVSPFS spinel coating a) FESEM (In-Lens) image and b & c) TEM image and d) schematic presentation of the deposited particles [Publication VI].

The employed spray parameters had a direct influence on the microstructure of the HVSPFS coatings, as shown in Fig. 26. According to the results, the solution precursor flow rate, total gas flow rate and spray distance were linked to each other. A low precursor flow rate required a lower total gas flow rate and lower spray distance. When the precursor flow rate was increased, the situation was reversed. If the spray distance was kept constant, the particle residence time was decreased and porous coatings were formed. A higher gas flow rate also favours the atomization of droplets and induces more energy for thermal decomposition and pyrolysis reactions.
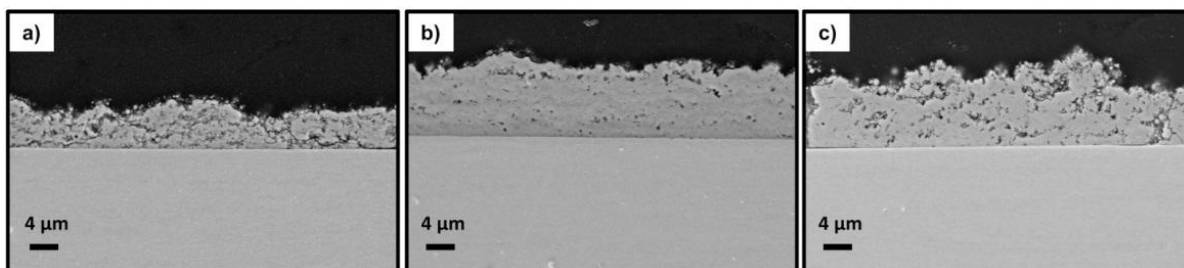
FIGURE 26 Cross-section SE images of the coatings sprayed at a fixed solution flow rate and standoff distance but altering the total gas flow rate where a) represents a relatively low gas flow rate, b) the optimized gas flow rate and c) a relatively high gas flow rate [Publication V].

The as-sprayed microstructure is related to particle formation mechanisms, i.e. how the droplets undergo the materials synthesis as described in the introduction section. The optimal particle formation was achieved by inducing effective droplet break-up by employing the axial injection of the precursor and a high gas flow rate. The combustion of gases results in the formation of shock diamonds, which most probably promote droplet breakup. In order to avoid the formation of hollow particles, precursor droplets should obtain a diameter less than 5 µm, as they are most likely to form dense spray particles and dense coatings. Droplets of this size range or smaller have a uniform increase in solid concentration as the solvent evaporates. [114]

The splats and sub-micron particles were formed from the liquid-to-solid phase transformation. As the precursor droplet is exposed to a thermal flame, the temperature starts to increase stepwise and eventually the precursor goes through a similar thermal decomposition process, as shown in Fig. 21. Basu et al. [116] have suggested three different precipitation routes. In the first case, the uniform concentration of solution increases steadily through the droplet volume and solid particles are formed. In the second case, the surface part is evaporated and supersaturated. As a result, the surface is pyrolyzed and the droplet obtains an eggshell structure. Eventually, as pressure inside the droplet increases, the shell ruptures. In the final step, the synthesized eggshells are partially or fully molten and deposited onto the substrate. In the third case, an elastic shell is formed, deflated and as a result solids are formed.

However, the presence of nanoparticles implies the presence of gas-to-solid conversion. The particles in Fig. 25 have the same morphology and size range as the TiO_2 particles produced by the LFS process reported in [130], [131]. In gas-to-solid conversion, a precursor will form a gas phase. This gas phase thermally decomposes resulting in a gas phase containing metallic ions. As a result, crystallized nanoparticles are formed through the nucleation process [84].

Chemical and phase analysis

Since the coatings were formed from thermally decomposed precursors, the as-sprayed $MnCo_{1.9}Fe_{0.1}O_4$ and $Mn_{1.5}Co_{1.5}O_4$ coatings were analysed by FTIR to reveal whether the as-

sprayed coatings had any traces of partially pyrolyzed nitrates. The IR spectra of the diluted and calcined precursor powders and the as-sprayed coatings are presented in Fig. 27. The similarities in the spectra should reveal if the material synthesis is only partially completed in the HVSPFS processes.
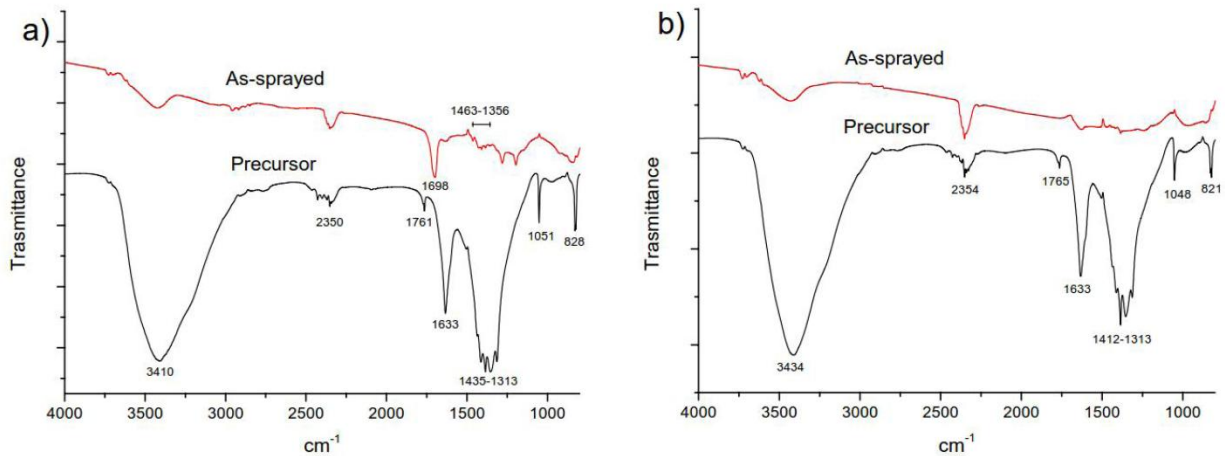

FIGURE 27 IR spectra of the FTIR analyses obtained from a) $MnCo_{1.9}Fe_{0.1}O_4$ and b) $Mn_{1.5}Co_{1.5}O_4$ precursor powders and as-sprayed coatings [Publication VI].

The absorption bands located at 1633 cm^{-1} and 3410–3434 cm^{-1} refer to the bend and stretching mode of the O-H groups, respectively [128]. The absorption bands of nitrate groups were observed at 821–828 cm^{-1}, 1313–1412 cm^{-1}, and 2350–2354 cm^{-1} [132]. Since these absorption bands were observed in the spectra of as-sprayed coatings, it is most likely that the as-sprayed coatings contained some small traces of nitrate compound. However, according to the intensity of the absorption bands, it can be stated that the amount of nitrates was insignificant.

The crystallographic phase studies of the as-sprayed $MnCo_2O_4$ coating are presented in Fig. 28 and those of the $MnCo_{1.9}Fe_{0.1}O_4$ and $Mn_{1.5}Co_{1.5}O_4$ coatings in Fig. 29. The as-sprayed coatings were formed of multi-phase structures consisting of spinels and simple cubic oxides identified as (Mn,Co,Fe)O. In addition, Chen et al. [120] have reported the presence of amorphous phases. Decomposition of spinel and formation of simple cubic oxides are the consequence of the fast cooling rate of the deposited material, as was observed and confirmed in the conventional thermal spray technique. However, the presence of the spinel phase could be due to the larger heat load produced by the deposition process. This was a result of the short spray distance to the substrate. The dual phase structure was observed to form when $MnCo_2O_4$-based suspensions [127] and $MnCo_2O_4$ forming solutions [112] were deposited with a modified APS process. Fast cooling and the size of the deposited particles caused the average crystallite size of the spinel phases to remain between 4–8 nm. According to the FESEM and TEM studies in Fig. 25 and crystallite sizes obtained in XRD studies, it can be expected that the sub-micron particles had polycrystalline characteristics, whereas nanoparticles had a more single crystal structure. In addition, the width of

the peaks can be explained by fine equiaxed grains. Bertolissi et al. [89] have suggested that the fast cooling rate of small splats induces a situation where homogeneous nucleation is competitive or predominant against heterogeneous nucleation.
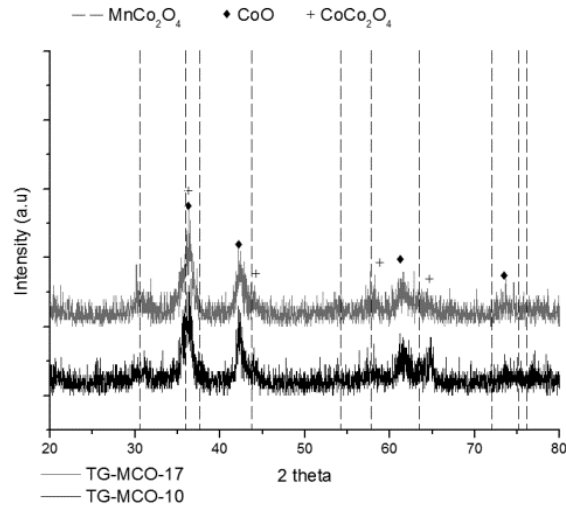
FIGURE 28 Crystallographic phase studies of the as-sprayed HVSPFS $MnCo_2O_4$ coating [Publication V].
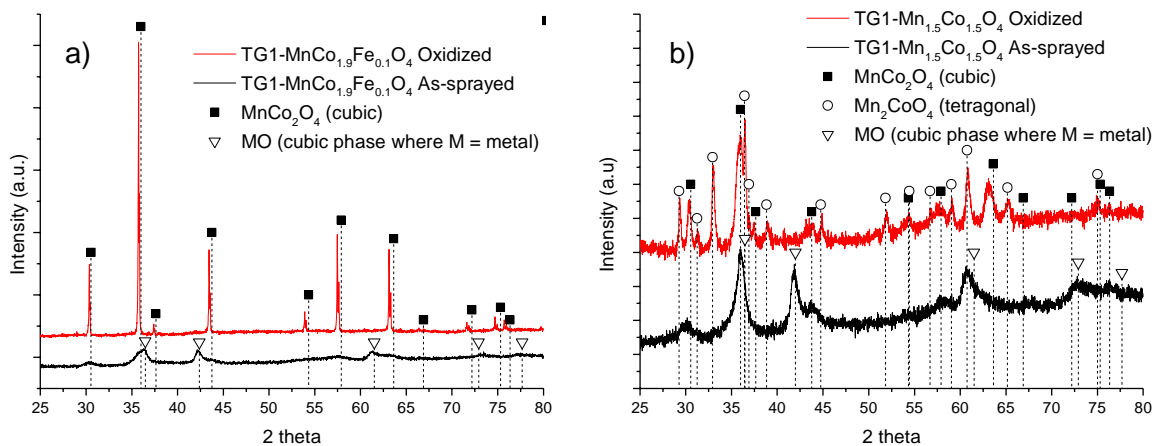
FIGURE 29 Crystallographic phase studies of the as-sprayed and oxidized (at 850ºC in air for 500 hours) HVSPFS a) $MnCo_{1.9}Fe_{0.1}O_4$ coatings and b) $Mn_{1.5}Co_{1.5}O_4$ coatings [Publication VI].

According to the EDS analysis, the quantitative ratios of Mn:Co were 37.5:62.5 in at% for the as-sprayed $MnCo_2O_4$ coatings. The cationic ratio of Mn:Co should be 1:2, but it was close to 1:1.67. For the $Mn_{1.5}Co_{1.5}O_4$ coatings, the relative Mn:Co proportions were 55.1:44.9. The cationic ratio should be 1:1 but it was 1:0.81. The results indicate that partial evaporation of Co is plausible; considering that the measured results are near the limit of accuracy of the EDS system, the

evaporation was low. The quantitative EDS ratios for Mn:Co:Fe cations were 38.5:57.9:4.6 in at% for the $MnCo_{1.9}Fe_{0.1}O_4$ coatings. These results have close correlation with the calculated 33.3:63.3:3.3 values. According to the results, $(Mn,Co)_3O_4$ spinels are more sensitive to the selective evaporation of elements than Fe-doped spinels.

5.3 High temperature behaviour of thermally sprayed coatings

This section summarizes the behaviour of both APS and HVSPFS as-sprayed coatings in a long-term (500 and 1000 hours) oxidation cycle. The oxidizing atmospheres and test temperatures of the order of 700 to 850°C represent the cathode side atmosphere in the SOFC system. A temperature of 850°C can be considered relatively high in SOFC applications, but was used to accelerate microstructural and chemical changes since the length of the test cycle was only 500 hours.

5.3.1 Restoration of the spinel phase

The cubic structure formed during the APS and HVSPFS processes is metastable, meaning that the crystallographic phase structure changes when suitable energy is induced. Relying on the results published in [80], [81], the decomposed spinel structure can be restored to the original spinel structure in an oxidizing atmosphere. This was confirmed by the XRD analysis shown in Figs. 29 and 30 obtained from the coatings after the oxidation cycles.
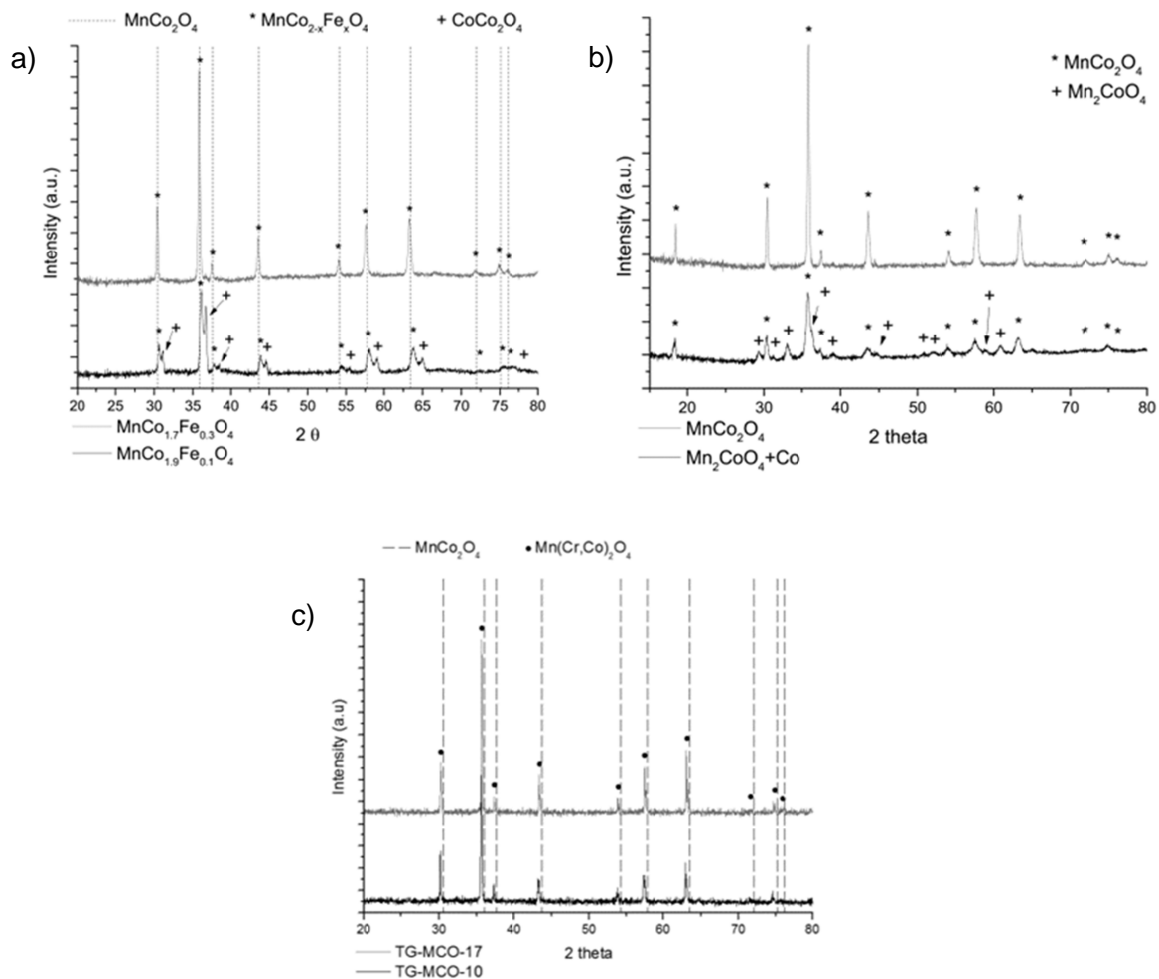
FIGURE 30 Crystallographic phase studies of the oxidized spinel coatings. a) APS $(Mn,Co,Fe)_3O_4$ at 700°C in air [Publication III], b) APS $(Mn,Co)_3O_4$ at 700°C in air [Publication IV] and c) HVSPFS $MnCo_2O_4$ coatings at 800°C in air [Publication V] for 1000 hours.

The oxidized APS and HVSPFS $(Mn,Co,Fe)_3O_4$ coatings showed the presence of a cubic phase, as shown in Fig. 29a and 30a, with a shifted diffraction pattern, due to cationic replacement in the spinel lattice as explained in 5.1.1. In addition, a $CoCo_2O_4$ phase was observed when the APS $MnCo_{1.9}Fe_{0.1}O_4$ coating was oxidized. The oxidized APS and HVSPFS $MnCo_2O_4$ coatings had a close correlation to the cubic $MnCo_2O_4$ spinel, as shown in Figs. 30b and 30c. However, the oxidized coatings with the nominal composition of $Mn_{1.5}Co_{1.5}O_4$ (Fig. 29b and 30c) had both cubic and tetragonal $MnCo_2O_4$ and Mn_2CoO_4 phases, proving that the Co-alloyed Mn_2CoO_4 spinel powder reacted and formed the desired dual phase structure as intended. The dual phase cubic-tetragonal structure is observed to form when $Mn_{1.5}Co_{1.5}O_4$ spinels are oxidized as confirmed by Yang et al. [42]. Tetragonal-cubic phase transformation occurs at 400°C [38] when the stoichiometric factor x is between 0.3–0.9 in the $Mn_{1+x}Co_{2-x}O_4$ system [133].

The recovery process of the decomposed spinel structure was studied by placing a free-standing APS $MnCo_{1.7}Fe_{0.3}O_4$ coating (without substrate) on platinum foil and heat-treating it stepwise. It was analysed simultaneously by XRD, as shown in Fig. 31. The spinel structure started to be restored at 400°C. According to the peak intensity levels, the most dynamic recovery process of the decomposed spinel was between 600°C and 800°C (highlighted area). The shifting of the Bragg angle to a lower 2-theta value was caused by an increase of the d-spacing value due to the thermal expansion of the spinel lattice. However, at a temperature of 1000°C, the spinel transformed back to simple metal oxides. According to the results, the phase was preserved when cooled down to room temperature, indicating a more stable phase structure compared to that formed during the spraying process. The results were similar to the study of Kiefer et al. [46], who obtained multi-phase structures of $MnCo_2O_4$, CoO and Co_3O_4 phases after heat treatment of $MnCo_2O_4$ spinel at 1200°C.
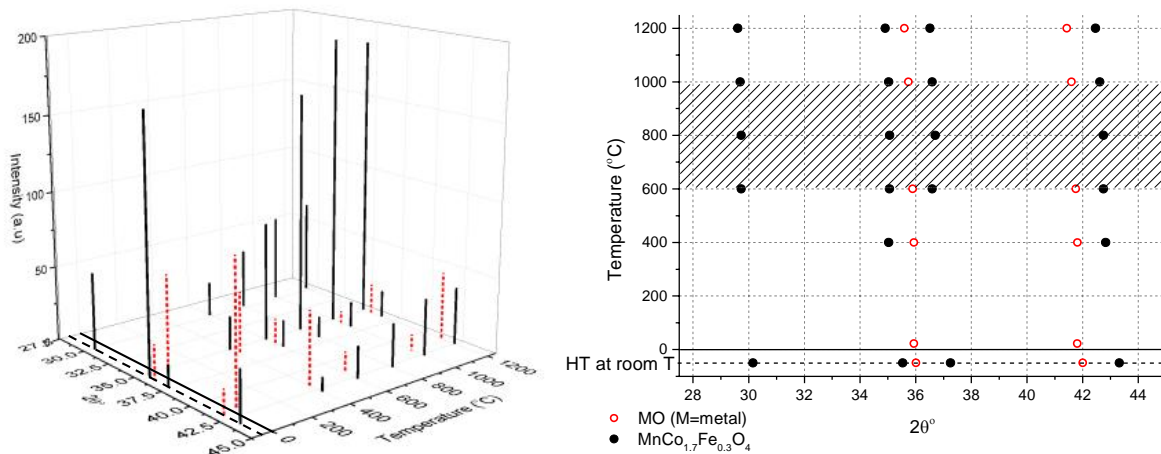
FIGURE 31 Recovery process of the APS and decomposed $MnCo_{1.7}Fe_{0.3}O_4$ coatings [Publication III].

5.3.2 Long-term microstructural and compositional changes

As the as-sprayed APS (Figs. 32 and 33) and HVSPFS (Fig. 34) coatings were placed in a high temperature oxidizing environment, the microstructure changed and the cracks and inter-splat porosity disappeared. The oxidized coatings contained unconnected voids. The voids were exhibited through a thickness gradient. Although the voids can be considered as disadvantageous structural faults, the coatings seemed to obtain a dense microstructure, without any signs of significant open porosity.
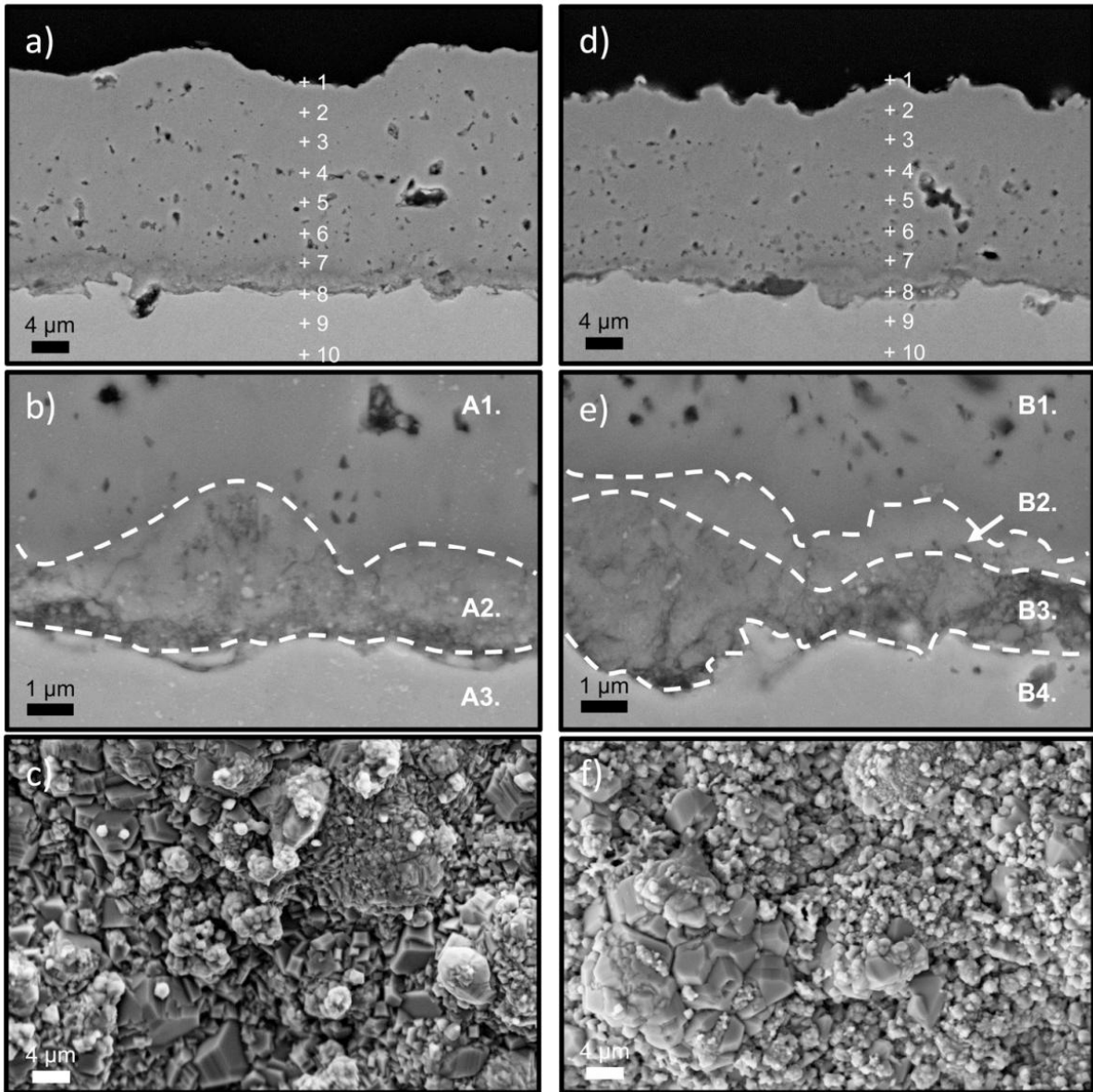
FIGURE 32 Cross-section and surface topography images and EDS point and area analyses of oxidized $MnCo_{1.9}Fe_{0.1}O_4$ (a-c) and $MnCo_{1.7}Fe_{0.3}O_4$ spinel coatings (d-e). The measurement location of the EDS analyses is marked on the FE-SEM (SE) images. The results obtained from point analyses (a, d) are presented in Table 7.1 and area analyses (b, e) and (c, f) in Table 8, respectively [Publication III]. Oxidation cycle was performed at 700°C in air for 1000 hours.
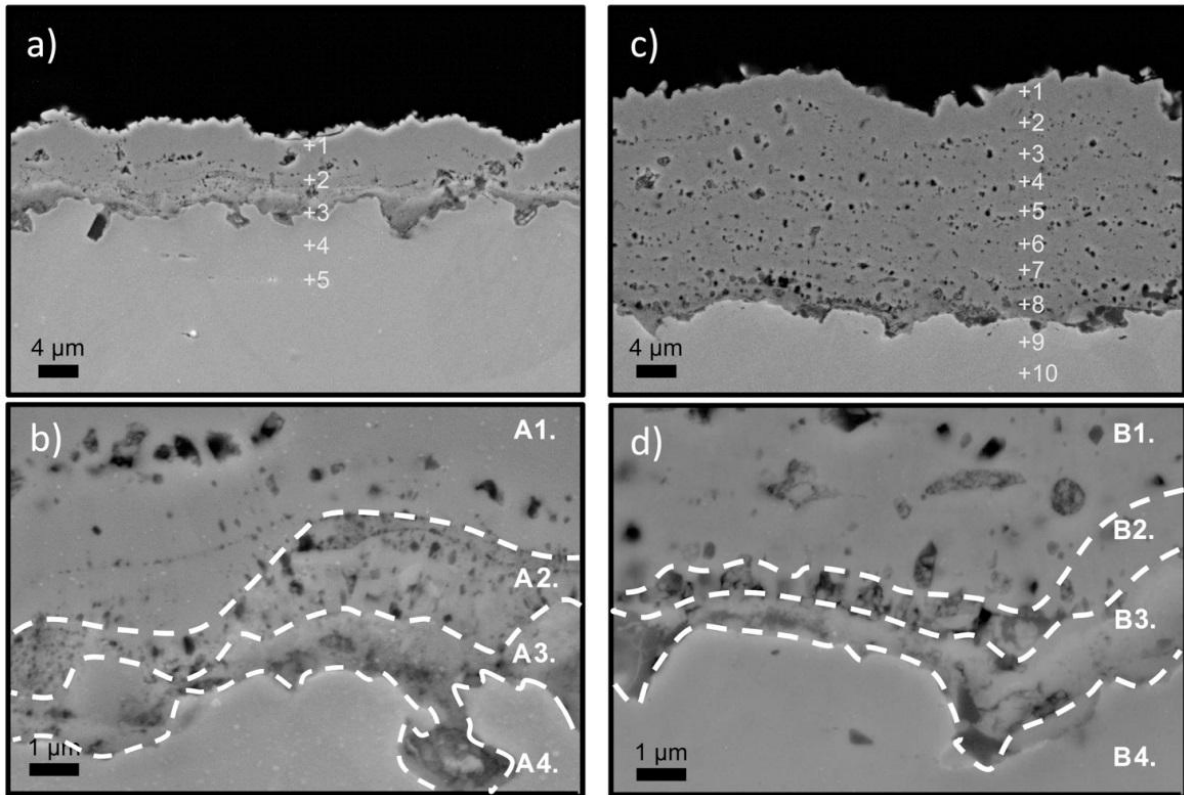
FIGURE 33 Cross-sectional SE images and EDS line analysis of oxidized a-b) $MnCo_2O_4$ and c-d) Mn_2CoO_4+Co coatings. The locations of the EDS point analysis are marked on the FESEM (SE)-images a) and c) and the results are presented in Table 7.1 The results obtained by the EDS area analysis from the cross-section images b) and d) are presented in Table 8 [Publication IV]. Oxidation cycle was performed at 700ºC in air for 1000 hours.

FIGURE 34 Cross-sectional FE-SEM images of oxidized HVSPFS coatings and high magnification of oxide scale images a-b) $MnCo_{1.9}Fe_{0.1}O_4$ and c-d) $Mn_{1.5}Co_{1.5}O_4$. The numbers in a) and c) show the EDS point analysis spots which are presented in Table 7.2 and the lines in b) and d) show the EDS scan traces presented in Fig. 36 [Publication VI]. Oxidation cycle was performed at 850°C in air for 500 hours.

The void coarsening originated from sintering. During sintering, the surface area that was bounded to inter-splat porosity, cracks and segmentation cracks decreased and at the same time the size of the crystallites and grains increased. In other words, the reduction of the total free energy (ΔG_T) shown in Equation 5, is the driving force for the sintering process.

$$\Delta G_T = \Delta G_v + \Delta G_b + \Delta G_s \tag{5},$$

where, ΔG_v, ΔG_b and ΔG_s determine the total free energy change bounded on the volume, grain boundaries and particle surfaces, respectively. [55] Therefore sintering of the as-sprayed coatings generally depends on the same factors as in conventional bulk ceramic processes.

The major force involved in sintering is the energy change associated with the particle surfaces $\Delta G_s = \gamma_s \Delta A_s$, where γ_s is the specific surface energy of material and A_s is surface area change during sintering. Equation 6 shows a simplified model for sintering pressure (stress or potential) for porous solid containing spherical pores,

$$\sigma = 2\gamma_s/r \tag{6}$$

where r represents the pore radius. Equation 6 shows that densification is more rapid for porous solid containing small pore size i.e., tighter pore curvature due to higher vacancy concentration near the surface [55], [56], [134]. According to Equation 5 and 6, the total free energy of APS and HVSPFS coatings is considerable, due to the fact that the majority of the free energy is associated in the surfaces of the micron, sub-micron and especially nano-sized particles. The free energy is enhanced by the energy bound to the small crystallite size due to the high number of grain boundaries (ΔG_b). In addition, sintering is enhanced by: i) the residual stresses due to rapid cooling of the deposited material and ii) the disordered and metastable crystal structure as confirmed by the XRD studies.

The sintering behaviour of the HVSPFS coatings should be more rapid than that of APS coatings due to smaller particle size. In general, the sintering temperature for the material systems formed of micron-sized particles is $0.5–0.8T_m$ (where T_m is the melting temperature of the material in degrees Kelvin). However, it is generally accepted that a large quantity of free energy is induced in material systems formed of nanosized particles and therefore the sintering temperature is most likely to be in the range of $0.2–0.3T_m$ [56].

In general, the conventional sintering process can be categorized in three different stages, where the first stage presents the neck formation of the touching particles. However, according to the fracture surfaces of the HVSPFS coatings presented in Figs. 22 and 24, the coatings were relatively dense, formed of the separate and partially densified spray particles, as presented schematically in Fig. 35. The partially densified particles (molten stage when deposited) formed larger aggregates, and the separate particles (molten but solidified when deposited) formed the agglomerates. Since the as-sprayed coatings were mostly formed of the particles close to the morphology of the aggregates, the as-sprayed state is more close to second stage when compared to the conventional sintering process. At the second stage, the most of the particles have formed necks with the touching particles, resulting in the microstructure containing open tubular pores with the total density of 6% to 95%.
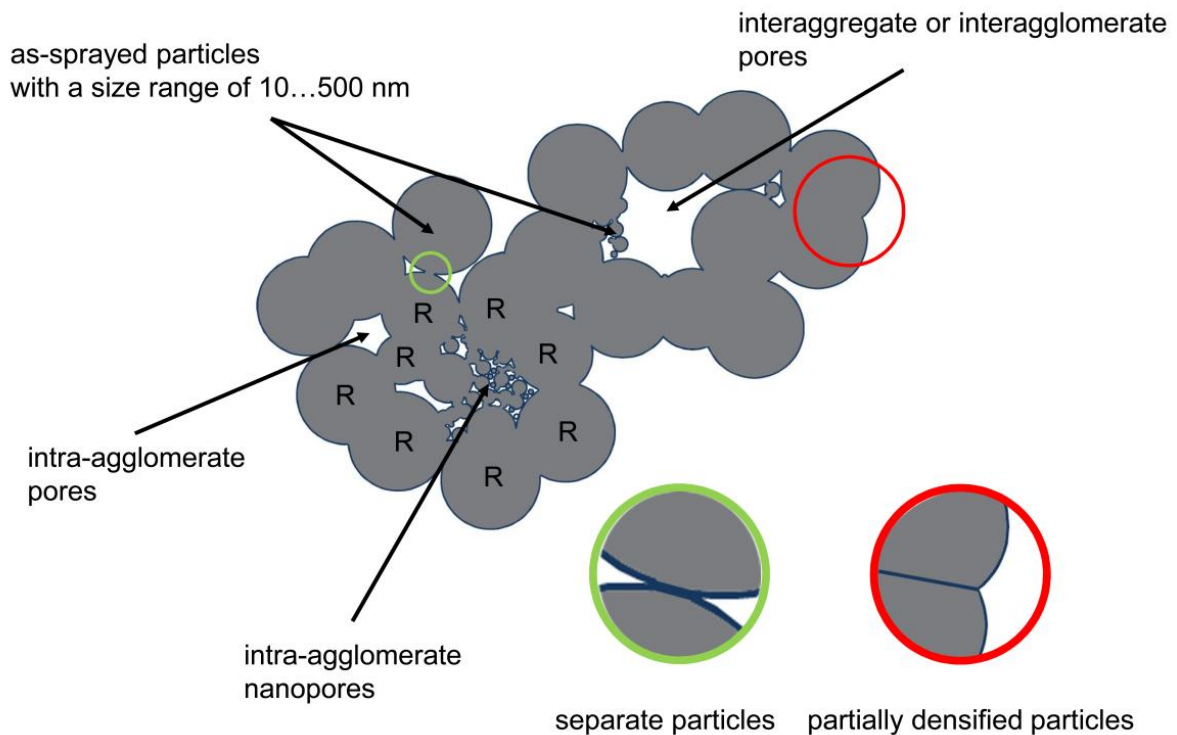
FIGURE 35 Schematic presentation of the as-sprayed HVSPFS coatings with spray particle alignment and pore structures. The particles indicated with R characterize the rigid frame around the nanoparticles.

Cross-sectional and fracture surface inspections showed that the porosity had a close correlation for interaggregate and intra-agglomerate pores presented by Mayo [56], in addition to the segmentation cracks formed as the thermal stresses exceeded the cohesion of the coating. The porosity that was observed in the cross-sectional studies was in the size range of hundreds of nanometers up to some micrometers. However, it can be expected the porosity included also intra-agglomerate nanopores. The nanopores were most likely located between the accumulated nanoparticles as presented in Fig. 35. The existence of the nanopores is justified, since those were formed to the suspension plasma sprayed YSZ coatings as reported in [129], [135], that fairly similar deposition method compared to HVSPFS.

When energy is applied, in other words heat, densification i.e. sintering start to occur and the third stage of the sintering process is achieved. Since the coating thickness is not changed and the oxidation temperature is rather low compared to conventional sintering processes, the mass transport mechanism is most likely dominated only by the surface diffusion [55], [134]. In case of the cavities/tubular pores formed from the connecting nanopores and segmentation crack, the pores shrink in radius due to Raylight instabilities described by Mayo [56] or by elastic strain relaxation described by Bacciochini et al. [129], leading to microstructure with closed spherical pores as confirmed in Figs. 32 – 34.

The probable cause for remnant porosity and coarsening of the pores in the oxidized coatings shown in Figs. 32 – 34 is i) the presence of rigid frame that can be either substrate or large spray particles around the nanoparticles, ii) pore geometry and iii) pore coordination number. Firstly, the rigid frame causes the anisotropic shrinkage i.e. constrained sintering. The strain is more homogenous in the vertical direction (perpendicular to the rigid frame e.g., substrate) than in the lateral direction. According to [136], [137] the lateral strain on the coating surface is larger than next to the substrate, which results in an inhomogeneous density distribution and therefore the remnant porosity is localized near the substrate. The similar behaviour was observed when nanoparticles were surrounded by the larger spray particles (marked with R in Fig. 35). Nanoparticles obtain stronger sintering behaviour compared to submicron particles due to the total free energy as described previously. However, submicron particles operate as a rigid frame and prevent any changes in length c.f. the substrate. Secondly, the pore geometry may favour the pore growth as the sides are convex to the pore, that is the most likely situation for the as-sprayed coatings formed from the particles with the round morphology. Thirdly, the pore coordination number determinates if the pore shrinks or grows. In three dimension space, the critical coordination number is 12. The pores with the coordination number less than 12 will decrease in size, and the pores with the coordination number higher than 12 will increase in size [134]. Particularly for the intra-agglomerate nanopores, the coordination number may easily be higher than 12.

Iron-doped spinel coatings suffered migration of Fe and Co cations during the high temperature oxidation cycle, as shown in Table 7. Migration can be considered the most plausible explanation, since elemental analysis showed that selective evaporation did not occur during the high temperature deposition process. Both the iron-doped APS and HVSPFS coatings suffered Fe loss at the surface part of the coatings. For APS coatings, Co migrated towards the surface, whereas for HVSPFS coatings, Co migrated towards the substrate. Although migration was observed, the desired phases were still present, as confirmed in the XRD analysis, although with a slight shifting of the peak patterns.

TABLE 7.1   EDS spectra and relative amount of Cr in the points indicated in Figs. 32 and 33. The results are presented in at%.

$MnCo_{1.9}Fe_{0.1}O_4$							$MnCo_2O_4$						
Spectrum	O	Mn	Co	Fe	Cr	Cr/(Co+Mn+Fe)	Spectrum	O	Mn	Co	Fe	Cr	Cr/(Co+Mn+Fe)
1.	46.7	16.7	36.6	0.0	0.0	0.0	1.	59.8	17.4	24.3	1.0	0.6	0.0
2.	59.3	13.5	27.2	0.0	0.0	0.0	2.	61.4	13.2	23.3	1.0	1.0	0.0
3.	58.4	14.4	26.2	1.0	0.0	0.0	3.(scale)	28.5	-	-	51.4	20.1	0.4
4.	58.8	14.3	25.8	1.4	0.0	0.0	4.	-	-	-	77.6	22.5	0.3
5.	58.4	14.6	25.5	1.5	0.0	0.0	5.	-	-	-	76.2	23.2	0.3
6.	58.2	14.4	25.0	2.5	0.0	0.0							
7.	51.5	16.1	27.6	3.9	0.9	0.0							
8. (scale)	35.2	0.0	0.0	42.4	22.5	0.5							
9.	0.0	0.0	0.0	78.4	21.6	0.3							
10.	0.0	0.0	0.0	78.4	21.6	0.3							
$MnCo_{1.7}Fe_{0.3}O_4$							Mn_2CoO_4+Co						
Spectrum	O	Mn	Co	Fe	Cr	Cr/(Co+Mn+Fe)	Spectrum	O	Mn	Co	Fe	Cr	Cr/(Co+Mn+Fe)
1.	39.2	5.7	53.5	1.7	0.0	0.0	1.	56.9	24.6	18.5	-	-	0.0
2.	58.7	12.4	25.9	2.9	0.0	0.0	2.	57.7	23.6	18.7	-	-	0.0
3.	59.0	13.4	23.6	4.0	0.0	0.0	3.	57.6	22.7	18.9	0.9	-	0.0
4.	58.2	14.3	22.6	5.0	0.0	0.0	4.	53.3	26.4	20.4	-	-	0.0
5.	58.5	14.3	21.4	5.8	0.0	0.0	5.	57.4	23.9	18.0	0.7	-	0.0
6.	58.6	14.4	19.9	6.8	0.4	0.0	6.	48.4	28.1	22.5	1.0	-	0.0
7.	56.7	14.3	19.9	8.5	0.7	0.0	7.	58.0	21.2	19.6	0.9	0.4	0.0
8. (scale)	61.7	2.1	0.8	3.7	31.7	4.8	8. (scale)	53.9	19.1	19.3	1.8	5.9	0.1
9.	0.0	0.0	0.0	78.1	21.9	0.3	9.	-	-	-	76.8	23.2	0.3
10.	0.0	0.0	0.0	77.9	22.1	0.3	10.	-	-	-	76.9	23.1	0.3

TABLE 7.2 EDS spectra and relative amount of Cr in the points indicated in Fig. 34. The results are presented in at%.

TG1-$MnCo_{1.9}Fe_{0.1}O_4$							TG2-$Mn_{1.5}Co_{1.5}O_4$						
Spectrum	O	Mn	Co	Fe	Cr	Cr/(Mn+Co+Fe)	Spectrum	O	Mn	Co	Fe	Cr	Cr/(Mn+Co+Fe)
1.	57.3	22.5	20.2	0.0	0.0	0.0	1.	58.6	20.9	20.5	0.0	0.0	0.0
2.	57.5	16.3	24.6	1.6	0.0	0.0	2.	60.4	18.5	20.1	0.0	0.0	0.0
3.	58.6	15.9	23.9	1.7	0.0	0.0	3.	62.0	21.3	16.7	0.0	0.0	0.0
4.	63.4	14.2	21.2	1.4	0.0	0.0	4.	58.1	20.8	21.1	0.0	0.0	0.0
5.	55.1	17.3	26.0	1.6	0.0	0.0	5.	56.6	25.3	18.1	0.0	0.0	0.0
6.	57.5	16.9	24.0	1.6	0.0	0.0	6.	59.3	23.5	17.2	0.0	0.0	0.0
7.	58.6	16.3	23.2	1.9	0.0	0.0	7.	58.6	22.5	18.9	0.0	0.0	0.0
8.	56.3	17.1	24.6	2.0	0.0	0.0	8.	51.2	23.3	24.9	0.0	0.6	0.0
9.	58.4	16.3	23.5	1.8	0.0	0.0	9.	64.5	19.9	15.4	0.0	0.3	0.0
10.	57.9	16.7	23.5	2.0	0.0	0.0	10.	15.8	42.5	41.4	0.0	0.0	0.0
11.	58.3	15.8	23.5	2.2	0.3	0.0	11.	62.0	24.2	13.8	0.0	0.0	0.0
12.	59.3	15.6	22.5	2.3	0.3	0.0	12.	58.4	20.3	21.4	0.0	0.0	0.0
13.	58.7	15.6	23.2	2.0	0.6	0.0	13.	62.0	18.3	19.7	0.0	0.0	0.0
14. (scale)	65.6	0.0	0.0	0.0	34.4		14.	57.9	21.3	20.1	0.0	0.7	0.0
15.	32.0	0.0	0.0	42.2	25.7	0.6	15. (scale)	60.6	1.6	1.8	0.0	36	10.6
16.	0.0	0.0	0.0	77.5	22.5	0.3	16.	34.8	1.6	0.0	32.9	30.8	0.9
17.	0.0	0.0	0.0	77.5	22.5	0.3	17.	0.0	0.0	0.0	77.0	23.0	0.3
							18.	0.0	0.0	0.0	77.7	22.3	0.3

5.3.3 Cr barrier properties

The main purpose of the coatings is to prevent Cr migration, which is the main reason for the degradation, as explained in the Introduction. Migration originates from the high temperature oxidation as Cr-rich oxide scale forms on the substrates, producing highly volatile Cr compounds. The ideal situation would be to prevent the formation of the scale fully. However, as the cross-section images showed, the Cr-rich scale was formed due to the high temperature oxidation cycle. The most likely reasons were the partial diffusion of oxygen through the spinel coating and the high specific surface area associated with the surfaces of the nano- and sub-micron particles that contained enough oxygen for the scale to form. Although scale was formed, no spallation or similar breakaway oxidation was observed in the APS and HVSPFS coatings compared to the coatings reported in [31].

According to the EDS analysis data presented in Table 8, the oxide scale formed under the APS deposited spinel coatings had a dual-layer structure. The composition of the layer next to the substrate was close to the nominal composition of Cr_2O_3. This was confirmed by XRD analysis for the $(Mn,Co,Fe)_3O_4$ coating presented in Fig. 37a, and by Raman spectroscopy analysis for the $MnCo_2O_4$ coating presented in Fig. 37b–c. A reaction layer was formed above the Cr_2O_3 scale, which was a mixture of the deposited coating and migrated chromium with a composition close to $(Mn,Co,Cr)_3O_4$ or $(Co,Cr)_3O_4$. The EDS line and area analysis data obtained from the oxide scale formed between the HVSPFS coatings and substrates (Fig. 36) showed the presence of Cr_2O_3 and a Cr-containing spinel-type reaction layer, which was similar to the layers formed under the APS sprayed coatings.

TABLE 8   EDS analysis spectra of the areas presented in Figs. 32 and 33. The results are presented in at%. Modified from [Publications III and IV].

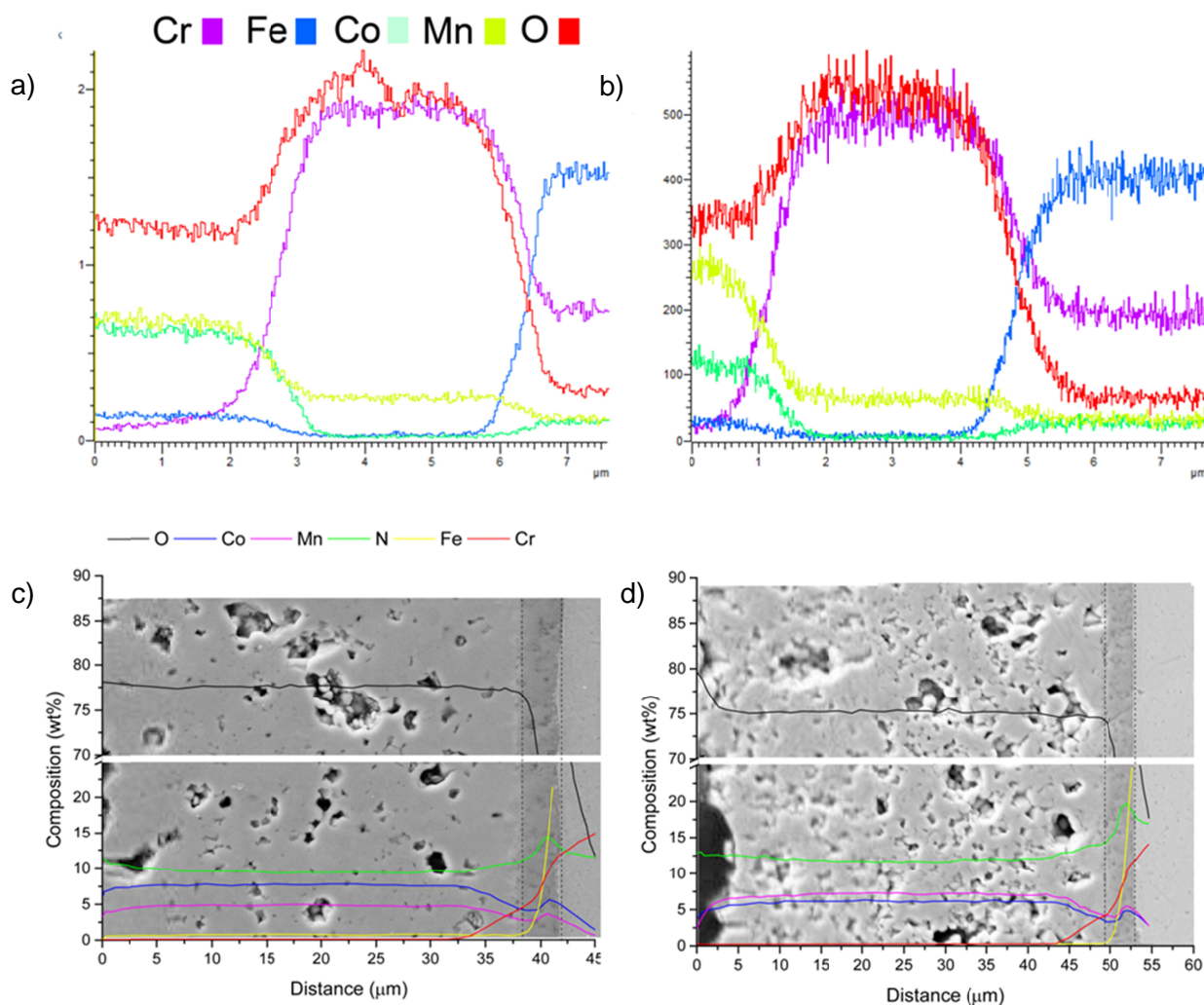| $MnCo_{1.9}Fe_{0.1}O_4$					
Area	Cr	Mn	Fe	Co	O
A1.	0.8	13.6	3.3	23.4	58.9
A2.	31.2	0.9	2.7	2.0	63.1
A3.	20.7	0.4	77.3	0.5	1.3
$MnCo_{1.7}Fe_{0.3}O_4$					
Area	Cr	Mn	Fe	Co	O
B1.	0.9	13.7	8.0	19.8	57.6
B2.	24.3	2.5	1.5	8.0	63.7
B3.	32.1	1.9	2.8	0.7	62.6
B4.	20.7	0.5	73.6	0.4	4.7
$MnCo_2O_4$					
Area	Cr	Mn	Fe	Co	O
A1.	0.5	14.1	0.6	23.6	60.4
A2.	5.9	11.0	0.8	19.8	62.5
A3.	26.9	3.5	2.6	3.8	63.2
A4.	22.0	0.3	75.0	0.5	2.3
Mn_2CoO_4+Co					
Area	Cr	Mn	Fe	Co	O
B1.	0.7	19.5	1.1	18.3	60.4
B2.	11.1	12.0	2.5	13.9	60.4
B3.	21.6	2.7	16.6	4.6	54.5
B4.	22.6	0.6	74.1	0.5	1.8

FIGURE 36 EDS line analysis data of the oxide scales formed when using a) $MnCo_{1.9}Fe_{0.1}O_4$ and b) $Mn_{1.5}Co_{1.5}O_4$ coatings. RF-GD-OES elemental analysis of c) $MnCo_{1.9}Fe_{0.1}O_4$ and d) $Mn_{1.5}Co_{1.5}O_4$ coatings. Oxidation cycle was performed at 850°C in air for 500 hours. [Publication VI]

Unlike the other oxidized coatings, the Mn_2CoO_4+Co coating did not show the presence of a Cr_2O_3 layer. According to the EDS study, the oxide scale had a composition that closely corresponded to $FeCr_2O_4$. This was confirmed by the Raman studies shown in Fig. 37c–d. The Raman spectra of the oxide scale showed a broad shoulder peak at 500 cm,$^{-1}$ most likely caused by a mixture of Fe_2O_3 and $FeCr_2O_4$ phases. For Fe_2O_3, the peak positions are at 549 and 681 cm^{-1}, but the reaction with Cr causes the peaks to transition to 500 and 691 cm^{-1}, respectively [138], as shown in Fig. 37d. According to the results presented in [139], the presence of $FeCr_2O_4$ should be more favourable than Cr_2O_3, as harmful Cr-species obtain higher vapour pressure over Cr_2O_3 than $FeCr_2O_4$ in SOFC operating conditions.
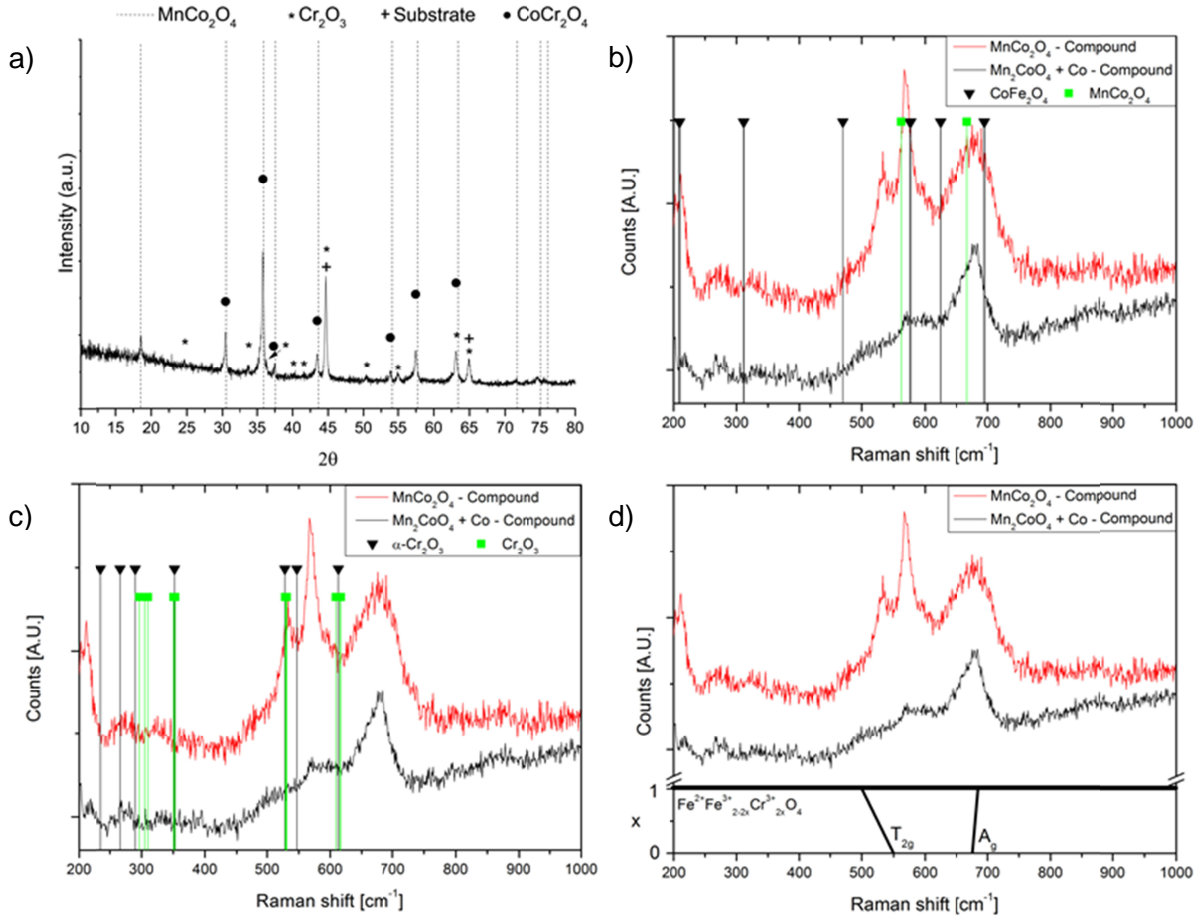
FIGURE 37 Oxide scale analysis of the oxidized (1000 hours at 700ºC in air) spinel coatings. The XRD analysis of $(Mn,Co,Fe)_3O_4$ is presented in (a) and the Raman spectra of the oxidized $(Mn,Co)_3O_4$ coating is in (b & c). The transition data of Fe_2O_3–$FeCr_2O_4$ is in (d). The figure is modified from [Publications III and IV].

As the coatings had dense microstructures, it is to be expected that migration is the main phenomena for Cr species to transport through a thickness gradient. For this reason, the migration was studied by the EDS point analysis method, as presented in Figs. 32, 33 and 34, and reported in Tables 7.1 and 7.2. In addition, the HVSPFS coatings were studied by the RF-GD-OES method, shown in Fig. 36c and 36d. RF-GD-OES provides more comprehensive results as the measurements were obtained from a 5 mm spot size.

The EDS results show that spinel coatings effectively prevented Cr migration. According to the results, Cr was observed from a distance of 6–10 μm from the scale as the APS coatings were oxidized. The measurements showed that a 10 μm $MnCo_2O_4$ coating was inadequate for protection, as Cr was transferred though the coating. The protection in long-term (5–10 years) use is related

to the material and thickness of the coating, and in order to obtain the required protection, the minimum coating thickness should therefore be exceeded.

The most promising Cr barrier properties for APS coatings were obtained when Mn_2CoO_4+Co ($Mn_{1.5}Co_{1.5}O_4$) powder was used to deposit a $Mn_{1.5}Co_{1.5}O_4$ coating. Not only did metallic Co enhance the denseness, but the multiphase structure inhibited Cr and oxygen migration and the Co-rich phases functioned as Cr traps for the migrated Cr. As Persson et al. [31] have calculated, the thermodynamic driving force, i.e. Gibbs energy change (ΔG) between Cr_2O_3, Mn_3O_4 and CoO, is more negative when the Mn content is lower. This means that a reduction in Mn content increases the thermodynamic driving force for the reactions between Cr_2O_3, Mn_3O_4 and CoO. Under the circumstances, Co-rich inclusions should be more reactive with migrated Cr cations than the Mn_2CoO_4 phase.

The HVSPFS coatings showed good Cr barrier properties. A closer comparison of the EDS results indicated that the $Mn_{1.5}Co_{1.5}O_4$ coating gave a somewhat better barrier against Cr migration than the $MnCo_{1.9}Fe_{0.1}O_4$ coating. This assumption was based on the distance that Cr migrated during the oxidation cycle. The results of the influence of the spinel composition on the Cr barrier properties were comparable to data obtained from APS spinel coatings. However, the oxidation cycle was relatively short, only 500 hours, and therefore a long-term (5–10 years) conclusion cannot be accurately estimated. The small distance of the Cr migration from the oxide scale was confirmed by RF-GD-OES analysis. The overall migration remained under 10 µm. Relying on the results obtained from the EDS and the RF-GD-OES studies, HVSPFS spinel coatings have at least as good Cr barrier properties as APS spinel coatings.

5.3.4 ASR properties

The electrical properties of APS and HVSPFS coatings were analysed by using the four-point measurements method simultaneously during the oxidation cycles. This test procedure was used to obtain ASR values, as shown in Fig. 38. The measurements were executed without contact pastes between the coatings. With this test arrangement, the results present only the coating-coating contacts and the changes (structural, microstructural and chemical) that occurred due to the high temperature and oxidizing atmosphere.
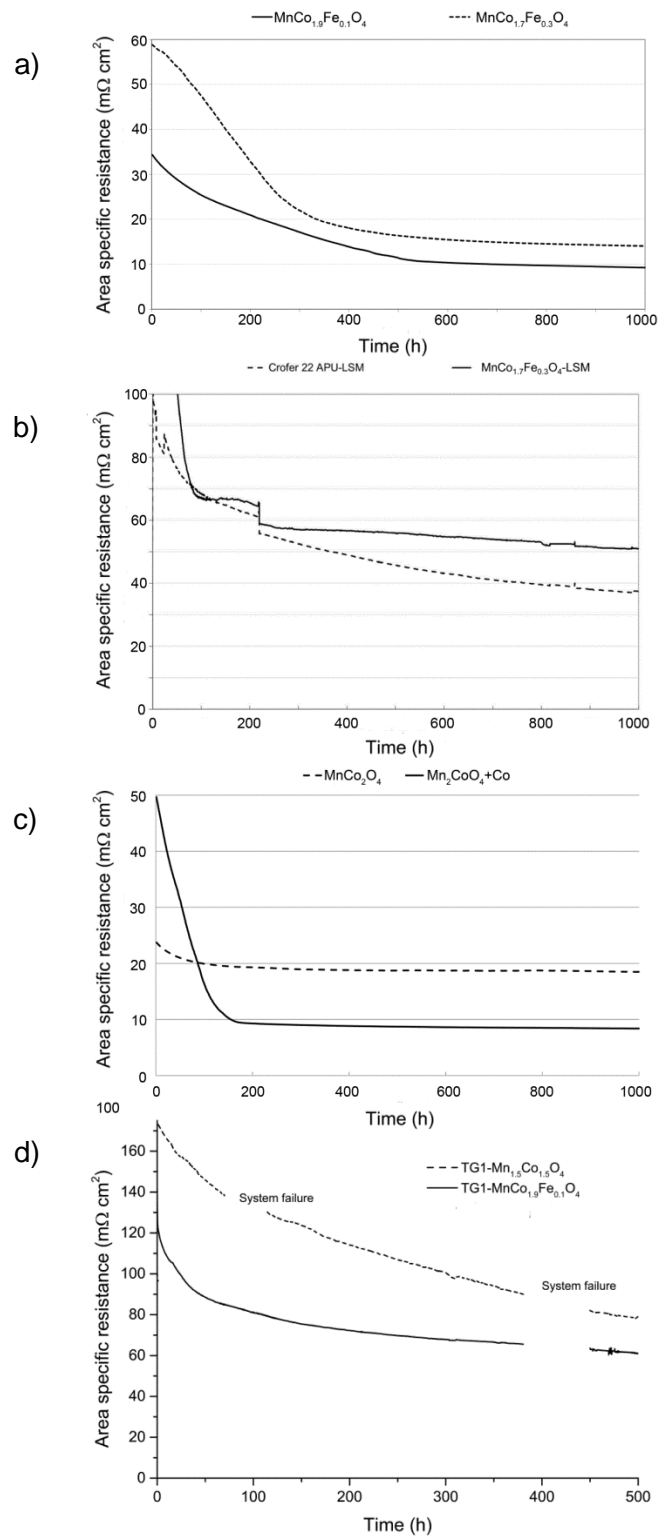
FIGURE 38 ASR data of the a) APS $MnCo_{2-x}Fe_xO_4$ b) APS $MnCo_{1.7}Fe_{0.3}O_4$-LSM and Crofer 22 APU-LSM c) APS $(Mn,Co)_3O_4$ and d) HVSPFS $MnCo_{1.9}Fe_{0.1}O_4$ and $Mn_{1.5}Co_{1.5}O_4$ spinel coatings. The figure is modified from [Publications III, IV and VI].

Due to the structural, microstructural and chemical changes that occurred due to sintering, the ASR values dropped significantly for the first few hundred hours. As the external load was applied, the number of contact points increased in the coating-coating interface due to the creep of the corrugated substrates. In addition, the surface irregularities deformed and the actual contact area increased as Dey et al. [140] have explained using a plastic deformation model. Furthermore, electrical conduction was enhanced by crystallographic changes, as the metastable phase was restored back to the $(Mn,Co)_3O_4$ and $(Mn,Co,Fe)_3O_4$ phases.

After the most rapid microstructural and chemical changes that occurred at the beginning of the oxidation cycle, the ASR values levelled off. The ASR values continued to decrease but at a much more moderate rate. This was a consequence of grain growth and the ongoing sintering process. As is widely accepted, the conduction mechanism in Mn-containing spinels is the small polaron hopping mechanism [24], [44], meaning that the electron is excited across the band gap from the valence band to the conduction band and a hole is formed in the valence band (intrinsic semiconductor) [45]. Due to the small polaron hopping, single crystallites/grains are ideal for conduction, whereas the grain boundaries cause scattering due to the grain boundary phases. The grain boundary phases can be considered as an amorphous phase, which most plausibly increases the resistivity.

At the end of the 1000-hour oxidation cycle, the ASR values for the APS $(Mn,Co,Fe)_3O_4$ spinels levelled off at 9.20 mΩ·cm^2 and 14.10 mΩ·cm^2 for the $MnCo_{1.9}Fe_{0.1}O_4$ and $MnCo_{1.7}Fe_{0.3}O_4$ coatings, respectively. These values are comparable to the study of Kiefer et al. [46], as the conductivities (varying sintering temperature) were in the range of 30–37 S/cm and 22–30 S/cm at 800 ˚C, for $MnCo_{1.9}Fe_{0.1}O_4$ and $MnCo_{1.7}Fe_{0.3}O_4$, respectively. For the APS $(Mn,Co)_3O_4$ coatings, the ASR values decreased to 18.50 mΩ·cm^2 and 8.40 mΩ·cm^2 for $MnCo_2O_4$ and Mn_2CoO_4+Co coatings, respectively. Yang et al. [42] have studied and reviewed similar performances for $Mn_{1.5}Co_{1.5}O_4$ and $MnCo_2O_4$ bulk samples, obtaining conductivity values of 40–60 S/cm and 15–25 S/cm, respectively, in relation to temperatures from 700 to 800 ˚C in air. Wang et al. [43] have measured ~68 S/cm value for $Mn_{1.5}Co_{1.5}O_4$ spinels at 800 ˚C in air. The $MnCo_{1.7}Fe_{0.3}O_4$-LSM and Crofer 22 APU-LSM spacer behaved similarly to the coating-coating tests as the conductivity improved due to sintering of the coating, the LSM-spacer and coating-spacer interface. Eventually, the ASR value levelled off at 50 mΩ·cm^2 at the end of the oxidation cycle.

The HVSPFS coatings achieved relatively high ASR values and were compared to the APS coatings. The lowest ASR values of 61 mΩ·cm^2 were obtained for the $MnCo_{1.9}Fe_{0.1}O_4$ and 77 mΩ·cm^2 for the $Mn_{1.5}Co_{1.5}O_4$ coating. The differences in the ASR values can be explained by i) the coating thicknesses and ii) the employed contact pressures. The APS coatings had a thickness of 12–20 µm, whereas the HVSPFS coatings achieved thicknesses of between 37–44 µm. In addition, the contact pressure of 4.50 kPa was significantly lower compared to the optimal 0.064–0.074 MPa

[140], which decreased the plastic deformation between the contact irregularities and therefore led to higher ASR values.

The ASR results of the APS and HVSPFS coatings present the [spinel coating] – [(spinel-based reaction layer) – (Cr-rich oxide layer)] – [substrate] material systems that were confirmed to be formed by the cross-sectional and various elemental analysis. Although $(Mn,Co,Fe)_3O_4$ spinel possesses good electrical conductivity, the conductivities were also influenced by the Cr oxide scale and the reaction layers. For example, the electrical conductivity of Cr_2O_3 is from 0.006–0.163 S/cm at 700 °C in air [141]. If a $(Mn,Cr)_3O_4$ reaction layer is formed, the conductivity is 0.001 S/cm (Mn:Cr=1:2) to 0.031 S/cm (Mn:Cr=1:1), at 700 °C in air [40]. Fergus et al. have reported that Cr substitution in the $(Mn,Co)_3O_4$ spinel lattice decreases the electrical conductivity in relation to the Cr content. The conductivity values of spinel vary from 0.003 S/cm (Mn,Co:Cr=1:2) to 1.30 S/cm (Mn,Co:Cr=2:1) at 700 °C in air [141], which is considerably lower than the conductivity of pure $MnCo_2O_4$ spinels. For this reason, the growth of scale and the extensive diffusion of Cr cations should be minimized.

6   Concluding remarks and suggestions for future work

The performance of the protective coatings in SOFC interconnects is strongly linked to the chemical composition and microstructure of the deposited coatings. Since degradation of the cathode is a consequence of reactions between the cathode materials and volatile Cr oxide and oxyhydroxides, i.e., CrO_3, $CrO_2(OH)_2$ and $CrO_2(OH)$, which are transported through the gas phase on the triple-phase boundary (TPB), these coatings should have a dense microstructure. A dense microstructure is essential in harsh environments (high humidity and operating temperature) in order to decrease the growth of Cr-rich oxide scale, which may lead to uncontrolled breakaway oxidation and/or increase the ohmic resistance of the substrate-coating systems. In addition, migration should be considered as a possible transport mechanism for Cr to reach the TPB. This was confirmed by formation of Cr-rich reaction layers, e.g., Cr-containing spinels, showing that at least 10 µm of coating thickness is needed in order to provide a buffer for harmful Cr, especially in long-term use.

In this work, protective $MnCo_2O_4$, $Mn_{1.5}Co_{1.5}O_4$ and Fe-doped $MnCo_{1.9}Fe_{0.1}O_4$, $MnCo_{1.8}Fe_{0.2}O_4$ and $MnCo_{1.7}Fe_{0.3}O_4$ coatings were deposited with various thermal spray processes. Atmospheric plasma spraying (APS) was employed as a conventional thermal spraying process, whereas high velocity solution precursor flame spraying (HVSPFS) represents a novel deposition technique in the thermal spraying research field. Both processes show great potential due to their scalability for industrial-scale production. However, in order to answer the requirements as described previously, the following claims should be taken into account:

- *Agglomerated and sintered spray powder with a cermet structure should be used in conventional thermal spraying when depositing a protective spinel coating for SOFC interconnectors.*

    Although promising results of the thermally sprayed spinel coatings were obtained using ceramic spinel powder, the basic problem is the inter-splat crack network formed between the deposited splats. This crack network may be responsible for providing a pathway for volatile Cr species to be transported to the cathode. In addition, it is clear that the crack network increases the ohmic resistance of the deposited coating by poor inter-lamellar contact with the neighbouring splats. The use of powder with agglomerated morphology, with the smallest possible primary particle size, will enhance the melting of the powder feedstock, resulting in a dense microstructure. Secondly, simultaneous substrate heating significantly decreases the inter-splat crack network, as the deposited splat obtains an optimal discoidal form when

deposited on the substrate. However, it should be noted that simultaneous substrate heating might not always be a feasible method for producing coatings in terms of production facilities and due to the dimensions of the ICs.

By selecting a suitable alloying component, such as the metallic Co in this study, multifunctional properties can be obtained. The alloying component fills the inter-lamellar spaces between the splats and i) improves gas density, ii) improves the electrical contact in inter-splat bonding, iii) acts as a reactive element by trapping the migrated Cr cations, iv) is a dopant to form more electrically conductive spinels.

- *Spinel coatings with advantageous properties for SOFC interconnects are obtained by using the high velocity solution precursor flame spray (HVSPFS) process.*

The clear advantage of the solution precursor thermal spray processes is the total length of the production chain. As the materials synthesis takes place in the spraying process, there is no need for separate materials synthesis, powder or paste preparation process phases as in the conventional thermal spraying or the wet-ceramic processes. These phases require time (labour and storage costs) and energy (electricity), which inevitably leads to an increase in production costs. In addition, it was shown that the coatings could be produced by using relatively cheap raw materials, for instance metal nitrates.

It was shown that nano-scale coating structures could be obtained by using solution precursor thermal spray processes instead of dry powder. The main difference was in the size of the particles from which the coatings were formed. When using a modified high velocity oxy-fuel spraying system, i.e. high velocity solution precursor flame spraying (HVSPFS), the coatings were formed of particles with a size range of 10 nm up to a few micrometres. The small particle size is the consequence of good atomization and evaporation of the precursor when injected into the high velocity thermal flame. The TEM and SEM analyses indicated that nanoparticles with a size range of 10 to 500 nm dominated the coating formation. These particles, as previously specified, were formed through the liquid-to-solid and gas-to-solid conversion route.

The as-sprayed coatings had a dense microstructure, which is favourable for preventing Cr transport and enabling good electrical properties. The dense microstructure was a consequence of the small particle size, but also of the high deposition velocity of the nanoparticles, which enabled closely packed particle structures. Since it can be expected that the mass of the sub-micron and nano-scaled particles is negligible, the flight velocity of the particles was close to the speed of the combustion flame.

- *$Mn_{1.5}Co_{1.5}O_4$ and $MnCo_{1.9}Fe_{0.1}O_4$ spinels should be deposited by processes that produce a metastable phase structure, small particle and crystallite size.*

According to the literature, $Mn_{1.5}Co_{1.5}O_4$ and $MnCo_{1.9}Fe_{0.1}O_4$ spinels have favourable properties. The APS and HVSPFS processes produce coatings with good Cr barrier properties, in addition to an acceptable level of ASR values. These processes enable high deposition temperatures, and as a result, the coatings are formed through fast changes of solid-molten-solid states. As a consequence, coatings are formed of sub-micron nano-scale particles with nano-scale crystallite sizes with metastable properties. Together, these factors enhanced the sintering behaviour of the as-sprayed coatings when used in the SOFC stack.

Further studies should be carried out on HVSPFS spinel coatings and the deposition process. Although the results are promising, more studies needs to be done to confirm the long term stability of HVSPFS spinel coatings. The conventional thermal spray process is robust and well known process and therefore widely used in various applications. However, the HVSPFS process is a novel deposition technique and various process variables, e.g. hardware, solution precursor, combustion and gas-ratios needs to be studied more closely in order to obtain the similar robust production level as in conventional thermal spray methods. Furthermore, the use of different solution precursors, suspensions and for example two component suspension-solution-type of precursors should be studied in order to find out the potential of the HVSPFS technique.

References

[1] The International Energy Agency, "Key world energy statistics," 2013.

[2] "Fuel Cells and Hydrogen Joint Undertaking Programme Review 2011," 2011.

[3] T. I. E. Agency, "World energy investments outlook," 2014.

[4] A. J. Appleby, "From Sir William Grove to today: fuel cells and the future," J. Power Sources, vol. 29, no. 1–2, pp. 3–11, 1990.

[5] J. M. Andújar and F. Segura, "Fuel cells: History and updating. A walk along two centuries," Renew. Sustain. Energy Rev., vol. 13, no. 9, pp. 2309–2322, 2009.

[6] R. J. Kee, P. Korada, K. Walters, and M. Pavol, "A generalized model of the flow distribution in channel networks of planar fuel cells," J. Power Sources, vol. 109, pp. 148–159, 2002.

[7] S. C. Singhal and K. Kendall, "Introduction to SOFCs," in High Temperature and Solid Oxide Fuel Cells. Fundamentals, Design and Applications, Elsevier, 2003, pp. 1–22.

[8] C. Sun, R. Hui, and J. Roller, "Cathode materials for solid oxide fuel cells: a review," J. Solid State Electrochem., vol. 14, no. 7, pp. 1125–1144, 2009.

[9] Y. Tao, J. Shao, W. G. Wang, and J. Wang, "Optimisation and evaluation of $La_{0.6}Sr_{0.4}CoO_{3-\delta}$ cathode for intermediate temperature solid oxide fuel cells," Fuel Cells, vol. 9, no. 5, pp. 679–683, 2009.

[10] S. P. Jiang and S. H. Chan, "A review of anode materials development in solid oxide fuel cells," J. Mater. Sci., vol. 39, pp. 4405–4439, 2004.

[11] J. Fergus, "Oxide anode materials for solid oxide fuel cells," Solid State Ionics, vol. 177, no. 17–18, pp. 1529–1541, 2006.

[12] W. Z. Zhu and S. C. Deevi, "Development of interconnect materials for solid oxide fuel cells," Mater. Sci. Eng. A, vol. 348, no. 1–2, pp. 227–243, 2003.

[13] J. Wu and X. Liu, "Recent development of SOFC metallic interconnect," J. Mater. Sci. Technol., vol. 26, no. 4, pp. 293–305, 2010.

[14] J. W. Fergus, "Metallic interconnects for solid oxide fuel cells," Mater. Sci. Eng. A, vol. 397, no. 1–2, pp. 271–283, 2005.

[15] Z.-Y. Chen, L.-J. Wang, F.-S. Li, and K.-C. Chou, "Oxidation mechanism of Fe–16Cr alloy as SOFC interconnect in dry/wet air," J. Alloys Compd., vol. 574, pp. 437–442, 2013.

[16] C. Gindorf, L. Singheiser, and K. Hilpert, "Vaporisation of chromia in humid air," J. Phys. Chem. Solids, vol. 66, no. 2–4, pp. 384–387, 2005.

[17] K. Hilpert, D. Dos, M. Miller, D. H. Peck, and R. Weiss, "Chromium vapor species over solid oxide fuel cell interconnect materials and their potential for degradation processes," J. Electrochem. Soc., vol. 143, no. 11, pp. 3642–3647, 1996.

[18] J. Fergus, "Effect of cathode and electrolyte transport properties on chromium poisoning in solid oxide fuel cells," Int. J. Hydrogen Energy, vol. 32, no. 16, pp. 3664–3671, 2007.

[19] J. A. Schuler, Z. Wuillemin, A. Hessler-Wyser, C. Comminges, N. Y. Steiner, and J. Van herle, "Cr-poisoning in (La,Sr)(Co,Fe)O$_3$ cathodes after 10,000h SOFC stack testing," J. Power Sources, vol. 211, pp. 177–183, 2012.

[20] F. Chen, E. Sun, J. Yamanis, J. Hawkes, J. Smeggil, S. Warrier, and J.-W. Kim, "Cr poisoning effect for solid oxide fuel cells," in Materials Science & Technology 2006 Conference and Exhibition, 2006, pp. 303–311.

[21] J. Y. Kim, N. L. Canfield, L. A. Chick, K. D. Menhardt, and V. L. Sprenkle, "Chromium poisoning effect on various cathodes," in Ceramic Engineering and Science Proceeding, 2005, pp. 129–138.

[22] J. Wu, D. Yan, J. Pu, B. Chi, and L. Jian, "The investigation of interaction between $La_{0.9}Sr_{0.1}MnO_3$ cathode and metallic interconnect for solid oxide fuel cell at reduced temperature," J. Power Sources, vol. 202, pp. 166–174, 2012.

[23] R. Sachitanand, M. Sattari, J. E. Svensson, and J. Froitzheim, "Evaluation of the oxidation and Cr evaporation properties of selected FeCr alloys used as SOFC interconnects," Int. J. Hydrogen Energy, vol. 38, no. 35, pp. 15328–15334, 2013.

[24] Z. Lu, J. Zhu, E. Andrew Payzant, and M. P. Paranthaman, "Electrical conductivity of the manganese chromite spinel solid solution," J. Am. Ceram. Soc., vol. 88, no. 4, pp. 1050–1053, 2005.

[25] N. J. Magdefrau, L. Chen, E. Y. Sun, and M. Aindow, "Effects of alloy heat treatment on oxidation kinetics and scale morphology for Crofer 22 APU," J. Power Sources, vol. 241, pp. 756–767, 2013.

[26] L. Niewolak, E. Wessel, L. Singheiser, and W. J. Quadakkers, "Potential suitability of ferritic and austenitic steels as interconnect materials for solid oxide fuel cells operating at 600°C," *J. Power Sources*, vol. 195, no. 22, pp. 7600–7608, 2010.

[27] M. Palcut, L. Mikkelsen, K. Neufeld, M. Chen, R. Knibbe, and P. V. Hendriksen, "Corrosion stability of ferritic stainless steels for solid oxide electrolyser cell interconnects," *Corros. Sci.*, vol. 52, no. 10, pp. 3309–3320, 2010.

[28] W. Z. Zhu and S. C. Deevi, "Opportunity of metallic interconnects for solid oxide fuel cells: a status on contact resistance," Mater. Res. Bull., vol. 38, no. 6, pp. 957–972, 2003.

[29] L. Yngve and N. Truls, "Spinel and perovskite functional layer between plansee metallic interconnect (Cr-5 wt% Fe-1wt % Y_2O_3) and ceramic $(La_{0.85}Sr_{0.15})_{0.91}MnO_3$ cathode materials for solid oxide fuel cells," J. Electrochem. Soc., vol. 147, no. 9, pp. 3251–3256, 2000.

[30] M. Zahid, I. Arul Raf, F. Tietz, P. Lersch, and D. Stöver, "Electrical conductivity of perovskites in the quasi-ternary system $La_{0.8}Sr_{0.2}MnO_3$-$La_{0.8}Sr_{0.2}CoO_3$-$La_{0.8}Sr_{0.2}FeO_3$ for application as cathode-interconnect contact layer in SOFC," in Proceedings of the Ninth International Symposium on Solid Oxide Fuel Cells, 2005, p. 1708.

[31] Å. H. Persson, L. Mikkelsen, P. V. Hendriksen, and M. A. J. Somers, "Interaction mechanisms between slurry coatings and solid oxide fuel cell interconnect alloys during high temperature oxidation," J. Alloys Compd., vol. 521, pp. 16–29, 2012.

[32] J.-J. Huang, Y.-P. Fu, J.-Y. Wang, Y.-N. Cheng, S. Lee, and J.-C. Hsu, "Characterization of Fe–Cr alloy metallic interconnects coated with LSMO using the aerosol deposition process," Mater. Res. Bull., vol. 51, pp. 63–68, 2014.

[33] W.-J. Shong, C.-K. Liu, C.-Y. Chen, C.-C. Peng, H.-J. Tu, G. T.-K. Fey, R.-Y. Lee, and H.-M. Kao, "Effects of lanthanum-based perovskite coatings on the formation of oxide scale for ferritic SOFC interconnect," Mater. Chem. Phys., pp. 10–15, 2011.

[34] M. Palcut, L. Mikkelsen, K. Neufeld, M. Chen, R. Knibbe, and P. V. Hendriksen, "Improved oxidation resistance of ferritic steels with LSM coating for high temperature electrochemical applications," Int. J. Hydrogen Energy, pp. 1–8, 2011.

[35] M. Palcut, R. Knibbe, K. Wiik, and T. Grande, "Cation inter-diffusion between $LaMnO_3$ and $LaCoO_3$ materials," Solid State Ionics, vol. 202, no. 1, pp. 6–13, 2011.

[36] S. Miyoshi and M. Martin, "B-Site cation diffusivity of Mn and Cr in perovskite-type $LaMnO_3$ with cation-deficit nonstoichiometry," Phys. Chem. Chem. Phys., vol. 11, no. 17, pp. 3063–3070, 2009.

[37] H. Kurokawa, C. P. Jacobson, L. C. DeJonghe, and S. J. Visco, "Chromium vaporization of bare and of coated iron–chromium alloys at 1073 K," Solid State Ionics, vol. 178, no. 3–4, pp. 287–296, 2007.

[38] Y. Fang, C. Wu, X. Duan, S. Wang, and Y. Chen, "High-temperature oxidation process analysis of $MnCo_2O_4$ coating on Fe–21Cr alloy," Int. J. Hydrogen Energy, vol. 36, no. 9, pp. 2–7, 2011.

[39] N. J. Magdefrau, L. Chen, E. Y. Sun, J. Yamanis, and M. Aindow, "Formation of spinel reaction layers in manganese cobaltite – coated Crofer22 APU for solid oxide fuel cell interconnects," J. Power Sources, vol. 227, pp. 318–326, 2013.

[40] X. Chen, P. Hou, C. Jacobson, S. Visco, and L. Dejonghe, "Protective coating on stainless steel interconnect for SOFCs: oxidation kinetics and electrical properties," Solid State Ionics, vol. 176, no. 5–6, pp. 425–433, 2005.

[41] E. Aukrust and A. Muan, "Phase relations in the system cobalt oxide – manganese oxide in air," J. Am. Ceram. Soc., vol. 46, no. 10, p. 511, 1963.

[42] Z. Yang, G. Xia, X. Li, and J. Stevenson, "$(Mn,Co)_3O_4$ spinel coatings on ferritic stainless steels for SOFC interconnect applications," Int. J. Hydrogen Energy, vol. 32, no. 16, pp. 3648–3654, 2007.

[43] K. Wang, Y. Liu, and J. W. Fergus, "Interactions between SOFC interconnect coating materials and chromia," J. Am. Ceram. Soc., vol. 94, no. 12, pp. 4490–4495, 2011.

[44] Y. Liu, J. W. Fergus, K. Wang, and C. Dela Cruz, "Crystal structure, chemical stabilities and electrical conductivity of Fe-doped manganese cobalt spinel oxides for SOFC interconnect coatings," J. Electrochem. Soc., vol. 160, no. 11, pp. F1316–F1321, 2013.

[45] M. Barsoum, Fundamentals of Ceramics. McGraw-Hill Companies, Inc., 1997, p. 668.

[46] T. Kiefer, M. Zahid, F. Tietz, D. Stöver, and Z. H.-R., "Electrical conductivity and thermal expansion coefficients of spinel in the series $MnCo_{2-x}Fe_xO_4$ for application as a protective layer in SOFC," in Proceeding of the 26th Riso International Symposium on Materials Science: Solid State Electrochmistry, 2005, pp. 261–266.

[47] V. Miguel-Pérez, A. Martínez-Amesti, M. L. Nó, A. Larrañaga, and M. I. Arriortua, "The effect of doping $(Mn,B)_3O_4$ materials as protective layers in different metallic interconnects for solid oxide fuel cells," J. Power Sources, vol. 243, pp. 419–430, 2013.

[48] J.-J. Choi, J. Ryu, B.-D. Hahn, W.-H. Yoon, B.-K. Lee, and D.-S. Park, "Dense spinel $MnCo_2O_4$ film coating by aerosol deposition on ferritic steel alloy for protection of chromic evaporation and low-conductivity scale formation," J. Mater. Sci., vol. 44, no. 3, pp. 843–848, 2008.

[49] Z. Yang, G.-G. Xia, G. D. Maupin, and J. W. Stevenson, "Conductive protection layers on oxidation resistant alloys for SOFC interconnect applications," Surf. Coat. Technol., vol. 201, no. 7, pp. 4476–4483, 2006.

[50] B.-K. Park, J.-W. Lee, S.-B. Lee, T.-H. Lim, S.-J. Park, C.-O. Park, and R.-H. Song, "Cu- and Ni-doped $Mn_{1.5}Co_{1.5}O_4$ spinel coatings on metallic interconnects for solid oxide fuel cells," Int. J. Hydrogen Energy, vol. 38, no. 27, pp. 12043–12050, 2013.

[51] Y. Xu, Z. Wen, S. Wang, and T. Wen, "Cu doped Mn–Co spinel protective coating on ferritic stainless steels for SOFC interconnect applications," Solid State Ionics, vol. 192, no. 1, pp. 561–564, 2011.

[52] Y. Zhenguo, G. Xia, and J. W. Stevenson, "$Mn_{1.5}Co_{1.5}O_4$ spinel layers on ferritic stainless steels for SOFC interconnect applications," Electrochem. Solid-State Lett., vol. 8, no. 3, pp. 1–3, 2005.

[53] T. Uehara, N. Yasuda, M. Okamoto, and Y. Baba, "Effect of Mn–Co spinel coating for Fe–Cr ferritic alloys ZMG232L and 232J3 for solid oxide fuel cell interconnects on oxidation behavior and Cr-evaporation," J. Power Sources, vol. 196, no. 17, pp. 7251–7256, 2010.

[54] X. Montero, F. Tietz, D. Sebold, H. Buchkremer, A. Ringuede, M. Cassir, A. Laresgoiti, and I. Villarreal, "$MnCo_{1.9}Fe_{0.1}O_4$ spinel protection layer on commercial ferritic steels for interconnect applications in solid oxide fuel cells," J. Power Sources, vol. 184, no. 1, pp. 172–179, 2008.

[55] J. S. Reed, Principles of ceramics processing, Second Edi. Toronto: Johan Wiley & Sons, 1995, p. 658.

[56] M. J. Mayo, "Processing of nanocrystalline ceramics from ultrafine particles," Int. Mater. Rev., vol. 41, no. 3, pp. 85–115, 1996.

[57] Y.-S. Chou, J. W. Stevenson, G.-G. Xia, and Z.-G. Yang, "Electrical stability of a novel sealing glass with (Mn,Co)-spinel coated Crofer22APU in a simulated SOFC dual environment," J. Power Sources, vol. 195, no. 17, pp. 5666–5673, 2010.

[58] Z. Yang and J. W. Stevenson, "$Mn_{1.5}Co_{1.5}O_4$ spinel layers on ferritic stainless steels for SOFC interconnect applications," Electrochem. Solid-State Leffers, vol. 8, no. 3, pp. 1–3, 2005.

[59] X. Xin, S. Wang, J. Qian, C. Lin, Z. Zhan, and T. Wen, "Development of the spinel powder reduction technique for solid oxide fuel cell interconnect coating," Int. J. Hydrogen Energy, vol. 37, no. 1, pp. 471–476, 2012.

[60] A. M. Dayaghi, M. Askari, and P. Gannon, "Pre-treatment and oxidation behavior of sol–gel Co coating on 430 steel in 750°C air with thermal cycling," Surf. Coatings Technol., vol. 206, no. 16, pp. 3495–3500, 2012.

[61] W. Zhang, J. Pu, B. Chi, and L. Jian, "$NiMn_2O_4$ spinel as an alternative coating material for metallic interconnects of intermediate temperature solid oxide fuel cells," J. Power Sources, vol. 196, no. 13, pp. 5591–5594, 2011.

[62] B. Hua, J. Pu, W. Gong, J. Zhang, F. Lu, and L. Jian, "Cyclic oxidation of Mn–Co spinel coated SUS 430 alloy in the cathodic atmosphere of solid oxide fuel cells," J. Power Sources, vol. 185, no. 1, pp. 419–422, 2008.

[63] W. Qu, J. Li, and D. G. Ivey, "Sol–gel coatings to reduce oxide growth in interconnects used for solid oxide fuel cells," J. Power Sources, vol. 138, no. 1–2, pp. 162–173, 2004.

[64] L. C. Klein, Sol-Gel Technology for Thin Films, Fibers, Preforms, Electronics and Specialty Shapes. 1988, p. 428.

[65] C. C. Mardare, H. Asteman, M. Spiegel, A. Savan, and A. Ludwig, "Investigation of thermally oxidised Mn–Co thin films for application in SOFC metallic interconnects," Appl. Surf. Sci., vol. 255, no. 5, pp. 1850–1859, 2008.

[66] N. V. Gavrilov, V. V. Ivanov, A. S. Kamenetskikh, and A. V. Nikonov, "Investigations of Mn–Co–O and Mn–Co–Y–O coatings deposited by the magnetron sputtering on ferritic stainless steels," Surf. Coatings Technol., vol. 206, no. 6, pp. 1252–1258, 2011.

[67] H. Zhang, J. Wu, X. Liu, and A. Baker, "Studies on elements diffusion of Mn/Co coated ferritic stainless steel for solid oxide fuel cell interconnects application," Int. J. Hydrogen Energy, vol. 38, no. 12, pp. 5075–5083, 2013.

[68] K. O. Hoyt, P. E. Gannon, P. White, R. Tortop, B. J. Ellingwood, and H. Khoshuei, "Oxidation behavior of $(Co,Mn)_3O4$ coatings on preoxidized stainless steel for solid oxide fuel cell interconnects," Int. J. Hydrogen Energy, vol. 37, no. 1, pp. 518–529, 2012.

[69] J. G. Grolig, J. Froitzheim, and J.-E. Svensson, "Coated stainless steel 441 as interconnect material for solid oxide fuel cells: oxidation performance and chromium evaporation," J. Power Sources, vol. 248, pp. 1007–1013, 2014.

[70] K. Uusi-Esko, "Synthesis and characterization of ternary manganese oxides," Aalto University, 2011.

[71] L. Pawlowski, The science and engineering of thermal spray coatings, Second edi., vol. 34, no. 1. Chichester: John Wiley & Sons, 1995, p. 626.

[72] H. Kreye and F. Gärtner, "High velocity oxy-fuel flame spraying- state of the art, new developments and alternatives," in 6. Kolloquium Hochgeschwindigkeits-Flammspritzen, 2003, pp. 5–17.

[73] C. Law, a Makino, and T. Lu, "On the off-stoichiometric peaking of adiabatic flame temperature," Combust. Flame, vol. 145, no. 4, pp. 808–819, 2006.

[74] W. Wu, W. Guan, G. Wang, W. Liu, Q. Zhang, T. Chen, and W. G. Wang, "Evaluation of $Ni_{80}Cr_{20}/(La_{0.75}Sr_{0.25})_{0.95}MnO_3$ dual layer coating on SUS 430 stainless steel used as metallic interconnect for solid oxide fuel cells," Int. J. Hydrogen Energy, vol. 39, no. 2, pp. 996–1004, 2014.

[75] S. J. Han, Y. Chen, and S. Sampath, "Role of process conditions on the microstructure, stoichiometry and functional performance of atmospheric plasma sprayed $La(Sr)MnO_3$ coatings," J. Power Sources, vol. 259, pp. 245–254, 2014.

[76] S. D. Park, S. Kumar, S. C. Lee, and C. Lee, "Effects of silver addition on mechanical properties of plasma sprayed SOFC interconnect layer," in International Thermal Spray Conference, 2008, pp. 1035–1038.

[77] D. P. Lim, D. S. Lim, J. S. Oh, and I. W. Lyo, "Influence of post-treatments on the contact resistance of plasma-sprayed LaSrMnO coating on SOFC metallic interconnector," Surf. Coat. Technol., vol. 200, no. 5–6, pp. 1248–1251, 2005.

[78] J. Lagerbom, U. Kanerva, A. Nikkilä, T. Varis, and M. Kylmälahti, "Phase stability and structure of conductive perovskite ceramic coatings by thermal spraying," in Thermal Spray 2008: Crossing Borders, 2008, pp. 1091–1096.

[77] M. J. G. Vargas, M. Zahid, F. Tietz, and A. Aslanides, "Use of SOFC metallic interconnect coated with spinel protective layers using the APS technology," ECS Trans., vol. 7, no. 1, pp. 2399–2405, 2007.

[79] E. Saoutieff, G. Bertrand, M. Zahid, and L. Gautier, "APS deposition of $MnCo_2O_4$ on commercial alloys K41X used as solid oxide fuel cell interconnect: the importance of post heat-treatment for densification of the protective layer," ECS Trans., vol. 25, no. 2, pp. 1397–1402, 2009.

[80] O. Thomann, M. Pihlatie, M. Rautanen, O. Himanen, J. Lagerbom, M. Mäkinen, T. Varis, T. Suhonen, and J. Kiviaho, "Development and application of HVOF sprayed spinel protective coating for SOFC interconnects," J. Therm. Spray Technol., vol. 22, no. 5, pp. 631–639, 2013.

[82] Y.-Z. Hu, C.-X. Li, G.-J. Yang, and C.-J. Li, "Evolution of microstructure during annealing of $Mn_{1.5}Co_{1.5}O_4$ spinel coatings deposited by atmospheric plasma spray," Int. J. Hydrogen Energy, vol. 39, no. 25, pp. 13844–13851, 2014.

[83] J. Karthikeyan, C. Berndt, J. Tikkanen, S. Reddy, and H. Herman, "Plasma spray synthesis of nanomaterial powders and deposits," Mater. Sci. Eng. A, vol. 238, no. 2, pp. 275–286, 1997.

[84] J. Tikkanen, "Liquid flame spray development and its applications," Tampere University of Technology, 1999.

[85] J. Karthikeyan, C. C. Berndt, J. Tikkanen, J. Y. Wang, A. H. King, and H. Herman, "Preparation of nanophase materials by thermal spray processing of liquid precursors," Nanostructured Mater., vol. 9, no. 1–8, pp. 137–140, 1997.

[86] L. Pawlowski, "Suspension and solution thermal spray coatings," Surf. Coat. Technol., vol. 203, no. 19, pp. 2807–2829, 2009.

[87] C. K. Muoto, E. H. Jordan, M. Gell, and M. Aindow, "Identification of desirable precursor properties for solution precursor plasma spray," J. Therm. Spray Technol., vol. 20, no. 4, pp. 802–816, 2011.

[88] D. Chen, E. H. Jordan, and M. Gell, "Effect of solution concentration on splat formation and coating microstructure using the solution precursor plasma spray process," Surf. Coatings Technol., vol. 202, no. 10, pp. 2132–2138, 2008.

[89] G. Bertolissi, C. Chazelas, G. Bolelli, L. Lusvarghi, M. Vardelle, and A. Vardelle, "Engineering the microstructure of solution precursor plasma-sprayed coatings," J. Therm. Spray Technol., vol. 21, no. 6, pp. 1148–1162, 2012.

[90] P. Fauchais, V. Rat, J. F. Coudert, N. Caron, and Wittmann-Teneze K., "Parameters controlling liquid plasma spraying: solutions, sols, or suspensions," J. Therm. Spray Technol., vol. 17, no. 1, pp. 31–59, 2008.

[91] D. Chen, E. Jordan, and M. Gell, "Thermal and crystallization behavior of zirconia precursor used in the solution precursor plasma spray process," J. Mater. Sci., vol. 42, no. 14, pp. 5576–5580, 2007.

[92] L. Xie, "Processing parameter effects on solution precursor plasma spray process spray patterns," Surf. Coatings Technol., vol. 183, no. 1, pp. 51–61, 2004.

[93] D. Chen, E. H. Jordan, M. Gell, and X. Ma, "Dense alumina–zirconia coatings using the solution precursor plasma spray process," J. Am. Ceram. Soc., vol. 91, no. 2, pp. 359–365, 2008.

[94] L. Xie, X. Ma, E. H. Jordan, N. P. Padture, D. T. Xiao, and M. Gell, "Deposition of thermal barrier coatings using the solution precursor plasma spray process," J. Mater. Sci., vol. 39, no. 5, pp. 1639–1646, 2004.

[95] L. Xie, D. Chen, E. Jordan, a Ozturk, F. Wu, X. Ma, B. Cetegen, and M. Gell, "Formation of vertical cracks in solution-precursor plasma-sprayed thermal barrier coatings," Surf. Coatings Technol., vol. 201, no. 3–4, pp. 1058–1064, 2006.

[96] X. Ma, F. Wu, J. Roth, M. Gell, and E. Jordan, "Low thermal conductivity thermal barrier coating deposited by the solution plasma spray process," Surf. Coatings Technol., vol. 201, no. 7, pp. 4447–4452, 2006.

[97] F. Wu, E. Jordan, X. Ma, and M. Gell, "Thermally grown oxide growth behavior and spallation lives of solution precursor plasma spray thermal barrier coatings," Surf. Coatings Technol., vol. 202, no. 9, pp. 1628–1635, 2008.

[98] D. Chen, M. Gell, E. H. Jordan, E. Cao, and X. Ma, "Thermal stability of air plasma spray and solution precursor plasma spray thermal barrier coatings," J. Am. Ceram. Soc., vol. 90, no. 10, pp. 3160–3166, 2007.

[99] M. Gell, E. H. Jordan, M. Teicholz, B. M. Cetegen, N. P. Padture, L. Xie, D. Chen, X. Ma, and J. Roth, "Thermal barrier coatings made by the solution precursor plasma spray process," J. Therm. Spray Technol., vol. 17, no. 1, pp. 124–135, 2007.

[100] A. Jadhav, N. Padture, F. Wu, E. Jordan, and M. Gell, "Thick ceramic thermal barrier coatings with high durability deposited using solution-precursor plasma spray," Mater. Sci. Eng. A, vol. 405, no. 1–2, pp. 313–320, 2005.

[101] E. H. Jordan, L. Xie, X. Ma, M. Gell, N. P. Padture, B. Cetegen, A. Ozturk, J. Roth, T. D. Xiao, and P. E. C. Bryant, "Superior thermal barrier coatings using solution precursor plasma spray," J. Therm. Spray Technol., vol. 13, pp. 57–65, 2004.

[102] R. Rampon, F.-L. Toma, G. Bertrand, and C. Coddet, "Liquid plasma sprayed coatings of yttria-stabilized zirconia for SOFC electrolytes," J. Therm. Spray Technol., vol. 15, no. 4, pp. 682–688, 2006.

[103] M. Marr, J. Kuhn, C. Metcalfe, J. Harris, and O. Kesler, "Electrochemical performance of solid oxide fuel cells having electrolytes made by suspension and solution precursor plasma spraying," J. Power Sources, vol. 245, pp. 398–405, 2014.

[104] Y. Wang and T. W. Coyle, "Solution precursor plasma spray of nickel-yittia stabilized zirconia anodes for solid oxide fuel cell application," J. Therm. Spray Technol., vol. 16, no. 5–6, pp. 898–904, 2007.

[105] C. Metcalfe, E. Lay-Grindler, and O. Kesler, "Characterization of Ni–YSZ anodes for solid oxide fuel cells fabricated by solution precursor plasma spraying with axial feedstock injection," J. Power Sources, vol. 247, pp. 831–839, 2014.

[106] P. Fauchais, R. Etchart-Salas, C. Delbos, M. Tognonvi, V. Rat, J. F. Coudert, and T. Chartier, "Suspension and solution plasma spraying of finely structured layers: potential application to SOFCs," J. Phys. D. Appl. Phys., vol. 40, no. 8, pp. 2394–2406, 2007.

[107] C.-X. Li, S. Liu, Y. Zhang, and C.-J. Li, "Characterization of the microstructure and electrochemical behavior of $Sm_{0.7}Sr_{0.3}Co_{3-\delta}$ cathode deposited by solution precursor plasma spraying," Int. J. Hydrogen Energy, vol. 37, no. 17, pp. 13097–13102, 2012.

[108] D. Chen, E. Jordan, and M. Gell, "Porous TiO_2 coating using the solution precursor plasma spray process," Surf. Coatings Technol., vol. 202, no. 24, pp. 6113–6119, 2008.

[109] D. Chen, E. H. Jordan, M. Gell, and X. Ma, "Dense TiO_2 coating using the solution precursor plasma spray process," J. Am. Ceram. Soc., vol. 91, no. 3, pp. 865–872, 2008.

[110] D. Chen, E. H. Jordan, M. Gell, and M. Wei, "Apatite formation on alkaline-treated dense TiO$_2$ coatings deposited using the solution precursor plasma spray process.," Acta Biomater., vol. 4, no. 3, pp. 553–9, 2008.

[111] Y. Xiao, L. Song, X. Liu, Y. Huang, T. Huang, Y. Wu, J. Chen, and F. Wu, "Nanostructured bioactive glass–ceramic coatings deposited by the liquid precursor plasma spraying process," Appl. Surf. Sci., vol. 257, no. 6, pp. 1898–1905, 2011.

[112] J. Puranen, J. Laakso, L. Hyvärinen, M. Kylmälahti, and P. Vuoristo, "Influence of spray parameters and characteristics of solutions on microstructure and phase composition of solution precursor atmospheric plasma sprayed (SPPS) Mn-Co spinel coating," in Thermal Spray 2012: Proceedings of the International Thermal Spray Conference (ASM International), 2012, no. 3, pp. 810–815.

[113] J. Puranen, J. Laakso, L. Hyvärinen, M. Kylmälahti, and P. Vuoristo, "High temperature oxidation behaviour of MnCo$_2$O$_4$ coating on Crofer 22 APU manufactured by a novel solution precursor plasma spray process (SPPS)," in 10th Fuel Cell Science, Engineering and Technology Conference, 2012, vol. 2, pp. 1–6.

[114] S. Basu and B. M. Cetegen, "Modeling of liquid ceramic precursor droplets in a high velocity oxy-fuel flame jet," Acta Mater., vol. 56, no. 12, pp. 2750–2759, 2008.

[115] A. Ozturk and B. M. Cetegen, "Experiments on ceramic formation from liquid precursor spray axially injected into an oxy-acetylene flame," Acta Mater., vol. 53, no. 19, pp. 5203–5211, 2005

[116] B. M. Cetegen and S. Basu, "Review of modeling of liquid precursor droplets and particles injected into plasmas and high-velocity oxy-fuel (HVOF) flame jets for thermal spray deposition applications," J. Therm. Spray Technol., vol. 18, no. 5–6, pp. 769–793, 2009.

[117] E. Dongmo, A. Killinger, M. Wenzelburger, and R. Gadow, "Numerical approach and optimization of the combustion and gas dynamics in high velocity suspension flame spraying (HVSFS)," Surf. Coatings Technol., vol. 203, no. 15, pp. 2139–2145, 2009.

[118] A. Ozturk and B. M. Cetegen, "Modeling of precipitate formation in precursor droplets injected axially into an oxygen/acetylene combustion flame," Mater. Sci. Eng. A, vol. 422, no. 1–2, pp. 163–175, 2006.

[119] E. Dongmo, R. Gadow, A. Killinger, and M. Wenzelburger, "Modeling of combustion as well as heat, mass, and momentum transfer during thermal spraying by HVOF and HVSFS," J. Therm. Spray Technol., vol. 18, no. 5–6, pp. 896–908, 2009.

[120] D. Chen, E. H. Jordan, and M. Gell, "Solution precursor high-velocity oxy-fuel spray ceramic coatings," J. Eur. Ceram. Soc., vol. 29, no. 16, pp. 3349–3353, 2009.

[121] "Crofer 22 APU," 2010. Product sheet.

[122] R. D. Shannon, "Revised effective ionic radii and systematic studies of interatomie distances in halides and chaleogenides," Acta Crystallogr. Sect. A, vol. 32, no. 5, pp. 751–767, 1976.

[123] R. McPherson and B. V. Shafer, "interlamellar contact within plasma-sprayed coatings," Thin Solid Films, vol. 97, pp. 201–204, 1982.

[124] M. Marr and O. Kesler, "Permeability and microstructure of suspension plasma-sprayed YSZ electrolytes for SOFCs on various substrates," J. Therm. Spray Technol., vol. 21, no. 6, pp. 1334–1346, 2012.

[125] D. Gallant, M. Pézolet, and S. Simard, "Optical and physical properties of cobalt oxide films electrogenerated in bicarbonate aqueous media.," J. Phys. Chem. B, vol. 110, no. 13, pp. 6871–80, 2006.

[126] J. Y. Eun, Y. Y. Mi, M. Ji-Woong, and H. Hae Jin, "Fabrication of a MnCo$_2$O$_4$ gadolinia-doped ceria (GDC) dual-phase composite membrane for oxygen separation," J. Korean Ceram. Soc., vol. 47, no. 2, pp. 199–204, 2010.

[127] J. Puranen, L. Hyvärinen, J. Lagerbom, M. Kylmälahti, H. Koivuluoto, and P. Vuoristo, "Suspension plasma spraying (SPS) of manganese-cobalt spinel coatings," in International Thermal Spray Conference, 2011, pp. 1201–1205.

[128] T. Nissinen, M. Leskelä, M. Gasik, and J. Lamminen, "Decomposition of mixed Mn and Co nitrates supported on carbon," Thermochim. Acta, vol. 427, no. 1–2, pp. 155–161, 2005.

[129] A. Bacciochini, F. Ben-Ettouil, E. Brousse, J. Ilavsky, G. Montavon, A. Denoirjean, S. Valette, and P. Fauchais, "Quantification of void networks of as-sprayed and annealed nanostructured yttria-stabilized zirconia (YSZ) deposits manufactured by suspension plasma spraying," Surf. Coatings Technol., vol. 205, no. 3, pp. 683–689, 2010.

[130] A. Maury-Ramirez, J.-P. Nikkanen, M. Honkanen, K. Demeestere, E. Levänen, and N. De Belie, "TiO_2 coatings synthesized by liquid flame spray and low temperature sol–gel technologies on autoclaved aerated concrete for air-purifying purposes," Mater. Charact., vol. 87, pp. 74–85, 2014.

[131] J.-P. Nikkanen, S. Heinonen, E. H. Saarivirta, M. Honkanen, and E. Levänen, "Photocatalytically active titanium dioxide nanopowders: Synthesis, photoactivity and magnetic separation," IOP Conf. Ser. Mater. Sci. Eng., vol. 47, p. 012066, 2013.

[132] R. M. Silverstein and F. X. Webster, Spectrometric identification of organic compounds, Sixth edit. John Wiley & Sons, 1997.

[133] S. Naka, M. Inagaki, and T. Tanaka, "On the formation of solid solution in $Co_{3-x}Mn_xO_4$ system," J. Mater. Sci., vol. 7, no. 4, pp. 441–444, 1972.

[134] M. Rahaman, Ceramic processing. Roca Raton, Florida: Taylor & Francis, 2007.

[135] A. Bacciochini, J. Ilavsky, G. Montavon, A. Denoirjean, F. Ben-ettouil, S. Valette, P. Fauchais, and K. Wittmann-teneze, "Quantification of void network architectures of suspension plasma-sprayed (SPS) yttria-stabilized zirconia (YSZ) coatings using Ultra-small-angle X-ray scattering (USAXS)," Mater. Sci. Eng. A, vol. 528, no. 1, pp. 91–102, 2010.

[136] E. Levänen and T. Mäntylä, "Effect of sintering temperature on functional properties of alumina membranes," J. Eur. Ceram. Soc., vol. 22, pp. 613–623, 2002.

[137] C. Jamin, T. Rasp, T. Kraft, and O. Guillon, "Constrained sintering of alumina stripe patterns on rigid substrates: Effect of stripe geometry," J. Eur. Ceram. Soc., vol. 33, no. 15–16, pp. 3221–3230, 2013.

[138] M. D. A. C. Belo, M. Walls, N. E. Hakiki, J. Corset, E. Picquenard, G. Sagonb, and D. Noel, "Composition , structure and properties of the oxide films formed on the stainless steel 316L in a primary type pwr environment," Corros. Sci., vol. 40, no. 2, pp. 447–463, 1998.

[139] G. Yang, S. Simner, J. Stevenson, and P. Singh, "SOFC IC overview and CTP status," SECA CTP IC Meeting, 2004. [Online]. Available: http://www.netl.doe.gov/File%20Library/Research/Coal/energy%20systems/fuel%20cells/proceedings/IC-PNNL-Singh.pdf (Cited 20.3.2014)

[140] T. Dey, D. Singdeo, M. Bose, R. N. Basu, and P. C. Ghosh, "Study of contact resistance at the electrode–interconnect interfaces in planar type Solid Oxide Fuel Cells," J. Power Sources, vol. 233, pp. 290–298, 2013.

[141] J. W. Fergus, K. Wang, and Y. Liu, "Transition metal spinel oxide coatings for reducing chromium poisoning in SOFCs," vol. 33, no. 40, pp. 77–84, 2011.

Publication I

The Structure and Properties of Plasma Sprayed Iron Oxide Doped Manganese Cobalt Oxide Spinel Coatings for SOFC Metallic Interconnectors

by

J. Puranen, J. Lagerbom, L. Hyvärinen, M. Kylmälahti, O. Himanen, M. Pihlatie, J. Kiviaho, and P. Vuoristo

The Structure and Properties of Plasma Sprayed Iron Oxide Doped Manganese Cobalt Oxide Spinel Coatings for SOFC Metallic Interconnectors

Jouni Puranen, Juha Lagerbom, Leo Hyvärinen, Mikko Kylmälahti, Olli Himanen, Mikko Pihlatie, Jari Kiviaho, and Petri Vuoristo

Manganese cobalt oxide spinel doped with Fe$_2$O$_3$ was studied as a protective coating on ferritic stainless steel interconnects. Chromium alloying causes problems at high operation temperatures in such oxidizing conditions where chromium compounds evaporate and poison the cathode active area, causing the degradation of the solid oxide fuel cell. In order to prevent chromium evaporation, these interconnectors need a protective coating to block the chromium evaporation and to maintain an adequate electrical conductivity. Thermal spraying is regarded as a promising way to produce dense and protective layers. In the present work, the ceramic Mn-Co-Fe oxide spinel coatings were produced by using the atmospheric plasma spray process. Coatings with low thickness and low amount of porosity were produced by optimizing deposition conditions. The original spinel structure decomposed because of the fast transformation of solid-liquid-solid states but was partially restored by using post-annealing treatment.
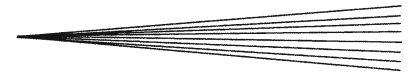
1. Introduction

Interconnectors (ICs) are used in a solid oxide fuel cell (SOFC) to provide an even fuel and oxidant distribution through a cell construction, to prevent fuel and oxygen gases from mixing and to connect the cells electrically in series. Traditional IC materials used in the electrolyte-supported cells, where operating temperatures were above 800 °C, were mainly alloyed lanthanum chromites (Ref 1, 2). By using the anode-supported cells, it is pos-

Jouni Puranen, Leo Hyvärinen, Mikko Kylmälahti, and **Petri Vuoristo**, Department of Materials Science, Tampere University of Technology, Tampere, Finland; **Juha Lagerbom**, VTT, Research Centre of Finland, Tampere, Finland; and **Olli Himanen, Mikko Pihlatie,** and **Jari Kiviaho**, VTT, Research Centre of Finland, Espoo, Finland. Contact e-mail: jouni.puranen@tut.fi.

sible to use a thinner electrolyte layer and in this way decrease the SOFC operating temperature under 800 °C. Lower operating temperatures give the advance of using new material alternatives. These have been developed in order to obtain better electrical properties and especially to lower manufacturing costs when designing co-, cross- and counterflow gas channel configurations. Potential materials for this use are chromium-based alloys, for example, ferritic stainless steels. Chromium alloying gives good corrosion protection and moderate corrosion resistance at high operating temperatures (600-800 °C) and in highly oxidizing environments (Ref 2).

The corrosion protection is based on the forming of Cr$_2$O$_3$ scale on the steel surface. Chromium oxide tends to have low electrical resistivity at elevated temperatures (1×10^2 Ω/cm at 800 °C) and by alloying other elements, for example, manganese, the formed oxide layer properties can be modified (Ref 2-4). The risk of using high chromium alloyed steels is the forming and the evaporation of chromium trioxide CrO$_3$ and chromium hydroxides CrO$_2$(OH)$_2$, depending on the cathode side inlet atmosphere. These compounds may transfer to a cathode active area (triple phase boundary, TPB), the area where oxygen is able to ionize. Compounds reduce back to Cr$_2$O$_3$ and cause the decreasing of the size of the active area causing a drop in the efficiency of the cell. This process is called chromium poisoning or degradation. The types of used cathode materials have an effect on the degradation speed. Some previous studies have reported that especially cathodes with higher amount of Sr alloying (La-Sr-Co-Fe, La-Sr-Fe, and La-Sr-Mn) suffer the most Cr-poisoning effect. One possible reason for this is that Sr reacts with Cr

and forms the SrCrO$_4$ phase. Degradation speed was the lowest when used cathode materials did not contain any Sr alloying, for example, La-Ni-Fe (Ref 5-7).

The protective coatings are used in order to minimize the oxidation of the IC and to prevent the evaporation of chromium compounds. Ensuring long-term usability, the coatings must fulfill the following requirements: (i) an excellent electrical conductivity with the objective of 100% electronic conduction so the effect of ohmic losses does not negatively affect the power density of the stack; (ii) a good chemical, microstructural, and phase stability at the stack operating temperature in an oxidizing environment; (iii) the coefficient of thermal expansion (CTE) of the coating should be near the other stack components such as the metallic IC and the cathode; (iv) a thermal conductivity at the lowest limit of 5 W/m/K at the point when generated heat from the cathode is transferred to the anode for endothermic fuel reformation reactions; and (v) the coatings together with the metallic substrate should have high temperature strength and creep resistance and provide structural support when used as a stationary and an auxiliary power unit under external stresses and vibrations (Ref 2).

The coating materials that have been previously studied as protective coatings are mainly the so-called perovskite materials with a chemical structure of (AB)$_2$O$_3$, where A and B are metallic cations. The most used materials have been lanthanum-manganese oxides (Ref 8-12) and lanthanum-cobalt/chromium oxides (Ref 3, 9, 12-18) with selected alloying, mainly in order to modify electrical and diffusion barrier properties. The use of these coatings is based on the same kind of composition and crystal structure as in the cathode materials. The coatings and the cathode have the same kind of mechanical behavior in elevated temperatures. The main difference between the cathode and the protective coating is that whereas the cathode layer is porous the protective coating needs to be dense to prevent the evaporation of harmful chromium compounds and oxidation of the substrate. Thermal spraying (Ref 8-16, 18) and spin coating (Ref 17) are used as a fabrication method. The main problem in all studies still seems to be manufacturing dense and thin coating structures so that the oxidation of substrate materials can fully be eliminated in long-time exposure.

An interesting alternative for perovskite are materials with a spinel structure, (AB)$_3$O$_4$, where A and B are metallic cations. Some previous studies have been published where spinel materials with a composition of manganese-cobalt oxides (Ref 3, 12, 19-21) and manganese-chromium oxides (Ref 20) have been used as the protective coating layer against the evaporation of harmful chromium compounds, working as an active layer forming more stable chromium oxide compounds. Larring et al. (Ref 12) found in their experiments that (Mn,Co)$_3$O$_4$ spinel worked effectively as a chromium barrier, even when compared with often used perovskite materials. They also discovered that the mechanical properties of the coating seem to match the used substrate alloy. When using iron (Fe) doped manganese-cobalt oxide spinel, it is possible to improve the electrical and mechanical

properties of the coating. Studies have shown that a proper amount of Fe in MnCo$_{2-x}$Fe$_x$O$_4$ is in the range of $0.1 < x < 0.25$ (Ref 22). The spinel coatings are mainly manufactured by slurry painting/spraying (Ref 12, 19-21), physical vapor deposition (Ref 23), and DC electrodeposition methods (Ref 24) but there are no studies where Mn-Co spinel, especially with Fe alloying, are being manufactured by thermal spaying. In this article, the suitability of atmospheric plasma spraying (APS) is being studied as a fast manufacturing method for producing thin, under 50 μm thick, protective coatings for thin 0.2 mm ferritic stainless steel substrates.

2. Experimental

2.1 Powder Manufacturing

Fe$_2$O$_3$ doped Mn-Co spinel powder was produced by solid state synthesis and agglomerated to spherical form by spray drying. MnCo$_{1.8}$Fe$_{0.2}$O$_4$ (MCF) powder was prepared by weighing appropriate amounts of MnCO$_3$, CoCO$_3$, and Fe$_2$O$_3$ powders together and milling them for 20 h in a drum ball mill. After the milling, the mixture was calcinated at 1000 °C in air for 6 h to obtain the spinel structure. The powder was dispersed in water using 1 wt.% of dispersant (Dispex A40, Ciba, Basel, Switzerland) by a planetary ball mill, 2 h at 300 rpm with ZrO$_2$ balls (Fritsch pulverisette 5, Fritsch GmbH, Germany). 2 wt.% of bonding agent (PVA, Celanese, Dallas) was added to the slurry by a high shear mixer. The suspension was spray dried by spray dryer (Niro pilot, GEA Niro, Soeborg, Denmark). A rotary nozzle with high rotation speed was used in order to get the fine agglomerate size needed for thin coating production. The powder was sintered at 1150 °C to improve powder strength, where an isothermal step at 500 °C for 2 h was used in order to pyrolyze the PVA without fracturing the agglomerates. After sintering, the powder was sieved. Particle size of $-29 + 13$ μm (d90-d10) was measured by laser diffraction sensor (Helos, Sympatec GmbH, Clausthal-Zellerfeld, Germany).

2.2 Coating Manufacturing

The coatings were produced by using a plasma gun (F4-MB, Sulzer Metco, Winterthur, Switzerland). Parameters were selected so that the influence of the used gun power on coating properties could be studied. The lowest energy parameter at which a stable coating could be produced was selected to be as parameter P1. More detailed parameters can be seen in Fig. 1. Constant spraying distance (120 mm) and surface speed were assured by using an X-Y manipulator. The desired average coating thickness was about 15-20 μm.

Samples sprayed with parameters 1, 7, and 9 were annealed to examine the restoring of the spinel structure. The samples were annealed at 800 °C for 3 h at normal atmosphere and the crystal structure was then analyzed. By choosing samples 1, 7, and 9 the influence of gun power could be estimated.

The substrate material was ThyssenKrupp VDM Crofer 22 APU specially tailored for SOFC use (Cr: 20-24 wt.%). The thickness of the substrate was 0.2 mm with 70×70 mm outer dimensions. The substrates were grit blasted (240 grit Al_2O_3) before plasma spraying so that the needed adhesion could be reached. Grit blasting was performed to both sides to avoid the bending of the thin substrate. After being plasma sprayed, the samples were laser cut to 15×20 mm pieces. The pieces were then molded in cold resin in a chamber under reduced pressure to prevent cracking and to give the samples an extra support while grinding and polishing.

2.3 Characterization Methods

The powder and the coatings were analyzed by using a scanning electron microscope (SEM) (Philips XL 30, Philips, Amsterdam, Netherlands). Secondary electron (SE) and back-scattering electron (BSE) modes were used for morphological inspections and energy dispersed spectroscopy (EDS) mode was used for quantitative analysis of
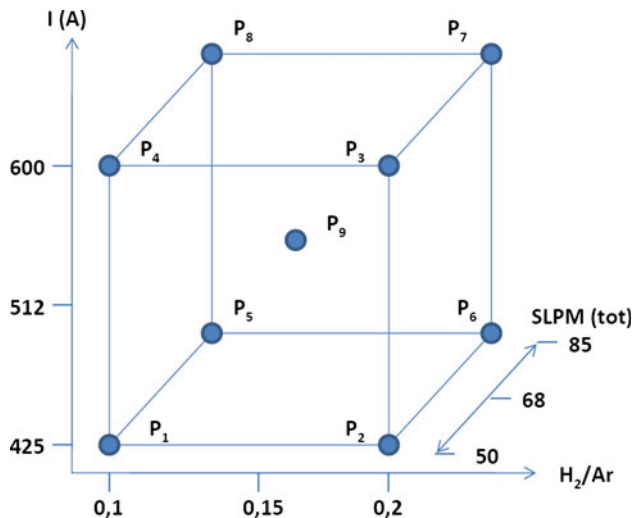
the elements. Porosity values were calculated by using an image analysis tool. Qualitative phase analysis of the powder and as-sprayed and annealed coatings was performed by using a x-ray diffractometer using Cu-K$_\alpha$ radiation source (Siemens D-500, Siemens, Berlin, Germany).

Hardness tests were performed by using a microhardness tester (MMT-X7, Matsuzawa, Akita, Japan). The hardness values were measured using a 250 mN cell load. Using this extraordinarily low test load, it was ensured that an indentation mark did not extend outside of the coatings' cross-section area. Results are the average values of five separate measurements.

3. Results and Discussion

3.1 Powder Characterization

The powder morphology is presented in Fig. 2. The particles were spherical because of spray drying and formed of primary particles of the size of 2-3 μm which can be seen from a cross-sectional SEM image. Some particles were attached to each other which affected flow properties negatively in a powder feeder, but the powder was still sprayable. When the chemical composition of the powder was analyzed, the amount of Fe seemed to be higher than it should be (Table 1). The calculated amount of Fe was 6.7%, but the analyzed value was 12.4%.

Fig. 1 Plasma spraying parameters

Table 1 Amount of elements in atomic percentages (at.%) (EDS)

Elements	Powder	P1	P2	P3	P4
Mn (33.3)	31.3	30.5	31.4	32.0	31.0
Fe (6.7)	12.4	11.9	12.2	13.0	12.2
Co (60)	56.3	57.6	56.4	55.4	56.8

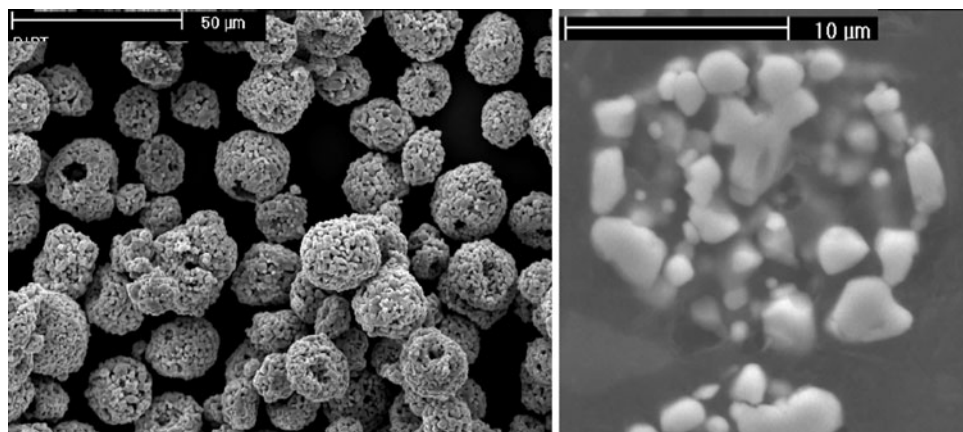|	P5	P6	P7	P8	P9
Mn	29.3	30.7	31.2	30.0	30.4
Fe	12.5	11.7	12.0	11.7	11.7
Co	58.1	57.6	56.9	58.3	58.0

Fig. 2 Secondary electron image (SEM) of MCF-spinel powder (left). Cross-sectional secondary electron image (SEM) of MCF-spinel powder (right)

The amount was probably altered because Fe-K$_\alpha$ radiation was at the same value when compared to manganese-K$_\beta$ radiation and Fe-K$_\beta$ radiation was at the same value compared to cobalt-K$_\alpha$ radiation. Overlapping of radiation peaks increases the values, even though the mixture ratios were correct when the powder was manufactured.

3.2 Coating Structural Characterization

The coatings (Fig. 3) had a typical plasma-sprayed structure. In all the coatings, some pores, cracks and some large pull-outs were present. Clear boundaries in separate spraying layers were not present. The desired coating thickness was achieved with a relatively dense microstructure with small variations of porosity (Table 2). The coatings had a good adhesion to the substrate and no visible cracking on the interface, but in some coatings vertical cracks were present, especially in the coatings where high energy parameters were used. This might be the result of small differences in CTE values. For MnCo$_{1.8}$Fe$_{0.2}$O$_4$ sintered at 1000 °C the CTE value is 12.3 × 10^{-6}/K (Ref 22) and for Crofer 22 APU depending on the temperature while spraying it, the CTE values varies (200-1000 °C) 10.3-12.7 × 10^{-6}/K (Ref 25). These cracks may offer a pathway for oxygen access and chromium evaporation.

3.3 Coating Chemical and Phase Analysis

The influence of the spraying parameters on selective compound evaporation is presented in Table 1. Values have been calculated by analyzing the whole image area.
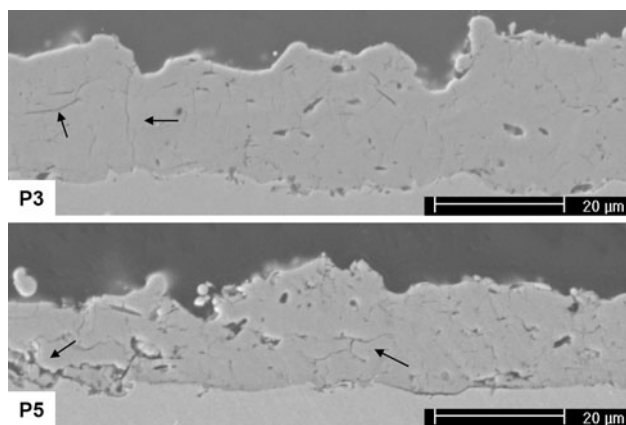

Fig. 3 Cross-sectional secondary electron image (SEM) of plasma sprayed spinel coatings. Lowest porosity coating (P3) and highest porosity coating (P5)

Table 2 Amount of porosity in percentages (%)

Parameter	Porosity, %	Parameter	Porosity, %
P1	6.1	P6	6.6
P2	5.3	P7	5.7
P3	3.8	P8	5.3
P4	5.7	P9	6.7
P5	6.9		

When comparing EDS measurements with the values of the powder, significant alteration could not be noticed. In this case, the coating compositions were not altered, although high energetic spraying parameters were used. It is possible that the coatings include smaller areas where selective evaporation has occurred. The reason for this is the fluctuation of plasma flame/energy resulting in molten droplets with altered composition. Due to the same reason, a similar variation of Fe amount can be seen in EDS analysis as was observed in the powder's case.

When analyzing the crystal structures of the as-sprayed coatings (Fig. 4), it can be noticed that the original spinel structure is decomposed. Peaks in the coatings were analyzed to be near the FeO (wuestite) kind of structure with a cubic form. When comparing low energy spraying parameters with high energy parameters the peaks were equal, meaning that the variations of spraying parameters did not affect the formed crystal structure. The reason for the presented structure lies in the coating preparation method where material is melted and cooled rapidly. When droplets hit the substrate and metastable crystal structures, material decomposition occurs and new compositions are being formed.

The XRD results of pre-selected annealed samples (Fig. 5) reveal that the spinel structure can be restored by using a separate annealing. When comparing the coatings with the powder, it can be seen that small intensity peaks of MnCo$_{1.8}$Fe$_{0.2}$O$_4$ spinel are present. In sample P1 there is also a high intensity peak of Fe, which was the result of the reflection of the substrate material and can be neglected. In all the coatings, the peaks of an FeO kind of structure and Co$_3$O$_4$ spinel were also present. The peaks of FeO were a result of a situation where the restoring of the spinel structure was not fully completed and where it may need more time for a complete reformation reaction. The presence of Co$_3$O$_4$ spinel peaks was an interesting result. These peaks might be the result of the selective evaporation of those components which cannot be seen in the EDS analysis taken from the whole coating area.
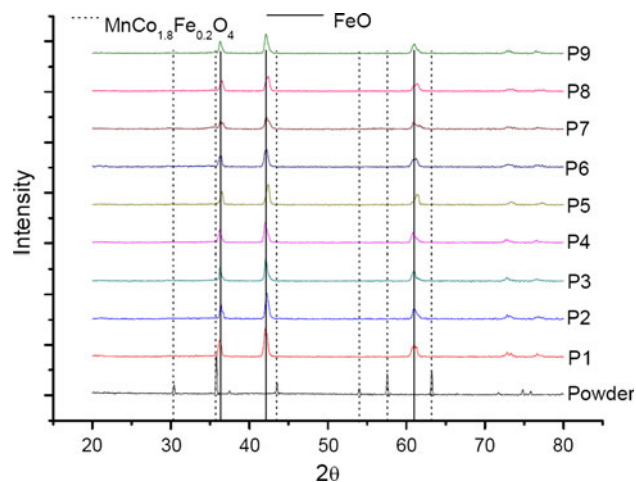

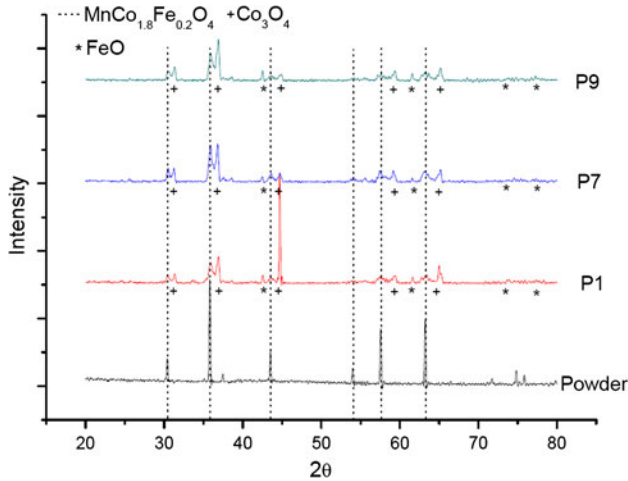**Fig. 4** XRD-analysis of as-sprayed coatings with all spraying parameters

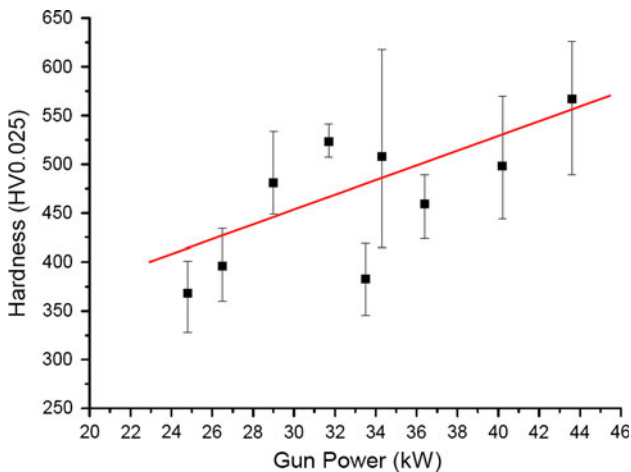**Fig. 5** XRD analysis of selected annealed coatings

Fig. 6 Hardness values related to used gun power

In this case, it may be that manganese was evaporated during spraying. The result of this was the metastable form of Mn-Co-Fe spinel, Fe oxide and an excess amount of cobalt in the form of cobalt oxide spinel. Lim et al. (Ref 11) got the same results of evaporation of manganese when plasma spraying perovskite structured $La_{0.8}Sr_{0.2}MnO_3$ on metallic ICs.

3.4 Coatings' Mechanical Properties

Hardnesses of the protective coatings varied from 320 to 600 $HV_{0.025}$. When plotting the hardness as a function of gun power (Fig. 6) and inspecting the interdependency fitting with linear regression (R value 0.521), it can be seen that the hardness values are related to the used gun power. By increasing the used gun power by 80%, the coatings' hardness values increased by 35% on average.

The reason for the increased hardness values could be related to single splat behavior in the coating process. When low gun power was used the particles were not able to fully melt and, as a result, coatings contained partially melted particles. These particles have poor adhesion and degrade the internal strength of the coating. When the used gun power was increased, the single particles were able to melt more homogeneously and form a coating where un-melted particles were not present. The coating was then formed of splats with good adhesion, which may influence the crack networks between splats so that they are smaller compared to the coatings prepared by using low gun power. In this case, the use of high energy parameters is an advantage that could provide a coating which provides better protection against chromium evaporation from the substrate.

4. Conclusions

The spinel materials are an interesting option for protective coatings on ferritic stainless steels instead of perovskites that are already being used. Earlier studies in this area were based on manufacturing these coatings by slurry- or thin film techniques. In this study, APS has been used to produce Mn-Co-Fe spinel coating on the thin metallic IC in SOFCs.

The conventional plasma sprayed coating has always included some pores and cracks because of the nature of the spraying process. When plasma spraying Mn-Co-Fe spinel, the original $MnCo_{1.8}Fe_{0.2}O_4$ crystal structure seems to decompose in the fast changes of transformation (solid-liquid-solid) which leads to the forming of metastable compounds. Also some selective evaporation of the components, for example, manganese, can happen. The original spinel structure will decompose but it can be partially restored by using a separate annealing process. In this process, metastable phases will transform by diffusion and growth of grain size and form stable compositions, for example, Co_3O_4.

The mechanical properties of the coatings were highly dependent on the used spray parameters. By increasing the used gun power, a harder coating structure could be achieved and the amount of un-melted particles decreased. Negative influences of using high energy spraying parameters on coating composition in this research were not noticed.

References

1. J. Jeffrey and W. Fergus, Lanthanum Chromite-Based Materials for Solid Oxide Fuel Cell Interconnects, *Solid State Ion.*, 2004, **171**, p 1-15
2. W.Z. Zhu and S.C. Deevi, Development of Interconnect Materials for Solid Oxide Fuel Cells, *Mater. Sci. Eng.*, 2003, **A348**, p 227-243
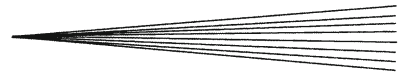
3. H. Kurokawa, P.Y. Hou, X. Chen, C. Jacobson, L. DeJonghe, and S.J. Visco, Effect of Protective Coatings for Alloy Interconnect on Oxidation and Cr Vaporization, *Materials Science and Technology*, Vol. 1, Materials and Systems, 2006, p 208-216

4. W.Z. Zhu and S.C. Deevi, Opportunity of Metallic Interconnects for Solid Oxide Fuel Cells: A Status on Contact Resistance, *Mater. Res. Bull.*, 2003, **38**, p 957-972

5. J.W. Fergus, Metallic Interconnects for Solid Oxide Fuel Cells, *Mater. Sci. Eng.*, 2005, **397**, p 271-283

6. F. Chen, E. Sun, J. Yamanis, J. Hawkes, J. Smeggil, S. Warrier, and J.-W Kim, Cr Poisoning Effect for Solid Oxide Fuel Cells, *Materials Science and Technology*, Vol. 1, Materials and Systems, 2006

7. J.Y. Kim, N.L. Canfield, L.A. Chick, K.D. Meinhardt, and V.L. Sprenkle, Chromium Poisoning Effects on Various Cathodes, *Ceram. Eng. Sci. Proc.*, 2008, **26**(4), p 129-138

8. H.W. Nie, T.L. Wen, and H.Y. Tu, Protection Coatings for Planar Solid Oxide Fuel Cell Interconnect Prepared by Plasma Spraying, *Mater. Res. Bull.*, 2003, **38**, p 1531-1536

9. J. Lagerbom, U. Kanerva, A.-P. Nikkilä, T. Varis, M. Kylmälahti, and P. Vuoristo, Phase Stability and Structure of Conductive Perovskite Ceramic Coatings by Thermal Spraying, *Proceedings of the International Thermal Spray Conference*, 2-4 June 2008 (Maastricht), CD-ROM

10. F. Changjing, S. Kening, and Z. Derui, Effects of $La_{0.8}Sr_{0.2}Mn$-$(Fe)O_3$ Protective Coatings on SOFC Metallic Interconnects, *J. Rare Earths*, 2006, **24**, p 320-326

11. D.P. Lim, D.S. Lum, J.S. Oh, and I.W. Lyo, Influence of Post-Treatment on the Contact Resistance of Plasma-Sprayed $La_{0.8}Sr_{0.2}MnO_3$ Coatings on SOFC Metallic Interconnector, *Surf. Coat. Technol.*, 2005, **200**, p 1248-1251

12. Y. Larring and T. Norby, Spinel and Perovskite Functional Layers Between Plansee Metallic Interconnect (Cr-5 wt% Fe-1 wt% Y_2O_3) and Ceramic $(La_{0.85}Sr_{0.15})_{0.91}MnO_3$ Cathode Materials for Solid Oxide Fuel Cell, *J. Electrochem. Soc.*, 2000, **47**(9), p 3251-3256

13. E. Garcia and T.W Coyle, Thermal Spray Deposition of Fuel Cell Interconnect Material, *Proceedings of the International Thermal Spray Conference*, 15-18 May 2006 (Seattle), CD-ROM

14. S.D. Park, S. Kumar, S.C. Lee, and C. Lee, Effects of Silver Addition on Mechanical Properties of Plasma Sprayed SOFC Interconnect Layer, *J. Therm. Spray Technol.*, 2008, **17**, p 708-714

15. S.Y. Hwang, J.H. Kim, B.G. Seong, and H. Yang, SOFC Interconnect Coating Using HVOF Process, *Proceedings of the International Thermal Spray Conference*, 15-18 May 2006 (Seattle), CD-ROM

16. R.H. Henne, T. Franco, and R. Ruckdäschel, High Velocity DC-VPS for Diffusion Protecting Barrier Layer in SOFCs, *Proceedings of the International Thermal Spray Conference*, 15-18 May 2006 (Seattle), CD-ROM

17. K. Fujita, K. Ogasawara, Y. Matsuzaki, and T. Sakarai, Prevention of SOFC Cathode Degradation in Contact with Cr-Containing Alloy, *J. Power Sources*, 2004, **131**, p 261-269

18. W.J. Quadakkers, H. Greiner, M. Hänsel, A. Pattanaik, A.S. Khanna, and W. Malléner, Compatibility of Perovskite Contact Layers Between Cathode and Metallic Interconnector Plates of SOFCs, *Solid State Ion.*, 1996, **91**, p 66-67

19. Z. Yang, G. Xia, and J.W. Stevenson, $Mn_{1.5}Co_{1.5}O_4$ Spinel Protection Layers on Ferritic Stainless Steels for SOFC Interconnect Applications, *Electrochem. Solid State Lett.*, 2005, **8**(3), p 168-170

20. X. Chen, P.Y. Hou, C.P. Jacobson, S.T. Visco, and L.C. De Jonghe, Protective Coatings on Stainless Steel Interconnect for SOFCs: Oxidation Kinetics and Electrical Properties, *Solid State Ion.*, 2005, **176**, p 425-433

21. Z. Yang, G.-G. Xia, X.-H. Li, and J.W. Stevenson $(Mn, Co)_3O_4$ Spinel Coatings on Ferritic Stainless Steels for SOFC Interconnect Applications, *Int. J. Hydrogen Energy*, 2007, **32**, p 3648-3654

22. T. Kiefer, M. Zahid, F. Tietz, D. Stöver, and H.-R. Zerfass, Electrical Conductivity and Thermal Expansion Coefficients of Spinel in the Series $MnCo_{2-x}Fe_xO_4$ for Application as a Protective Layer in SOFC, *Proceedings of the 26th Riso International Symposium on Materials Science*, Denmark, Roskilde, 2005

23. P.E. Gannona, V.I. Gorokhovsky, M.C. Deibert, R.J. Smith, A. Kayani, P.T. White, S. Sofie, Z. Yang, D. McCready, S. Visco, C. Jacobson, and H. Kurokawa, Enabling Inexpensive Metallic Alloys as SOFC Interconnects: An Investigation into Hybrid Coating Technologies to Deposit Nanocomposite Functional Coatings on Ferritic Stainless Steels, *Int. J. Hydrogen Energy*, 2007, **32**, p 3672-3681

24. J. Wu, Y. Jiang, C. Johnson, and X. Liu, DC Electrodeposition of Mn-Co Alloys on Stainless Steels for SOFC Interconnect Application, *J. Power Sources*, 2008, **177**, p 376-385

25. Material Data Sheet No. 4046 for Crofer 22 APU, ThyssenKrupp VDM

Publication II

Formation and Structure of Plasma Sprayed Manganese-Cobalt Spinel Coatings on Preheated Metallic Interconnector Plates

by

J. Puranen, J. Lagerbom, L. Hyvärinen, T. Mäntylä, E. Levänen, M. Kylmälahti, and P. Vuoristo

Formation and structure of plasma sprayed manganese-cobalt spinel coatings on preheated metallic interconnector plates

J. Puranen [a,*], J. Lagerbom [b], L. Hyvärinen [a], T. Mäntylä [a], E. Levänen [a], M. Kylmälahti [a], P. Vuoristo [a]

[a] Department of Materials Science, Tampere University of Technology, Tampere, Finland
[b] VTT, Technical Research Centre of Finland, Tampere, Finland

ARTICLE INFO

ABSTRACT

Manganese-cobalt spinels are promising materials for protective coatings on metallic interconnector plates in solid oxide fuel cells. These protective coatings are used to prevent growth and evaporation of chromium oxide, chromium poisoning and ageing phenomena of the cathode side of the fuel cell. It is well known that chromium trioxide and chromium hydroxide on interconnector plate may easily evaporate at high temperatures and transform back to chromium oxide at the cathodes active area and cause degradation of the solid oxide fuel cell performance.

In the present study, plasma spraying together with a substrate pre- and simultaneous heating was found to be an appropriate technique to control the formation and densification of the coating. When plasma spraying Mn-Co spinel powder for cold substrate, high cracking effect inside the splats and in the formed coating was noticed. When applying the molten drops to the substrate heated up to 450 °C amount of cracks in single splats and coatings could be mostly eliminated. The splats stayed in the liquid state longer, which effected for spreading properties and spinel structure could be better preserved by longer crystallize time.

© 2010 Elsevier B.V. All rights reserved.

1. Introduction

Interconnectors (ICs) are used in Solid Oxide Fuel Cells (SOFCs) to provide fuel and air (oxygen) distribution through the cell construction, to prevent fuel and oxygen gases from mixing together and electrically connect the cells in series. Sintered ceramics, such as lanthanum chromites, have been used as interconnectors, but these are expensive to manufacture and suffer lack of designing properties. In contrast, ferritic stainless steels are ideal materials for the application due to their thermal expansion behaviour, manufacturability, mechanical properties and durability. These steels have high chromium contents of the order of 22 wt.%, which give a good corrosion protection at high operating temperatures (700–800 °C) in oxidizing environment, by the formation of $(Mn,Cr)_2O_4$ layer on the surface. By alloying with other elements particularly manganese, the electrical properties of the formed oxide layer can be tailored for more suitable use for SOFC. High chromium alloying may still cause problems in certain atmospheres of the cell and formation of easily volatile chromium trioxide CrO_3 and chromium hydroxide $CrO_2(OH)_2$ may occur. These compounds generally evaporate more easily than Cr_2O_3, transfer to the cathode triple phase boundary (TPB) and transform back to Cr_2O_3 by lowering the area of the TPB. This causes the dropping of cell efficiency and gradual degradation of the cell [1–4].

In order to minimize oxidation of the interconnector and to prevent evaporation of the chromium compounds, protective perovskite (ABX_3) coatings have been studied [4–7]. Less tested but interesting new coating materials are so called spinels. The structural formula of spinel material is AB_2X_4, where A and B are metallic cations and X is anion, usually an oxygen ion. Some studies have been carried out by on spinel coatings to prevent Cr-poisoning and the results have revealed that spinel materials are promising protective coatings for ICs [4,8–12].

Several methods for producing the protective coatings have been evaluated. Some studies have shown that perovskite materials are sprayable by conventional thermal spray techniques such as atmospheric plasma spraying (APS) and high velocity oxy-fuel spraying (HVOF). The crystal structure and density of the produced coatings have been found fairly good. In some cases, when too energetic spraying parameters have been used in plasma spraying, the crystal structure of perovskite material is decomposed [5,6,13]. Using modified plasma spraying methods like vacuum plasma spraying, the desired properties like density can be increased [14,15]. When it comes to manufacturing spinel coatings used as a protective coating, slurry or screen printing methods have often been used. When using e.g. screen printing, an external sintering process is needed to densify the coating layer [8,10,11].

In the present work, atmospheric plasma spraying process was used together with pre- and simultaneous substrate heating to produce

* Corresponding author. Tel.: +358 40 849 0195.
  E-mail address: jouni.puranen@tut.fi (J. Puranen).

protective spinel coating onto the stainless ferritic steel substrates. The aim was to improve coating quality by densifying the coating structure. The studies show that when applying substrate heating during spraying, coating quality and mechanical properties, e.g. adhesion of the coating to the substrate, can be improved. The idea of applying heating is to contribute to single splat behaviour, which in turn has an important influence on the final coating properties. A common problem in plasma spaying is that when molten droplets hit the surface of the substrate material, the optimal disk shaped splats are not formed. Instead of even splat spreading high splashing effect may occur which increases the amount of porosity and heterogeneity of the formed coating. Possible reasons for high splashing effects are uneven spreading, surface irregularities, rapid and unequal local solidification and too low surface tension. Applying molten particles onto a substrate, splats remain in liquid state longer. Therefore more uniform solidification occurs as the splats have been managed to spread more evenly and fill surface irregularities [16,17].

2. Experimental

The Fe_2O_3 doped Mn-Co spinel powder used in the present work was produced by solid state synthesis. Spray drying was used to agglomerate the powder to a spherical form. The $MnCo_{1.8}Fe_{0.2}O_4$ powder was prepared by weighing appropriate amounts of $MnCO_3$, $CoCO_3$ and Fe_2O_3 powders together, milled and calcinated at 1000 °C in air for 6 h to get the spinel structure. The powder was dispersed in water with a dispersant (Dispex A40, 1 wt.%) by a planetary ball mill (2 h, 300 rpm, ZrO_2 balls). PVA (2 wt.%) as a bonding agent was added to the slurry by a dispergator mixer. The suspension was spray dried by Niro pilot spray dryer. Rotary nozzle with a high rotation speed was used in order to obtain fine agglomerate size needed for the production of a thin coating. The powder was sintered at 1150 °C to improve strength, during which an isothermal step 500 °C 2 h was used in order to pyrolyse the PVA without agglomerate fracture. After sintering, the powder (Fig. 1) was sieved and $-36 + 15$ µm (d90–d10) particle size was measured by Sympatec Helos laser diffractometer.

Substrate material was ThyssenKrupp VDM Crofer 22 APU, specially tailored for SOFC use. Thickness of the substrate was 0.2 mm which is designed to use at stack configuration. The substrate was finely grit blasted (36 mesh alumina sand) prior to plasma spraying. For splat studies, polished substrates were used.

Coatings were sprayed by using a Sulzer Metco A3000S plasma spray system equipped with a 55 kW F4-MB plasma gun. Parameters were selected so that low, moderate and high energy spraying conditions were provided. By this way, the influence of used gun power for splat formation and coating structure could be examined. Detailed spraying parameters are presented in Table 1. An X- Y-
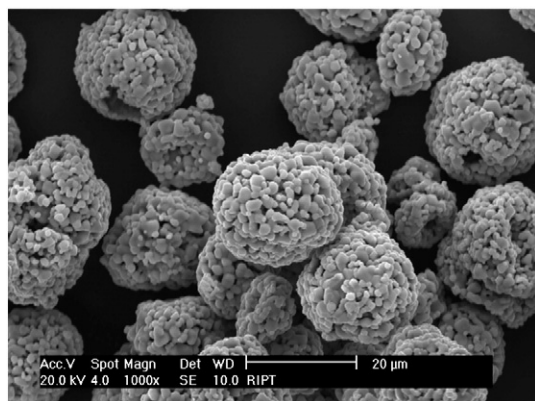

Fig. 1. Scanning electron microscope pictures (SE mode) of spray dried and sieved $MnCo_{1.8}Fe_{0.2}O_4$ powder.

Table 1
Plasma spraying parameters.

Parameter	I (A)	P (kW)	Ar (slpm)	H_2 (slpm)	Ar/H_2	Distance (mm)
P1 (low)	425	24,8	45	5	0,10	120
P1 + HT						
P2 (moderate)	512	33,5	59	9	0,15	
P2 + HT						
P3 (high)	600	43,6	71	14	0,2	
P3 + HT						

HT = preheated substrates 350, 450, and 550 °C.
Anode diameter: 6 mm.
Powder feed rate: 30 g/min.

manipulator was used to control the movement of the spray gun. The target average coating thickness was approximately 15–20 µm. For substrate preheating, a Minac 18/25 induction heater was used. Substrates were first heated to the desired temperature and kept at constant during the spraying process. The temperature measurement was done by using K-type thermocouple which was attached to an induction power controller. The advantage of using the controller was that it monitored the influence of plasma flame on substrate temperature and adjusted the proper heating power. Also the polished splat samples were heated and sprayed at the same time. After spraying, coated samples were cooled back to room temperature freely with the fixture. Recorded cooling rate was ~50 °C/min. The specimens were moulded in epoxy resin and conventional metallo-graphic preparation methods were used in grinding and polishing stages.

The powder and coating samples were analysed by using Phillips XL 30 scanning electron microscope (SEM) by secondary electron (SE) and energy dispersed spectroscopy (EDS) modes. Porosity values were calculated from cross-sectional images by ImageTool. The crystal structures were examined by using Siemens D-500 X-ray diffraction in as-sprayed state and the results were compared to the powder. Optical profilometer Wyko NT1100 was used for investigating a splat formation. From each sample ten single splats were analysed and the average splat height was calculated to get general estimation of splat spreading capabilities.

3. Results and discussion

Shapes of single splats were found to be uneven when sprayed on cold (22 °C) substrate. As it can be noticed in Fig. 2, the splashing effect and irregular cooling were dominating when the splat was formed. Some material peeling can also be noticed in the figures of individual splats. Peeling was mainly the outer edge problem but in some splats material was also missing in the centre of the splat. This can be the result of partially melted particles. When comparing the effect of spraying parameters, hardly any differences were noticed when the shape of the splats were compared. The average height of the splats was increased together with standard deviation value from 1.40 µm (sdv. 0.80 µm) to 1.50 µm (sdv. 1.07 µm) when used gun power was increased. The main reason of increased splat thickness is that larger particles are fully molten and thus form a splat. Increased standard deviation value proves that particles of wider range of size distribution are melting at the spraying process. When the substrate temperature was increased to 350 °C, 450 °C and 550 °C (Fig. 3), splats were then able to form more evenly and the resulted splat shapes were more disks like. At 350 °C formations of internal cracks in the splats have observed. Although the temperature of 350 °C is enough to achieve well spreading of molten droplets the problem was still a too high quenching rate, resulting in many internal cracks. These cracks can also be noticed in the coatings cross-sections. At temperature of 550 °C, the forming oxide layer increased the surface roughness and thus the splat spreading was not optimal anymore. Oxidation due to
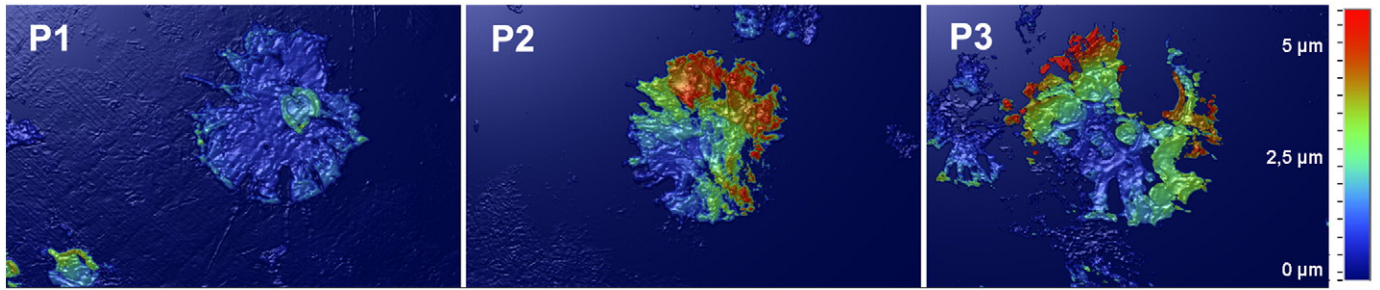
Fig. 2. Splat pictures taken with optical profilometer picture of single splats on cold substrate.
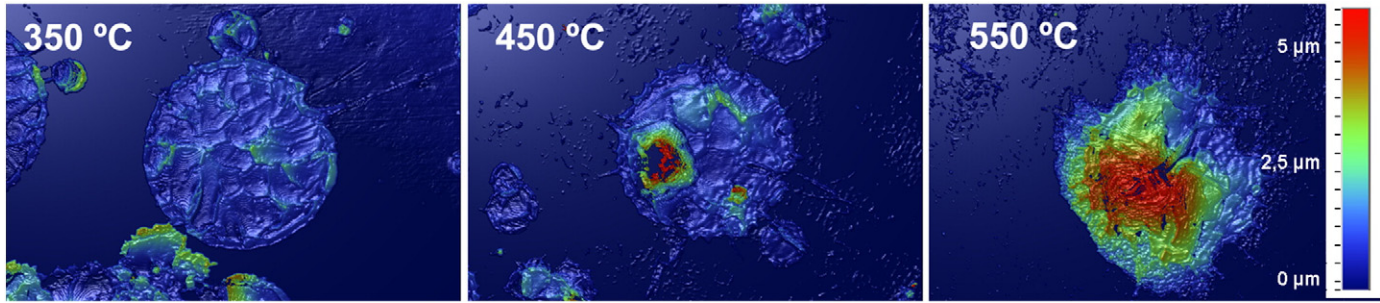

Fig. 3. Optical profilometer picture of single splats on hot substrate.

preheating may also affect adhesion and splashing of the splats. When the different spraying parameters were compared, no significant difference was noticed.

Cross-sectional images (Fig. 4) reveal the influence of substrate preheating. At low substrate temperatures 22 °C and 350 °C samples included pores and microcracks. In some cases the interface between the coating and substrate was poor. This is a negative factor when it comes to good electrical conductivity and diffusion barrier against chromium compounds. When the substrate temperature was increased the amount of micropores and cracks were significantly decreased. Porosity of coatings P1 and P3 sprayed at 350 °C was compared to the one of coatings sprayed at 550 °C, it decreases for P1 from 11.7% ± 1.7% to 6.0% ± 0.9% and for sample P3 from 8.6% ± 1.3% to 3.8% ± 0.7%. Although the porosity was decreased by more than 50% in each sample, at 550 °C some vertical cracks were still present. This might be caused by the too high cooling rate after the spraying and the small differences thermal expansion coefficient (CTE) of the coating and substrate material.

When analysing the crystal structures of the coatings sprayed with low energetic (P1) spraying parameters (Fig. 5) onto the cold substrate, it was noticed that the original spinel structure was decomposed. X-ray diffraction peaks in coatings were analysed to be near FeO (wuestite) kind of structure with cubic form. Comparing low gun power (P1) spraying parameters to high gun power (P3) parameters (Fig. 6), the peaks were the same so changes of spraying parameters did not affect the formed crystal structure when sprayed for 22 °C substrate. When sprayed onto heated substrates (450 °C– 550 °C), spinel structure was not fully decomposed. The low intensity peaks of $Mn_xCo_{3-x-z}Fe_zO_4$ spinel peaks are presented in Figs. 5 and 6. Restoring the spinel structure was not fully completed according to XRD-pattern of the simple cubic structure. $Mn_xCo_{3-x-z}Fe_zO_4$ spinel peaks may be the result that some alloyed iron is first crystallised form of iron oxide (FeO). When analysing the amount of elements by EDS-analysis, no selected evaporation of elements were noticed at sprayed coatings (Table 2) when compared to powder values. Total reformation reaction of spinel crystal structure needs more time to complete.
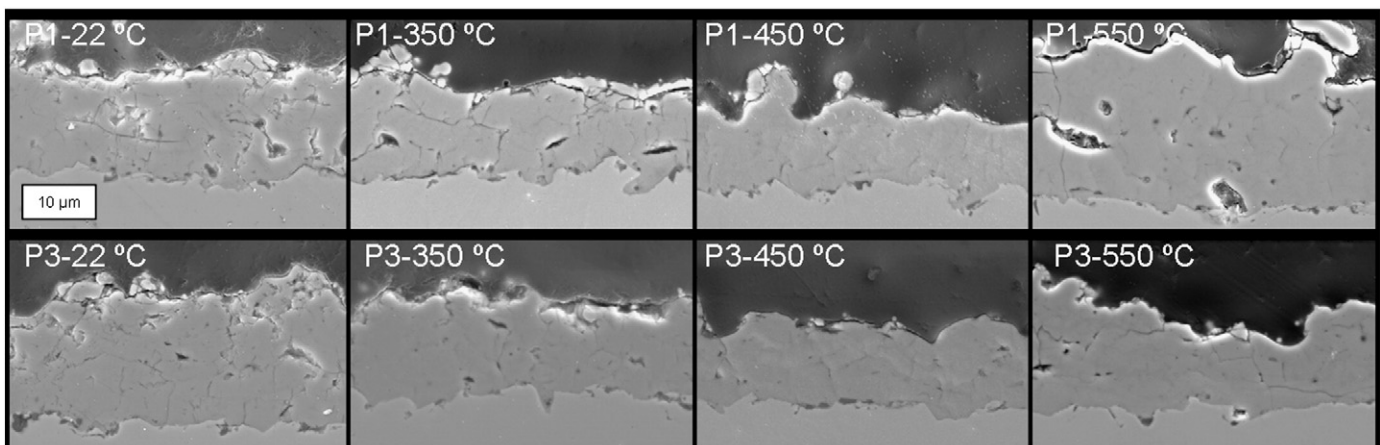

Fig. 4. Scanning electron microscope pictures (SE mode) of the coatings cross-sections.
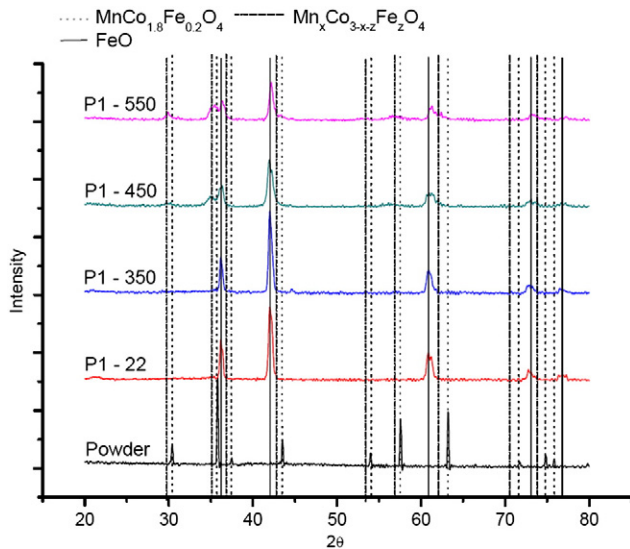
Fig. 5. X-ray diffraction curves with low energetic spraying parameters.

The spinel structure was restored by using a separate annealing process (Results will be published in other paper).

4. Conclusions

Plasma spraying is a relatively new method for producing the protective spinel coatings onto interconnector plates. Fast production rate and suitable method for corrugated substrate materials make thermal spraying an interesting manufacturing alternative for this use. The characteristic structure of plasma sprayed coatings might still cause some problems when it comes to producing gas tight, well electrically conductive ceramic layers. Problems may also occur when the required coating thickness is low, of the order of 30 μm or lower.

One promising way to manipulate the plasma sprayed coating structure is to use substrate pre- and simultaneous heating while spraying. The main focus is to generate conditions in which the spreading of the molten droplets is optimal and discoidal form can be achieved and splashing effects fully avoided. When increasing the substrate temperature, the splats are more fluidal. This leads to better
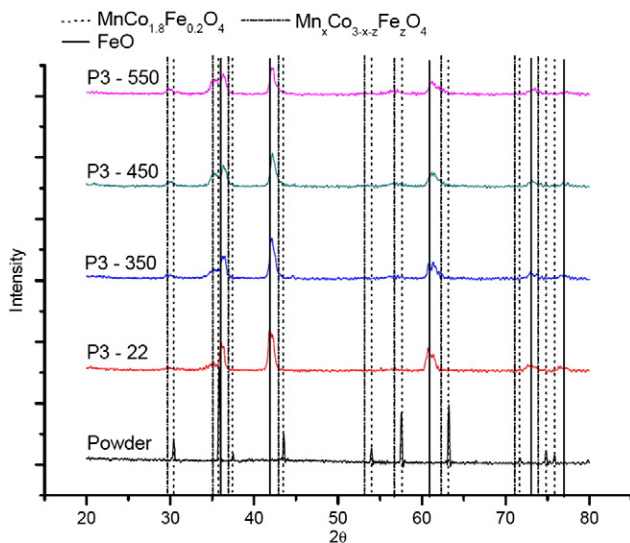

Fig. 6. X-ray diffraction curves with high energetic spraying parameters.

Table 2
Amount of elements in atomic percentages (at %) (EDS).

	Manganese	Cobalt	Iron	Oxygen
Calculated	14.29	25.71	2.86	57.14
Powder	22.40	40.10	8.86	28.64
Parameter 1				
22 °C	19.17	36.43	7.87	36.52
350 °C	20.24	39.46	8.25	32.05
450 °C	18.70	37.28	8.03	36.00
550 °C	18.83	36.78	7.60	36.79
Parameter 3				
22 °C	20.03	37.67	8.03	34.28
350 °C	18.94	36.91	8.16	35.98
450 °C	19.25	36.79	7.93	36.02
550 °C	17.81	33.45	7.00	41.74

covering properties at the substrate surface and splat-splat boundaries so less gas entrapment occurs. These offer a baseline (mechanism), how cracks and especially microcracks can be eliminated from the coating. At this study a sufficient temperature to provide optimal spreading for Mn-Co spinels was found to be around 450 °C. For high heating rate, keeping the constant substrate temperature while spraying and controlling the cooling rate the induction heater was noticed to work well. Amount of microcracks on single splats and porosity in the coatings were notably lower compared to the material which was sprayed on a cold substrate, where the amount of cracks and open porosity was excessively high. These microcracks and possible open porosity are probably the biggest risk to chromium barrier failure. The use of a higher substrate temperature may not offer any extra benefits. On the contrary, using too high substrate temperatures may influence negatively to the residual stresses formed on cooling and forming of the too thick and electrically insulating chromium oxide layer. In this study using over 550 °C substrate temperatures caused some larger vertical and horizontal cracks to the coatings due to stresses of small differences between CTE-values. This can probably be avoided using a lower cooling rate than 50 °C/min.

An interesting observation in plasma spraying Mn-Co spinel powder was the decomposition of the spinel structure. Composition of the formed phase is not clear but it is the similar crystal structure as wuestite FeO. The reason for the crystal structure probably is the coating preparation method where material is melted and cooled rapidly and FeO kind of crystal structure is able to form first. High quenching rate occurs when droplets hit the substrate material and metastable crystal structure is then formed. More composition and phase analysis need to be done to reveal mechanisms which are taken place during thermal spraying. Applying substrate heating, this quenching rate can be lowered and $Mn_xCo_{3-x-z}Fe_zO_4$-spinel phase preserved. Substrate temperature needs to be above 450 °C for spinel phase to be noticed by X-ray analysis. Longer holding time together at high temperature or annealing process may restore the original crystal structure.

References

[1] W.Z. Zhu, S.C. Deevi, Mater. Res. Bull. 38 (2003) 957.
[2] J.W. Fergus, Mater. Sci. Eng., A 397 (2005) 271.
[3] F. Chen, E. Sun, J. Yamanis, J. hawkes, J. Smeggil, s. Warrier, J.-W. Kim, Materials Science and Technology, Mater. Syst. Volume 1 (2006) Chicinnati.

[4] Kurokawa, P.Y. Hou, X. Chen, C. Jacobson, L. DeJonghe, S.J. Visco, Materials Science and Technology, Mater. Syst. Volume 1 (2006) Chicinnati.
[5] J. Lagerbom, U. Kanerva, A.-P. Nikkilä, T. Varis, M. Kylmälahti, P. Vuoristo, Conference Proceedings of the International Thermal Spray Conference, 2008 Maastricht.
[6] S. Park, S. Kumar, H. Ha, C. Lee, J. Therm. Spray Technol. 17 (2008) 708.
[7] H.W. Nie, T.IL. Wen, H.Y. Tu, Mater. Res. Bull. 38 (2003) 1531.
[8] X. Chen, P.Y. hou, P. Jacobson, S.T. Visco, L.C. De Jonghe, Solid State Ionics 176 (2005) 425.
[9] W. Qu, L. Jian, J.M. Hill, D.G. Ivey, J. Power Sources 153 (2006) 114.
[10] Z. Yang, G. Xia, J.W. Stevenson, Electrochem. Solid-State Lett. 8 (3) (2005) 168.
[11] Z. Yang, G.-G. Xia, X.-H. Li, J.W. Stevenson, Int. J. Hydrogen Energy 32 (2007) 3648.
[12] T. Kiefer, M. Zahid, F. Tietz, D. Stöver, H.-R. Zerfass, Proceeding of the 26th Riso International Symposium on Materials Science, Solid State Electrochemistry, 2005 Denmark.
[13] S.Y. Hwang, J.H. Kim, B.G. Seong, H. Yang, Conference Proceedings of the International Thermal Spray Conference, 2006 Seattle.
[14] C. Verdy, C. Zhang, D. Sokolov, H. Liao, D. Klein, C. Coddet, Conference Proceedings of the International Thermal Spray Conference, 2008 Maastricht.
[15] R.H. Henne, T. Franco, R. Ruckdäschel, J. Therm. Spray Technol. 15 (4) (2006) 695.
[16] S. Sampath, X.Y. Jiang, J. Matejicek, A.C. Leger, A. Vardelle, Mater. Sci. Eng. A272 (1999) 181.
[17] C. Petot, M. Ducos, Petpt-Ervas, J. Euro. Ceram. Soc. 15 (1995) 637.

Publication III

Post-Mortem Evaluation of Oxidized Atmospheric Plasma Sprayed Mn-Co-Fe Oxide Spinel Coatings on SOFC Interconnectors
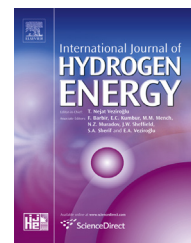
by

J. Puranen, M. Pihlatie, J. Lagerbom, G. Bolelli, J. Laakso, L. Hyvärinen, M. Kylmälahti, O. Himanen, J. Kiviaho, L. Lusvarghi and P. Vuoristo

Post-mortem evaluation of oxidized atmospheric plasma sprayed Mn–Co–Fe oxide spinel coatings on SOFC interconnectors

Jouni Puranen [a,*], Mikko Pihlatie [b], Juha Lagerbom [c], Giovanni Bolelli [d], Jarmo Laakso [a], Leo Hyvärinen [a], Mikko Kylmälahti [a], Olli Himanen [b], Jari Kiviaho [b], Luca Lusvarghi [d], Petri Vuoristo [a]

[a] Tampere University of Technology, Department of Materials Science, 33101 Tampere, Finland
[b] VTT, Technical Research Centre of Finland, Espoo, Finland
[c] VTT, Technical Research Centre of Finland, Tampere, Finland
[d] University of Modena and Reggio Emilia, Department of Engineering "Enzo Ferrari", Modena, Italy

ARTICLE INFO

ABSTRACT

Interconnects employed in solid oxide fuel cells require electrically conductive protective coatings such as those based on manganese cobalt oxide spinels in order to prevent evaporation of volatile Cr(VI)-compounds and to minimize high temperature corrosion. $MnCo_{2-x}Fe_xO_4$ based (where $x = 0.1$ and 0.3) oxide spinel protective coatings were manufactured by the atmospheric plasma spraying process on Crofer 22 APU substrates. The coated substrates were oxidized at $700\,^\circ$C in air for 1000 h and post-mortem analyses were conducted to study the performance of the thermal sprayed coatings. During the high temperature oxidation, a four-point on-line measurement technique was used for area specific resistance studies. The $MnCo_{1.7}Fe_{0.3}O_4$ coating was tested together with the $La_{0.85}Sr_{0.15}Mn_{1.1}O_3$-spacer.

The atmospheric plasma sprayed $MnCo_{2-x}Fe_xO_4$ showed excellent Cr-barrier properties and decreased oxidation of the substrate. In addition, resistance as low as 9.20 mΩ cm^2 values was obtained after the 1000 h oxidation cycle. The $MnCo_{1.9}Fe_{0.1}O_4$ coating manufactured by the atmospheric plasma spraying process is a promising candidate for SOFC interconnect applications.

Introduction

Interconnects (ICs) are used in solid oxide fuel cells (SOFCs) to connect the cells in series electrically and provide distribution of the fuel gas and the oxidant gas to the electrodes. Recent developments in solid oxide fuel cells, i.e. the anode supported cells, enable lower SOFC operating temperatures of the order of 600–800 °C. The intermediate temperature (IT)-SOFCs allow new materials, e.g. high chromium-containing

---

(18–24 wt-%) ferritic stainless steels to be employed in ICs. Ferritic stainless steels are recognised to be the materials with the greatest potential for metallic ICs due to: i) low raw material and manufacturing costs, ii) high enough electrical and thermal conductivity, iii) similar thermal expansion behaviour with other cell materials and iii) improved design properties for the complex IC surface profiles [1].

The ferritic stainless steel ICs must be coated prior to the use in the SOFCs to protect the cathode from degradation. Degradation occurs on the cathode side due to oxidation of the ferritic stainless steel and the presence of gaseous H_2O in the atmosphere, which increases the probability of the formation of volatile Cr^{6+} species, e.g. CrO_3 and $CrO_2(OH)_2$ compounds. These Cr-containing compounds transport through the gas-phase into the triple phase boundaries (TPBs). As a TPB is the shared interface of the cathode, the electrolyte and the gas phases, the oxygen vacancies and electron holes are available for Cr-containing compounds to concentrate and to electrically reduce back to Cr_2O_3 (for the manganese containing cathode) or $SrCrO_4$ and Cr_2O_3 (for the non-manganese containing cathode). As a result, the active TPB area decreases, which causes degradation of the cell [2–4].

Spinel materials (($(A,B)_3O_4$), more precisely $(Mn,Co)_3O_4$, seem to be the most suitable materials for the protective coatings on the ferritic stainless steel ICs. The coating-IC system should incorporate: i) similar coefficients of thermal expansion (CTE) with other cell materials [5]; ii) suitable electrical properties, i.e. high enough electrical conductivity at the SOFCs operating temperatures [5]; iii) low diffusion coefficient of Cr-ions and ability to form stable Cr-containing spinels [6]; iv) chemical, microstructural, and phase stability, in addition to the ability to withstand vibrations without harmful fatigue or cracking of the coating in an oxidizing, high temperature environment [5,6]; and v) an economic manufacturing process for mass production [5].

Although the $(Mn,Co)_3O_4$ spinels show good results as protective coatings, Kiefer et al. have studied the properties of iron doped oxide spinel coatings. They varied the amount of iron so that the composition matched $MnCo_{2-x}Fe_xO_4$ (where $x = 0$, 0.1, 0.25, 0.5 and 1). The most promising composition in terms of electrical conductivity and CTE, were the Fe-doped spinels with the stoichiometric factor of iron in the range of 0.1–0.25. Electronic conductivity ranged from 25 up to 37.5 S/cm at 800 °C in air [7]. Miguel-Pérez et al. [8] obtained conductivity values of 72 S/cm for $MnCo_{1.9}Fe_{0.1}O_4$ at 800 °C in air. This was close to the results of Liu et al. [9] who measured conductivity of 85 S/cm for $MnCo_{1.85}Fe_{0.15}O_4$ at 800 °C in air. Further increase of iron decreased the electrical conductivity [7,9].

Due to the complex structure of $MnCo_{2-x}Fe_xO_4$ and the mixed oxidation states of the cations, it is difficult to determine the exact cation site distribution in the Mn–Co–Fe spinel system. Miguel-Pérez et al. [8] have reviewed the system and proposed the following cation distribution for the Mn–Co–Fe spinels: $(Co^{2+},Mn^{2+},Fe^{3+})(Co^{2+},Co^{3+},Mn^{3+},Mn^{4+},Fe^{2+},Fe^{3+})_2O_4$. Liu et al. [9] proposed that Co cations have a stronger tendency to occupy tetrahedral sites compared to Mn cations, and Fe cations have a lower tendency to occupy tetrahedral sites than Co and Mn cations.

Due to the presence of mixed valence states at octahedral sites in the $(A,B)_3O_4$ spinel system, the activation energy (E_a) for $MnCo_{1.9}Fe_{0.1}O_4$ is 0.38 eV. This is lower than to the E_a for $MnCo_2O_4$, which is 0.44 eV. Iron doping improves movement of the charge carriers and therefore increases the electronic conductivity of the spinel [8]. However, the study of Liu et al. [9] suggested that iron doping would actually decrease the electron conduction, which occurs via the small polaron hopping mechanism as the distance between the neighbouring octahedral sites increases.

Few studies are available in the open literature, related to the properties of the $MnCo_{2-x}Fe_xO_4$ coatings on ferritic stainless steel ICs manufactured with different deposition methods. Thomann et al. have tested the electrical properties of high velocity oxy-fuel sprayed $MnCo_{1.8}Fe_{0.2}O_4$ coatings on Crofer 22 APU together with a $La_{0.85}Sr_{0.15}Mn_{1.1}O_3$ spacer. Relatively thin (15–18 μm) and dense coatings were deposited, and a resistivity of 20 mΩ cm^2 was obtained after a 1000 h test cycle [10]. Miguel-Pérez et al. [8] reached ~0.8 Ω cm^2 for colloidal spray deposited $MnCo_{1.9}Fe_{0.1}O_4$ coatings on Crofer 22 APU together in a complete cell (LSF40/SDC-YSZ) at 800 °C after a 100 h test cycle. In addition, Montero et al. have studied the electrical properties of screen-printed $MnCo_{1.9}Fe_{0.1}O_4$ coatings on Crofer 22 APU with LSCF-LSF layers (260 h) and only the LSCF contact layer (1000 h), obtaining resistivities of 36 mΩ cm^2 and 33 mΩ cm^2, respectively [11].

Thermal spraying can be considered one of the most promising techniques to produce dense protective coatings on the metallic ICs, due to scalability for mass production. For the other available methods e.g., wet-ceramic processes, a one- or two-step post-deposition heat treatment process is always required in addition to the deposition process, in order to obtain dense coatings. The advantage in the thermal spray processes is that dense coatings are produced without sintering heat treatments as the coatings are formed of molten or semi-molten droplets [12].

Promising results are obtained for $(Mn,Co,Fe)_3O_4$ as protective coatings on ferritic stainless steel. However, thermal spraying causes decomposition of the spinel structure as reported in earlier studies [10,13–15]. Although decomposition has been observed, studies of the decomposition and recovery of the spinel structure is rather limited. In addition, long-term oxidation studies of atmospheric plasma sprayed $(Mn,Co,Fe)_3O_4$ have not been reported.

In this study, atmospheric plasma sprayed $MnCo_{1.9}Fe_{0.1}O_4$ and $MnCo_{1.7}Fe_{0.3}O_4$ coatings were evaluated as protective coatings on Crofer 22 APU ferritic stainless steel. Chemical and crystallographic analyses were performed on the as-sprayed coatings to obtain a detailed description of the decomposition of the spinel, and to find a suitable recovery temperature. The Cr-barrier and area specific electrical resistance properties were studied with a four-point resistance measurement method at the same time as the coatings were oxidized at 700 °C in air for 1000 h.

Experimental

The substrate material was Cr-alloyed (Cr: 20–24 wt%) ferritic stainless steel, grade Crofer 22 APU (ThyssenKrupp VDM

GmbH, Werdohl, Germany) specially designed for SOFCs. Two different substrate thicknesses were employed in this study: 0.2 and 0.5 mm. In addition, the coatings were sprayed on 25.4 mm diameter aluminium disks, which were used for quantitative X-ray fluorescence studies. Prior to the spray process, the substrates were grit blasted using 240 grit Al_2O_3-sand to improve the adhesion of the as-sprayed coatings.

Two powders with different chemical compositions were studied. The first powder was commercially acquired agglomerated and sintered $MnCo_{1.9}Fe_{0.1}O_4$ spinel powder (H.C. Starck, Goslar, Germany) with a particle size range of $-31 + 15$ μm ($d_{90}-d_{10}$) measured by laser diffraction (Helos, Sympatec GmbH, Clausthal-Zellerfeld, Germany). The second powder was an agglomerated and sintered $MnCo_{1.7}Fe_{0.3}O_4$ spinel powder produced in-house. The powder synthesis is described in greater detail in our previous studies [14,15]. The particle size range was $-29 + 13$ ($d_{90}-d_{10}$).

The coatings were deposited using a Sulzer Metco A3000S atmospheric plasma spray system with a 55 kW F4-MB (Sulzer Metco, Winterthur, Switzerland) plasma gun. Optimization of the spraying parameters [14] and the advantages of simultaneous heating (450 °C) of the substrates, including the set-up of the heating system, are reported in previous studies [15]. Table 1 presents detailed atmospheric plasma spraying parameters.

The coated specimens were oxidized for 1000 h at 700 °C in air, and the area specific resistance (ASR) measurements were done in-situ using a four-point method. The ASR measurements were executed with two different system set-ups presented in Fig. 1. In both tests, 1.0 mm platinum (Pt) leads were spot welded on the 1.0 mm steel plates at the bottom and top of the test stack to provide direct current. The voltage drop across the deposited coatings was measured by two 0.5 mm Pt-leads. 1 mm thick flat steel plates were used as separator disks between the stacked samples. An Agilent data logger with multi-plexer was used to measure the ASR data expressed in mΩ cm².

In the first ASR test procedure (Fig. 1(a)), the actual measurement was obtained without any contact or cathode layer between the coated samples. The results represented the pure coating–coating contact. Coated and corrugated 0.2 mm Crofer 22 APU was used in contact with the coated 1.0 mm flat Crofer 22 APU coupons. The contact area was formed between the tops of the corrugation ridges an actual contact area of 1.25 cm². The samples were held together by a force of 49 N when tested at 700 °C in air for 1000 h. The contact pressure was 0.40 MPa. Direct current (DC) was estimated to be 640 mA/cm².

In the second ASR test procedure (Fig. 1(b)), two flat (26*26*0.2 mm) $MnCo_{1.7}Fe_{0.3}O_4$ coated Crofer 22 APU were

tested together with $La_{0.85}Sr_{0.15}Mn_{1.1}O_3$ (LSM) cathode spacer (IRD Fuel Cells A/S, Denmark) to simulate the contact resistance with the cathode. The contact load was 20 N, so contact pressure was 29.5 kPa and the direct current density 200 mA/cm². The samples were heated (15 °C/min) up to 850 °C and sintered 12 h to improve the contact between the samples and the spacer, then cooled to 700 °C for the ASR test which was carried out for 1000 h.

The cross-section and surface topography inspections were done by a field-emission scanning electron microscopy (FESEM, Carl Zeiss ULTRAplus, Oberkochen, Germany) using secondary electron (SE)-image mode. Quantitative elemental analyses were conducted by energy dispersive X-ray spectroscopy (EDS, INCA Energy 350, Oxford Instruments, Oxfordshire, UK), X-ray fluorescence (XRF: Advant'X spectrometer, ThermoFisher Scientific, Waltham, MA, USA), and inductively coupled plasma − atomic emission spectrometry (ICP − AES: Liberty 200, Varian Inc., Palo Alto, CA, USA). The XRF analysis was performed on the coated aluminium disks, as described above. For ICP − AES analysis, the coating was removed from the substrate, manually ground in an agate mortar and dissolved in an aqueous HCl solution. Before the cross-sectional studies the as-sprayed and oxidized samples were cut, then mounted in epoxy in a chamber under reduced pressure to avoid cracking and to give support while polishing cross-section surfaces.

Qualitative phase analyses were conducted using an X-ray diffractometer (XRD, Empyrean, PANalytical B.V., ALMELO, Netherlands) with Cu-Kα radiation source. The data was background corrected and crystallographic data, such as crystallite size and d-spacing values were assessed by High-Score Plus' software, which employs Scherrer formula. Additional phase analyses were performed by micro-Raman spectroscopy (LabRam, Horiba Jobin-Yvon, Villeneuve D'Ascq, France) on the top surfaces and the polished cross-sections of the as-deposited samples, using a 632.81 nm-wavelength He:Ne laser focused through a 100× objective.

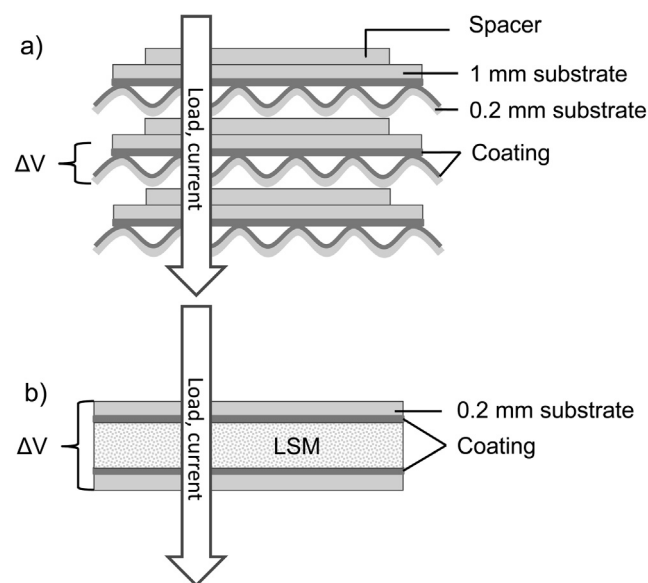Fig. 1 – ASR set-ups for a) coating–coating b) coating-$La_{0.85}Sr_{0.15}Mn_{1.1}O_3$-coating test.

Table 1 – Atmospheric plasma spraying (APS) parameters.						
Coating	I (A)	P (kW)	Ar (slpm)	H_2 (slpm)	Distance (mm)	Spray layers
$MnCo_{1.9}Fe_{0.1}O_4$ $MnCo_{1.7}Fe_{0.3}O_4$	425	25	45	5	120	6
Anode diameter: 6 mm. Simultaneous substrate heating temperature: 450 °C.						
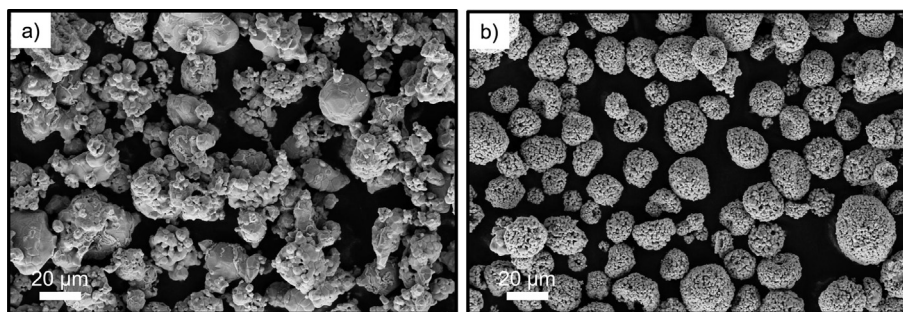
Fig. 2 – Morphology (FE-SEM)-images of the agglomerated a) $MnCo_{1.9}Fe_{0.1}O_4$ and b) $MnCo_{1.7}Fe_{0.3}O_4$ spray powders.

The elevated temperature XRD studies were done with a PANalytical X'Pert PRO diffractometer equipped with a high temperature stage. A free-standing coating sample of 10×20 mm size was placed on a resistance-heated Pt strip whose temperature was monitored through a thermocouple. Patterns were acquired under isothermal conditions at 25 °C, 400 °C, 600 °C, 800 °C, 1000 °C and 1200 °C. Heating from one temperature to the next took place in 24 min in all cases. Acquisition conditions included a step size of 0.020°, a counting time of 2.70 s/step and an angular range of $28° \leq 2\theta \leq 47°$.

Results and discussion

Powder feedstock

Fig. 2 shows the morphologies of the $MnCo_{1.9}Fe_{0.1}O_4$ and $MnCo_{1.7}Fe_{0.3}O_4$ powders. The powders were formed of agglomerated primary particles. The $MnCo_{1.7}Fe_{0.3}O_4$ powder seemed to have more spherical particles, whereas the $MnCo_{1.9}Fe_{0.1}O_4$ powder had a blockier morphology. The agglomerated morphology is a consequence of the spray drying process, in which the aim is to improve the spray powder flow properties in the thermal spray feeding system.

According to the EDS analysis, the relative amounts of elements (Mn,Co:Fe) were 96.7:3.30 and 87.5:12.5 in at-% for the $MnCo_{1.9}Fe_{0.1}O_4$ and $MnCo_{1.7}Fe_{0.3}O_4$ powders, respectively. The X-ray diffraction pattern of the $MnCo_{1.9}Fe_{0.1}O_4$ and $MnCo_{1.7}Fe_{0.3}O_4$ powders corresponded to the cubic $MnCo_2O_4$ phase, shown in Fig. 3. The patterns were shifted to lower Bragg angles, which was caused by the increase of unit cell volume as the Co cations were replaced by the Fe cations. The d-spacing values were calculated from the main peaks located near 35.7°, which belong to crystallographic plane (311) were 0.25 nm and 0.26 nm for $MnCo_{1.9}Fe_{0.1}O_4$ and $MnCo_{1.7}Fe_{0.3}O_4$, respectively. The Fe cations have a higher ionic radius compared to Co cations. The radii for Co^{3+} and Fe^{3+} cations are 0.61 Å and 0.645 Å, respectively [16]. The average crystallite size for the $MnCo_{1.9}Fe_{0.1}O_4$ powder was 27 nm and for $MnCo_{1.7}Fe_{0.3}O_4$ powders 229 nm. The higher Fe content can be considered a possible cause for the larger crystallite size. The influence of iron content on the average crystallite size was confirmed by calcining at 900 °C in air for 20 h. According to the HighScore Plus analysis software, average crystallite sizes were 27 nm and 2.60 μm for $MnCo_{1.9}Fe_{0.1}O_4$ and

$MnCo_{1.7}Fe_{0.3}O_4$, respectively. Moreover, Miguel-Pérez et al. [8] observed that iron doping increases the average primary particle size.

As-sprayed coatings

Fig. 4 shows the polished cross-section views of the as-sprayed coatings. Coatings with thicknesses of 20.30 μm (sdv. 3.60 μm) and 18.90 μm (sdv. 2.80 μm) were obtained by using the $MnCo_{1.9}Fe_{0.1}O_4$ and $MnCo_{1.7}Fe_{0.3}O_4$ spray powder, respectively, with the spray parameters presented in Table 1. According the cross-section images, the microstructures of the as-spayed coatings were fairly dense with some pores and inter-splat porosity. These pores are well known as characteristic features for thermally sprayed coatings [12]. Some un- or partially molten $MnCo_{1.9}Fe_{0.1}O_4$ particles were observed in the cross-sectional images, as the blocky morphology prevents the heat transfer of the plasma into the inner part of the spray particle and therefore delays melting.

Simultaneous substrate heating is an efficient way to decrease the amount of inter-lamellae gaps and segmentation cracks in thermally sprayed coatings as shown in Ref. [15]. McPherson et al. [17] have observed that the average inter-
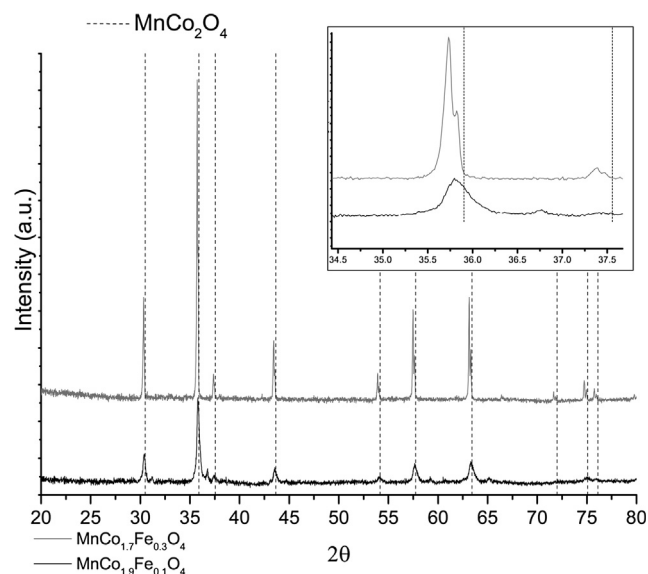

Fig. 3 – Crystallographic phase analysis of agglomerated $MnCo_{1.9}Fe_{0.1}O_4$ and $MnCo_{1.7}Fe_{0.3}O_4$ oxide spinel powders.
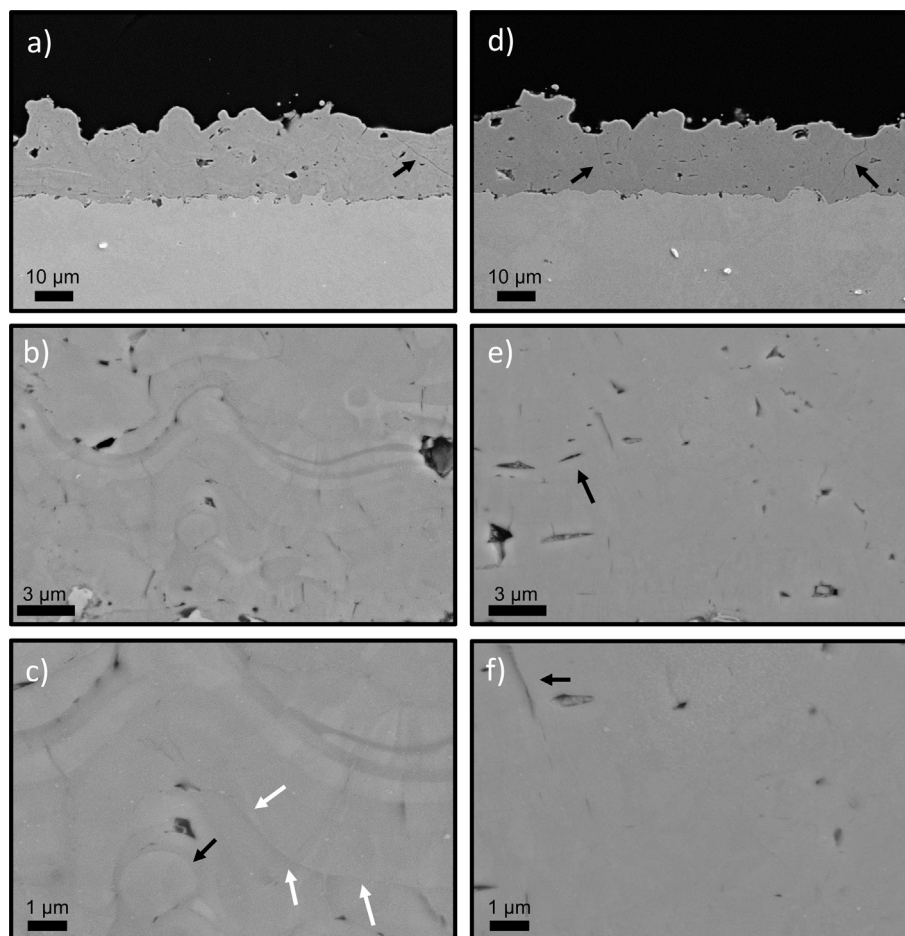
Fig. 4 – Cross-section images of as-sprayed a–c) $MnCo_{1.9}Fe_{0.1}O_4$ d-f) $MnCo_{1.7}Fe_{0.3}O_4$ spinel coatings. Black arrows point the typical coating faults such as segmental cracks (a, d) um-molten spray particle (c) and lamellar gaps (d–f). White arrows point desirable spat-splat interaction (c). FE-SEM (SE) images.

lamellae gaps in atmospheric plasma sprayed (without substrate heating) coatings varies from 0.01 to 0.1 μm, and, in addition the real area of splat–splat contact is only 25% of the total splat area. Poor inter-splat bonding increases the ohmic resistance. Moreover, elimination of the segmentation cracks is very important as those dominate the gas leakage in relatively thin coatings [18]. The lamellae gaps and the segmentation cracks are most likely formed due to the relaxation of stresses, which are a consequence of fast cooling rate of the deposited coating material. Some randomly located cracks were still observed in the cross-sectional studies as shown in Fig. 4(d) as a consequence of the sample preparation process of the thin substrates. White arrows Fig. 4(c) show the desired type of inter-splat bonding which presumably improves the Cr-barrier properties and the electrical conductivity.

As reported in previous studies [10,13–15,19], the (MnCo(-Fe))$_3$O$_4$ spinel decomposes during the thermal spray process. This was confirmed with the qualitative XRD studies of the as-sprayed $MnCo_{1.9}Fe_{0.1}O_4$ and $MnCo_{1.7}Fe_{0.3}O_4$ coatings presented in Fig. 5. The phase resulting from the decomposition corresponds to a cubic M-oxide (where M = Fe or Co) phase. Thomann et al. [10] proposed that one possible phase could be MnO. The decomposition phenomena can be decreased by

using simultaneous substrate heating, as some low intensity peak of the spinel were observed in the XRD studies. It is most likely that Fe doping may favour the formation of the spinel, as the amount of the spinel phase was higher in the coating where the stoichiometric factor of iron was 0.3. This hypothesis is also supported by the observation from the calcination test carried out on the spray powders, where crystallite growth increased with higher iron content.

The decomposed phase structure was also analysed by μ-Raman spectroscopy, since it is a sensitive analysis method for materials with poor crystallinity. Fig. 6 shows the μ-Raman spectra of the as-sprayed $MnCo_{1.7}Fe_{0.3}O_4$ coating and the feedstock powder. Results show the same decomposition of the spinel structure as observed in the XRD studies. Instead of the two peaks at 491 and 632 cm^{-1} found in the spectra of the feedstock powder, and characteristic of crystalline $MnCo_{1.7}Fe_{0.3}O_4$, the as-sprayed coatings had three peaks at 543, 623 and 672 cm^{-1}. The difference between the cross-section and surface analysis was minimal. Contrary to the XRD studies, the Raman spectra did not exhibit correlation with peaks for CoO, or for other compounds such as $MnFe_2O_4$ or MnO_2 phases. In the literature [20], the Raman peaks of MnO_2 between 500 cm^{-1} to 700 cm^{-1} are attributed to the stretching mode of
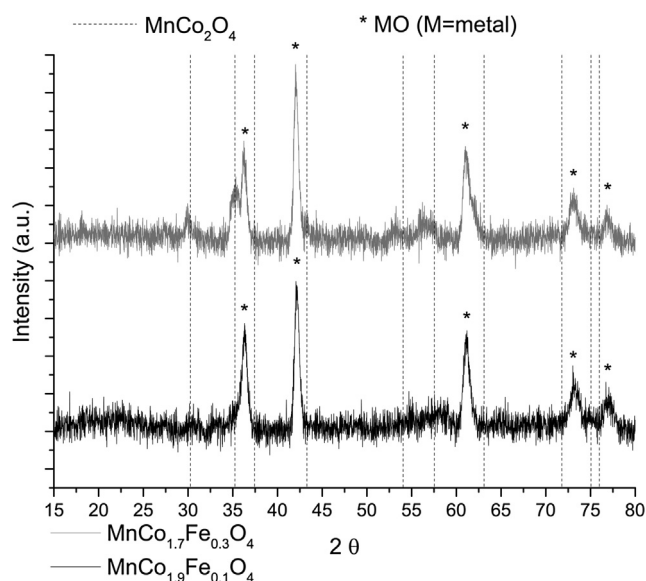
Fig. 5 — Crystallographic phase studies of the as-sprayed $MnCo_{1.9}Fe_{0.1}O_4$ and $MnCo_{1.7}Fe_{0.3}O_4$ oxide spinel coatings.

MnO_6 octahedra. However, in this study the peaks of pure MnO_2 shown in Fig. 6 are shifted compared to the crystallized $MnCo_{1.7}Fe_{0.3}O_4$. This shift relates to the difference between the stretching modes of MnO_2 and $MnCo_{1.7}Fe_{0.3}O_4$. In the case of the CoO phase, the Raman peaks should be located at 484 and 693 cm^{-1} and for Co_3O_4 at 197, 485, 523, 624 and 693 cm^{-1} [21]. The exact crystallographic structure of the as-sprayed coatings could therefore not be assessed by the XRD and μ-Raman spectroscopy due to the limitation of the available databases.

In order to exclude the influence of selective evaporation of metal ions for decomposition of the spinel, quantitative chemical analyses were performed for the as-sprayed $MnCo_{1.7}Fe_{0.3}O_4$ coating and the $MnCo_{1.7}Fe_{0.3}O_4$ spray powder. The r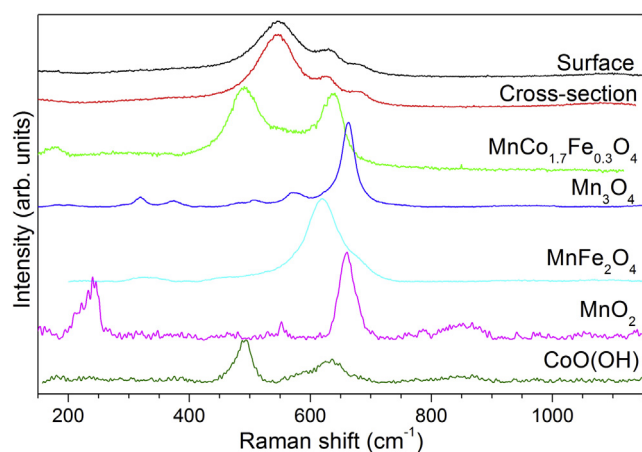esults of the XRF, ICP-AES and EDS studies are presented in Table 2. The difference between the relative amounts of the elements in the powder and in the as-sprayed coatings was insignificant. It can be clearly established that selective evaporation of the metal ions did not occur during the deposition process, to the extent that it could be measured with the analysis methods used in this study. Hence, it can be stated that decomposition of the spinel was not caused by selective evaporation and atmospheric plasma spraying can be safely be used for the deposition of the $MnCoFeO_4$ spinels.

Based on the quantitative (XRF, ICP-AES and EDS) results, our previous studies [14,15], and results obtained by Thomann et al. [10], decomposition of the spinel is the result of the rapid cooling rate of the deposited material which did not allow the ideal $Mn^{2+}(Co^{3+}, Fe^{3+})_2O_4^{2-}$ spinel structure to form. Due to the multiple oxidation states of the elements as Pérez et al. [8] have suggested and to the high process temperature, coatings with mixed phases of cubic and partially amorphous characters are formed.

The decomposed spinel structure can be restored to the original spinel structure by a simple heat-treatment process in air as reported in Refs. [10,13–15,23]. In order to study the recovery process of the decomposed spinel more closely, the free-standing $MnCo_{1.7}Fe_{0.3}O_4$ coating (without substrate) was placed on platinum foil and heat-treated stepwise and analysed simultaneously by XRD as shown in Fig. 7. As observed, the spinel structure already starts to be restored at 400 °C. According to peak intensity levels, the spinel was completely restored between 600 °C and 800 °C (highlighted area). The shifting of the Bragg angle to a lower 2-theta value was caused by the increase of the d-spacing value due to the thermal expansion of the spinel with temperature.

When the recovery temperature exceeded 1000 °C, the restored spinel decomposed back to the cubic structure. Contrary to the metastable structure obtained in the deposition process, the spinel decomposed irreversibly into simple metal oxides, which were observed after the cooling cycle at room temperature (HT). The results were similar to the study of Kiefer et al. [7] who obtained multi-phase structures of $MnCo_2O_4$, CoO and Co_3O_4 phases after heat treatment of the $MnCo_2O_4$ spinel at 1200 °C.

Oxidized coatings

Fig. 8 shows the cross-section view of the oxidized spinel samples. The initial microstructure was changed during the 1000 h oxidation cycle. Instead of the cracks and inter-splat

Fig. 6 — μ-Raman spectra of the powder and as-sprayed $MnCo_{1.7}Fe_{0.3}O_4$ spinel coating. Reference spectra of Mn_3O_4, MnO_2 and CoO(OH) were plotted based on the spectral data taken from. [22].

| Table 2 — Element concentration in % weight (XRF, ICP-AES and EDS).			
	Mn	Co	Fe
X-ray fluorescence			
$MnCo_{1.7}Fe_{0.3}O_4$ spray powder	27.1	61.9	11.0
As-sprayed $MnCo_{1.7}Fe_{0.3}O_4$ coating	27.1	62.0	10.9
Inductively coupled plasma spectrometry			
$MnCo_{1.7}Fe_{0.3}O_4$ spray powder	27.9	60.8	11.3
As-sprayed $MnCo_{1.7}Fe_{0.3}O_4$ coating	27.6	60.7	11.4
Energy dispersive X-ray spectroscopy			
$MnCo_{1.7}Fe_{0.3}O_4$ spray powder	31.4	56.2	12.4
As-sprayed $MnCo_{1.7}Fe_{0.3}O_4$ coating	31.9	56.3	11.8
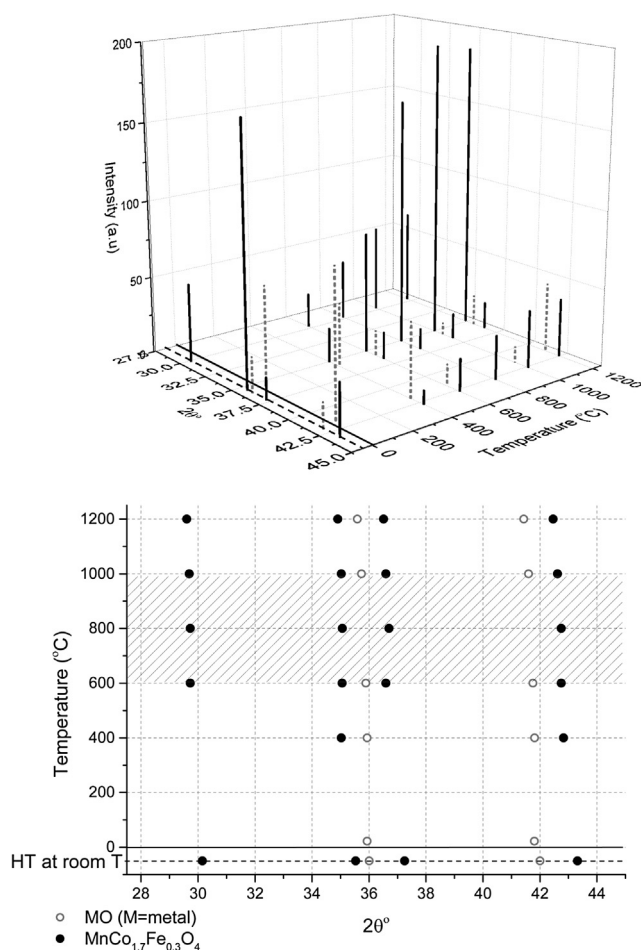
Fig. 7 — Stepwise heat-treatment process for the as-sprayed $MnCo_{1.7}Fe_{0.3}O_4$ spinel coatings. Peak position and relative intensity levels of spinel and decomposed cubic phases (top) and projected $x-y$ plane (lower). Dashed lines and grey dots present the decomposed structure and solid lines and black dots the MnCoFe spinel.

porosity, the oxidized coatings contained un-connected voids. The void distribution exhibited a through thickness gradient, in a way that the top part of the coating was mostly dense, with more pores next to the substrate. Thomann et al. [10] have observed a similar kind of microstructure in a high velocity oxy-fuel (HVOF) sprayed $(Mn,Co,Fe)_3O_4$ coating. Although the voids can be considered disadvantageous structural faults, the coatings seemed to be fairly dense microstructure, without a sign of open porosity.

Residual stresses and the disordered metastable crystal structure, as observed in the XRD studies, enhance the mass transport properties, caused partial sintering observed as void coarsening. During sintering inter-splat porosity, cracks and segmentation cracks reorganize so that a lower net surface energy is obtained. The temperature at which sintering occurs is $0.5-0.8 * T_m$ (where T_m is the melting temperature of the material in degrees Kelvin) when the material system is formed of micron sized particles, and $0.2-0.3 * T_m$ for nano-sized particles. In addition to particle size, the sintering temperature depends on the intercrystallite/intra-agglomerate

pore distribution and pore curvature [24]. The pore curvature in this study means the contact point of two neighbouring splats (Fig. 4(e)). The melting temperature of the Mn—Co spinels is from 1300 °C to 1400 °C, according to Eun et al. [25] and from 1600 °C to 1700 °C according to Aukrust et al. [26]. It can be expected that the melting temperature lies somewhere between 1300 °C and 1700 °C depending on the material composition, and so sintering most likely occurred during the oxidation cycle at 700 °C.

The authors consider that the void redistribution is a consequence of many individual factors. Firstly, the top parts of the coatings were denser i.e. the inter-splat caps were smaller compared to those layers next to the substrate. This was caused by the progressively increasing surface temperature during the spray process due to the lower heat transfer properties of the coating compared to the substrate. The, higher surface temperature enhanced the formation of denser coating layers. Secondly, the selective evaporation, enrichment or loss due to the migration of elements to the surface changed the sintering behaviour of the spinel material. Thirdly, the substrate was a rigid element that caused anisotropic shrinkage behaviour of the coating [27].

The EDS analysis listed in Table 3 and pointed out in Fig. 8 revealed relatively high Fe loss and Co enrichment on the surface of the oxidized coatings. According to the authors' knowledge, the evaporation of Fe is not reported in the open literature when similar coatings have been oxidized. Partial evaporation of the elements can be excluded, as it was not observed to occur during the high temperature deposition process. Therefore, it can be presumed that Fe cations migrated towards or into the Cr-rich oxide scale and Co diffused towards to surface.

Due to the long term exposure at 700 °C in air, oxide scales were indeed formed between the substrates and the spinel coatings, as observed in cross-section images (Fig. 8) and confirmed by the EDS analysis presented in Table 4. The EDS area analysis indicated that the oxide scales were mostly formed of Cr cations and O anions, referring to the formation of Cr_2O_3. When the $MnCo_{1.7}Fe_{0.3}O_4$ coating was oxidized the oxide scale seemed to have a dual layer structure. In addition to a Cr_2O_3 layer, the EDS analysis indicated formation of a Cr- and Co-rich layer with a close correlation for $(Co,Cr)_3O_4$.

The oxidized $MnCo_{1.7}Fe_{0.3}O_4$ coating was carefully ground with 1200 grit paper to reveal the oxide scale beneath the coating. Fig. 9 shows the X-ray diffraction pattern of the revealed oxide scale. The peak pattern corresponded to Cr_2O_3 and $(Mn,Co,Fe)_3O_4$ spinel phases in addition to the Crofer 22 APU substrate. The results were comparable to the results obtained by Fang et al. [28], as they also detected Cr_2O_3 and $MnCoCrO_4$. The exact determination of the $(Co,Cr)_3O_4$ composition is problematic using the XRD analysis, as the XRD pattern [29] has the same peak positions as those of $(Mn,Co)_3O_4$ and $(Mn,Co,Fe)_3O_4$ phases as shown in Fig. 9.

Fig. 10 shows the X-ray diffraction patterns of the oxidized coatings. The original spinel phases were observed after the oxidation cycle in accordance with the in-situ high temperature XRD analysis as previously described. In addition, the $CoCo_2O_4$ phase was observed when $MnCo_{1.9}Fe_{0.1}O_4$ was used as the coating material. Both spinels had close correlation with $MnCo_2O_4$. The average crystallite sizes for the oxidized

$MnCo_{1.9}Fe_{0.1}O_4$ and $MnCo_{1.7}Fe_{0.3}O_4$ coatings were 22 nm and 45 nm, respectively. For the $MnCo_{1.7}Fe_{0.3}O_4$ coatings, the crystallite size was notably smaller than that of the powder feedstock (280 nm). The small crystallite size is a consequence of decomposition of spinel and formation of simple cubic oxides during the thermal spray process, in addition to the migration of elements, such as the loss of Fe cations.

The Cr-migration was measured by the EDS point and area analysis methods. The relative EDS intensities of the elements are presented in Table 3 (point analyses across the coating thickness) and in Table 5 (area analysis on top surfaces). Relatively low Cr values were obtained for the coatings. The coatings effectively decreased the Cr-migration rate, as point analyses show zero Cr content 10 μm from the substrate. According to the area analysis, $MnCo_{1.9}Fe_{0.1}O_4$ fully prevented the Cr migration whereas existence of some Cr was indicated in the $MnCo_{1.7}Fe_{0.3}O_4$. Therefore, $MnCoFeO_4$ spinel coatings with a thickness of 20 μm should provide adequate Cr-barrier properties at 700 °C.

The ASR data for the oxidized $MnCo_{1.9}Fe_{0.1}O_4$ and $MnCo_{1.7}Fe_{0.3}O_4$ are presented in Fig. 11. The significant drop in the ASR values for the first few hundreds of hours can be explained by i) increase in the contact area, as the corrugated

Table 3 — EDS analysis spectra of the analysis points presented in Fig. 8. The results are presented in at-%.

Spectrum	O	Mn	Co	Fe	Cr	Cr/(Co + Mn + Fe)
$MnCo_{1.9}Fe_{0.1}O_4$						
1.	46.7	16.7	36.6	0.0	0.0	0.0
2.	59.3	13.5	27.2	0.0	0.0	0.0
3.	58.4	14.4	26.2	1.0	0.0	0.0
4.	58.8	14.3	25.8	1.4	0.0	0.0
5.	58.4	14.6	25.5	1.5	0.0	0.0
6.	58.2	14.4	25.0	2.5	0.0	0.0
7.	51.5	16.1	27.6	3.9	0.9	0.0
8.	35.2	0.0	0.0	42.4	22.5	0.5
9.	0.0	0.0	0.0	78.4	21.6	0.3
10.	0.0	0.0	0.0	78.4	21.6	0.3
$MnCo_{1.7}Fe_{0.3}O_4$						
1.	39.2	5.7	53.5	1.7	0.0	0.0
2.	58.7	12.4	25.9	2.9	0.0	0.0
3.	59.0	13.4	23.6	4.0	0.0	0.0
4.	58.2	14.3	22.6	5.0	0.0	0.0
5.	58.5	14.3	21.4	5.8	0.0	0.0
6.	58.6	14.4	19.9	6.8	0.4	0.0
7.	56.7	14.3	19.9	8.5	0.7	0.0
8.	61.7	2.1	0.8	3.7	31.7	4.8
9.	0.0	0.0	0.0	78.1	21.9	0.3
10.	0.0	0.0	0.0	77.9	22.1	0.3

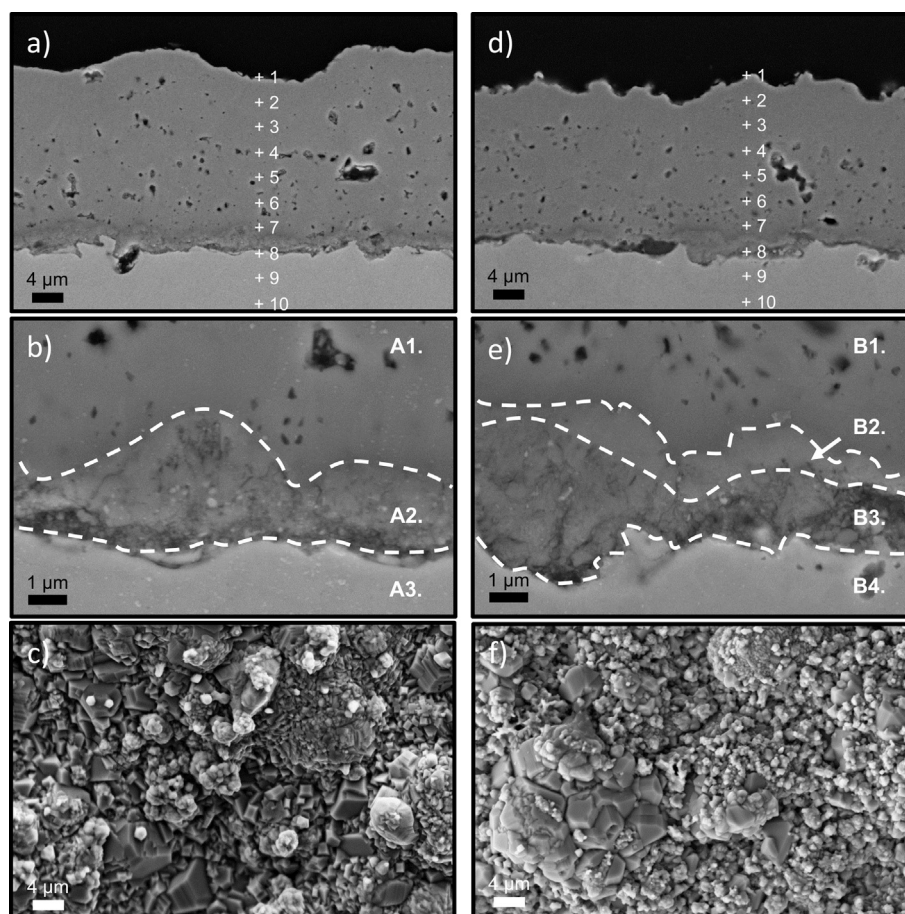**Fig. 8 — Cross-section and surface topography images and EDS point and area analyses of oxidized $MnCo_{1.9}Fe_{0.1}O_4$ (a—c) $MnCo_{1.7}Fe_{0.3}O_4$ spinel coatings (d & e). The measurement location of the EDS analyses are marked on the FE-SEM (SE)-images. The results obtained from point analyses (a, d) are presented in Table 3 and area analyses (b, e) and (c, f) in Tables 4 and 5, respectively.**

Table 4 – EDS area analysis spectra of the oxide scales (Fig. 8) formed between the oxidized coatings. The results are presented in at-%.

Area	Cr	Mn	Fe	Co	O
$MnCo_{1.9}Fe_{0.1}O_4$					
A1.	0.8	13.6	3.3	23.4	58.9
A2.	31.2	0.9	2.7	2.0	63.1
A3.	20.7	0.4	77.3	0.5	1.3
$MnCo_{1.7}Fe_{0.3}O_4$					
B1.	0.9	13.7	8.0	19.8	57.6
B2.	24.3	2.5	1.5	8.0	63.7
B3.	32.1	1.9	2.8	0.7	62.6
B4.	20.7	0.5	73.6	0.4	4.7

substrates deformed (creep) due to external force and high temperature, ii) sintering and crystallographic changes i.e. restoration of the spinel structure, crystallite growth and material transport to inter-splat caps and contact areas, which eventually improved electrical conduction. The values levelled off to 9.20 mΩ cm^2 and 14.10 mΩ cm^2 for $MnCo_{1.9}Fe_{0.1}O_4$ and $MnCo_{1.7}Fe_{0.3}O_4$, respectively, at the end of the 1000 h test cycle. The relative order of the conductivity of the iron doped spinels is in line with the study of Kiefer et al. [7].

Fig. 12 shows ASR data and cross-section view of the $MnCo_{1.7}Fe_{0.3}O_4$-LSM and Crofer 22 APU-LSM spacer. The same decrease in the ASR values, as in the coating–coating test was observed for the first 300 h. This drop in values is linked to the same behaviour of the coating and the LSM spacer as described for the coating-coatings test procedure. ASR reached a value of 50 mΩ cm^2 after the 1000 h test cycle. The continuous decrease in the ASR values is also strongly linked to the slow sintering mechanisms of the porous LSM spacer (Area 4 in Fig. 12(b)). Due to this porous structure, the number of the contact points in the coating-LSM interface increased over oxidation time due to mutual reactions and material transport. The same Cr-rich oxide scale with the thickness a
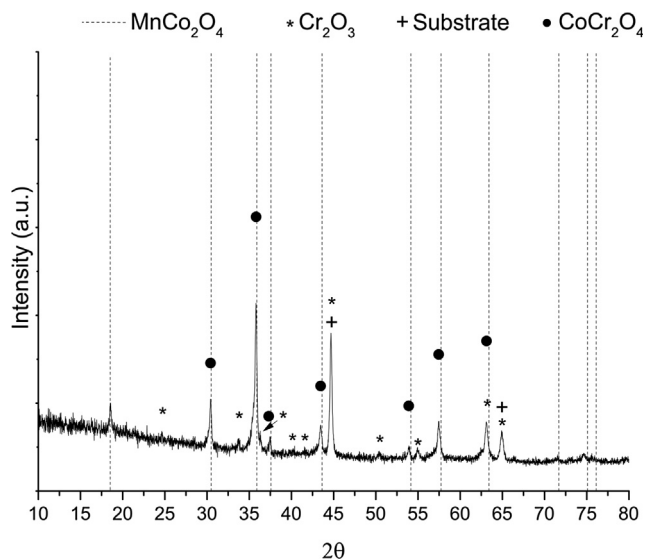

Fig. 9 – Crystallographic phase analysis of the sub-scale formed between the oxidized $MnCo_{1.7}Fe_{0.3}O_4$ coating and Crofer 22 APU substrate.
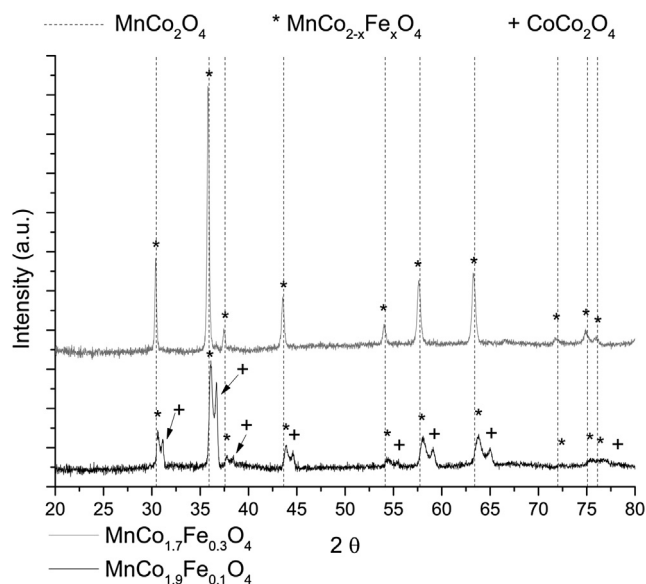

Fig. 10 – Crystallographic phase studies of the oxidized $MnCo_{1.9}Fe_{0.1}O_4$ and $MnCo_{1.7}Fe_{0.3}O_4$ oxide spinel coatings after 1000 h oxidation at 700 °C.

5 μm was formed (Area 2 in Fig. 12(b)), but due to the dense spinel coating, further migration of Cr was effectively blocked.

Atmospheric plasma sprayed iron doped oxide spinel coatings, and especially $MnCo_{1.9}Fe_{0.1}O_4$ exhibited low ASR values due to low coating thickness, dense microstructure and Cr-free composition with effective Cr-barrier properties. Since the ASR test procedures vary among published studies, the exact benchmarking of the coating properties between deposition methods cannot be done. In general, the ASR values were on the same level with the studies reviewed in the introduction.

It is evident that atmospheric plasma spraying can produce dense spinel coatings for the SOFC interconnects. Dense microstructure is the most important factor to provide adequate protection against volatile Cr-compounds and to obtain low ohmic resistances in long term use. Since the dense microstructure is obtained during the spraying process, post-deposition heat treatment processes are no longer needed. Although atmospheric plasma spraying can be considered high temperature deposition process, selective evaporation of elements does not occur during the deposition process.

Conclusion

Iron doped oxide spinels are promising candidates for protective coatings on the SOFC interconnects in order to provide

Table 5 – Cr-content in wt-% from the surface by the EDS area (50 μm * 35 μm in Fig. 8) analysis.

Sample	Cr (wt%)	Mn (wt%)	Fe (wt%)	Co (wt%)
$MnCo_{1.9}Fe_{0.1}O_4$	0.0	29.1	1.6	69.4
$MnCo_{1.7}Fe_{0.3}O_4$	0.7	30.5	7.4	61.5
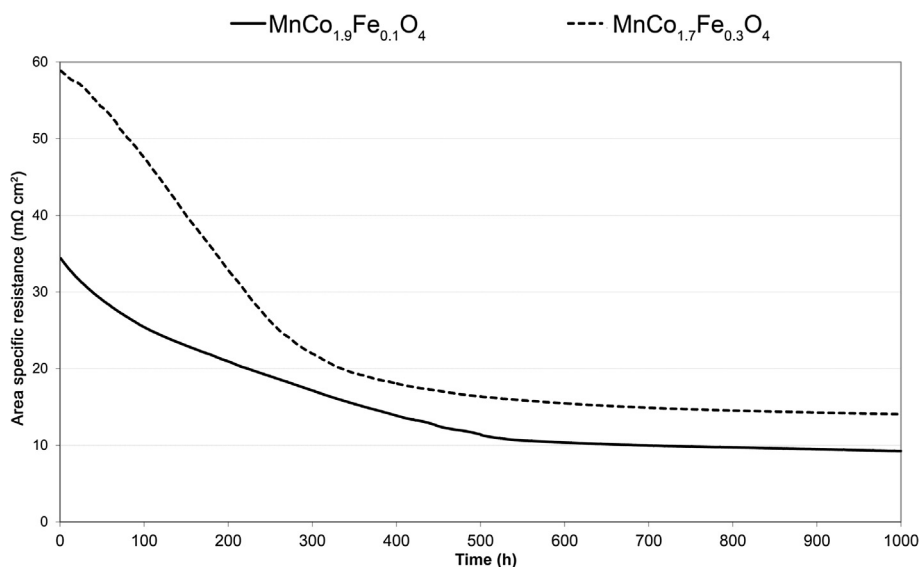
Fig. 11 — ASR values of oxidized $MnCo_{1.9}Fe_{0.1}O_4$ and $MnCo_{1.7}Fe_{0.3}O_4$ spinel coatings-coating.

good Cr-barrier properties and sufficiently high electrical conductivity. In this study, $MnCo_{1.9}Fe_{0.1}O_4$ and $MnCo_{1.7}Fe_{0.3}O_4$ coatings were manufactured using the atmospheric plasma spraying process with a simultaneous substrate heating setup. The clear advantage of this process is that dense coatings were sprayed without post-deposition heat treatments. Although thermal spraying is a high temperature deposition process, selective evaporation of elements did not occur.

Although coatings with optimal microstructures were sprayed, the spinels decomposed during the spraying process. This was caused by the high cooling rate of the deposited splats, which prevented the formation of the desired spinel structure. Tests demonstrated that being metastable, the as-sprayed structure could be restored to the original spinel by a simple heat treatment process in air. The spinel re-crystallization process starts at 400 °C, and is most effective from 600 °C to 800 °C. The same test showed that the iron doped spinels have a maximum operating temperature of 1000 °C. Above this, the spinel decomposes and forms simple metal oxides.

According to the ASR results, iron doping improves the electrical conductivity of the $(Mn,Co)_3O_4$ based spinels. Values as low as 9.20 mΩ cm^2 and 14.10 mΩ cm^2 for $MnCo_{1.9}Fe_{0.1}O_4$
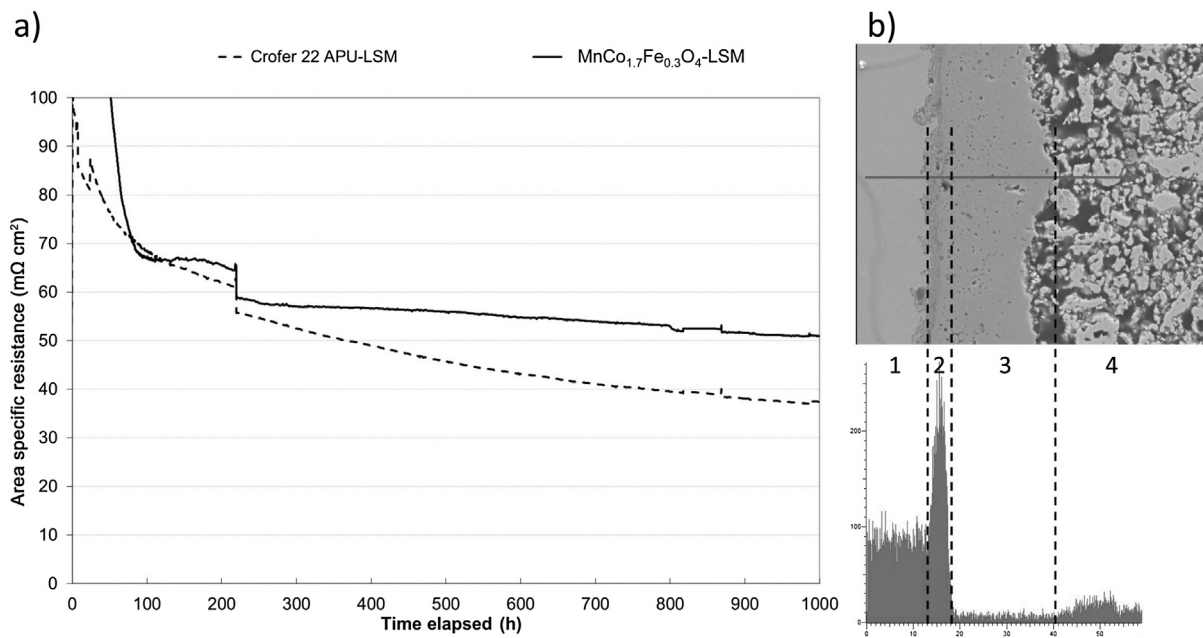

Fig. 12 — ASR values of $MnCo_{1.7}Fe_{0.3}O_4$-LSM contact and Crofer 22 APU-LSM contact (a), and cross-sectional SEM micrograph of the Crofer 22 APU-$MnCo_{1.7}Fe_{0.3}O_4$-LSM contact with EDX linescan of the Cr concentration (b).

and $MnCo_{1.7}Fe_{0.3}O_4$, respectively, were obtained at the end of the 1000 h oxidation cycle at 700 $^\circ$C in air. As the tests were completed without contact paste, the values represent a dry coating–coating contact. The $MnCo_{1.7}Fe_{0.3}O_4$ coating was tested together with an LSM-based and 50 mΩ cm^2 values were reached at the end of the 1000 h test cycle.

According to the results obtained in this study, both compositions exhibited effective Cr-barrier properties against volatile Cr(VI) compounds and migration of Cr cations. The $MnCo_{1.9}Fe_{0.1}O_4$ spinel is the most promising spinel composition for the SOFC interconnects. The results demonstrated that, the atmospheric plasma spraying process is a viable technique for manufacturing protective coatings for the SOFC interconnectors. Dense microstructures effectively blocked the Cr-migration, in addition the Cr-free spinel and dense microstructure contributed to a low electrical resistance.

Acknowledgements

REFERENCES

[1] Wu J, Liu X. Recent development of SOFC metallic interconnect. J Mater Sci Technol 2010;26:293–305.

[2] Fergus J. Effect of cathode and electrolyte transport properties on chromium poisoning in solid oxide fuel cells. Int J Hydrogen Energy 2007;32:3664–71.

[3] Chen F, Sun E, Yamanis J, Hawkes J, Smeggil J, Warrier S, et al. Cr poisoning effect for solid oxide fuel cells. Technol 2006 Conf Exhib 2006:303–11.

[4] Kim JY, Canfield NL, Chick LA, Menhardt KD, Sprenkle VL. Chromium poisoning effect on various cathodes. Ceram Eng Sci Proc 2005:129–38.

[5] Zhu WZ, Deevi SC. Development of interconnect materials for solid oxide fuel cells. Mater Sci Eng A 2003;348:227–43.

[6] Zhu WZ, Deevi SC. Opportunity of metallic interconnects for solid oxide fuel cells: a status on contact resistance. Mater Res Bull 2003;38:957–72.

[7] Kiefer T, Zahid M, Tietz F, Stöver D, Zerfass H-R. Electrical conductivity and thermal expansion coefficients of spinel in the series $MnCo_{2-x}Fe_xO_4$ for application as a protective layer in SOFC. In: Proc 26th Riso Int Sym Mater Sci: solid state electrochemistry, Roskilde; 2005. p. 261–6.

[8] Miguel-Pérez V, Martínez-Amesti A, Nó ML, Larrañaga A, Arriortua MI. The effect of doping $(Mn,B)_3O_4$ materials as protective layers in different metallic interconnects for SOFC. J Power Sources 2013;243:419–30.

[9] Liu Y, Fergus JW, Wang K, Dela Cruz C. Crystal structure, chemical stabilities and electrical conductivity of Fe-doped manganese cobalt spinel oxides for SOFC interconnect coatings. J Electrochem Soc 2013;160:F1316–21.

[10] Thomann O, Pihlatie M, Rautanen M, Himanen O, Lagerbom J, Mäkinen M, et al. Development and application of HVOF sprayed spinel protective coating for SOFC interconnects. J Therm Spray Technol 2013;22:631–9.

[11] Montero X, Tietz F, Sebold D, Buchkremer H, Ringuede A, Cassir M, et al. $MnCo_{1.9}Fe_{0.1}O_4$ spinel protection layer on commercial ferritic steels for interconnect applications in solid oxide fuel cells. J Power Sources 2008;184:172–9.

[12] Pawlowski L. The science and engineering of thermal spray coatings. 2nd ed. Chichester: John Wiley & Sons; 1995 [Chapter 6: Coating build-up].

[13] Saoutieff E, Bertrand G, Zahid M, Gautier L. APS deposition of $MnCo_2O_4$ on commercial alloys K41X used as solid oxide fuel cell interconnect: the importance of post heat-treatment for densification of the protective layer. ECS Trans 2009;25:1397–402.

[14] Puranen J, Lagerbom J, Hyvärinen L, Kylmälahti M, Himanen O, Pihlatie M, et al. The structure and properties of plasma sprayed iron oxide doped manganese cobalt oxide spinel coatings for SOFC metallic interconnectors. J Therm Spray Technol 2010;20:154–9.

[15] Puranen J, Lagerbom J, Hyvärinen L, Mäntylä T, Levänen E, Kylmälahti M, et al. Formation and structure of plasma sprayed manganese-cobalt spinel coatings on preheated metallic interconnector plates. Surf Coat Technol 2010;205:1029–33.

[16] Shannon RD. Revised effective ionic radii and systematic studies of interatomie distances in halides and chaleogenides. Acta Crystallogr Sec A 1976;32:751–67.

[17] McPherson R, Shafer BV. Interlamellar contact within plasma-sprayed coatings. Thin Solid Films 1982;97:201–4.

[18] Marr M, Kesler O. Permeability and microstructure of suspension plasma-sprayed YSZ electrolytes for SOFCs on various substrates. J Therm Spray Technol 2012;21:1334–46.

[19] Puranen J, Hyvärinen L, Lagerbom J, Kylmälahti M, Koivuluoto H, Vuoristo P. Suspension plasma spraying (SPS) of manganese-cobalt spinel coatings. In: Int. Therm. Spraying Conf., Hamburg; 2011. p. 1201–5.

[20] Cetinkaya T, Tocoglu U, Uysal M, Guler MO, Akbulut H. A parametric study on the rapid synthesis of one dimensional (1D) α-MnO_2 nanowires. Microelectron Eng 2014;126:54–9.

[21] Gallant D, Pézolet M, Simard S. Optical and physical properties of cobalt oxide films electrogenerated in bicarbonate aqueous media. J Phys Chem B 2006;110:6871–80.

[22] RRUFF project database: http://rruff.info/ [last accessed: 22.04.14].

[23] Puranen J, Laakso J, Kylmälahti M, Vuoristo P. Characterization of high-velocity solution precursor flame-sprayed manganese cobalt oxide spinel coatings for metallic SOFC interconnectors. J Therm Spray Technol 2013;22:622–30.

[24] Mayo MJ. Processing of nanocrystalline ceramics from ultrafine particles. Int Mater Rev 1996;41:85–115.

[25] Eun JY, Mi YY, Ji-Woong M, Hae Jin H. Fabrication of a $MnCo_2O_4$ gadolinia-doped ceria (GDC) dual-phase composite membrane for oxygen separation. J Korean Ceram Soc 2010;47:199–204.

[26] Aukrust E, Muan A. Phase relations in the system cobalt oxide – manganese oxide in air. J Am Ceram Soc 1963;46:511.

[27] Jamin C, Rasp T, Kraft T, Guillon O. Constrained sintering of alumina stripe patterns on rigid substrates: effect of stripe geometry. J Eur Ceram Soc 2013;33:3221–30.

[28] Fang Y, Wu C, Duan X, Wang S, Chen Y. High-temperature oxidation process analysis of $MnCo_2O_4$ coating on Fe–21Cr alloy. Int J Hydrogen Energy 2011;36:2–7.

[29] Mączka M, Ptak M, Kurnatowska M, Hanuza J. Synthesis, phonon and optical properties of nanosized $CoCr_2O_4$. Mater Chem Phys 2013;138:682–8.

Publication IV

Influence of Powder Composition and Manufacturing Method on Electrical and Chromium Barrier Properties of Atmospheric Plasma Sprayed Spinel Coatings Prepared From MnCo$_2$O$_4$ and Mn$_2$CoO$_4$+Co Powders on Crofer 22 APU Interconnectors

by
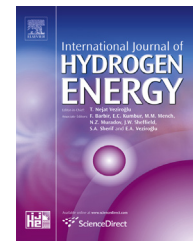
J. Puranen, M. Pihlatie, J. Lagerbom, T. Salminen, J. Laakso, L. Hyvärinen, , M. Kylmälahti, O. Himanen, J. Kiviaho and P. Vuoristo

Influence of powder composition and manufacturing method on electrical and chromium barrier properties of atmospheric plasma sprayed spinel coatings prepared from $MnCo_2O_4$ and Mn_2CoO_4 + Co powders on Crofer 22 APU interconnectors

CrossMark

Jouni Puranen [a,*], Mikko Pihlatie [b], Juha Lagerbom [c], Turkka Salminen [d], Jarmo Laakso [a], Leo Hyvärinen [a], Mikko Kylmälahti [a], Olli Himanen [b], Jari Kiviaho [b], Petri Vuoristo [a]

[a] Tampere University of Technology, Department of Materials Science, P.O. Box 589, FI-33101, Tampere, Finland
[b] VTT, Technical Research Centre of Finland, P.O. Box 1000, FI-02044, VTT, Finland
[c] VTT, Technical Research Centre of Finland, P.O. Box 1300, FI-33101, Tampere, Finland
[d] Tampere University of Technology, Optoelectronics Research Centre, P.O. Box 692, FI-33101, Tampere, Finland

ARTICLE INFO

ABSTRACT

Protective coatings based on manganese cobalt oxide spinels are required in solid oxide fuel cells (SOFCs) to prevent the evaporation of volatile Cr(VI)-compounds from the metallic interconnectors and to minimize high temperature corrosion. Atmospheric plasma spraying (APS) was used to manufacture dense manganese cobalt oxide protective coatings on Crofer 22 APU substrates by employing two different spinel powders. The spray powders were $MnCo_2O_4$ and Mn_2CoO_4 + Co (equivalence for $Mn_{1.5}Co_{1.5}O_4$). The Mn_2CoO_4 + Co powder was prepared by agglomerating the oxide powder with fine metallic cobalt powder. The coated substrates were oxidized at 700 °C in air for 1000 h. During the high temperature oxidation, a four-point on-line measurement technique with a current density of 640 mA/cm² was simultaneously used for area specific resistance (ASR) studies. The coatings were characterized by X-ray diffraction (XRD), field-emission scanning electron microscopy (FESEM), an energy dispersive spectrometer (EDS) and Raman spectroscopy.

The APS coatings had dense microstructure, which decreased the oxidation of the substrate. The $MnCo_2O_4$ coating showed indication of some Cr-migration, whereas Mn_2CoO_4 + Co showed good Cr-barrier properties. The ASR test showed that APS coated Mn_2CoO_4 + Co is a promising candidate material for SOFC interconnect applications.

Copyright © 2014, Hydrogen Energy Publications, LLC. Published by Elsevier Ltd. All rights reserved.

Introduction

Chromium-containing ferritic stainless steels show the highest potential for solid oxide fuel cell interconnects (ICs) due to i) high mechanical strength, ii) ideal thermal conductivity, iii) excellent electronic conductivity, iv) coefficient of thermal expansion (CTE) match with state-of-the-art solid oxide cells and v) their reasonably low manufacturing costs, even for more complex IC profiles [1]. The use of ferritic stainless steels is based on the acceptable corrosion behaviour, which is based on the formation of chromium rich oxide scale e.g. Cr_2O_3 at the typical SOFCs' operating temperatures the order of 600—800 °C.

Under appropriate conditions Cr_2O_3 reacts with water molecules (cathode side atmosphere) and may form CrO_3 and $CrO_2(OH)_2$ compounds [2]. These harmful Cr-compounds tend to migrate to a triple phase boundary (TPB), which is a shared active interface between the cathode, electrolyte and oxidant gas phases. On the TPB, these Cr-compounds reduce to Cr_2O_3 (manganese containing cathode) or as $SrCrO_4$ and Cr_2O_3 (non-manganese containing cathode) causing degradation of the cell by decreasing the total area of the TPB [3—5].

It is well known that the ferritic stainless steel ICs must be coated prior to the use in the SOFCs. The coating prevents Cr-transport and thereby protects the cathode from degradation. The basic requirements for the [interconnect]-[coating] system are:

- low diffusion coefficient of Cr-ions and low transport of Cr-compounds [6],
- excellent electrical conductivity, with the objective of 100% electronic conduction [7],
- chemical, microstructural and phase stability [6,7],
- coefficient of thermal expansion (CTE) match with the other stack components [7],
- the coatings, together with the metallic substrate, should present high temperature strength, creep and spallation resistance [7],
- simple and economical manufacturing process in mass production [7].

Recent studies focus on the use of $(Mn,Co)_3O_4$ spinels, due to their excellent electrical properties [8—12] and the compatibility of coefficient of thermal expansion (CTE) with ferritic stainless steels [11]. The $(Mn,Co)_3O_4$ spinel coatings provide sufficiently low ASR values as reviewed in Table 1, low Cr-transport rate [2] and formation of stable Cr-containing spinels [13]. Although promising results have been reported, the study of Persson et al. indicates that the $(Mn,Co)_3O_4$ coatings may suffer from the phenomenon known as break-away oxidation-effect (uncontrolled oxidation) above than 900 °C after 1000 h oxidation, or when the thickness of the oxide scale exceeds 10—15 µm. The break-away oxidation was not observed at lower temperatures [14].

The spinels can be deposited either by conventional wet ceramic processes [8,10,11,14,15,18—23], by electrophoretic deposition (EPD) [24—26] or by a sputtering process [10,13,16,27,28]. Post heat-treatment/sintering is typically required in the previous processes, except in the sputtering

Table 1 – Comparison of $(Mn,Co)_3O_4$ coatings manufactured with various methods.

Method	Material	Thickness (µm)	Substrate	Contact paste/Cathode	ASR test time (h)	Test temperature (°C)	ASR (mΩ cm²)	Ref.
Slurry painted	$Mn_{1.5}Co_{1.5}O_4$	20	Ducrolloy alloy	Perovskite/LSM	10000 (prediction)		24	[8]
Screen-printed	$Mn_{1.5}Co_{1.5}O_4$	10	Crofer 22 APU	$La_{0.8}Sr_{0.2}Co_{0.5}Mn_{0.5}O_3/La_{0.8}Sr_{0.2}FeO_3$	1000	800	11.4	[15]
Screen-printed	$Mn_{1.5}Co_{1.5}O_4$	10	Crofer 22 APU	Platinum/LSF	500	800	7.5	[10]
Thermally grown	$Mn_{1.5}Co_{1.5}O_4$	10	Crofer 22 APU	Platinum/LSF	300	800	14	[10]
RF-sputtered	$Mn_{1.5}Co_{1.5}O_4$	1	Crofer 22 APU	Platinum/LSF	275	800	19	[10]
Slurry-spraying	$MnCo_2O_4$	15–20	430SS		60/120	800/850	2.3	[9]
Slurry-spraying	$MnCo_2O_4$	15–20	430SS		50000 (prediction)	850	500	[9]
Magnetron sputtering	$MnCo_2O_4$	15	Fe–21Cr	Platinum/—	1000	750	5	[13]
Magnetron sputtering	$MnCo_2O_4$	3	Crofer 22 APU	$-/La_{0.7}Sr_{0.3}MnO_3$	1000	800	9	[16]
Magnetron sputtering	$MnCo_2O_4$	3	Crofer 22 APU	$-/La_{0.7}Sr_{0.3}MnO_3$	5000	800	6	[16]
Thermal spraying	$MnCo_2O_4$	20–28	Cfrofer 22 APU	$-/La_{0.85}Sr_{0.15}Mn_{1.1}O_3$	1000	700	20	[12]
Thermal spraying	$MnCo_2O_4$		F17TNb	$-/LSMC$	575	800	50	[17]

processes. The post heat-treatment removes the organic binders and to sinter the primary particles in order to obtain well-adhered coatings with a dense microstructure [29]. This is usually a two-step process for $(Mn,Co)_3O_4$ spinel containing pastes [11,15,19–21,23] or spinel-forming carbonate slurries [8]. In these cases the deposited paste or slurry is first heat-treated in a reducing $(H_2/Ar/H_2O)$ atmosphere, in a process called reactive sintering, followed by the heat-treatment in an oxidizing atmosphere (air). Sintering can also be a one-step heat-treatment process in an oxidizing atmosphere, but at considerably higher temperatures as Yoo et al. [25] have reported, by sintering an electrophoretically deposited $Mn_{1.5}Co_{1.5}O_4 - La_{0.8}Sr_{0.2}MnO_3$ dual layer coating at 1200 °C in air for 2 h.

Due to the heat-treatments, Cr-rich scale is generally formed between the substrate and the coating as for instance, reported by Uehara et al. [21]. This oxidation is the consequence of the porous microstructure that is formed during the reactive sintering from segregated MnO and Co phases [11,23]. Before the dense coating is finally obtained in an oxidizing atmosphere, the porous microstructure enables the oxidation of the substrates. It is noteworthy that the Cr-rich scale can form even if the coatings are heat-treated only in a reducing (97% H_2/3% H_2O) atmosphere as Zhang et al. [24] have reported in their study.

Thermal spraying, compared to other available methods, produces relatively dense microstructures directly without subsequent sintering processes. The coatings are formed of mostly molten, and in some circumstances semi-molten droplets which impact the substrate and form well adhered solidified lamellas called splats [30]. This as-sprayed structure is generally sufficiently dense, and therefore time-consuming heat-treatment processes are not required.

Although, cross-sectional studies [12,31–35] and the Cr-barrier properties [12,17,33] of the thermally sprayed $(Mn,Co)_3O_4$ spinel coatings have been reported, the long-time ageing tests, area specific resistance (ASR) properties, post-modern analysis of the oxide scales formed between the substrates and the atmospheric plasma sprayed (APS) $MnCo_2O_4$ and $Mn_{1.5}Co_{1.5}O_4$ spinel coatings have not been studied. The ASR, and Cr-barrier properties of the atmospheric plasma sprayed coatings produced from the powder of $MnCo_2O_4$ and Mn_2CoO_4 doped with metallic Co coatings on thin Crofer 22 APU substrates were studied at 700 °C in air for 1000 h and reported in this study.

Experimental

The substrate material was Cr-alloyed (Cr: 20–24 wt%) ferritic stainless steel grade Crofer 22 APU (ThyssenKrupp VDM GmbH, Werdohl, Germany) designed for the SOFCs. This experiment employed two different substrate thicknesses: 0.2 mm and 0.1 mm. The substrate with the thickness of 0.2 mm was corrugated on 34 * 34 mm² area. This corrugated area simulated the profiles of the gas channel networks. The flat substrate with the thickness of 1.0 mm was a counterpart on area specific resistance (ASR) tests as will be described later. In addition, the flat 0.2 mm thin Crofer 22 APU was utilized for the cross-sectional studies of the as-sprayed

coatings. Prior to the spray process, the substrates were grit blasted with 240 grit Al_2O_3 sand, in order to roughen the surface and thereby improving the adhesion of the as-sprayed coatings to the substrate. Grit blasting was utilized for both sides of the substrates in order to even out the stresses, formed during the blasting process.

Two different spray powders with different chemical compositions were used in this study. The first powder was commercially acquired $MnCo_2O_4$ spinel powder (The Swiss Federal Laboratories for Materials Science and Technology, Switzerland) with the particle size range of $-33 + 6$ μm $(d_{90}-d_{10})$ measured by laser diffraction (Helos, Sympatec GmbH, Clausthal-Zellerfeld, Germany). The powder was the same as Thomann et al. [12] used in the HVOF process.

The second powder was self-made cermet (ceramic-metallic) $Mn_2CoO_4 + Co$ spinel powder. The Mn_2CoO_4 spinel was mixed together with finely dispersed metallic Co-particles. The intention was to reduce porosity (cracks and pores) of the as-sprayed coating as Co works as a binder during spraying, similarly to cermet type of tungsten carbide cobalt coatings [36]. As these type of coatings should exhibit longer lifespans at high temperatures, oxidation of the added Co and the subsequent reaction with Mn_2CoO_4 could ideally form $Mn_{1.5}Co_{1.5}O_4$ which consists of the $[Mn_{1+\delta}Co_{2-\delta}O_4]_{cubic}$ and $[Mn_{2-\delta}Co_{1-\delta}O_4]_{tetragonal}$ phases and no other undesirable compounds or side products. Park et al. have studied similar cermet based powder by spray drying $La_{0.6}Sr_{0.4}Co_{0.2}Fe_{0.8}O_3$ powder together with finely dispersed Ag-powder. The cross-sectional studies clearly showed that Ag alloying effectively reduced the amount of cracks, but unlike in this study Ag was inert with the $La_{0.6}Sr_{0.4}Co_{0.2}Fe_{0.8}O_3$ phase [37].

The $Mn_2CoO_4 + Co$ powder was produced by solid-state synthesis. In the solid-state synthesis, appropriate amounts of $MnCO_3$ and $CoCO_3$ were weighted and milled for 20 h in a drum ball mill. After the milling, the mixture of the powders was calcinated at 800 °C in air for 6 h to obtain the spinel structure. The obtained spinel powder was mixed with metallic Co powder. The amount of Co used together with the spinel Mn_2CoO_4 had equivalence with the $Mn_{1.5}Co_{1.5}O_4$ composition. The mixture of Mn_2CoO_4 powder and metallic Co was dispersed in water using 1 wt% of dispersant (Dispex A40, Ciba, Basel, Switzerland) by a planetary ball mill for two hours at 300 rpm with steel balls and vials (Fritsch pulverisette 5, Fritsch GmbH, Germany) to form a suspension. As an organic binder, 2 wt% of polyvinyl acetate (PVA, Celanese, Dallas, USA) was added to the suspension by a high shear mixer. The suspension was spray dried by a spray dryer (Niro pilot, GEA Niro, Soeborg, Denmark). A rotary atomizer with high rotation speed was used in order to get the fine agglomerated powder. The agglomerated powder was sintered at 1050 °C in Ar + 3% H_2 to improve the strength of the powder without oxidizing Co. Isothermal step at 500 °C was used for two hours in order to pyrolyse the PVA without fracturing the spray dried agglomerates. The powder batch underwent a sieving process, selecting particles in the size range of $-36 + 11$ μm $(d_{90}-d_{10})$, to be suitable for the APS process.

The coatings were deposited by using the Sulzer Metco A3000S atmospheric plasma spray (APS) system with a 55 kW F4-MB (Sulzer Metco, Winterthur, Switzerland) plasma gun on the heated substrates. Optimization of the torch specific

spraying parameters [32] and the advantages of simultaneous heating, including the set-up of the heating system, is reported in Ref. [31]. Table 2 shows the detailed spraying parameters employed in the present study.

Area specific resistance (ASR) tests were utilized by using a four-point method (Fig. 1) for the coated samples at 700 °C in air for 1000 h. The ASR values were measured by using the corrugated and coated 0.2 mm Crofer 22 APU in contact with the flat and coated 1.0 mm Crofer 22 APU coupons. The top of corrugation ridges formed the actual contact area calculated as 1.25 cm^2. The samples were arranged as a stack and pressed together by a force of 49 N, whereby the estimated contact pressure was 0.40 MPa. Dey et al. have studied the influence of contact pressure for the contact resistance on the cathode-interconnect interface. The contact pressure of 0.064 MPa generated the lowest contact resistance. Higher contact pressure than 0.064 MPa had only marginal influence on the contact resistivity [38]. Therefore the pressure applied in this study, provided a good electrical contact between the samples. Direct current (DC), estimated as 640 mA/cm^2, was run through 1.0 mm platinum (Pt) leads point welded in 1.0 mm steel plates at the bottom and top of the test sample stack. The voltage difference was measured by two 0.5 mm Pt-leads, one welded on the flat and coated substrate, and the other on the corrugated and coated substrate. With this test arrangement, the voltage difference was measured over two coated and facing substrates. In order to obtain ASR values for the single coated sample the values were dived by two. In addition, uncoated 1.0 mm thick flat steel plates were used as separator disks between the stacked samples.

The ASR tests were accomplished without any contact paste, such as platinum or perovskite based pastes. It is well known that these pastes improve the electrical contact between the coatings and therefore decrease the ohmic resistance, but by eliminating the contact paste, it was confirmed that the results described only the deposited coatings.

The coating cross-section and powder morphology inspections were done by a field-emission scanning electron microscopy (FESEM, Carl Zeiss ULTRAplus, Oberkochen, Germany) attached with energy-dispersive X-ray spectroscopy (EDS, INCA Energy 350, Oxford Instruments, Oxfordshire, UK) employed for elemental analyses. The qualitative phase analyses of the coatings were done by using X-ray diffractometer (XRD, Empyrean, PANalytical B.V., ALMELO, Netherlands) with Cu-K$_\alpha$ radiation source and with Raman Spectroscopy. Raman spectra were measured with an Andor Shamrock 303 spectrograph and a Newton 940P cooled CCD-camera. The excitation laser was a 532 nm wavelength Cobolt Samba with a beam diameter of 0.7 mm.

Epoxy resin was used to mould coated samples in a chamber under reduced pressure to prevent the cracking and
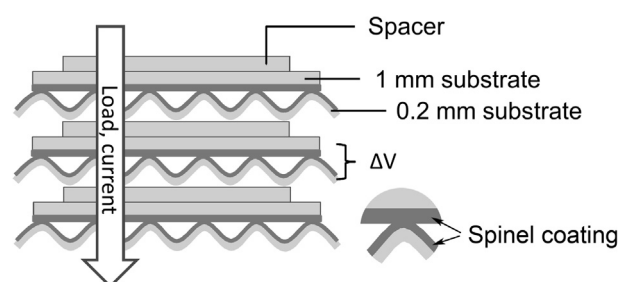

Fig. 1 – ASR measurement arrangement for coated samples. Light grey presents the Crofer 22 APU substrate and dark grey presents the as-sprayed coatings.

give support while grinding, and polishing the cross-section surfaces.

Results and discussion

Powders

The commercial fused and crushed MnCo$_2$O$_4$ spinel powder contained partially agglomerated and sintered particles as shown in Fig. 2(a). The relative amount of Mn and Co was 35:65 at-%, obtained by the EDS area analysis, which corresponds to the stoichiometric composition of MnCo$_2$O$_4$. The material synthesis was partially completed according to the qualitative XRD analysis shown in Fig. 3. The powder contained Mn$_{1.5}$Co$_{1.5}$O$_4$ and CoO phases, which should eventually form the cubic MnCo$_2$O$_4$ spinel structure.

The Mn$_2$CoO$_4$ + Co powder obtained by the spray-drying process exhibited an agglomerated morphology as shown in Fig. 2(b). Due to the spray-drying process, the number of non-agglomerated primary particles was significantly lower in comparison to the MnCo$_2$O$_4$ powder. The premise of using the spray-drying process is to improve the flowability properties of the powder. The relative amount of Mn and Co was 58:42 at-%. The powder contained MnO and Co phases as shown in Fig. 3. This dual phase structure was expected to form, due to heat-treating in a reducing atmosphere. Xianshuang et al. [39] have obtained the same phases when post heat-treating Mn$_{0.9}$Y$_{0.1}$Co$_2$O$_4$ spinel powder in H$_2$ atmosphere. The average Co particle size was 1.80 μm (standard deviation 0.49 μm) pointed with the white arrows in Fig. 2(b).

As-sprayed samples

Fig. 4 presents the polished cross-section surfaces of the APS sprayed coatings. The average coating thicknesses (40

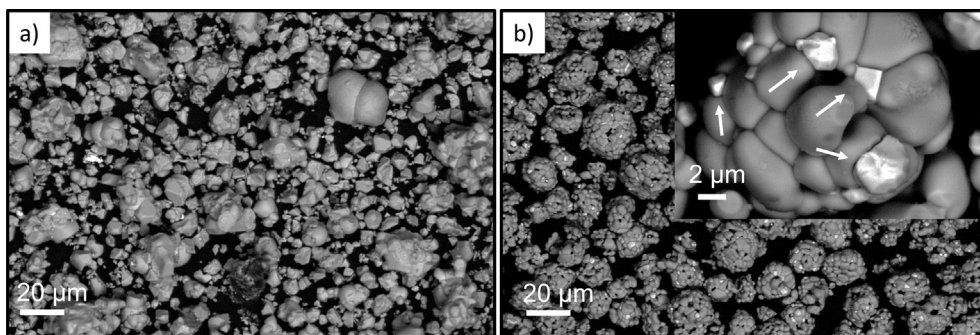| Table 2 – Atmospheric plasma spraying (APS) parameters.						
Powder/sample code	I (A)	P (kW)	Ar (slpm)	H$_2$ (slpm)	Spray distance (mm)	No. of spray layers
MnCo$_2$O$_4$	425	25	45	5	120	6
Mn$_2$CoO$_4$ + Co						
Anode diameter: 6 mm						
Simultaneous substrate heating temperature: 450 °C						

Fig. 2 – Morphology inspection of a) commercial MnCo$_2$O$_4$ powder and b) Mn$_2$CoO$_4$ + Co powder (white arrows indicate the Co phase). Backscattered electron FESEM-images.

measuring points) were 11.50 μm (sdv. 3.02 μm) and 18.70 μm (sdv. 3.85 μm) μm for the MnCo$_2$O$_4$ and Mn$_2$CoO$_4$ + Co coatings, respectively. Obtaining a thin coating with uniform thickness is usually a challenge in the APS process, due to the fairly thick lamellae/splat thickness caused by large agglomerate size. In this study, the powder particle size ranges were −33 + 6 μm (d$_{90}$–d$_{10}$) and −36 + 11 μm (d$_{90}$–d$_{10}$) for the MnCo$_2$O$_4$ and Mn$_2$CoO$_4$ + Co powders, respectively and the spinel powder, used in our previous study [31], with similar size range formed splats with the thickness of 1.40–1.50 μm. Therefore, desired coating thickness is achieved by a few tens of overlapping spray splats, which increased the possibility of uneven coating formation.

In general, the thermally sprayed coatings contain interlamellar cracks and pores [30], but by optimized spraying parameters, it is feasible to produce coatings for SOFC applications with adequate density as shown in Refs. [12,31,32,35]. The clear advantage is that, dense microstructure can be produced without the separate post heat-treatment processes and hence, the Cr-rich oxide layer is not formed as discussed in the introduction.

In order to achieve adequate density, spraying parameters should be optimized so that the on-flight particle temperature exceeds the melting point, but remains significantly under the boiling point of the materials, in order to avoid selective evaporation of the species with high vapour pressures. For the MnCo$_2$O$_4$, the optimal in-flight particle temperature should be at least 1700 °C, according to melting temperature of (Mn,Co)$_3$O$_4$ which varies from 1570 °C to 1760 °C (in air), in relation to the relative content of Mn and Co [40]. According to the EDS analysis, the elemental compositions of Mn and Co were 32:67 at-%, which was comparable with the powder feedstock. For the Mn$_2$CoO$_4$ + Co powder, melting temperature of Co is 1495 °C [41] and 1875 °C (in air) for MnO [42]. However, plasma changes the melting behaviour of the materials. This is probably caused by the selective evaporation of Mn during the spraying process, as the elemental composition was 51:49 in at-% for the as-sprayed coating. Lim et al. [43] also observed the selective evaporation of Mn when spraying La$_{0.8}$Sr$_{0.2}$MnO$_3$ powder.

The density of the as-sprayed coatings is enhanced by the simultaneous substrate heating. With the simultaneous substrate heating, the amount of inter-splat cracks and segmentation cracks can be reduced due to the controlled cooling rate of the deposited splats and the coating after the spraying process [31].

White arrows in Fig. 4 show good splat bonding was obtained by the substrate heating. In principle, this kind of inter-splat bonding should provide coatings with lower ohmic resistance. The cross-section analysis shows some randomly located closed pores and inter-splat cracks. These pores are a consequence of gas entrapment. Fig. 2(b) shows that the agglomerated spray particle is formed of partially sintered primary particles and therefore has a porous microstructure, as shown in cross-sectional studies reported in Ref. [32]. The porous structure can cause trapping of gas inside the particle, leading to formation of pores.

Metallic Co as a binder mixed with the Mn$_2$CoO$_4$ spinel particles enhanced the density even further. Also, the porous agglomerated morphology may contribute to the melting process from inside the agglomerate. This was verified in the cross-section images (Fig. 4(d and e)), as the amount of the cracks was decreased compared to the MnCo$_2$O$_4$ coating. It is most likely that the melted Co particles were evenly distributed in the gaps and oxidized or mixed with the Mn$_2$CoO$_4$ spinel phase as relatively low amounts of Co precipitations,
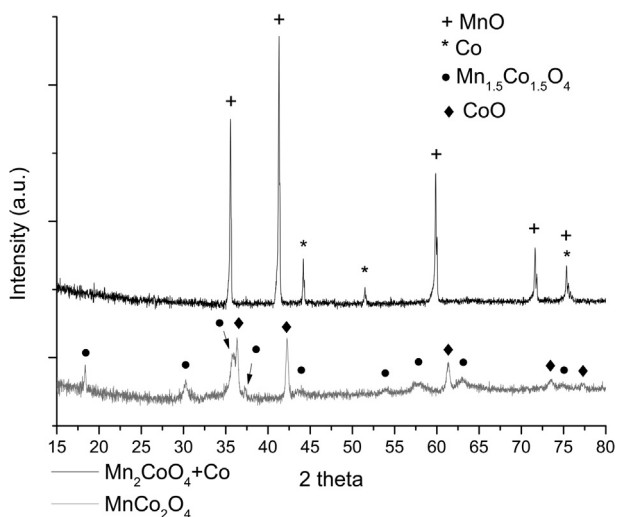

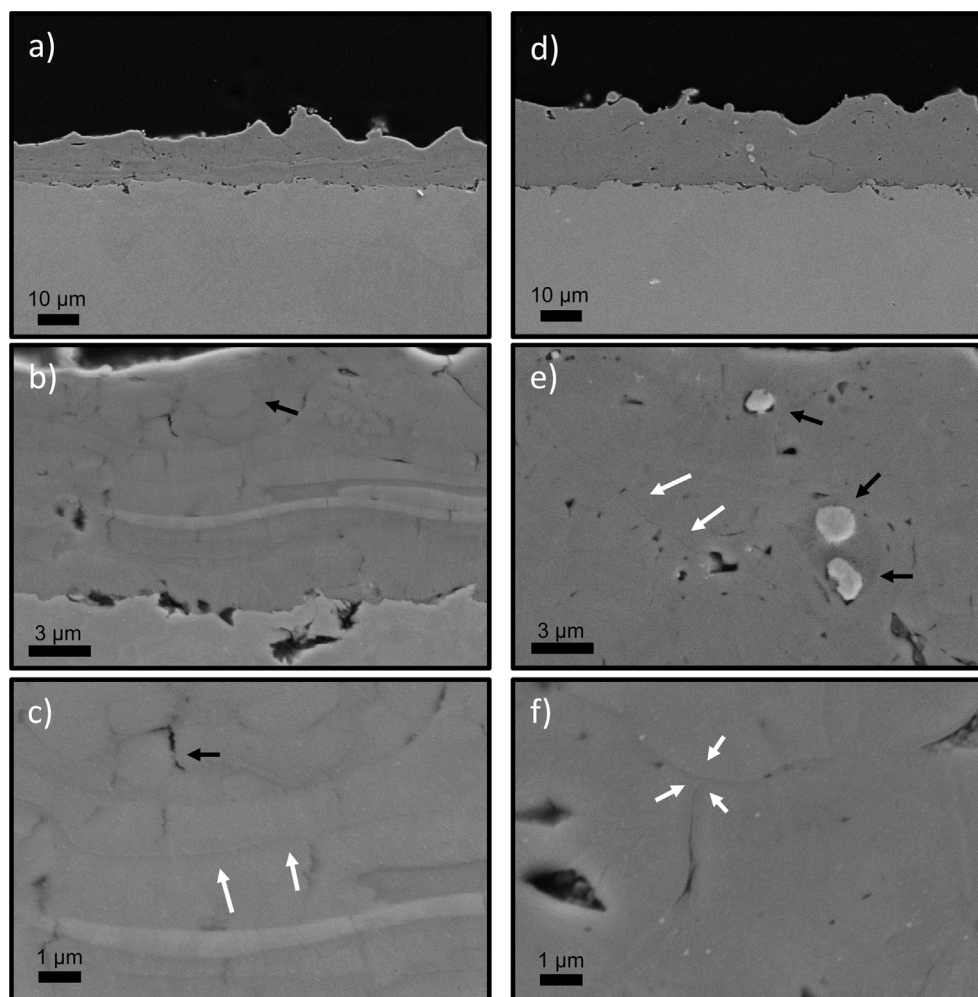**Fig. 3 – Crystallographic phase XRD analysis of the MnCo$_2$O$_4$ and Mn$_2$CoO$_4$ + Co powder feedstock.**

Fig. 4 – Cross-section images of the as-sprayed a–c) $MnCo_2O_4$ and d–f) Mn_2CoO_4 + Co coatings. Black arrow shows an un-molten $MnCo_2O_4$ particle in (b) and partially molten or un-molten Co particles in (e). White arrows shows well adhered splat boundaries in (c, e, f) FESEM (SE)-images.

pointed with black arrows in Fig. 4(e), which were observed in the cross-section studies.

As anticipated, the spinel decomposed during the deposition process and a simple cubic metal-oxide phase was formed as shown in Fig. 5. Such decomposition has been observed to occur only in thermally sprayed coatings [12,31–33], due to the rapid cooling of the spray splats [12,31]. This cubic structure is a metastable phase, but restorable to the original crystallographic spinel structure by a post heat-treatment procedure as reported e.g. in Refs. [12,35]. In some cases, the decomposition can be partially prevented by the simultaneous substrate heating as observed in our previous study reported in Ref. [31].

Oxidized (ASR tested) samples

Fig. 6 presents the cross-section images of the oxidized $MnCo_2O_4$ and Mn_2CoO_4 + Co coatings. The typical as-sprayed lamellae structure was not observed after the oxidation. The coatings contained submicron to micron sized isolated voids and the overall porosity was increased. The cross sectional
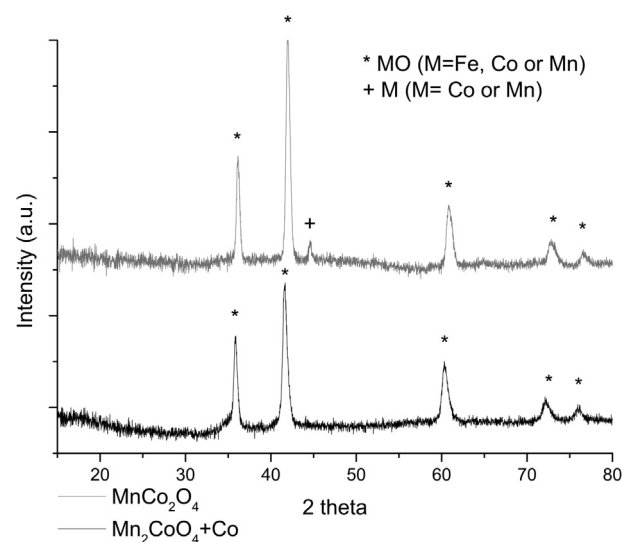

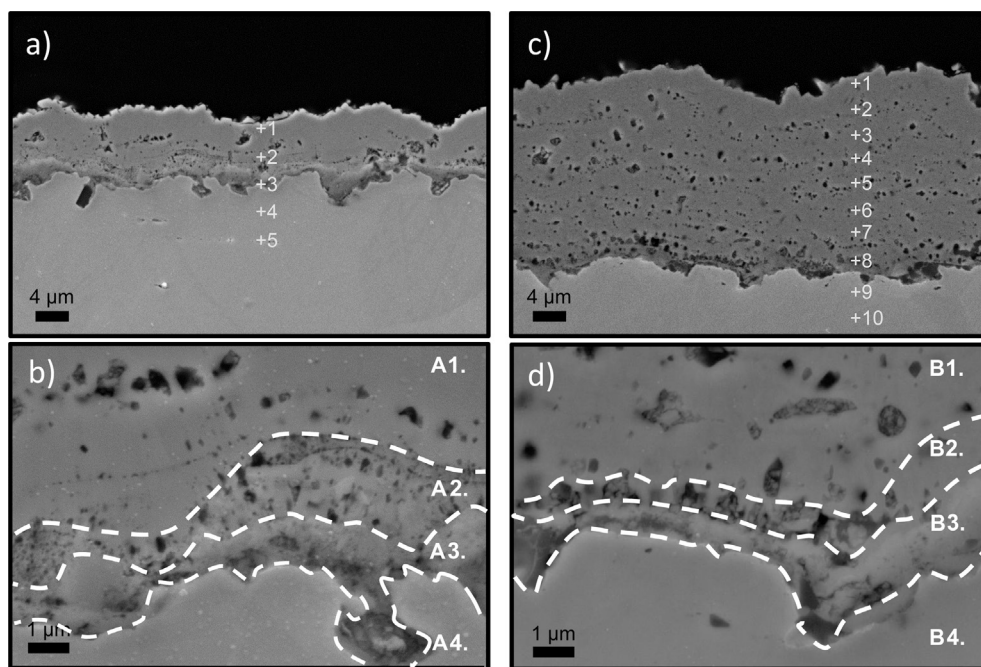**Fig. 5** – Crystallographic phase studies of the as-sprayed $MnCo_2O_4$ and Mn_2CoO_4 + Co coatings.

Fig. 6 — Cross sectional SE-images and EDS line analysis of the oxidized a & b) MnCo$_2$O$_4$ and c & d) Mn$_2$CoO$_4$ + Co coatings. The locations of the EDS point analysis are marked on the FESEM (SE)-images a) and c) and the results are presented in Table 3. The results obtained by the EDS area analysis from the cross-section images b) and d) are presented in Table 4.

studies do not show presence of open porosity. A similar kind of microstructure was observed in the oxidized (Mn,Co(Fe))$_3$O$_4$ coatings produced by the wet ceramic processes [10,19], magnetron sputtering [13] and HVOF spraying [12].

It is evident that, isolated voids are the consequence of a sintering process. In sintering, the surface energy of the particles/agglomerates (splats in thermal spraying) tends to decrease and the centres of the particles move close together through the necking, the surface and grain boundary diffusion. As a consequence, the inter-splat cracks form larger voids observed as void coarsening [29].

Sintering occurs if the temperature satisfies the material-specific requirements. The temperature depends on the particle sizes, intercrystallite/intra-agglomerate pore distribution, in addition to pore curvatures, which are related to the surface area, thus to the amount of the surface energy. For the micron-sized particles, the onset temperature for the sintering is 0.5–0.8 * T_m, where T_m is the melting temperature of material in the Kelvin scale. If nano-sized particles are involved, the onset temperature can be as low as 0.2–0.3 * T_m. In other words, the activation of the mass transport mechanisms for material transport to occur is related to the particle and crystallite sizes [29,44,45]. The oxidation temperature of 700 °C satisfies the sintering conditions the thermal sprayed coatings under the circumstances as i) the micron-sized splats and the nano-sized particles are present on the as-sprayed coatings [30], ii) the inter-lamellar gaps varies from 0.01 to 0.1 μm [46] and iii) mass transport mechanisms are most likely enhanced by the thermal and residual stresses together with metastable structures formed during the spraying process.

The phase stability was evaluated by using the XRD analyses and the results are shown in Fig. 7. The oxidized

MnCo$_2$O$_4$ coating (Fig. 7(a)) had a close correlation to the cubic MnCo$_2$O$_4$ spinel. The XRD pattern was slightly shifted to a lower Bragg angle due to the migration of Cr cations, and partial substitution of Mn or Co in the spinel lattice. The migration of the Cr cations was confirmed by the results obtained with EDS point analysis in Fig. 6 and presented in Table 3. Due to this Cr migration MnCrCoO$_4$ spinel phase is formed as Fang et al. [13] demonstrated in their study.

Fig. 7 shows both cubic and tetragonal MnCo$_2$O$_4$ and Mn$_2$CoO$_4$ phases for the oxidized Mn$_2$CoO$_4$ + Co coating. This dual phase structure is usually observed when the

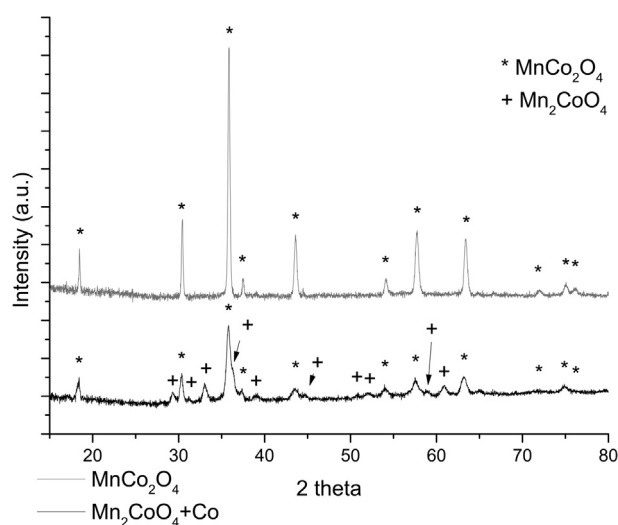**Fig. 7** — Crystallographic phase analysis of oxidized a) MnCo$_2$O$_4$ and Mn$_2$CoO$_4$ + Co spinel coatings.

Table 3 — EDS spectra and relative amount of Cr in the points indicated in Fig. 6. The result are in at-%.

Spectrum	O	Mn	Co	Fe	Cr	Cr/(Co + Mn + Fe)
$MnCo_2O_4$						
1	59.8	17.4	24.3	1.0	0.6	0.0
2	61.4	13.2	23.3	1.0	1.0	0.0
3	28.5	—	—	51.4	20.1	0.4
4	—	—	—	77.6	22.5	0.3
5	—	—	—	76.2	23.2	0.3
Mn_2CoO_4 + Co						
1	56.9	24.6	18.5	—	—	0.0
2	57.7	23.6	18.7	—	—	0.0
3	57.6	22.7	18.9	0.9	—	0.0
4	53.3	26.4	20.4	—	—	0.0
5	57.4	23.9	18.0	0.7	—	0.0
6	48.4	28.1	22.5	1.0	—	0.0
7	58.0	21.2	19.6	0.9	0.4	0.0
8	53.9	19.1	19.3	1.8	5.9	0.1
9	—	—	—	76.8	23.2	0.3
10	—	—	—	76.9	23.1	0.3

$Mn_{1.5}Co_{1.5}O_4$ spinels are oxidized as Yang et al. [11] confirmed. Tetragonal-cubic phase transformation occurs at 400 °C [13], when the stoichiometric factor x is between 0.3 and 0.9 in $Mn_{1+x}Co_{2-x}O_4$ [47]. Since cubic and tetragonal phases were observed and metallic Co, or Co-oxides were not, most of the Co-particles reacted with Mn_2CoO_4, as was intended.

Although, the high temperature corrosion of the substrates was not completely prevented, the use of the coating decreased the growth rate of the oxide scale. As observed, thin oxide scales with the thicknesses of 2.50 μm and 1.90 μm were formed when using the $MnCo_2O_4$ and Mn_2CoO_4 + Co coatings, respectively. The EDS analysis indicated that the oxide scale had a dual layer structure of Cr-rich oxide-layer and $MnCoCrO_4$ layer as shown in Fig. 6(b and d). Although the oxide scales were formed, noticeable spallation was not observed that would indicate coating failure.

The EDS area analysis showed that Cr_2O_3 layer (A3. in Table 4 and in Fig. 6(b)) and $MnCoCrO_4$ layer (A2. in Table 4 and in Fig. 6(b)) were formed on the substrate when $MnCo_2O_4$ was used as coating material, which is in line with the studies of Fang et al. [13] with a difference that the thickness of the oxide scale formed in this study was one fifth compared to the magnetron sputtered $MnCo_2O_4$ coating. Hence the APS coatings exhibit good tendency for to prevent further oxidation of the substrate. The same $MnCoCrO_4$ layer (B2. in Table 4 and in

Table 4 — EDS spectra and relative amount of elements in the areas indicated in Fig. 6. The result are in at-%.

Area	Cr	Mn	Fe	Co	O
$MnCo_2O_4$					
A1.	0.5	14.1	0.6	23.6	60.4
A2.	5.9	11.0	0.8	19.8	62.5
A3.	26.9	3.5	2.6	3.8	63.2
A4.	22.0	0.3	75.0	0.5	2.3
Mn_2CoO_4 + Co					
B1.	0.7	19.5	1.1	18.3	60.4
B2.	11.1	12.0	2.5	13.9	60.4
B3.	21.6	2.7	16.6	4.6	54.5
B4.	22.6	0.6	74.1	0.5	1.8

Fig. 6(d)) was formed when the Mn_2CoO_4 + Co coating was oxidized, but most likely on top of $(FeCr)_3O_4$ layer (B3. in Table 4 and in Fig. 6(d)) as EDS analysis suggests.

Since the coatings had dense microstructure according to the cross-section images, it can be expected that migration was the main transport phenomena for Cr species to penetrate the protective coatings. Therefore, the relative amount of migrated Cr was determined by using the EDS point analysis data and the results are presented in Table 3. This gives relatively good estimations of the Cr-barrier properties. As expected, the highest Cr ratio was obtained near the oxide scale. The relative amount of Cr decreased significantly in terms of coating thickness, but still some migrated Cr was observed in the surface part of the oxidized $MnCo_2O_4$ coating. Although the $MnCo_2O_4$ coating provided a fairly good barrier against the growth of the oxide scale it is plausible that the 10 μm thick $MnCo_2O_4$ coating is insufficient to provide the required protection against Cr-migration in long term use, particularly at higher temperatures, as observed by Persson et al. [14] oxidizing 10 μm thick $MnCo_2O_4$ coatings at 900 °C.

By using the Mn_2CoO_4 + Co powder and a thicker coating structure, the Cr transport was significantly inhibited. As shown in Table 3, Cr-species were not observed on the surface layer of the Mn_2CoO_4 + Co coating. Persson et al. have calculated the thermodynamic driving force i.e. Gibbs energy change (ΔG) between Cr_2O_3, Mn_3O_4 and CoO, when the total number of cations is 1.0, and they suggested that the energy change is more negative when Mn content is lower. In other words, reduction of Mn content increases the thermodynamic driving force for reactions between Cr_2O_3, Mn_3O_4 and CoO [14]. Under the circumstances, the Mn_2CoO_4 phase should be less reactive with Co rich inclusions and migrated Cr cations, than for example $MnCo_2O_4$ phase. If so, the Co rich inclusions would work as traps for the migrated Cr cations. This would partially explain the reason why the Mn_2CoO_4 + Co coating provides better protection against outwardly diffusing Cr cations, although the total stoichiometric quantity of Mn is higher in the Mn_2CoO_4 + Co coating compared to the $MnCo_2O_4$ coating.

In addition to the EDS and XRD studies, the Cr migration was studied by using Raman spectroscopy (Fig. 8(a)) The surfaces of both coatings showed relatively similar spectra with the main features at 586 and 679 cm^{-1} for oxidized $MnCo_2O_4$ and at 570 and 681 cm^{-1} for the oxidized Mn_2CoO_4 + Co coatings. The results do not indicate the presence of Cr_2O_3 compounds when compared to the peak positions reported in the literature [48]. If the Cr was migrated in the case of $MnCo_2O_4$ coating, as the EDS studies suggested, more stable Cr containing spinels i.e. $MnCoCrO_4$ were formed.

In order to analyse the composition of the oxide scale, the oxidized coatings were removed by grinding. The main features of the Raman spectra of the oxide scale correspond to the features of $MnCo_2O_4$ spinel [49], as shown in Fig. 8(b). This was caused by spinel that still remained on the analysis area despite of grinding. The peaks at 271, 327 and 534 cm^{-1}, observed between the $MnCo_2O_4$ coating and Crofer 22 APU (Fig. 8(c)), were identified as Cr_2O_3 [48]. The results confirm the formation of a Cr_2O_3 layer, also observed in the EDS analysis. In contrast to the $MnCo_2O_4$ coating, similar Cr_2O_3 peak pattern was not observed on the oxide scale formed between the oxidized Mn_2CoO_4 + Co coating and Crofer 22 APU.
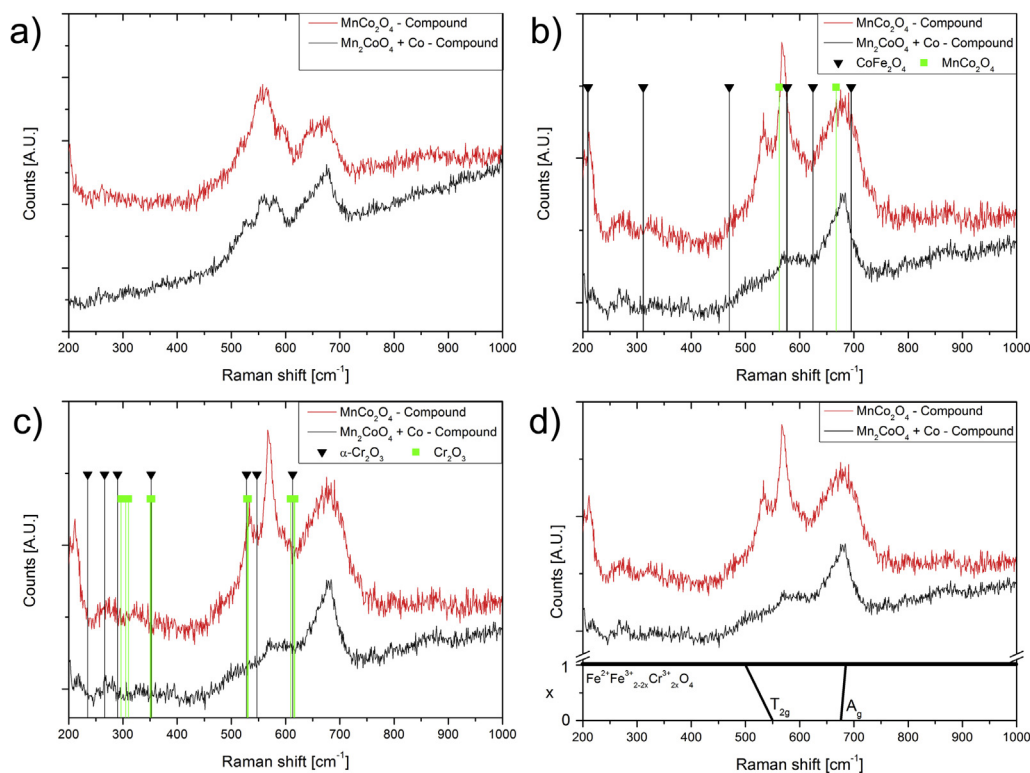
Fig. 8 — Raman spectra of the oxidized $MnCo_2O_4$ and Mn_2CoO_4 + Co coatings as a) surface, b and c) oxide scale analysis and d) Fe_3O_4–$FeCr_2O_4$ transition as shown in Ref. [50] plotted with oxide scale analysis.

The analysis (Fig. 8(d)) showed that the oxide scale formed beneath the Mn_2CoO_4 + Co had a broad shoulder peak at 500 cm^{-1}. According to Belo et al. it is most likely caused by a mixture of the Fe_3O_{4-} and $FeCr_2O_4$ phases. For Fe_3O_{4-} the peak positions are at 549 and 681 cm^{-1}, but the reaction with Cr causes the peaks to transition to 500 and 691 cm^{-1}, respectively [50]. The EDS analysis also supports the existence of the $FeCr_2O_4$ layer. The $FeCr_2O_4$ has lower vapour pressure than Cr_2O_3 which is more favourable in the SOFC operation conditions according to [51].

The ASR results of the oxidized $MnCo_2O_4$ and Mn_2CoO_4 + Co coatings on Crofer 22 APU are presented in Fig. 9. The ASR values decrease notably until 19.10 $m\Omega$ cm^2 and 9.50 $m\Omega$ cm^2 values were obtained for the $MnCo_2O_4$ and Mn_2CoO_4 + Co coatings, respectively. The most reasonable explanation for the rapid drop was an increase in the actual contact area due to the creep of the corrugated substrate, in addition to sintering and restoration of the spinel structure.

After the contact areas were deformed and the microstructure and phase compositions reached their equilibrium, the ASR values decreased linearly as the function of time, until 18.50 $m\Omega$ cm^2 and 8.40 $m\Omega$ cm^2 for $MnCo_2O_4$ and Mn_2CoO_4 + Co coatings, respectively, were reached at the end of the 1000 h test cycle. This decrease of the ASR values is an indication that sintering continued and the number of contact points increased during the test after the initial drop.

The Mn_2CoO_4 + Co coating seemed to perform better on the ASR tests compared to the coatings made of $MnCo_2O_4$, despite the twofold-coating thickness. Yang et al. [11] have studied and reviewed similar performances for $Mn_{1.5}Co_{1.5}O_4$ and

$MnCo_2O_4$ bulk samples obtaining the conductivity values of ~40—60 S/cm and ~15—25 S/cm, respectively, in relation to temperature from 700 to 800 °C in air. Wang et al. [52] have measured ~68 S/cm value for the $Mn_{1.5}Co_{1.5}O_4$ spinels at 800 °C in air.

The electrical properties of the bulk materials do not fully explain the differences in the ASR values, especially when the Mn_2CoO_4 + Co coating was twice as thick compared to the $MnCo_2O_4$ coating. The following reasonable explanations for the differences in the ASR values are i) higher Cr substitution in the $MnCo_2O_4$ spinel lattice and ii) the dense microstructure of the Mn_2CoO_4 + Co coating. As stated above, the Cr migration was observed by the XRD and the EDS analysis. Fergus et al. have reported that the Cr substitution in $(Mn,Co)_3O_4$
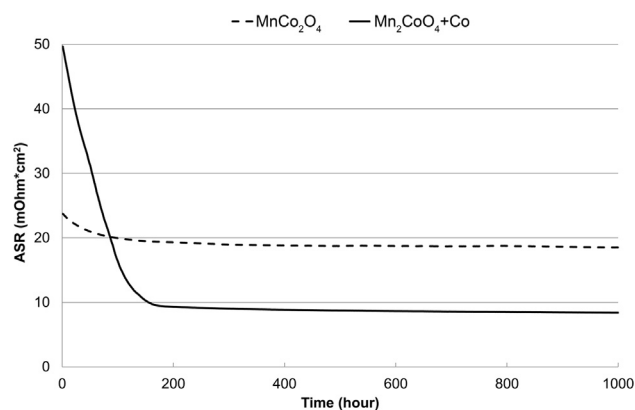

Fig. 9 — Area specific resistance (ASR) for coated samples.

spinel lattice decreases the electrical conductivity in relation to Cr content. The conductivity values of the spinel vary from 0.003 S/cm (Mn,Co:Cr = 1:2) to 1.30 S/cm (Mn,Co:Cr = 2:1) at 700 °C in air [53], which is notably lower compared to the conductivity of the pure $MnCo_2O_4$ spinel as reported previously. In addition, the cross section studies showed that the Mn_2CoO_4 + Co coating obtained superior intersplat bonding, which enhanced the electronic conduction compared to the $MnCo_2O_4$ coating.

Although the oxide scales were in the same range in thickness, it should be considered that Cr based spinel compounds tend to have notably lower conductivity than $(Mn,Co)_3O_4$ spinels. Therefore, the good barrier against the oxidation IC steel should prevent the increase of ohmic resistances. The electrical conductivity of Cr_2O_3 is from 0.006 to 0.163 S/cm at 700 °C in air [53]. If the $(Mn,Cr)_3O_4$ reaction layer is formed, the conductivity is 0.001 S/cm (Mn:Cr = 1:2) to 0.031 S/cm (Mn:Cr = 1:1), at 700 °C in air [9].

Although the ASR tests were performed without conductive pastes, the ASR values of the APS coated spinel coatings were at the same range compared to the other studies available and reviewed in Table 1. It should be taken into account that, the ASR test arrangements vary between the reviewed studies, and therefore comparison can be only indicative. In general, the dense microstructure decreases the ohmic resistance. This was confirmed with the rather low ASR values obtained for the coating manufactured with thin film techniques, HVOF process and result obtained in this study. In addition, dense microstructure decreases the growth rate of the oxide scales providing lower total ohmic resistance for [spinel coating] − [(spinel-type reaction layer) − (Cr-rich oxide layer)] − [substrate] systems as shown in this study.

Conclusions

Atmospheric plasma spraying was used to manufacture protective $MnCo_2O_4$ and Mn_2CoO_4 + Co (equivalent to $Mn_{1.5}Co_{1.5}O_4$) coatings on Crofer 22 APU and to study high temperature corrosion, Cr-barrier and ASR properties of the substrate-coating system. The as-sprayed coatings were tested at 700 °C in air for 1000 h by using the four-point measurement method.

The $Mn_{1.5}Co_{1.5}O_4$ spinel formula was obtained by spraying cermet based Mn_2CoO_4 powder, mixed with finely dispersed metallic Co particles. The powder was heat-treated in a reducing atmosphere prior to the spraying process. The powder formed both $[Mn_{1+\delta}Co_{2-\delta}O_4]_{cubic}$ and $[Mn_{2-\delta}Co_{1-\delta}O_4]_{tetragonal}$ phases during the high temperature oxidation cycle. The Co alloying has the purpose of decreasing the porosity of the coatings by filling the pores and the inter-splat cracks/gaps between the deposited splats. The benefit of the Co alloying was confirmed, and the density of the as-sprayed coatings was improved. It should be highlighted that coatings with dense microstructures were obtained without post heat-treatments, and so the unwanted Cr-rich oxide scales were not formed during the manufacturing phase.

The amount of the porosity increased during the high temperature oxidation cycle. The cross-sectional analysis showed that the porosity consistent of un-connected voids. In addition, the Cr rich oxide scale was formed between the Crofer 22 APU substrates and the spinel coatings. The coating material defined the oxide scale composition, which was a dual layer structure of Cr_2O_3 or $FeCr_2O_4$ and $MnCoCrO_4$ layers. The EDS point analysis and crystallographic phase analysis revealed that a small amount of Cr migrated into the $MnCo_2O_4$ spinel lattices. Furthermore, the EDS analysis revealed Cr-migration through the $MnCo_2O_4$ coating. The results demonstrated that the 10 μm thick $MnCo_2O_4$ coating can decrease the oxidation rate of the substrate, but is inadequate to provide good Cr-barrier properties against Cr-migration. The same test showed that the Mn_2CoO_4 + Co coatings offered superior Cr-barrier properties and decreased the oxidation rate of the substrate.

The ASR values decreased for the first few hundred hours, due to creep of the corrugated substrate, recovery of the spinel structure and sintering of the microstructure. The ASR values levelled off to 8.40 mΩ cm² and 18.50 mΩ cm² for Mn_2CoO_4 + Co and $MnCo_2O_4$ coatings, respectively after 1000 h oxidation cycle. The superiority of the Mn_2CoO_4 + Co coating can be explained by i) better electrical conductivity of $Mn_{1.5}Co_{1.5}O_4$ compared to $MnCo_2O_4$ ii) decreased migration of Cr cations into the spinel lattice and iii) better oxidation barrier, and therefore decreased oxide scale growth rate.

According to the results, atmospheric plasma spraying, in addition to the HVOF spraying, is a promising technique to produce dense coatings that provide good protection against volatile Cr-species. The use of cermet-based powders (mixture of metallic and ceramic phases) shows a clear advantage, when the aim is to decrease the amount and the size of the inter-splat cracks. Some well-known disadvantages must be taken into account when using thermal spraying to produce protective coatings, which are: i) the substrates must be grit-blasted prior to the spray process which may cause e.g. bending of the substrate ii) decomposition of spinel structure, which is however restorable.

Acknowledgements

REFERENCES

[1] Wu J, Liu X. Recent development of SOFC metallic interconnect. J Mater Sci Technol 2010;26:293–305.

[2] Kurokawa H, Jacobson CP, DeJonghe LC, Visco SJ. Chromium vaporization of bare and of coated iron−chromium alloys at 1073 K. Solid State Ionics 2007;178:287–96.

[3] Chen F, Sun E, Yamanis J, Hawkes J, Smeggil J, Warrier S, et al. Cr poisoning effect for solid oxide fuel cells. 2006 Conf. Exhib Mater Sci Technol 2006:303–11.

[4] Kim JY, Canfield NL, Chick LA, Menhardt KD, Sprenkle VL. Chromium poisoning effect on various cathodes. Ceram Eng Sci Proc 2005:129–38.

[5] Fergus J. Effect of cathode and electrolyte transport properties on chromium poisoning in solid oxide fuel cells. Int J Hydrogen Energy 2007;32:3664–71.

[6] Zhu WZ, Deevi SC. Opportunity of metallic interconnects for solid oxide fuel cells: a status on contact resistance. Mater Res Bull 2003;38:957–72.

[7] Zhu WZ, Deevi SC. Development of interconnect materials for solid oxide fuel cells. Mater Sci Eng A 2003;348:227–43.

[8] Yngve L, Truls N. Spinel and perovskite functional layer between plansee metallic interconnect (Cr-5 wt% Fe-1 wt% Y_2O_3) and ceramic $(La_{0.85}Sr_{0.15})_{0.91}MnO_3$ cathode materials for solid oxide fuel cells. J Electrochem Soc 2000;147:3251–6.

[9] Chen X, Hou P, Jacobson C, Visco S, Dejonghe L. Protective coating on stainless steel interconnect for SOFCs: oxidation kinetics and electrical properties. Solid State Ionics 2005;176:425–33.

[10] Yang Z, Xia G-G, Maupin GD, Stevenson JW. Conductive protection layers on oxidation resistant alloys for SOFC interconnect applications. Surf Coat Technol 2006;201:4476–83.

[11] Yang Z, Xia G-G, Li X-H, Stevenson JW. $(Mn,Co)_3O_4$ spinel coatings on ferritic stainless steels for SOFC interconnect applications. Int J Hydrogen Energy 2007;32:3648–54.

[12] Thomann O, Pihlatie M, Rautanen M, Himanen O, Lagerbom J, Mäkinen M, et al. Development and application of HVOF sprayed spinel protective coating for SOFC interconnects. J Therm Spray Technol 2013;22:631–9.

[13] Fang Y, Wu C, Duan X, Wang S, Chen Y. High-temperature oxidation process analysis of $MnCo_2O_4$ coating on Fe–21Cr alloy. Int J Hydrogen Energy 2011;36:2–7.

[14] Persson ÅH, Mikkelsen L, Hendriksen PV, Somers MAJ. Interaction mechanisms between slurry coatings and solid oxide fuel cell interconnect alloys during high temperature oxidation. J Alloys Compd 2012;521:16–29.

[15] Zhenguo Y, Xia G, Stevenson JW. $Mn_{1.5}Co_{1.5}O_4$ spinel layers on ferritic stainless steels for SOFC interconnect applications. Electrochem Solid-State Lett 2005;8:1–3.

[16] Gavrilov NV, Ivanov VV, Kamenetskikh AS, Nikonov AV. Investigations of Mn–Co–O and Mn–Co–Y–O coatings deposited by the magnetron sputtering on ferritic stainless steels. Surf Coat Technol 2011;206:1252–8.

[17] Garcia-Vargas MJ, Zahid M, Tietz F, Aslanides A. Use of SOFC metallic interconnect coated with spinel protective layers using the APS technology. ECS Trans 2007;7:2399–405.

[18] Ebrahimifar H, Zandrahimi M. Oxidation and electrical behavior of AISI 430 coated with cobalt spinels for SOFC interconnect applications. Surf Coat Technol 2011;206:75–81.

[19] Montero X, Tietz F, Sebold D, Buchkremer H, Ringuede A, Cassir M, et al. $MnCo_{1.9}Fe_{0.1}O_4$ spinel protection layer on commercial ferritic steels for interconnect applications in solid oxide fuel cells. J Power Sources 2008;184:172–9.

[20] Chen L, Magdefrau N, Sun E, Yamanis J, Frame D, Burila C. Strontium transport and conductivity of $Mn_{1.5}Co_{1.5}O_4$ coated Haynes 230 and Crofer 22 APU under simulated solid oxide fuel cell condition. Solid State Ionics 2011;204–205:111–9.

[21] Uehara T, Yasuda N, Okamoto M, Baba Y. Effect of Mn–Co spinel coating for Fe–Cr ferritic alloys ZMG232L and 232J3 for solid oxide fuel cell interconnects on oxidation behavior and Cr-evaporation. J Power Sources 2010;196:7251–6.

[22] Yang Z, Xia G, Singh P, Stevenson JW. Electrical contacts between cathodes and metallic interconnects in solid oxide fuel cells. J Power Sources 2005;155:246–52.

[23] Choi JP, Scott Weil K, Matt Chou Y, Stevenson JW, Gary Yang Z. Development of MnCoO coating with new

aluminizing process for planar SOFC stacks. Int J Hydrogen Energy 2010;36:4549–56.

[24] Zhang H, Zhan Z, Liu X. Electrophoretic deposition of $(Mn,Co)_3O_4$ spinel coating for solid oxide fuel cell interconnects. J Power Sources 2011;196:8041–7.

[25] Yoo J, Woo S-K, Yu JH, Lee S, Park GW. $La_{0.8}Sr_{0.2}MnO_3$ and $(Mn_{1.5}Co_{1.5})O_4$ double layer coated by electrophoretic deposition on Crofer22 APU for SOEC interconnect applications. Int J Hydrogen Energy 2009;34:1542–7.

[26] Abdoli H, Alizadeh P. Electrophoretic deposition of $(Mn,Co)_3O_4$ spinel nano powder on SOFC metallic interconnects. Mater Lett 2012;80:53–5.

[27] Hoyt KO, Gannon PE, White P, Tortop R, Ellingwood BJ, Khoshuei H. Oxidation behavior of $(Co,Mn)_3O_4$ coatings on preoxidized stainless steel for solid oxide fuel cell interconnects. Int J Hydrogen Energy 2012;37:518–29.

[28] Mardare C, Asteman H, Spiegel M, Savan A, Ludwig A. Investigation of thermally oxidised Mn–Co thin films for application in SOFC metallic interconnects. Appl Surf Sci 2008;255:1850–9.

[29] Barsoum M. Fundamentals of ceramics. McGraw-Hill Companies, Inc; 1997 [Chapter 10: Sintering and grain growth].

[30] Pawlowski L. The science and engineering of thermal spray coatings. 2nd ed. Chichester: John Wiley & Sons; 1995 [Chapter 6: Coating build-up].

[31] Puranen J, Lagerbom J, Hyvärinen L, Mäntylä T, Levänen E, Kylmälahti M, et al. Formation and structure of plasma sprayed manganese-cobalt spinel coatings on preheated metallic interconnector plates. Surf Coat Technol 2010;205:1029–33.

[32] Puranen J, Lagerbom J, Hyvärinen L, Kylmälahti M, Himanen O, Pihlatie M, et al. The structure and properties of plasma sprayed iron oxide doped manganese cobalt oxide spinel coatings for SOFC metallic interconnectors. J Therm Spray Technol 2010;20:154–9.

[33] Saoutieff E, Bertrand G, Zahid M, Gautier L. APS deposition of $MncCo_2O_4$ on commercial alloys K41X used as solid oxide fuel cell interconnect: the importance of post heat-treatment for densification of the protective layer. ECS Trans 2009;25:1397–402.

[34] Vaßen R, Kaßner H, Stuke a, Hauler F, Hathiramani D, Stöver D. Advanced thermal spray technologies for applications in energy systems. Surf Coat Technol 2008;202:4432–7.

[35] Puranen J, Laakso J, Kylmälahti M, Vuoristo P. characterization of high-velocity solution precursor flame-sprayed manganese cobalt oxide spinel coatings for metallic sofc interconnectors. J Therm Spray Technol 2013;22:622–30.

[36] Bunshah R. Handbook of hard coatings. 1st ed. William Andrew; 2000.

[37] Park SD, Kumar S, Lee SC, Lee C. Effects of silver addition on mechanical properties of plasma sprayed SOFC interconnect layer. In: Lugscheider E, editor. Int. Therm. Spray Conf. Maastricht: DVS; 2008. p. 1035–8.

[38] Dey T, Singdeo D, Bose M, Basu RN, Ghosh PC. Study of contact resistance at the electrode–interconnect interfaces in planar type Solid Oxide Fuel Cells. J Power Sources 2013;233:290–8.

[39] Xin X, Wang S, Qian J, Lin C, Zhan Z, Wen T. Development of the spinel powder reduction technique for solid oxide fuel cell interconnect coating. Int J Hydrogen Energy 2012;37:471–6.

[40] Aukrust E, Muan A. Phase relations in the system cobalt oxide – manganese oxide in air. J Am Ceram Soc 1963;46:511.

[41] Cengel YA. Heat and mass transfer, a practical approach. 3rd ed. The McGraw-Hill Companies; 2007.

[42] FactSage 6.4; 20.3.2014. http://www.factsage.com/.

[43] Lim DP, Lim DS, Oh JS, Lyo IW. Influence of post-treatments on the contact resistance of plasma-sprayed LaSrMnO coating on SOFC metallic interconnector. Surf Coat Technol 2005;200:1248—51.

[44] Lu K. Nanoparticulate materials: synthesis, characterization, and processing. John Wiley & Sons; 2012 [Chapter 6: Sintering].

[45] Mayo MJ. Processing of nanocrystalline ceramics from ultrafine particles. Int Mater Rev 1996;41:85—115.

[46] McPherson R, Shafer BV. Interlamellar contact within plasma-sprayed coatings. Thin Solid Films 1982;97:201—4.

[47] Naka S, Inagaki M, Tanaka T. On the formation of solid solution in $Co_{3-x}Mn_xO_4$ system. J Mater Sci 1972;7:441—4.

[48] Hosterman BD. Raman spectroscopic study of solid solution spinel oxides [Dissertation]; 2011.

[49] Padmanathan N, Selladurai S. Mesoporous $MnCo_2O_4$ spinel oxide nanostructure synthesized by solvothermal technique for supercapacitor. Ionics 2013;20(4):79—87.

[50] Belo MDAC, Walls M, Hakiki NE, Corset J, Picquenard E, Sagonb G, et al. composition, structure and properties of the oxide films formed on the stainless steel 316l in a primary type PWR environment. Corros Sci 1998;40:447—63.

[51] Yang G, Simner S, Stevenson J, Singh P. SOFC IC Overview and CTP status. In: SECA CTP IC Meet; 2004. p. 1—57.. In: http://www.netl.doe.gov/publications/proceedings/04/seca-sofc/IC%20PNNL%20Singh.pdf [20.3.2014].

[52] Wang K, Liu Y, Fergus JW. Interactions between sofc interconnect coating materials and chromia. J Am Ceram Soc 2011;94:4490—5.

[53] Fergus JW, Wang K, Liu Y. Transition metal spinel oxide coatings for reducing chromium poisoning in SOFCs 2011;33:77—84.

Publication V

Characterization of High-Velocity Solution Precursor Flame-Sprayed Manganese Cobalt Oxide Spinel Coatings for Metallic SOFC Interconnectors

by

J. Puranen, J. Laakso, M. Kylmälahti, and P. Vuoristo

Journal of Thermal Spray Technology, 22, 5(2013), pp. 622–630

Characterization of High-Velocity Solution Precursor Flame-Sprayed Manganese Cobalt Oxide Spinel Coatings for Metallic SOFC Interconnectors

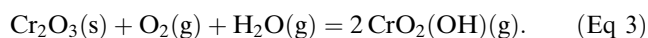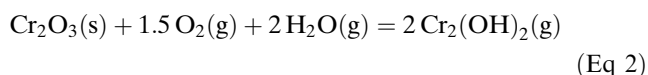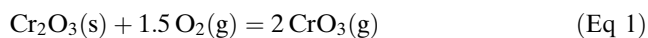### Jouni Puranen, Jarmo Laakso, Mikko Kylmälahti, and Petri Vuoristo

(Submitted October 15, 2012; in revised form February 13, 2013)

A modified high-velocity oxy-fuel spray (HVOF) thermal spray torch equipped with liquid feeding hardware was used to spray manganese-cobalt solutions on ferritic stainless steel grade Crofer 22 APU substrates. The HVOF torch was modified in such a way that the solution could be fed axially into the combustion chamber through 250- and 300-μm-diameter liquid injector nozzles. The solution used in this study was prepared by diluting nitrates of manganese and cobalt, i.e., $Mn(NO_3)_2 \cdot 4H_2O$ and $Co(NO_3)_2 \cdot 6H_2O$, respectively, in deionized water. The as-sprayed coatings were characterized by X-ray diffraction and field-emission scanning electron microscopy operating in secondary electron mode. Chemical analyses were performed on an energy dispersive spectrometer. Coatings with remarkable density could be prepared by the novel high-velocity solution precursor flame spray (HVSPFS) process. Due to finely sized droplet formation in the HVSPFS process and the use of as delivered Crofer 22 APU substrate material having very low substrate roughness ($R_a < 0.5$ μm), thin and homogeneous coatings, with thicknesses lower than 10 μm could be prepared. The coatings were found to have a crystalline structure equivalent to $MnCo_2O_4$ spinel with addition of Co-oxide phases. Crystallographic structure was restored back to single-phase spinel structure by heat treatment.

Keywords	HVOF, nanostructured materials, solid oxide fuel cells (SOFCs), solution

1. Introduction

The interconnectors in solid oxide fuel cells (SOFCs) are typically manufactured using ferritic stainless steels, including grades specifically developed for SOFC applications (Ref 1-3). At high operating temperatures, a Cr_2O_3 scale is known to form on the surface of the steel material in the oxidizing atmosphere of the cathode side. The Cr_2O_3 scale may then react with O_2 and H_2O molecules to form thin layers of CrO_3 and $Cr_2(OH)_2$ compounds as described in Eq 1-3.

$$Cr_2O_3(s) + 1.5\,O_2(g) = 2\,CrO_3(g) \qquad (Eq\ 1)$$

$$Cr_2O_3(s) + 1.5\,O_2(g) + 2\,H_2O(g) = 2\,Cr_2(OH)_2(g)$$
$$(Eq\ 2)$$

Jouni Puranen, Jarmo Laakso, Mikko Kylmälahti, and **Petri Vuoristo**, Department of Materials Science, Tampere University of Technology, Tampere, Finland. Contact e-mail: jouni.puranen@tut.fi.

$$Cr_2O_3(s) + O_2(g) + H_2O(g) = 2\,CrO_2(OH)(g). \qquad (Eq\ 3)$$

The vapor partial pressures of Cr-species increase as the temperature is increased, wherein $Cr_2(OH)_2(g)$ shows the largest vapor pressure at SOFC operating temperatures (600-800 °C). In addition, the vapor pressure of water tends to increase the volatility of $Cr_2(OH)_2(g)$ even further (Ref 3-5). These volatile chromium compounds migrate through the gas phase to the triple phase boundary (TPB) sites in the cathode layer. The TPB is the shared interface of the cathode, the electrolyte, and oxidant gas. Equations 1-3 are reversible, and on the TPB of these Cr-species are electrically reduced back to Cr_2O_3. Reduced Cr_2O_3 causes degradation by decreasing the total size of the effective area of the TPB sites (Ref 5, 6).

It is known that by using protective ceramic coatings on ferritic stainless steel interconnectors, the harmful degradation by Cr-poisoning can be decreased. Zhu et al. have listed (Ref 7) and reviewed (Ref 3) the basic criteria for SOFC interconnects (ICs) which can be treated as requirements for the protective coatings as being part of IC construction:

- low diffusion coefficient of Cr-ions and low transport of Cr-compounds;
- excellent electrical conductivity with the objective of 100 % electronic conduction;
- good chemical, microstructural and phase stabilities at the stack operating temperature in an oxidizing environment;

- coefficient of thermal expansion (CTE) to match with the other stack components such as the metallic interconnector and the cathode;
- good thermal conductivity, least 5 W/m per K, to transfer heat, generated at the cathode, to the anode for endothermic fuel reformation reactions,
- coatings together with the metallic substrate should have high-temperature strength, creep, and spallation resistance, and provide structural support when used as a stationary or an auxiliary power unit under external stresses and vibrations;
- easy and economic manufacturing process in mass production.

Yngve et al. have tested the effectiveness of various spinel- and perovskite-structured materials as protective coatings. Especially, $(Mn,Co)_3O_4$ provided excellent electrical properties (low ASR values) and low Cr cathode degradation (low Cr transport) in long-term (10 000 h) aging tests (Ref 8). In addition, $(Mn,Co)_3O_4$ spinels exhibited good linearity in CTE with temperature and a good CTE matching with other cell components such as ferritic stainless steels interconnects and various cathode materials, as shown in (Ref 1, 9). Several successful studies have reported that the required coating structures are obtained by means of conventional thermal spray techniques (Ref 10-12). Although fairly dense coatings can be obtained by thermal spraying, the $(Mn,Co)_3O_4$ crystal structure is not fully retained, as part of the coating material decomposes into the CoO phase (Ref 10, 12, 13). However, the original crystal structure can be restored by performing heat treatment, as reported elsewhere (Ref 10, 12).

When conventional thermal spray processes are used to prepare coatings, relatively long material and powder manufacturing process chains are required to have the feedstock material ready for spraying. Also, the type of raw materials determine which synthesis route (solid- or liquid-state) must be used. If an agglomerated spray powder is manufactured by solid-state synthesis (SSS), then the number of process steps is easily up to six as implemented in our previous study (Ref 11, 12). For liquid-state synthesis (LSS), the number of the process steps can be up to nine when spray drying is carried out after material synthesis as described in our previous study (Ref 14). However, novel spray processes, such as suspension thermal spray techniques, will decrease the number of process steps down to five or eight, depending on which type of raw materials are to be used, since spray drying is no longer needed (Ref 11, 12, 14). A more descriptive listing of process steps is presented in Fig. 1.

In addition to conventional and suspension thermal spray techniques, new process methods such as solution precursor thermal spray processes have been recently studied. In solution precursor thermal spray processes, the coatings are manufactured using atmospheric plasma spray (APS) or high-velocity oxy-fuel spray (HVOF) systems. The clear advantage in solution precursor thermal spray techniques is that the number of processing steps can be decreased to as low as two, to obtain as-sprayed coatings.

The main difference in this technique compared with conventional dry powder-spraying processes is that separate material synthesis and powder-preparation phases are no longer needed, as shown in Fig. 1.

Due to shear stress caused by the flowing gas, finely sized droplets are formed as the solution is injected into the thermal flame. The heat energy of the thermal flame is transferred into the droplets. Small droplet size and transferred heat energy enables (i) the evaporation of solvent, (ii) precipitation and pyrolysis metallic salts, and (iii) melting of synthesized material to occur in a short period of time. If these process steps are fully accomplished, then eventually the same material syntheses process steps are achieved as in the conventional powder manufacturing and spraying process. Therefore, fewer process steps are required in the solution precursor thermal spray process than in the conventional dry powder method to achieve the as-sprayed coatings (Ref 15, 16).

Studies of solution precursor thermal spraying have mainly been conducted in connection with solution precursor plasma-spraying processes (SPPS). For example, porous yttria-stabilized-zirconia (YSZ) TBC layers (Ref 17-22), dense (Ref 23)/porous (Ref 24) layers for SOFCs, and coatings with photocatalytic activity (Ref 25) have been manufactured by the SPPS process. In addition to the SPPS process, Chen et al. (Ref 26) have studied high-velocity solution precursor flame spray (HVSPFS) processes to manufacture Al_2O_3-ZrO_2 coatings.

In our previous studies (Ref 27, 28), the SPPS technique was used to prepare thin $(Mn,Co)_3O_4$ coatings. The results from the crystallographic studies were found to be promising, because the $MnCo_2O_4$ spinel phase structure was observed already in the as-sprayed coatings. The amount of the $MnCo_2O_4$ phase was the highest when water was used as a solvent. The mixture of deionized water and ethanol was found to increase the formation of the CoO phase. However, the cross-sectional SEM studies showed that the density of the as-sprayed coatings was not at an acceptable level; the coatings were found to contain a large amount of connected porosity (Ref 28). Clearly, coatings with connected open porosity would not prevent Cr-transport to the TPB by chromium-containing gas species (CrO_3 and $Cr_2(OH)_2$). Thus, the coatings should be as dense as possible in addition to the other previously listed properties.

A study by Chen et al. (Ref 26) clearly shows that dense coatings can be spayed using the HVSPFS technique with an axial liquid feeding. Therefore, the HVSPFS (or S-HVOF) technique was chosen for use in this present study to spray coatings from a $MnCo_2O_4$-forming liquid. In the HVSPFS process, the precursor was axially injected directly into the combustion chamber of the HVOF gun. Several spaying parameters were used to study the coating formation and to define optimal spray parameters.

2. Experimental Techniques

The solution used in this present study was prepared by dissolving stoichiometric weights of manganese and cobalt

	Diluting	Mixing/milling	Calcination	Milling	Calcination	Milling	Silting	Spray drying	Spray process
Conventional TS Powder: SSS or (LSS)	(1)	1(2)	2(3)	(4)	(5)	3(6)	4(7)	5(8)	6(9)
Suspension TS Powder: SSS or (LSS)	(1)	1(2)	2(3)	(4)	(5)	3(6)	4(7)		5(8)
Solution precursor TS Feedstock: LP	1								2

TS = thermal spraying   LSS = liquid-state synthesis
SSS = solid-state synthesis   LP = liquid precursors

Fig. 1 Comparison of the process steps for different thermal spray techniques

nitrates, i.e., $Mn(NO_3)_2 \cdot 4H_2O$ (Merck KGaA) and $Co(NO_3)_2 \cdot 6H_2O$ (BDH ProLabo), respectively, into deionized water to form $MnCo_2O_4$ coatings. Deionized water was used because of the promising results from our previous studies (Ref 28). The cationic concentration of the solution was 3 mol/L. After the nitrates were completely dissolved forming homogeneous solution, a viscosity of 3 mPa s was measured (Haake RheoStress 150, Thermo Fisher Scientific, Waltham, USA) at room temperature.

Crofer 22 APU (ThyssenKrupp VDM, Werdohl, Germany) with a thickness of 0.5 mm designed for the SOFC application was used as the substrate material. The Crofer 22 APU was cut down to 20×50 mm coupons. Prior to the spraying process, surface contaminations, e.g., grease, were removed from the surface of the substrate using ethanol. The surface roughness (R_a) of the Crofer 22 APU was less than 0.5 μm (Mitutoyo SJ-301 DIN1990 GAUSS, Singapore), measured perpendicular to the rolling direction of the sheet.

The coatings were manufactured by means of a modified TopGun HVOF torch (GTV Verschleiss-Schutz GmbH, Luckenbach, Germany) with a 22 mm combustion chamber and 130 mm expansion nozzle. The torch was modified by replacing the dry powder injector with a specially designed liquid injector nozzle system similar to that used by Toma et al. (Ref 29). Two nonatomizing solid stream liquid injector nozzles with diameters of 250 and 300 μm were used. The solution was axially injected into the combustion chamber of the HVOF gun. A pressurized vessel with a rotometer (calibrated for H_2O) was used for controlling the flow rate of solution. At least 4 bars had to be used, because of the back pressure of the HVOF torch. The movement of the HVOF torch was controlled by a x-y manipulator using a linear raster pattern with 3 mm line spacing.

The parameters were varied to study the effect of variations on the formation of the coatings. The total flow rate of combustion gases, solution flow rate, spraying distance, and diameter of the liquid injector nozzles were altered. The fuel gas, used in all experiments, was ethane (C_2H_4) and the oxidizing gas was oxygen (O_2). The normalized (based on the number of moles) stoichiometric

oxygen-ethane ratio (λ) was adjusted between 1.00-1.05. More detailed parameters are presented in Table 1.

The substrate coupons were fixed on the surface of a perforated plate, which effectively released heat (heat sink) from the substrates during the spraying process. Cooling of the substrates was further improved by adding an air-cooling system behind the perforated plate. The cooling system included airblades for the accurate control of air flow direction. It was assumed that the optimal flow direction was parallel to the substrates, since the air would transfer excess heat away from the perforated plate and the substrates, without disturbing the spray stream.

As the HVOF torches are designed only for dry powder spraying, the use of solution caused the slight sedimentation of spray feedstock on muzzle of the HVOF torch, which was observed to have a needle-like structure. After each spray layer, the coating process was paused to allow the specimen to cool down and to clean the liquid injection nozzle, the inner wall of expansion nozzle, and the muzzle. During the cleaning phase, the flow of solution precursor was changed to a flow of pure deionized water without shutting down the combustion process.

The cross sections, fracture surfaces, and topographies of the as-sprayed coatings were characterized using a field-emission scanning electron microscope (FESEM, UL-TRAplus, Carl Zeiss AG, Oberkochen, Germany) equipped with a secondary electron (SE) detector. Chemical analyses were done using an energy dispersive spectrometer (EDS, INCA Energy 350, Oxford Instruments, Oxfordshire, UK). Before cross-sectional studies of the microstructures, the as-sprayed coatings were molded in cold resin, ground, and polished. Qualitative analyses of the phases were done by means of an X-ray diffractometer (XRD, D-500, Siemens, Berlin, Germany) equipped with $Cu-K_\alpha$ radiation source.

3. Results and Discussion

The influence of the spray parameters, i.e., total gas flow, spraying distance and liquid feed rate for on coating formation is presented in Fig. 2. The solid line or solid

Table 1 HVSPFS spraying parameters

Sample	O_2, slpm	C_2H_4, slpm	Total gas flow, slpm	Solution flow rate, mL/min	Nozzle Ø, µm	Spray distance, mm
TG-MCO-1	177	56	233	20	250	80
TG-MCO-2						100
TG-MCO-3						120
TG-MCO-4				50	250	100
TG-MCO-5	215	69	284	20	250	100
TG-MCO-6						120
TG-MCO-7				50	250	80
TG-MCO-8						120
TG-MCO-9	228	76	304	20	250	100
TG-MCO-10						120
TG-MCO-11						140
TG-MCO-12				50	250	80
TG-MCO-13						100
TG-MCO-14				60	300	120
TG-MCO-15	253	83	336	20	250	120
TG-MCO-16						140
TG-MCO-17				40	300	120
TG-MCO-18				50	250	100
TG-MCO-19				100	300	120

Number of spray scans deposited: 6

circles indicate the use of the 250 µm liquid injection nozzle and the dashed and striped circles for the 300 µm liquid injection nozzle, respectively. Potential coatings for the ICs, which are free of open porosity and cracks (verified by FE-SEM cross-sectional studies), are presented as solid or striped circles. The spheres marked with dashed or solid lines are for porous coatings, which cannot be used as protective coatings, either because of a too low deposition rate, or a highly porous coating microstructure (verified by FE-SEM cross-sectional studies). The width of the circles indicates the flow rate (mL/min) of solution.

The area marked off with a black line in Fig. 2 defines the optimal spray parameter window for the hardware used to produce dense coatings for the SOFCs. In order to achieve spray dense coatings at 233 slpm total gas flow rate with 80-100 mm stand-off distances, the flow rate of the solution had to be limited to 20 mL/min (TG-MCO-1,2). A flow rate of 60 mL/min caused porous coatings to be deposited (TG-MCO-4). The use of 284-336 slpm total gas flow rates enabled the increase of solution feed rates, and dense coatings were sprayed using over 50 mL/min feed rates. The larger 300 µm liquid injection nozzle enabled the use of 100 mL/min solution feed rate. This was tested with the 336 slpm total gas flow rate and with 120-mm spray distance (TG-MCO-19). The cross-sectional evaluations revealed that no coating was deposited with the parameters used.

The most probable reason the for poor coating formation as presented in Fig. 3a., where the higher solution feed rates were used (TG-MCO-2 cf. -4 and TG-MCO-17 cf. -19), was that the coatings were formed of partially pyrolyzed or nonpyrolyzed precursor droplets. This occurred most probably because of insufficient energy and/or too short a residence time for complete pyrolysis. The partially pyrolyzed or nonpyrolyzed precursor droplets were also observed in our previous study (Ref 28), and the study of Chen et al. (Ref 15) when coatings were deposited by means of the APS process. The study of Chen et al. (Ref 15) indicated that partially pyrolyzed or nonpyrolyzed precursor droplets

were formed in the outer part of the plasma plume, because of lower flame temperature. In addition, the study of Bertolissi et al. (Ref 22) have shown that if the coating is formed of nonpyrolyzed particles, then the porosity is increased because of a spongy microstructure.

Several studies are focused on modeling the combustion kinetics and behavior of liquid droplets when injected into the combustion chamber of HVOF torch. Results indicate that the temperature of the thermal flame is decreased as the solution feed rate is increased, since more energy is consumed to evaporate the solvent (Ref 30-32). Furthermore, the higher flow rate causes the aggregation of droplets. As the droplets are aggregated, the heat-transfer efficiency from the gas phase into the droplets tends to decrease (Ref 31). It is most probable that inadequate flame temperatures with low heat-transfer properties are the reasons for an incomplete material synthesis (cf. APS process), and thus partially pyrolyzed or nonpyrolyzed precursor droplets are formed. Moreover, as the droplets traverse speed is increased, the evaporation point is shifted downstream toward the expansion nozzle (Ref 31). As a result of the shifted evaporation point, the droplet's residence time in thermal flame is decreased. Due to shorter residence time, it is most plausible that the droplets remained nonpyrolyzed.

In order to spray dense coatings by means of higher solution flow rates, the energy deficit had to be compensated. This was done by increasing total gas flow rate as shown in Fig. 2 (TG-MCO-4 cf. -13) and as observed in cross-sectional images presented in Fig. 3. As the results in modeling studies indicate, by increasing total gas flow rates, the evaporation point of the droplets is shifted to upstream, toward the combustion chamber. As a consequence of this, the heat-transfer properties across the droplet and gas phase boundary are improved.

The hot zone of the thermal flame tends to extend to a longer distance from the gun nozzle as total gas flow rate is increased (Ref 31). This was verified during the spraying
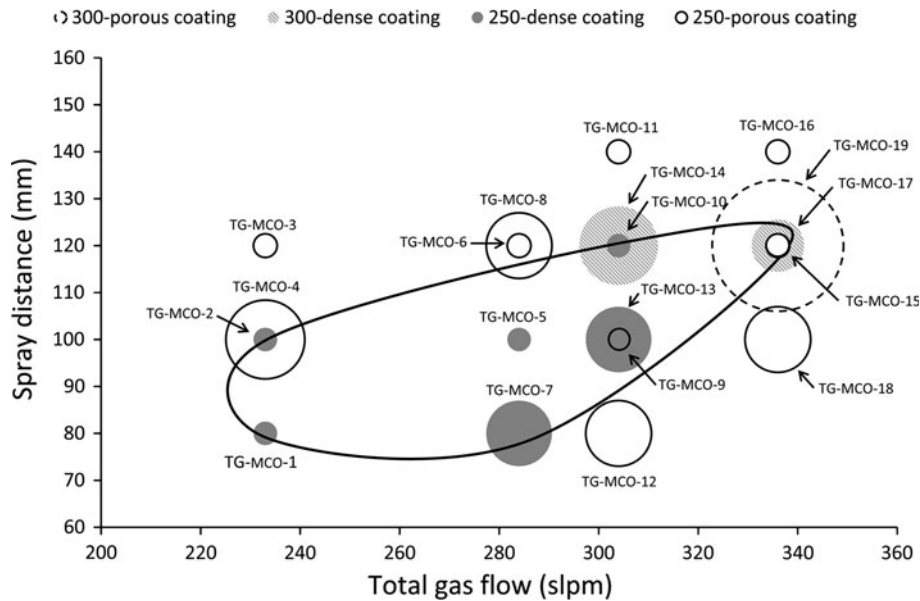
Fig. 2 The spray parameters and the solution feed rate (relative amount is indicated as the width of the circles) plotted in an x-y chart to obtain the optimal parameters for dense coating formation (black line)
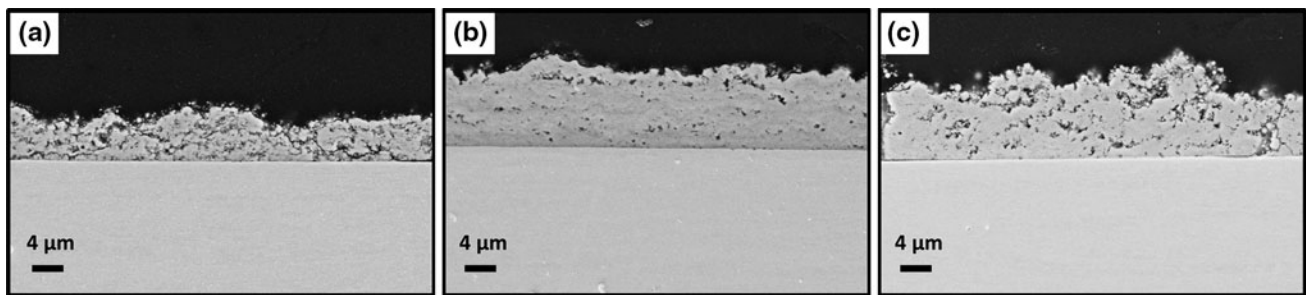

Fig. 3 Cross-sectional images (FE-SEM) of the coatings sprayed with using fixed solution flow rate and standoff distance but by altering total gas flow rate (a) TG-MCO-4 and (b) TG-MCO-13 and (c) TG-MCO-18

process with a longer thermal flame when gas flow rates of 284-336 slpm were used instead of 233 slpm. Therefore, the standoff distance was increased to prevent the overheating of the substrates. If the standoff distance was kept constant, then the coatings that are more porous were sprayed, as shown in Fig. 3c. It is probable that the porous structure was the consequence of only partially pyrolyzed particles due to shorter residence time (incomplete synthesis), caused by faster flame and droplet speed. The maximum standoff distance was limited to 120 mm. Standoff distances above this formed coatings with deposition of lower layer thickness (per spray scan) or highly porous microstructure. The most apparent reason for the porous microstructure is that the smallest precursor droplets were evaporated (without deposition) and the remaining particles were cooled down and re-solidified because of the temperature drop outside of the hot zone area. The melting temperature for $MnCo_2O_4$ lies between 1300 and 1400 °C in relation to relative content of Mn and Co (Ref 33).

The cross sections of the densest as-sprayed coatings are presented in Fig. 4. As shown, the coatings were well bonded with the fairly smooth ($R_a < 0.5$ μm) substrate. As Baccionichini et al. (Ref 34) have noted, substrate roughness should be the same order of magnitude as the flattened lamellae thickness. The topography and the fracture surface images revealed that the coatings were mainly formed of micron (not exceeding the length of the 2 μm bar) and submicron-sized granular shaped particles. Some random splats were detected, with 200-300 nm thickness, as the fracture surface indicates (Fig. 5a). The finely sized droplets favored good bonding with the relatively smooth substrate. Chen et al. have also reported relatively small splats when spraying YSZ coatings using a similar type of HVSPFS process using a Sulzer Metco DJ-2700 hybrid hardware. The diameter of the splats varied from 2 to 5 μm (Ref 26). As is obvious, due to the small splat and granule sizes, grit blasting is not required to improve the mechanical bonding between these coatings and the substrates.

Although Chen et al. reported as low as 2-5-μm splat sizes (Ref 26), the average dimensions of the as-sprayed particles were up to five times higher compared with the

particles observed in the present study. It is likely that the formation of smaller splats/particles is related to the diameter of the liquid injection nozzle used in the HVOF gun. Because there was no information of the size and type of the injector that Chen et al. have used in their studies, it can be assumed that the original powder injector in a DJ-2700 hybrid HVOF system was then used with diameter of 1.3 mm. If so, the diameter of the powder injector was wider compared with the hardware used in our study. Due to the wider nozzle used in the study by Chen et al, it is most probable that larger droplets were formed during the spraying process. (Ref 26).

A comparison between the HVSPFS and the SPPS (Ref 28) MnCo$_2$O$_4$ coatings shows clear differences in coating morphologies and coating density. Where the SPPS coatings showed fairly loosely packed granular particles (observed from the cross-sectional images), the HVSPFS coatings are found to be fairly dense. A high magnification inspection of the fracture surfaces suggest the existence of small granular and splat structures, due to the fairly flat fracture surface, as presented in Fig. 4 and 5. For the most part, the fracture surface passed through the grain boundaries (Fig. 5b) and the splats (Fig. 5a).

The axial injections of precursor and the shock diamonds, formed because of high gas velocity, cause effective droplet break-up during the spraying process. The aerodynamic simulations have shown that effective droplet break-up is obtained because of the rapid change of axial velocity across the shock diamonds which cause high aerodynamic forces on the precursor droplets (Ref 35). Higher gas flow, compared with the SPPS process, and the following higher particle velocity are the most probable reasons for higher packing density of the spray droplets, granules, and splats. Improved density may also be a result of partial sintering, due to the relatively high thermal load from the HVOF flame. This was actually observed in the SPPS coatings (Ref 28).

Porosity was mostly formed as randomly located unconnected pores. The cross-sectional and the fracture surface images (Fig. 3) indicated that the porosity was formed between the granules and the splats. Porosity may also form because of hollow spheres, as observed by Chen et al. (Ref 15, 26) when studying YSZ coatings. A risk of formation of the hollow particles is related to the solution concentration and the droplet size formed in the particular spraying process. Low solution concentration (Ref 15) and large droplet size (Ref 26, 35) apparently tend to form more hollow than denser particles. As our previous study (Ref 28) shows, the use of the cationic concentration of 3 mol/L seemed to help in the formation of dense MnCo$_2$O$_4$ particles in the SPPS process, and which is also favorable in the HVSPFS process.

Basu et al. have simulated the behavior of droplets with different diameters in the high-velocity oxy-fuel jet. Droplets with an initial diameter of 5 μm tend to break-up down to 0.5-1-μm droplets. Larger droplets, with a diameter of 30 μm will break-up down to 0.5-2-μm-diameter droplets. The simulations indicate that the droplets smaller than 5 μm will form dense spray particles, because of uniform increase in solid concentration as the solvent evaporates. In case of the larger droplets, a solid shell will form around the liquid core. The solid shell prevents the evaporation of solvent, and as a result the inner pressure of the droplet will increase. The pressure will eventually break the solid shell and the hollow particle is formed (Ref 35).

The crystallographic phase studies of the as-sprayed coatings are presented in Fig. 6a. As is shown, a multiphase structure consisting of the MnCo$_2$O$_4$, CoO and CoCo$_2$O$_4$ phases was observed in the densest coatings. Even though the multiphase structure was detected, a quantitative EDS analysis gave concentrations of Mn 37 at.% and Co 63 at.% in the TG-MCO-10 coating, and contents of Mn 38 at.% and of Co 62 at.% in the TG-MCO-17. The cationic ratio of Co:Mn should be 2:1. For TG-MCO-10 ratio, it is 1.70:1 and for TG-MCO-17 1.63:1. Considering the results, some selective evaporation of Co may occur during the spray process, although this is near the limit of accuracy of the EDS system. No change of composition was observed, regardless of the parameters used in this study. Similar dual-phase structures were observed in our previous studies, when MnCo$_2$O$_4$-based suspensions (Ref 14) and MnCo$_2$O$_4$-forming solutions (Ref 28) were thermally sprayed. The results of MnCo$_2$O$_4$ manufactured by the SPPS process revealed that CoO formation was related to the type of solvent and plasma gas composition used in the study. With water-based solutions and Ar-He plasma, a coating with the majority of MnCo$_2$O$_4$ phase was deposited. Upon increasing the heat content and viscosity and improving the heat-transfer properties of plasma gas by means of Ar-H$_2$ or Ar-He-H$_2$, the amount of CoO phase increased in the as-sprayed coatings. The same increase in CoO phase was observed as the exothermic properties of the solution was increased by means of water-ethanol mixture as solvent (Ref 28). The results, mentioned above, indicate that the HVSPFS process with a normalized oxygen-ethane ratio (λ) of 1.00-1.05 may produce a flame that exceeds the optimal in-flight droplet temperature to form exact MnCo$_2$O$_4$ structure after impacting to the substrate.

Different oxygen-ethane ratios or combustion gases should be tested to achieve a lower flame temperature and thus possibly to minimize the amount of the CoO phase. The parameters should be selected without decreasing the velocity of the flame, which favors the denser packing of the splats. The use of over-stoichiometric oxygen-ethylene ratio tends to decrease the flame temperature (Ref 36). Also, the higher gas flow increases the flame velocity, and the flame contains an excess amount of oxygen. This superfluous oxygen may improve the synthesis and increase the amount of spinel phase. Alternatively, use of hydrogen instead of ethylene decreases the flame temperature approximately to one in the range of 50-100 °C depending on the oxygen-fuel ratio (Ref 36).

It is most likely that in addition to a crystalline phase with small grain size, an amorphous phase is also formed, as observed because of the relatively wide XRD peaks. It is known that the width of the XRD peaks usually indicates a small grain size, but as Chen et al. have reported, mixtures of amorphous and crystalline phases were observed on HVSPFS-sprayed samples. The amorphous phase is usually
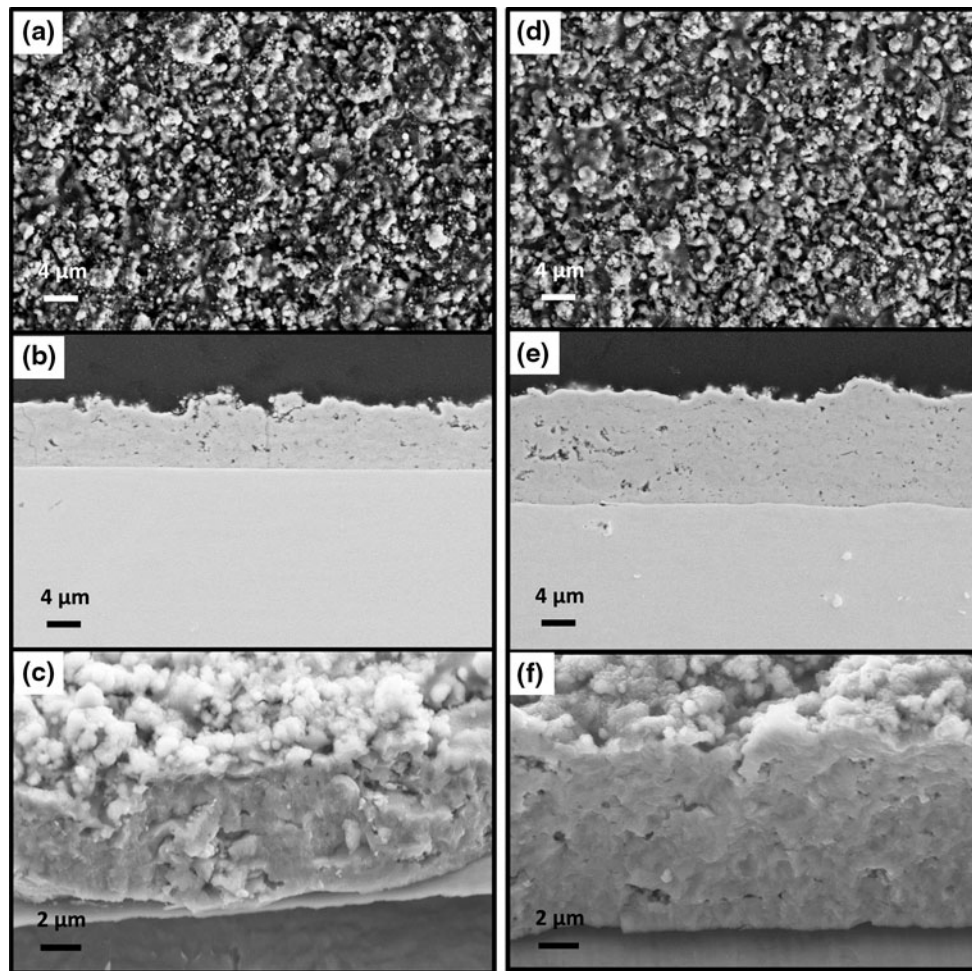
Fig. 4 Topography, cross-sectional and fracture surface SE images (FE-SEM) of (a-c) TG-MCO-10 and (d-f) TG-MCO-17
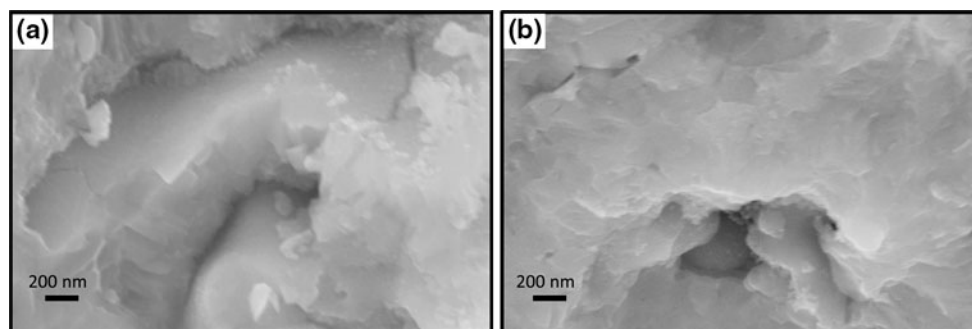

Fig. 5 Fracture surfaces images (FE-SEM) of as sprayed coatings, (a) TG-MCO-10 and (b) TG-MCO-17

formed because of the high cooling rate of the droplets, due to impacting and spreading on the substrate. Owing to the fast heat transfer toward substrate, deposited droplets do not have enough time to form the desired crystal structure (Ref 26). In addition, the width of the peaks can be explained with fine equiaxed grains. Bertolissi et al. (Ref 22) suggest that owing to fast cooling rate, caused by the small splat size, homogeneous nucleation is competitive or predominant against heterogeneous nucleation.

Although the dual-phase structure was obtained on the as-sprayed coatings, reported studies demonstrate that the original spinel structure can be easily restored by a heat treatment. Saoutieff et al. (Ref 10) have restored decomposed APS coatings. In addition, the coatings have been also restored in our previous studies as manufactured, by means of MnCo$_2$O$_4$ suspension (Ref 14) and MnCo$_2$O$_4$-forming solution (Ref 27). Samples TG-MCO-10 and -17 were heated for 1000 h at 800 °C air, to recover
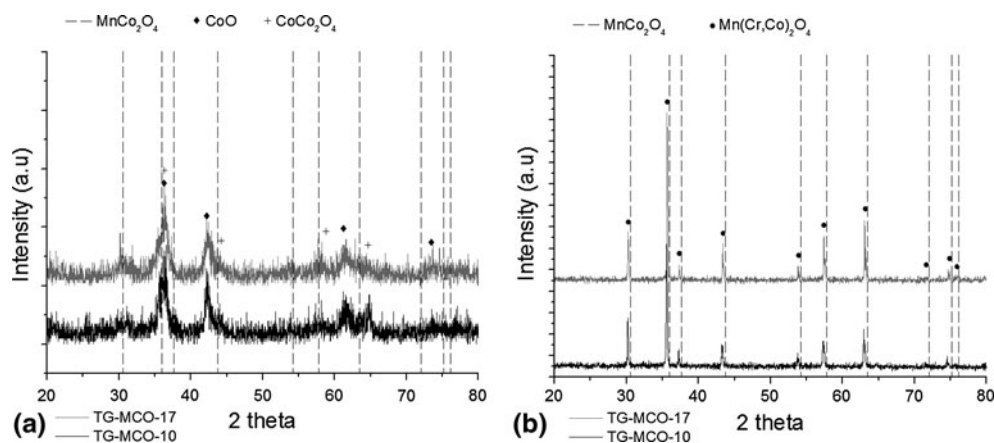
Fig. 6 Crystallographic phase (XRD) studies of (a) as-sprayed and (b) heat treated coatings

decomposed structure and confirm the long-term stability of spinel. As can be seen in Fig. 6b, the crystallographic structure of spinel was fully restored without any trace of Co-oxides. Due to the longer heat treatment process, the XRD pattern of spinel was slightly shifted to lower Bragg angles compared with the pure crystallographic structure of $MnCo_2O_4$. The XRD pattern was equivalent to $Mn(Cr,Co)_2O_4$. This was formed because of Cr migration from the substrate into $MnCo_2O_4$ spinel lattice caused by a longer duration of heat treatment.

4. Conclusion

High-velocity solution precursor flame spraying is a state-of-the-art process for the manufacturing of coatings or layers. Owing to the nature of the process, the coatings can be manufactured without the need for separate materials' synthesis or powder-preparation steps, e.g., spray-drying. In addition, new thin and dense coating structures with small grain sizes can be obtained. Dense and thin coatings are clearly a consequence of the ultrafine droplet formation in the HVSPFS process.

In this study, the HVSPFS technique was used to manufacture thin, less than 10 μm, dense coatings on ferritic stainless steel Crofer 22 APU substrates with a thickness of 0.5 mm. The solution was prepared by diluting manganese and cobalt nitrates in deionized water. A cationic concentration of 3 mol/L was used to obtain $MnCo_2O_4$ as-sprayed coatings. Several spray parameters including liquid injector nozzle diameter, gas composition, total gas flow rate, and solution precursor feed rates were studied to understand the coating formation mechanisms.

- The liquid injector nozzles should be selected in a way such that finely sized droplets are produced, forming dense pyrolyzed particles. In this study, liquid-injector nozzles with diameters of 250 and 300 μm produced droplets, which through the syntheses formed dense granular particles with diameters lower than 2 μm and in a majority of which are of submicron size.

- The solution precursor feed rate and the total gas feed rates were linked together. As observed in this study, the increase of solution feed rate required use of higher total gas flow rates to form high enough shear force for droplet break-up, to prevent aggregation, and to provide heat energy for the evaporation of solvent and pyrolysis of precursors. The effective solution feed rate was 20-60 mL/min with 304-336 slpm total gas flow rates. Oxygen and ethylene were used as the combustion gases with normalized oxygen-ethane ratio (λ) of 1.0-1.05.

- The standoff distance was related to the used total gas flow rates. Higher gas flow rates produced faster particle speed, which decreased particles' residence time in the thermal flame. With too short standoff distances, the substrates were overheated, and coatings were most probably formed of partially pyrolyzed particles. The densest coatings were formed at 120-mm as standoff distance and with 304-336 slpm as total gas flow rates. If longer standoff distance were used, then more porous coatings with low deposition rate per spray scan were obtained.

Although coatings with superior density were sprayed, the spinel structure was partially decomposed into Co-oxides during the HVSPFS process. Several studies have proven that the decomposed spinel structure can be restored by heat treatment. In this study, the crystallographic structure of spinel was restored by 1000-h heat treatment at 800 °C air. The long treatment time caused the XRD pattern to be shifted to the lower Bragg angles because of Cr migration into $MnCo_2O_4$ lattice, and therefore, $Mn(Cr,Co)_2O_4$ was formed.

References

1. J. Wu and X. Liu, Recent Development of SOFC Metallic Interconnect, *J. Mater. Sci. Technol.*, 2010, **26**(4), p 293-305
2. J. Froitzheim, G. Meier, L. Niewolak, P. Ennis, H. Hattendorf, L. Singheiser, and W. Quadakkers, Development of High Strength Ferritic Steel for Interconnect Application in SOFCs, *J. Power Sources*, 2008, **178**(1), p 163-173
3. W. Z. Zhu and S. C. Deevi, Development of Interconnect Materials for Solid Oxide Fuel Cells, *Mater. Sci. Eng., A*, 2003, **348**(1-2), p 227-243
4. C. Gindorf, L. Singheiser, and K. Hilpert, Vaporisation of Chromia in Humid Air, *J. Phys. Chem. Solids*, 2005, **66**(2-4), p 384-387
5. J. Fergus, Effect of Cathode and Electrolyte Transport Properties on Chromium Poisoning in Solid Oxide Fuel Cells, *Int. J. Hydrogen Energy*, 2007, **32**(16), p 3664-3671
6. F. Chen, E. Sun, J. Yamanis, J. Hawkes, J. Smeggil, S. Warrier, and J.-W. Kim, Cr Poisoning Effect for Solid Oxide Fuel Cells, *Mater. Sci. Technol.*, 2006, p 303-311
7. W.Z. Zhu and S.C. Deevi, Opportunity of Metallic Interconnects for Solid Oxide Fuel Cells: A Status on Contact Resistance, *Mater. Res. Bull.*, 2003, **38**(6), p 957-972
8. L.L. Yngve and N. Truls, Spinel and Perovskite Functional Layer Between Plansee Metallic Interconnect (Cr-5 wt % Fe-1 wt % Y_2O_3) and Ceramic ($La_{0.85}Sr_{0.15})_{0.91}MnO_3$ Cathode Materials for Solid Oxide Fuel Cells, *J. Electrochem. Soc.*, 2000, **147**(9), p 3251-3256
9. Z. Yang, G.-G. Xia, X.-H. Li, and J.W. Stevenson (Mn, Co)3O4 Spinel Coatings on Ferritic Stainless Steels for SOFC Interconnect Applications, *Int. J. Hydrogen Energy*, 2007, **32**(16), p 3648-3654
10. E. Saoutieff, G. Bertrand, M. Zahid, and L. Gautier, APS Deposition of $MnCo_2O_4$ on Commercial Alloys K41X Used as Solid Oxide Fuel Cell Interconnect: The Importance of Post Heat-Treatment for Densification of the Protective Layer, *ECS Trans.*, 2009, **25**(2), p 1397-1402
11. J. Puranen, J. Lagerbom, L. Hyvärinen, T. Mäntylä, E. Levänen, M. Kylmälahti, and P. Vuoristo, Formation and Structure of Plasma Sprayed Manganese-Cobalt Spinel Coatings on Pre-heated Metallic Interconnector Plates, *Surf. Coat. Technol.*, 2010, **205**(4), p 1029-1033
12. J. Puranen, J. Lagerbom, L. Hyvärinen, M. Kylmälahti, O. Himanen, M. Pihlatie, J. Kiviaho, and P. Vuoristo, The Structure and Properties of Plasma Sprayed Iron Oxide Doped Manganese Cobalt Oxide Spinel Coatings for SOFC Metallic Interconnectors, *J. Therm. Spray Technol.*, 2010, **20**(1-2), p 154-159
13. J. Puranen, L. Hyvärinen, J. Lagerbom, M. Kylmälahti, H. Koivuluoto, and P. Vuoristo, Manganese-cobalt Spinel Coatings for SOFC Metallic Interconnects Manufactured by Conventional Plasma Spraying (PS) and Suspension Plasma Spraying (SPS), *Fuel Cell Sci., Eng. Technol., Int. Conf., 9th*: August 7-10, 2011 (Washington, DC, USA), ASME, p 1-8
14. J. Puranen, L. Hyvärinen, J. Lagerbom, M. Kylmälahti, H. Koivuluoto, and P. Vuoristo, Suspension Plasma Spraying (SPS) of Manganese-Cobalt Spinel Coatings, *Thermal Spray 2011*, September 27-29, 2011 (Hamburg, Germany), DVS, p 1201-1205
15. D. Chen, E. Jordan, and M. Gell, Effect of Solution Concentration on Splat Formation and Coating Microstructure Using the Solution Precursor Plasma Spray Process, *Surf. Coat. Technol.*, 2008, **202**(10), p 2132-2138
16. L. Pawlowski, Suspension and Solution Thermal Spray Coatings, *Surf. Coat. Technol.*, 2009, **203**(19), p 2807-2829
17. D. Chen, E.H. Jordan, M. Gell, and X. Ma, Dense Alumina-Zirconia Coatings Using the Solution Precursor Plasma Spray Process, *J. Am. Ceram. Soc.*, 2008, **91**(2), p 359-365
18. L. Xie, X. Ma, E.H. Jordan, N.P. Padture, D.T. Xiao, and M. Gell, Deposition of Thermal Barrier Coatings Using the Solution Precursor Plasma Spray Process, *J. Mater. Sci.*, 2004, **39**(5), p 1639-1646
19. L. Xie, D. Chen, E. Jordan, A. Ozturk, F. Wu, X. Ma, B. Cetegen, and M. Gell, Formation of Vertical Cracks in Solution-Precursor Plasma-Sprayed Thermal Barrier Coatings, *Surf. Coat. Technol.*, 2006, **201**(3-4), p 1058-1064
20. C.K. Muoto, E.H. Jordan, M. Gell, and M. Aindow, Identification of Desirable Precursor Properties for Solution Precursor Plasma Spray, *J. Therm. Spray Technol.*, 2011, **20**(4), p 802-816
21. X. Ma, F. Wu, J. Roth, M. Gell, and E. Jordan, Low Thermal Conductivity Thermal Barrier Coating Deposited by the Solution Plasma Spray process, *Surf. Coat. Technol.*, 2006, **201**(7), p 4447-4452
22. G. Bertolissi, C. Chazelas, G. Bolelli, L. Lusvarghi, M. Vardelle, and A. Vardelle, Engineering the Microstructure of Solution Precursor Plasma-Sprayed Coatings, *J. Therm. Spray Technol.*, 2012, **21**(6), p 1148-1162
23. R. Rampon, F.-L. Toma, G. Bertrand, and C. Coddet, Liquid Plasma Sprayed Coatings of Yttria-Stabilized Zirconia for SOFC Electrolytes, *J. Therm. Spray Technol.*, 2006, **15**(4), p 682-688
24. Y. Wang and T.W. Coyle, Solution Precursor Plasma Spray of Nickel-Yttria Stabilized Zirconia Anodes for Solid Oxide Fuel Cell Application, *J. Therm. Spray Technol.*, 2007, **16**(5-6), p 898-904
25. D. Chen, E. Jordan, and M. Gell, Porous TiO_2 Coating Using the Solution Precursor Plasma Spray Process, *Surf. Coat. Technol.*, 2008, **202**(24), p 6113-6119
26. D. Chen, E.H. Jordan, and M. Gell, Solution Precursor High-Velocity Oxy-Fuel Spray Ceramic Coatings, *J. Eur. Ceram. Soc.*, 2009, **29**(16), p 3349-3353
27. J. Puranen, J. Laakso, L. Hyvärinen, M. Kylmälahti, and P. Vuoristo, High Temperature Oxidation Behaviour of $MnCo_2O_4$ Coating on Crofer 22 APU Manufactured by a Novel Solution Precursor Plasma Spray Process (SPPS), *Fuel Cell Sci., Eng. Technol., Int. Conf., 10th*, July 23-26 2012 (San Diego, CA, USA), ASME, p 1-6
28. J. Puranen, J. Laakso, L. Hyvärinen, M. Kylmälahti, and P. Vuoristo, Influence of Spray Parameters and Characteristics of Solutions on Microstructure and Phase Composition of Solution Precursor Atmospheric Plasma Sprayed (SPPS) Mn-Co Spinel Coating, *Thermal Spray 2012: Air, Land, Water and Human Body Thermal Spray Science and Applications*, May 21-23 2012 (Houston, TX, USA), DVS, p 810-815
29. F. Toma, L. Berger, T. Naumann, and S. Langner, Microstructures of Nanostructured Ceramic Coatings Obtained by Suspension Thermal Spraying, *Surf. Coat. Technol.*, 2008, **202**(18), p 4343-4348
30. E. Dongmo, R. Gadow, A. Killinger, and M. Wenzelburger, Modeling of Combustion as well as Heat, Mass, and Momentum Transfer during Thermal Spraying by HVOF and HVSFS, *J. Therm. Spray Technol.*, 2009, **18**(5-6), p 896-908
31. M. Taleby and S. Hossainpour, Numerical Investigation of High Velocity Suspension Flame Spraying, *J. Therm. Spray Technol.*, 2012, **21**(6), p 1163-1172
32. E. Dongmo, A. Killinger, M. Wenzelburger, and R. Gadow, Numerical Approach and Optimization of the Combustion and Gas Dynamics in High Velocity Suspension Flame Spraying (HVSFS), *Surf. Coat. Technol.*, 2009, **203**(15), p 2139-2145
33. J.Y. Eun, Y.Y. Mi, M. Ji-Woong, and H. Hae Jin, Fabrication of a $MnCo_2O_4$ Gadolinia-doped Ceria (GDC) Dual-phase Composite Membrane for Oxygen Separation, *J. Korean Ceram. Soc.*, 2010, **47**(2), p 199-204
34. A. Bacciochini, F. Ben-Ettouil, E. Brousse, J. Ilavsky, G. Montavon, A. Denoirjean, S. Valette, and P. Fauchais, Quantification of Void Networks of As-sprayed and Annealed Nanostructured Yttria-Stabilized Zirconia (YSZ) Deposits Manufactured by Suspension Plasma Spraying, *Surf. Coat. Technol.*, 2010, **205**(3), p 683-689
35. S. Basu and B.M. Cetegen, Modeling of Liquid Ceramic Precursor Droplets in a High Velocity Oxy-fuel Flame Jet, *Acta Mater.*, 2008, **56**(12), p 2750-2759
36. H. Kreye and F. Gärtner, High Velocity Oxy-Fuel Flame Spraying-State of the Art, New Developments and Alternatives, *6. Kolloquium Hochgeschwindigkeits-Flammspritzen*, November 27-28, 2003 (Erding, Germany), p 5-17

Publication VI

High Temperature Oxidation Tests for the High Velocity Solution Precursor Flame Sprayed Manganese-Cobalt Oxide Spinel Protective Coatings on SOFC Interconnector Steel
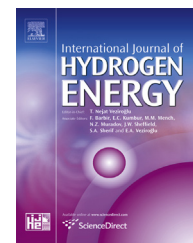
by

J. Puranen, J. Laakso, M. Honkanen, S. Heinonen, M. Kylmälahti, S. Lugowski, T. Coyle, O. Kesler and P. Vuoristo

High temperature oxidation tests for the high velocity solution precursor flame sprayed manganese–cobalt oxide spinel protective coatings on SOFC interconnector steel

CrossMark

Jouni Puranen [a,*], Jarmo Laakso [a], Mari Honkanen [a], Saara Heinonen [a], Mikko Kylmälahti [a], Stan Lugowski [b], Thomas W. Coyle [b], Olivera Kesler [c], Petri Vuoristo [a]

[a] Tampere University of Technology, Department of Materials Science, Tampere, Finland
[b] University of Toronto, Department of Materials Science and Engineering, Toronto, ON, Canada
[c] University of Toronto, Department of Mechanical and Industrial Engineering, Toronto, ON, Canada

ARTICLE INFO

ABSTRACT

High velocity solution precursor flame spray process was used to deposit $MnCo_{1.9}Fe_{0.1}O_4$ and $Mn_{1.5}Co_{1.5}O_4$ coatings on Crofer 22 APU ferritic stainless steel samples. The solution precursors were manufactured by diluting metal nitrates into deionized water. The as-sprayed coatings were oxidized at 850 °C for 500 h to evaluate Cr-barrier and electrical properties.

The post-mortem studies were performed with various qualitative and quantitative elemental analysis methods and a four-point measurement was used for the area specific resistance studies. The as-sprayed coatings were formed of single crystallite nanoparticles (10–20 nm) and polycrystalline sub-micron particles (100–500 nm). The small particle and crystallite size showed strong sintering behavior during the oxidation cycle. Cr-migration was fully prevented thought the oxidized coatings. The surface topography and grain growth dominated the electrical properties during the test cycle.

Introduction

Interconnectors are employed in solid oxide fuel cells (SOFCs) to connect the cells electrically in series and provide distribution of the oxidant and the fuel gases for the electrodes. As high chromium alloyed ferritic stainless steel interconnectors (ICs) are more commonly used in anode supported SOFCs,

some material-specific problems must be solved. The problem is related to the behavior of the ferritic stainless steels in range of the SOFC operating temperature of order of 600–800 °C. At this temperature range, ferritic stainless steel oxidizes and thus forms a Cr_2O_3 oxide layer. The Cr_2O_3 oxide layer reacts with the gaseous H_2O to form volatile CrO_3 and $CrO_2(OH)_2$ compounds [1].

Since CrO_3 and $CrO_2(OH)_2$ are volatile in the cathode side air atmosphere, they transport into the triple phase boundary (TPB), which is the shared interphase of the cathode, the electrolyte and the gas phase. According to Fergus [1], the TPB offers vacancies for CrO_3 and $CrO_2(OH)_2$ to reduce back to Cr_2O_3 or $SrCrO_3$. When reducing back to Cr_2O_3, the size of the TPB decreases over time causing the degradation of the cell [1–3].

It is generally accepted that in order to prevent or minimize degradation, protective coatings must be used on the ferritic stainless steel ICs. Ceramics with a spinel structure $(A,B)_3O_4$ show the greatest potential to be employed as protective coatings. The spinels of the greatest interest are $(Mn,Co)_3O_4$ [4,5] and $(Mn,Co,Fe)_3O_4$ [4,6,7] type materials, as these have i) similar coefficient of thermal expansion (CTE) behavior with the other fuel cell materials, ii) high enough electrical conductivity and iii) capability to form more stable Cr-containing spinels.

Many successful coating methods such as wet-slurry processes and sputtering are used to deposit protective coatings as reviewed for example in Refs. [8,9]. The main demands are dense microstructure and scalability into the industrial production with low production costs. Conventional thermal spraying with dry powder as material feedstock is one of the most potential manufacturing method for protective ceramic coatings, since it is widely used in other industrial areas where application specific type coatings are required [10]. The previous studies have shown that thermal spraying can be used to manufacture dense spinel coating on fairly thin substrates [11–17].

In this study, the protective coatings were manufactured by using high velocity solution precursor flame spraying (HVSPFS) process, which is a modified version of the high velocity oxy-fuel (HVOF) spraying process. The HVSPFS process can be considered as a novel process technique among all thermal spraying processes. In the conventional thermal spray processes, the material feedstock is in form of dry powder, which is usually preceded by long material synthesis chain. However, as our previous study [13] has clearly demonstrated, the HVSPFS process can significantly shorten the length of the overall production chain. In addition, the technique is a promising method to coatings from low cost raw-materials i.e., nitrates. Furthermore, new microstructures are obtained e.g., thin and dense microstructures formed of sub-micron sized particles. Due to small droplet and particle size the coating can be sprayed on smooth substrates without grit blasting as a surface preparation process prior to coating. In addition, as the HVSPFS coatings are dense enough, similar to atmospheric plasma sprayed coatings reported in Refs. [16,17], and therefore ready to be used in the SOFC stack on as-sprayed state without any densification post heat treatments.

Despite promising results are obtained by manufacturing $(Mn,Co)_3O_4$ coatings by the HVSPFS process [13], high temperature oxidation cycle tests have not yet been reported anywhere. The aim of a present study was to evaluate the high temperature behavior of HVSPFS $Mn_{1.5}Co_{1.5}O_4$ and $MnCo_{1.9}Fe_{0.1}O_4$ coatings oxidized at 850 °C in air for 500 h, which simulate start up phase and short term behavior when used directly in the SOFC. Post-mortem analyses, including

electron microscopy and various elemental analyses were performed to study the Cr-barrier properties of the HVSPFS spinel coatings. In addition an on-line four-point measurement method was used to collect area specific resistance data of the coated samples.

Experimental

Materials

High chromium alloy (20–24 wt-%) Crofer 22 APU (ThyssenKrupp VDM GmbH, Werdohl, Germany) ferritic stainless steel with thickness of 0.5 mm was used as the substrate material. The surface roughness was less than 0.5 μm (Mitutoyo SJ-301 DIN1990 GAUSS, Singapore), representing the surface quality as received from the factory. The substrates were cut into 25.4 mm diameter of disks, and prior to the spraying process the substrates were cleaned in an ethanol bath to remove surface contaminations.

Two different water based nitrate solutions were used as precursors in the HVSPFS coating process. The $Mn_{1.5}Co_{1.5}O_4$ and $MnCo_{1.9}Fe_{0.1}O_4$ forming solutions were manufactured by dissolving stoichiometric amounts of $Mn(NO_3)_2 \cdot 4H_2O$ (Merck KGaA), $Co(NO_3)_2 \cdot 6H_2O$ (BDH ProLab) and $Fe(NO_3)_3 \cdot 9H_2O$ (Merck KGaA) in molar ratios of 1:1.16 and 1:2.20:0.16, respectively into deionized water to form a desired solution precursors. The cationic concentration was 3 mol/L due to the promising results obtained in Refs. [13,18].

Deposition method

The coatings were manufactured with a modified high velocity oxy-fuel (HVOF) torch (GTV Verschleiss-Schutz GmbH, Luckenbach, Germany) with a 22 mm combustion chamber and a 135 mm expansion nozzle. In order to feed the solution into the torch, the dry powder feeding hardware was replaced with a specially designed non-atomizing solid stream liquid injector. This injector enabled axial feeding of the solution into the combustion chamber, by using 250 μm and 300 μm diameter nozzles. A pressurized vessel was used to control the feed rate of the solution. The detailed spraying parameters are presented in Table 1.

The movement of the HVOF torch was controlled by an x–y manipulator. The spray layers were obtained using a linear raster pattern with 3 mm line spacing. The substrates were fixed on a vacuum table that also provided the extra air-cooling.

Characterization

The properties of the solution precursor feedstock where analyzed in order to obtain detailed data of the atomization and thermal decomposition behavior during the spraying process. Rheological properties of the $Mn_{1.5}Co_{1.5}O_4$ and $MnCo_{1.9}Fe_{0.1}O_4$ solution precursors were analyzed with a rotational rheometer (Haake RheoStress 150, Thermo Fisher Scientific) at room temperature. Decomposition analyses were carried out by thermogravimetry combined with differential scanning calorimetry (DTA-DSC, PerkinElmer 6000). Prior to

Table 1 – Detailed HVSPFS parameters.						
Coating	Nozzle (μm)	Spray distance (mm)	Oxygen (slpm)	Ethene (slpm)	Flow rate (ml/min)	Spray layers
TG1-MnCo$_{1.9}$Fe$_{0.1}$O$_4$	250	80	215	70	34	6
TG1-Mn$_{1.5}$Co$_{1.5}$O$_4$	250	80	215	70	34	6
TG2-MnCo$_{1.9}$Fe$_{0.1}$O$_4$	300	120	253	83	27	6

the DTA-DSC tests, nitrates were dissolved into deionized water and dried at 50 °C to obtain homogenous precursor powder. The heating rate was 10 K/min using oxygen as the atmosphere.

The as-sprayed coatings were oxidized at 850 °C in air for 500 h and a four-point measurement method was simultaneously employed to obtain area specific resistance (ASR) data. The test emphasizes the behavior of the coatings in start up and the short period of time on the operation phase. It should be noted that these coatings are not meant to be heat treated in reducing or/and oxidizing atmosphere before the actual use in a stack. The direct current density was 500 mA/cm^2. The coatings were pressed against each other with a force of 9.81 N, which caused 4.50 kPa contact pressure. The measurement was performed without a contact paste, and therefore the results show only substrate-coating/coating-substrate contact data. Platinum wires were point welded to the specimen and the voltage drop was continuously measured with a multi-plexer equipment.

Microstructural cross section and fracture surface coating characterization were performed with a field-emission scanning electron microscope (FESEM, Carl Zeiss ULTRAplus), employed with energy dispersive X-ray spectroscopy (EDS, INCA Energy 350, Oxford Instruments). The coating thicknesses were measured from the cross section images by using 40 measuring points. In-flight and deposited particle characterizations were done with analytical transmission electron microscope (TEM, Jeol JEM 2010), combined with Energy Dispersive X-ray spectrometer (EDS, Noran Vatage, Termo scientific).

In order to obtain cross section for the FESEM characterization, the samples were moulded into epoxy resin in a chamber under reduced pressure. The cross section surfaces were ground and polished with SiC papers and diamond suspensions. For the TEM characterization, the deposited coating was carefully removed with the help of ethanol and collected on a copper grid with carbon film.

The nitrate precursors and the as-sprayed coatings were analyzed by Fourier Transform Infrared spectroscopy (FT-IR, Perkin Elmer Spectrum One) to determine the presence of nitrates in the as-sprayed coatings. The as-sprayed coatings were removed from the substrates and manually ground in an agate mortar. To obtain reference data, nitrates were dissolved into deionized water and dried at 50 °C. The powder samples were pressed into KBr pellets (sample/KBr ratio being 1/100) and the spectra were measured and presented in the range of 4000–750 cm^{-1}.

Quantitative elemental analyses for the oxidized coatings were obtained with a radio frequency glow discharge optical emission spectrometer (RF-GD-OES, HoribaJobin Yvon). The oxidized coating material was sputtered 5 mm spot size. The vaporized coating material was analyzed in order to obtain more comprehensive picture of the elemental diffusion during the oxidation cycle.

Qualitative phase analyses were obtained by X-ray diffraction (XRD, Empyrean, PANalytical B.V., Almelo, Netherlands) using Cu-Kα radiation source and analyzed with HighScore plus software. The program employs The International Centre for Diffraction Data (ICDD) for phase analysis and Scherrer equation for grain size measurements. The phase and grain size analyses were done for the as-sprayed and the oxidized coatings.

Results and discussion

Precursor feedstock

The rheological properties of the nitrate solutions used in the HVSPFS process are presented in Fig. 1. The Mn$_{1.5}$Co$_{1.5}$O$_4$ solution can be considered a Newtonian fluid since the shear stress increased linearly in terms of the shear rate, and therefore the viscosity remained constant, approximately 3.50 mPas. For the MnCo$_{1.9}$Fe$_{0.1}$O$_4$ nitrate solution, the rheological behavior was Newtonian in the shear rate range from 0 to 400 s^{-1}, with the viscosity value of 4.0 mPas. At a shear rate of 450 s^{-1}, the rheological behavior changed from Newtonian to dilatant, i.e., shear thickening. This means that the viscosity of the fluid increased in proportion to the shear rate. The most plausible explanation for the behavioral change from Newtonian to dilatant is the presence of Fe cations in the solution. The oxidation state for iron cations from the nitrates was +3, whereas for Mn and Co cations the oxidation state was +2.
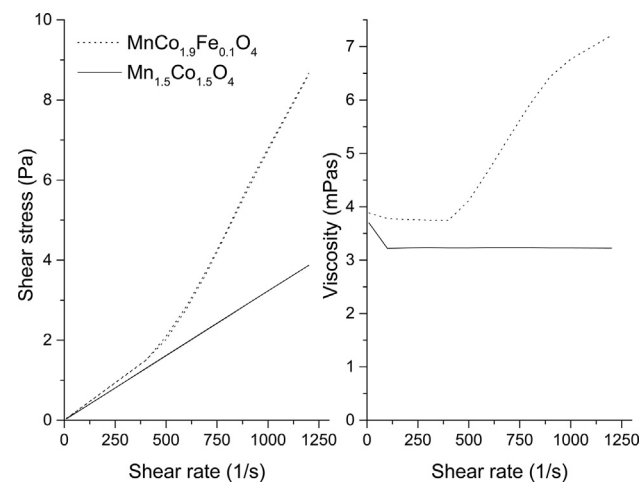

Fig. 1 – Rheological measurements of the nitrate precursor solutions.

Decomposition of nitrates and formation of $MnCo_{1.9}Fe_{0.1}O_4$ and $Mn_{1.5}Co_{1.5}O_4$ spinels were studied by TG-DSC analysis and the results are presented in Fig. 2. The graph shows the decomposition behavior of diluted and dried nitrate precursor powders. The endothermic peaks from 50 to 110 °C refer to evaporation of water. The peaks above 160 °C are related to formation of NO_x, as Nissinen et al. [19] have observed by heat treating Mn—Co nitrate powder. The exothermic peaks starting to form from at 285 °C and 330 °C relate to the final thermal decomposition of nitrates and the formation of $MnCo_{1.9}Fe_{0.1}O_4$ and $Mn_{1.5}Co_{1.5}O_4$ spinels, respectively. The decomposition was also confirmed by the TG-analysis, as in the mass obtained the minimum value. The crystallite formation is a relative slow process with causes broadening of the exothermic peaks. According to the result, iron doping may enhance formation of the spinel structure.

As-sprayed HVSPFS spinel coatings

The microstructural and elemental studies of the as-sprayed coatings were done with FESEM and EDS. Fig. 3 shows the polished cross-section SE-images of the as-sprayed coatings. According to the cross-section images, the TG1-$MnCo_{1.9}Fe_{0.1}O_4$ and TG1-$Mn_{1.5}Co_{1.5}O_4$, and TG2-$MnCo_{1.9}Fe_{0.1}O_4$ had a thickness of 37.0 μm (sdv. 2.0 μm), 44.0 μm (sdv. 4.0 μm) and 12.5 μm (sdv. 0.5 μm), respectively. The coatings were well adhered on the Crofer 22 APU substrate. The as-sprayed coatings were found to contain pores, which were localized between the spray layers. Although the coatings contained porosity, the cross-sectional images do not show the presence of open porosity.

As was found in our previous study focused on microstructural characterization of the HVSPFS $MnCo_2O_4$ coatings [13], the spray parameters can have a direct influence on the coating microstructure. It can be confirmed that the lamellar microstructure was a consequence of the relatively short spraying distance and the high feed rates of the precursor. The short spraying distance and high feed rate resulted in a denser spray pattern, which enhanced formation of the layered structure. In addition, it should be noted that shorter spraying distance increases the heat load to the substrate.

As observed from the cross-section images, the surface profiles of the samples TG1-$MnCo_{1.9}Fe_{0.1}O_4$ and TG1-$Mn_{1.5}Co_{1.5}O_4$ were relatively uneven compared to TG1-$MnCo_{1.9}Fe_{0.1}O_4$, confirmed also with the standard deviation values. This was a consequence of residuals formed during the spaying process. The term residual in this case refers to relatively large droplets formed during the deposition process. The residuals were formed as the precursor adhered and accumulated/aggregated inside the expansion nozzle of the HVOF torch. The gas flow detached agglomerated precursor/material from the wall and formed larger molten droplets. Similar precursor accumulation was observed in our previous study as a needle-like formation [13]. The HVOF torch used in this study is designed for dry powder spraying and the feed rate of the precursor would need to be optimized for the combustion chamber - expansion nozzle design.

The quantitative EDS ratios for Mn/Co/Fe cations were 38.5/57.9/4.6 and 38.2/57.3/4.5 at-% for TG1-$MnCo_{1.9}Fe_{0.1}O_4$ and TG2-$MnCo_{1.9}Fe_{0.1}O_4$, respectively. The desired ratio is 33.3/63.3/3.3 in at-%. For TG1-$Mn_{1.5}Co_{1.5}O_4$ the relative Mn/Co proportion was 55.1/44.9. The desired ratio for $Mn_{1.5}Co_{1.5}O_4$ is 50.0/50.0 in at-%. The results indicate that partial evaporation of Co is possible, and the same selective evaporation of Co was observed in our previous study [13].

Fig. 4 shows the FESEM- and TEM-images of the particles collected from the surface of the as-sprayed TG1-$MnCo_{1.9}Fe_{0.1}O_4$ coating. As stated in the Introduction, the HVSPFS coatings are formed from sub-micron and nanometer sized particles. This was confirmed when particle sizes and morphologies were compared to the coating topography of images shown in Ref. [13].

The sub-micron particles had a size range of 100—500 nm and nanoparticles were in the range of 10—20 nm. The sub-micron particles exhibited a perfectly round morphology, whereas the nanoparticles had a blockier morphology. The nanoparticles had a strong tendency to agglomerate and aggregate as shown in Fig. 4.

Due to the shear force of the turbulent combustion gases and low viscosity of the solution as shown in Fig. 1, the injected precursor stream effectively fragmented into smaller droplets [20]. The atomized droplet size defines the size class and the morphology of the pyrolyzed particles. The sub-
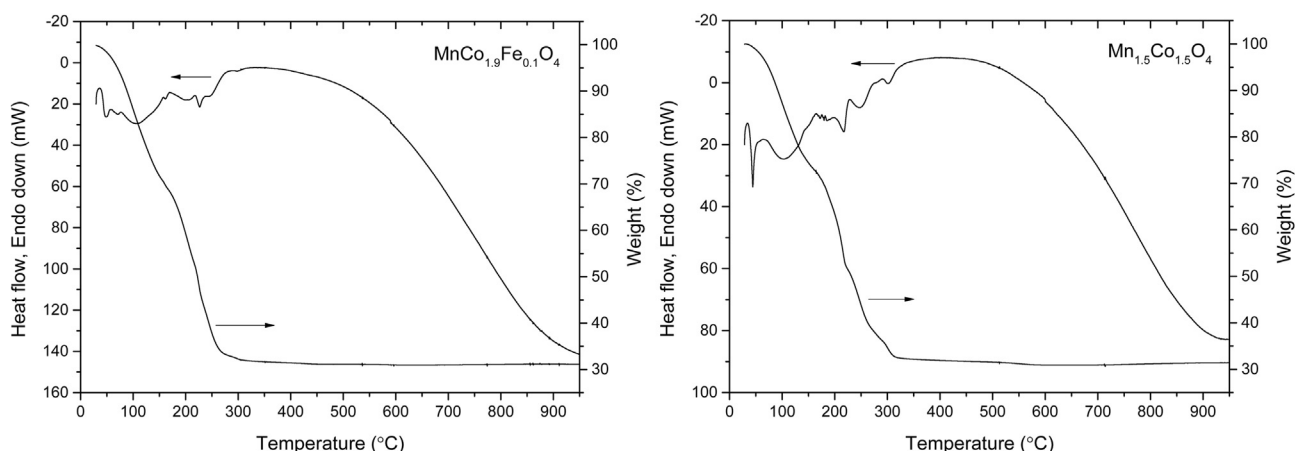

Fig. 2 — TG-DSC analysis of the dried nitrate precursor powders with nominal compositions.
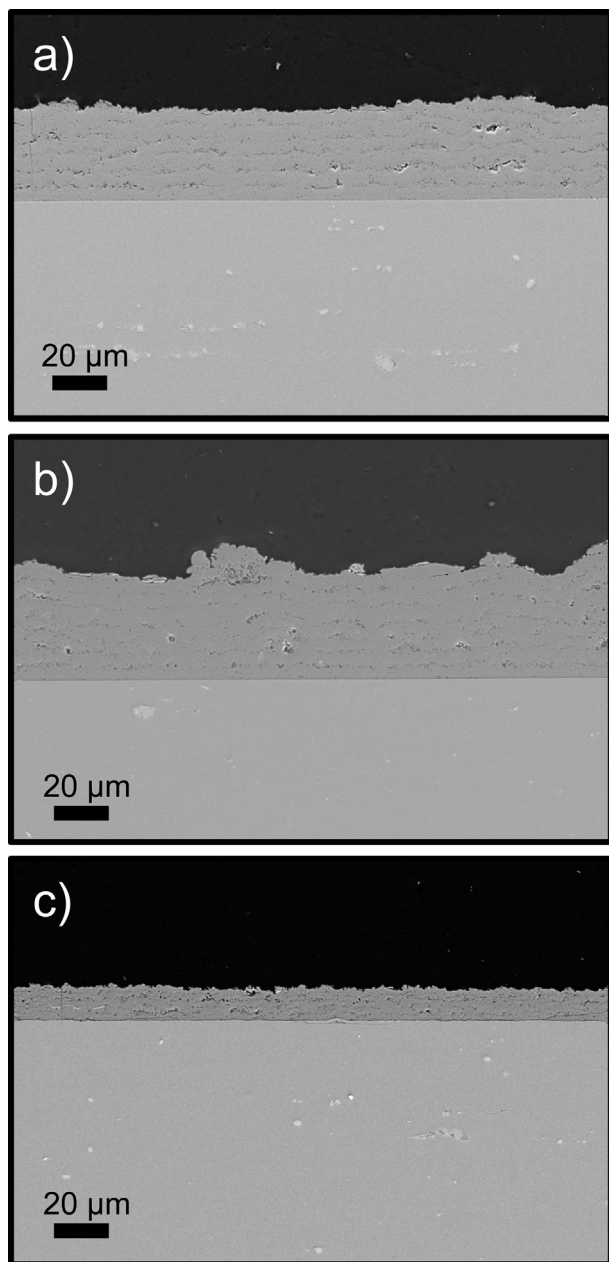
Fig. 3 – Cross-section FE-SEM images of the as-sprayed HVSPFS a) TG1-MnCo$_{1.9}$Fe$_{0.1}$O$_4$ b) TG1-Mn$_{1.5}$Co$_{1.5}$O$_4$ and c) TG2-MnCo$_{1.9}$Fe$_{0.1}$O$_4$ coatings.

micron particles are formed from the fragmented precursor droplets. As the precursor droplet is exposed to the thermal flame the temperature is increased at the surface. As a result, the solvent is evaporated and the precursor will go through a thermal decomposition process similar that shown in Fig. 2, forming a solid.

However, the exact size classification of the atomized precursor droplets cannot be done, since the precursor is fed in to the combustion chamber, fragmented and traveled through the expansion nozzle when exiting the torch. The total length of this distance is 157 mm, where the part of the traverse under influence on the thermal flame. Hereafter, the

droplets are exposed to the shear force of the shock diamonds as reported in Ref. [20].

Basu et al. have suggested three different precipitation routes when the particles are formed through the liquid-to-solid conversion during the spraying process. In the first case the uniform concentration of solution increases steadily though the droplet volume and solid particles are formed, which may subsequently sinter or melt. In the second case, the surface part is evaporated and supersaturated, leading to pyrolyzed material and an eggshell structure. Eventually as pressure inside the droplet is increased, the shell may be ruptured. In the final step, the synthesized eggshells are partially or fully melted and deposited on the substrate. In the third case, an elastic shell is formed and deflates, leading to formation of dense or porous deposits [21]. Dense particle formation is typical for solutions with high concentrations and small droplet size, whereas eggshell morphology is a typical formation route for precursors with low concentration or large precursor droplet size [22,23].

Based on the round morphology and size range, the sub-micron particles (Fig. 4) are most likely formed from the liquid-to-solid route. As the precursors were prepared near the maximum solubility level and the droplets were effectively atomized due to the shear force of the flowing combustion gases, it favored the formation of dense particles. It appears that the primary synthesis route for the nanoparticles was a gas-to-solid conversion route, as the particle size and morphology (Fig. 4c) are similar to the TiO$_2$ particles produced by the liquid flame spray (LFS) process reported in Refs. [24,25].

The gas-to-solid conversion, as described by Tikkanen, is the generally accepted synthesis route when producing the nanoparticles by the (LFS) process. As the droplet is exposed to the thermal flame it is fully evaporated into the gas phase. As the temperature is increased, the gas will decompose. In this case, the decomposed gas contains the metallic ions, which form crystallized nanoparticles through nucleation from the gas phase [26].

Fig. 5 shows the IR spectra of the FTIR analyses obtained from the dried precursor powder and the as-sprayed coatings. The comparison was done to evaluate nitrates residues after the spraying process. The absorption bands at the 1633 cm^{-1} and 3410–3434 cm^{-1} refer to the bend and stretching mode of O–H groups, respectively [19]. There are two reasonable explanations for the presence of water molecules: i) water was absorbed to the surface of the as-sprayed coatings or KBr pellets during the sample preparation process when exposed to air atmosphere, or ii) the as-sprayed coating contained residues since the nitrates are known to be hydrous compounds.

Absorption bands of nitrate groups were observed at 821–828 cm^{-1}, 1313–1412 cm^{-1}, and 2350–2354 cm^{-1} [27]. Since absorption bands were also observed in the spectra of the as-sprayed coating, it is most likely that the coatings contained some unpyrolyzed nitrate compounds, as the presence of the O–H group was confirmed. However, according to the intensity of the absorption bands it can be stated that the amount of nitrates was insignificant.

Fig. 6 shows the crystallographic phase analysis data of the as-sprayed and oxidized spinel coatings. According to the XRD studies, the as-sprayed coatings consisted of simple cubic
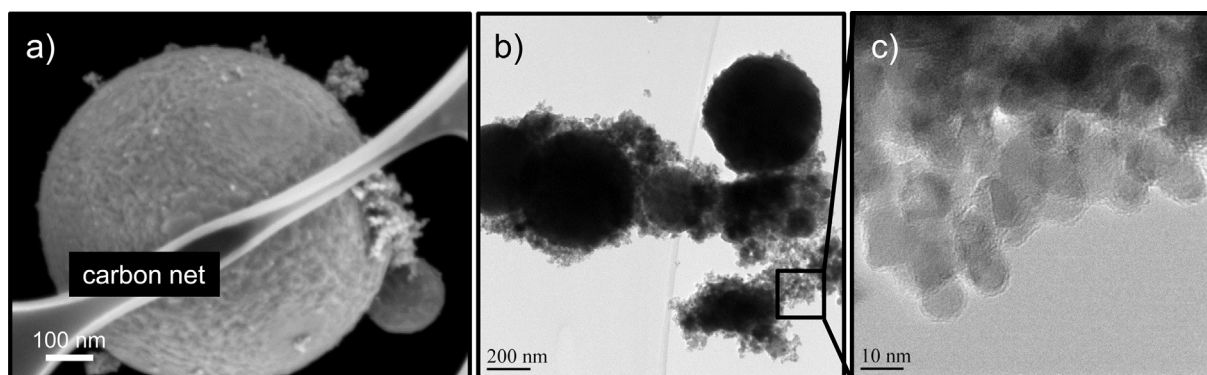
Fig. 4 – FESEM (InLens) image (a) and TEM-images (b and c) of the particles collected from the surface of the TG1-$MnCo_{1.9}Fe_{0.1}O_4$ as-sprayed coating.

oxides identified as the $(Mn,Co,Fe)O$ and $MnCo_2O_4$ (ICDD: 00-023-1237) phases. Decomposition of the spinel and formation of metastable simple cubic oxides are a consequence of the fast cooling rate of the deposited material, which can be restored to the desired spinel with a simple heat treatment process [12,14]. Due to the fast cooling rate the average crystallite size for the spinel phases stayed between 4 and 8 nm. According the FESEM and TEM images in Fig. 4, and crystallite sizes obtained from XRD studies, the sub-micron particles had polycrystalline characteristics, whereas the nanoparticles appeared to be single crystals.
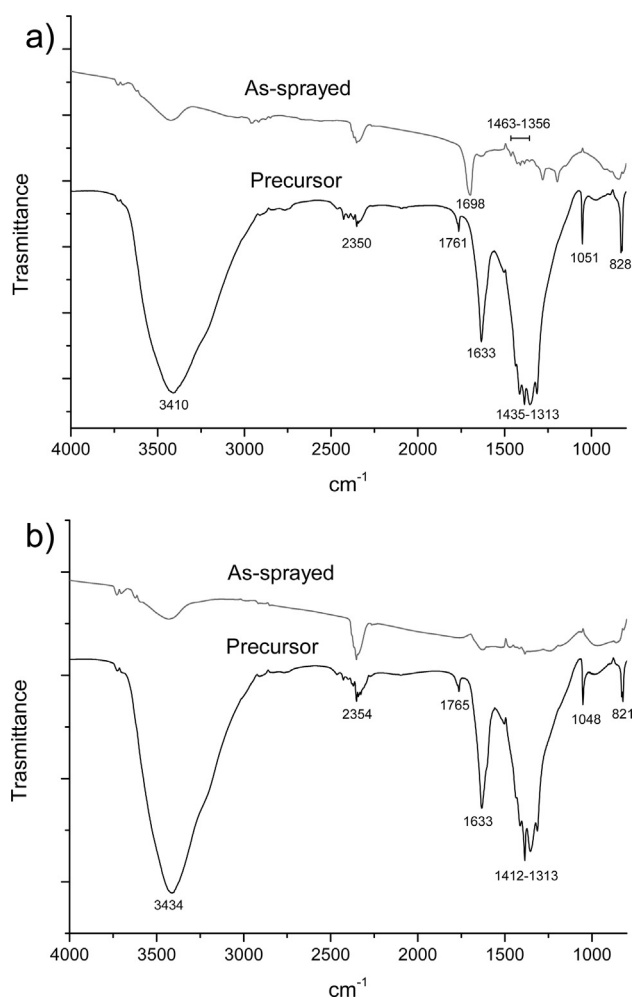
Oxidized HVSPFS spinel coatings

Fig. 7 shows the cross-section and the fracture surface images of the oxidized coatings, with high magnification cross-section inspections of the oxide scale. Coarsening of the voids present in the as-sprayed coating during the oxidation cycle was caused by sintering of the spinel coating. Although the coatings contained voids, there was no indication of significant open porosity through the thickness gradient.

Sintering can be considered as the densification of the as-sprayed coating and increase in crystallite/grain size through the decrease of the net of total free energy of the as-sprayed coatings. The coating sintering process depends on the same factors as conventional bulk ceramic processes, which are i) interacting particle morphologies and size distribution, ii) pore curvature and size distribution, which determines the energy change associated with the change in particle surface area (ΔG_s), the energy change related to the area of crystallite and grain boundaries (ΔG_b), and the energy change associated with any changes in volume (ΔG_v) as shown in Equation (1) [28].

$$\Delta G_t = \Delta G_s + \Delta G_b + \Delta G_v \tag{1}$$

It can be stated that the total free energy of the as-sprayed structure is considerable as the majority of the free energy is associated with the surfaces of the sub-micron and nanosized particles shown in Fig. 4. This free energy is of course enhanced by the energy of the crystallite and grain boundaries (G_b). Due to large surface and interfacial free energy of the nanosized particles, the sintering temperature can be in the range of $0.2–0.3 \ast T_m$, where T_m is melting temperature in the Kelvin scale [29]. In addition, the sintering is further enhanced by the i) residual stresses and, ii) disordered and metastable crystal structure formed during the spraying process, as observed in the XRD studies and presented in Fig. 6.
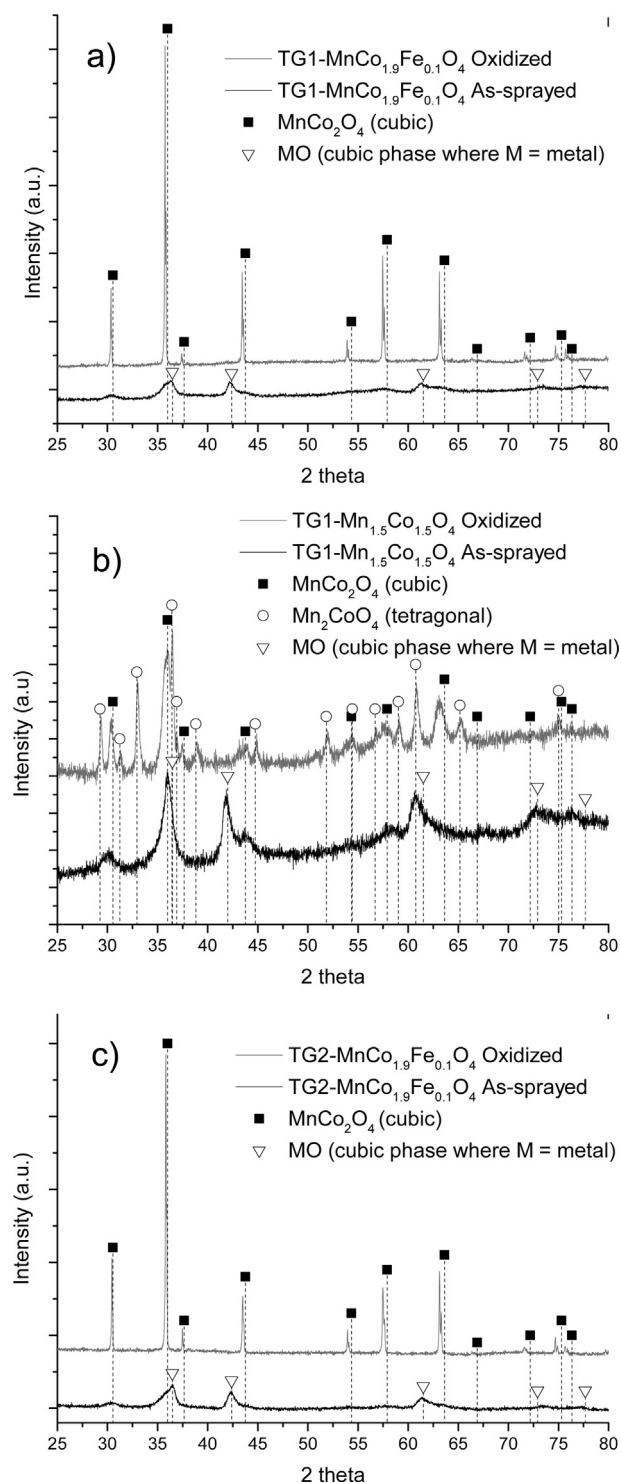

Fig. 5 – IR spectra of the FTIR analyses of the a) $MnCo_{1.9}Fe_{0.1}O_4$ and b) $Mn_{1.5}Co_{1.5}O_4$ precursor nitrate powders and as-sprayed coatings.

Fig. 6 — Crystallographic phase studies of the as-sprayed and oxidized a) TG1-MnCo$_{1.9}$Fe$_{0.1}$O$_4$ b) TG1-Mn$_{1.5}$Co$_{1.5}$O$_4$ and c) TG2-MnCo$_{1.9}$Fe$_{0.1}$O$_4$ coatings.

The remnant porosity in the oxidized coatings, which in some cases is localized near the substrate as observed in Fig. 7b and seen in conventional HVOF sprayed coatings [14], is most likely related to anisotropic shrinkage behavior. The strain is more homogenous in the vertical direction

(perpendicular to the substrate) than in the lateral direction due to the presence of the rigid substrate. According to Jamin et al. [30] the lateral strain at the coating surface is larger than next to the substrate, which results in an inhomogeneous density distribution and porosity localized near substrate.

The oxidized HVSPFS MnCo$_{1.9}$Fe$_{0.1}$O$_4$ coatings showed the presence of a cubic phase as shown in Fig. 6. This spinel structure is close to the MnCo$_2$O$_4$ phase (ICDD: 00-023-1237) with a shifted diffraction pattern. The shifting is a consequence of the increased lattice spacing since Fe^{3+} (0.645 Å) partially replaces Co^{3+} (0.610 Å) [31] in the spinel lattice. The average crystallite sizes were 740 nm and 690 nm for the oxidized TG1-MnCo$_{1.9}$Fe$_{0.1}$O$_4$ and TG2-MnCo$_{1.9}$Fe$_{0.1}$O$_4$ coatings, respectively. The spraying parameters had only marginal influence on the crystallite size before and after the oxidation cycle.

The Mn$_{1.5}$Co$_{1.5}$O$_4$ coating had a multi-phase structure closely related to cubic MnCo$_2$O$_4$ (ICDD: 00-023-1237) and tetragonal Mn$_2$CoO$_4$ phase (ICDD: 04-007-9472) and the simple cubic oxide. This cubic-tetragonal phase structure is known to form when the stoichiometric factor x is between 0.3 and 0.9 in Mn$_{1-x}$Co$_{2-x}$O$_4$ [32]. The average crystallite sizes were 25 nm and 12 nm for MnCo$_2$O$_4$ and Mn$_2$CoO$_4$, respectively. The simple metal oxides are most likely i) residues from the as-sprayed phase structure or ii) re-decomposed spinel due to the high oxidation temperature.

Due to the high temperature oxidation cycle, an oxide scale was formed at the coating/substrate interface. The most plausible reasons for the formation of the oxide scale were: i) diffusion of oxygen through the coatings and ii) the high specific surface area of the as-sprayed coatings associated with the surfaces of the nano- and sub-micron particles. Authors consider that the growth of the oxide scale is less influenced by the direct contact with the gas phase since the as-sprayed and remnant porosity did not exceed through the thickness gradient. The oxide scales were rather similar in the thicknesses varying between 2 and 3 μm. Formation of the oxide scales did not cause spallation or breakaway oxidation as reported in Refs. [33], although a relatively high oxidation temperature was used.

Fig. 8 shows the EDS line analysis data measured from the oxide scale perpendicular to the interface (Fig. 7) to provide the elemental profile. According to the data, the oxide scale contained mainly Cr and a small amount of Mn. In order to more accurately determine the composition, an area analysis was performed in the middle of the scale. The results had a close correspondence to Cr$_2$O$_3$. The amount of other elements, such as Al, Si, Ca, Mn, Fe, Co and Nb were under 1 at-%. Another explanation for the presence of Mn in the line analysis data is the overlap of peaks in the EDS spectra. The Cr$_{K\alpha2}$ peak is near the Mn$_{K\alpha1}$ peak position, which creates uncertainty in the line scan results indicating the presence of Mn.

Table 2 shows the relative amount of elements obtained from point analyses measured along a line with 3 μm spacing, as presented in Fig. 7. The tables show the migration distance of the Cr cations and therefore give a good estimation of the Cr-barrier properties of the spinel coatings. According to the results, the MnCo$_{1.9}$Fe$_{0.1}$O$_4$ coatings suffered Co and Fe cation loss at the surface. The values should be 27.1 and 1.4 in at-% for Co and Fe, respectively. Therefore the results indicate that
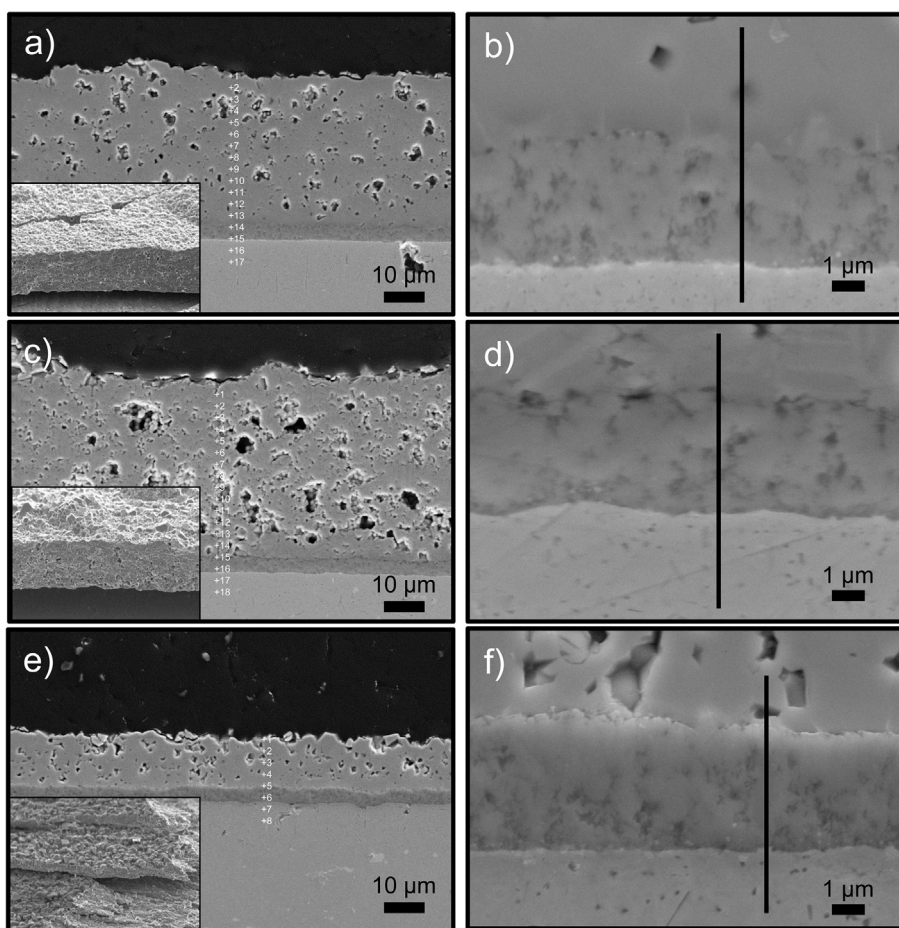
Fig. 7 — Cross-section FE-SEM images of the oxidized HVSPFS coatings and high magnification oxide scale images a—b) TG1-MnCo$_{1.9}$Fe$_{0.1}$O$_4$ c—d) TG1-Mn$_{1.5}$Co$_{1.5}$O$_4$ and e—f) TG2-MnCo$_{1.9}$Fe$_{0.1}$O$_4$. Numbers (a, c and e) show the EDS point analysis spots which are presented in Table 2 and lines (b, d and f) shows the EDS scan traces presented in Fig. 8.

Co and Fe cations migrated towards the substrate. Similar diffusion of Co cations was not observed when the Mn$_{1.5}$Co$_{1.5}$O$_4$ coating was oxidized.

The Mn$_{1.9}$Fe$_{0.1}$O$_4$ and Mn$_{1.5}$Co$_{1.5}$O$_4$ coatings exhibited good Cr-barrier features. According to the results, Mn$_{1.5}$Co$_{1.5}$O$_4$ coating showed superior barrier properties against Cr-migration. Cr was not observed 6 μm from the scale, although the coating was more porous next to the oxide scale.

The MnCo$_{1.9}$Fe$_{0.1}$O$_4$ coatings did not provide as good barrier against Cr migration as the Mn$_{1.5}$Co$_{1.5}$O$_4$ coating. A Cr free region was observed 12 μm from the oxide scale. However, further migration of the Cr cations was efficiently blocked.

In addition to the EDS point analyses, the RF-GD-OES was used to evaluate elemental distribution and Cr-barrier properties of the oxidized spinel coatings. Fig. 9 shows the elemental depth profile analyses of the oxidized spinel
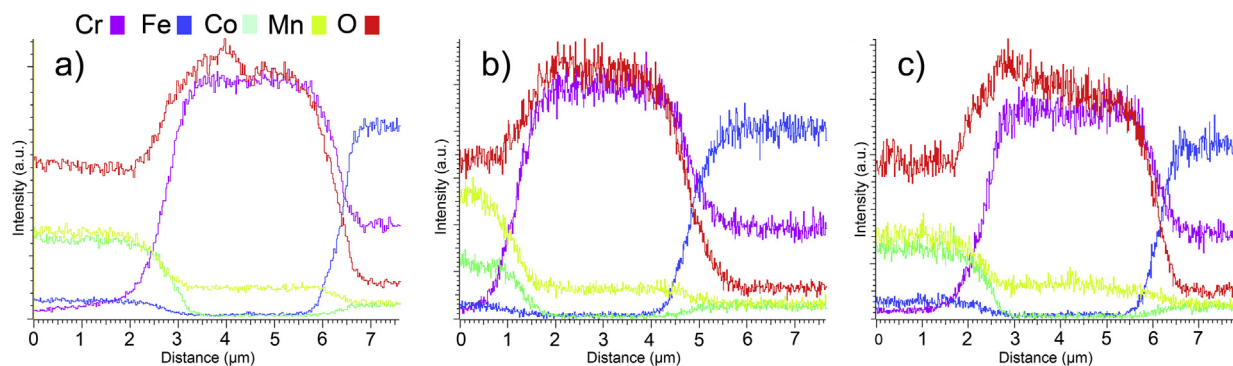

Fig. 8 — EDS line analysis of the oxide scale measured from oxidized a) TG1-MnCo$_{1.9}$Fe$_{0.1}$O$_4$ b) TG1-Mn$_{1.5}$Co$_{1.5}$O$_4$ and c) TG2-MnCo$_{1.9}$Fe$_{0.1}$O$_4$ coatings as presented in Fig. 7 (b, d and f).

Table 2 – EDS analysis spectra of the analysis points presented in Fig. 7. The results are presented in at-%.

Spectrum	O	Mn	Co	Fe	Cr
TG1-MnCo$_{1.9}$Fe$_{0.1}$O$_4$					
1	57.3	22.5	20.2	0.0	0.0
2	57.5	16.3	24.6	1.6	0.0
3	58.6	15.9	23.9	1.7	0.0
4	63.4	14.2	21.2	1.4	0.0
5	55.1	17.3	26.0	1.6	0.0
6	57.5	16.9	24.0	1.6	0.0
7	58.6	16.3	23.2	1.9	0.0
8	56.3	17.1	24.6	2.0	0.0
9	58.4	16.3	23.5	1.8	0.0
10	57.9	16.7	23.5	2.0	0.0
11	58.3	15.8	23.5	2.2	0.3
12	59.3	15.6	22.5	2.3	0.3
13	58.7	15.6	23.2	2.0	0.6
14 (scale)	65.6	0.0	0.0	0.0	34.4
15	32.0	0.0	0.0	42.2	25.7
16	0.0	0.0	0.0	77.5	22.5
17	0.0	0.0	0.0	77.5	22.5
TG2-Mn$_{1.5}$Co$_{1.5}$O$_4$					
1	58.6	20.9	20.5	0.0	0.0
2	60.4	18.5	20.1	0.0	0.0
3	62.0	21.3	16.7	0.0	0.0
4	58.1	20.8	21.1	0.0	0.0
5	56.6	25.3	18.1	0.0	0.0
6	59.3	23.5	17.2	0.0	0.0
7	58.6	22.5	18.9	0.0	0.0
8	51.2	23.3	24.9	0.0	0.6
9	64.5	19.9	15.4	0.0	0.3
10	15.8	42.5	41.4	0.0	0.0
11	62.0	24.2	13.8	0.0	0.0
12	58.4	20.3	21.4	0.0	0.0
13	62.0	18.3	19.7	0.0	0.0
14	57.9	21.3	20.1	0.0	0.7
15 (scale)	60.6	1.6	1.8	0.0	36.0
16	34.8	1.6	0.0	32.9	30.8
17	0.0	0.0	0.0	77.0	23.0
18	0.0	0.0	0.0	77.7	22.3
TG2-MnCo$_{1.9}$Fe$_{0.1}$O$_4$					
1	72.5	12.5	15.0	0.0	0.0
2	59.4	16.6	22.2	1.9	0.0
3	61.1	15.8	21.0	1.9	0.3
4	60.3	16.1	21.3	1.7	0.6
5	61.2	10.7	16.4	1.5	10.3
6 (scale)	64.5	0.0	0.0	0.0	35.6
7	0.0	0.0	0.0	76.8	23.2
8	0.0	0.0	0.0	83.6	16.4

coatings. In contrast to the EDS point and area analyses, the results here present elemental composition from a larger area (see experimental), and therefore the values are more representative of the average composition. It should be noted that as sputtering evaporates the material, even a small sample misalignment and pores might cause some variation in the results. This is due to fact that the sputtering plane may not be exactly parallel with the interfaces between layers. The results do not indicate the loss of Co or Fe on the surface, as it was observed in the EDS analysis. Either the migration was relatively small or the migration was more localized than the overall phenomena.

Cr was not observed at the surface which shows that Cr-migration was effectively blocked by the spinel coatings. The
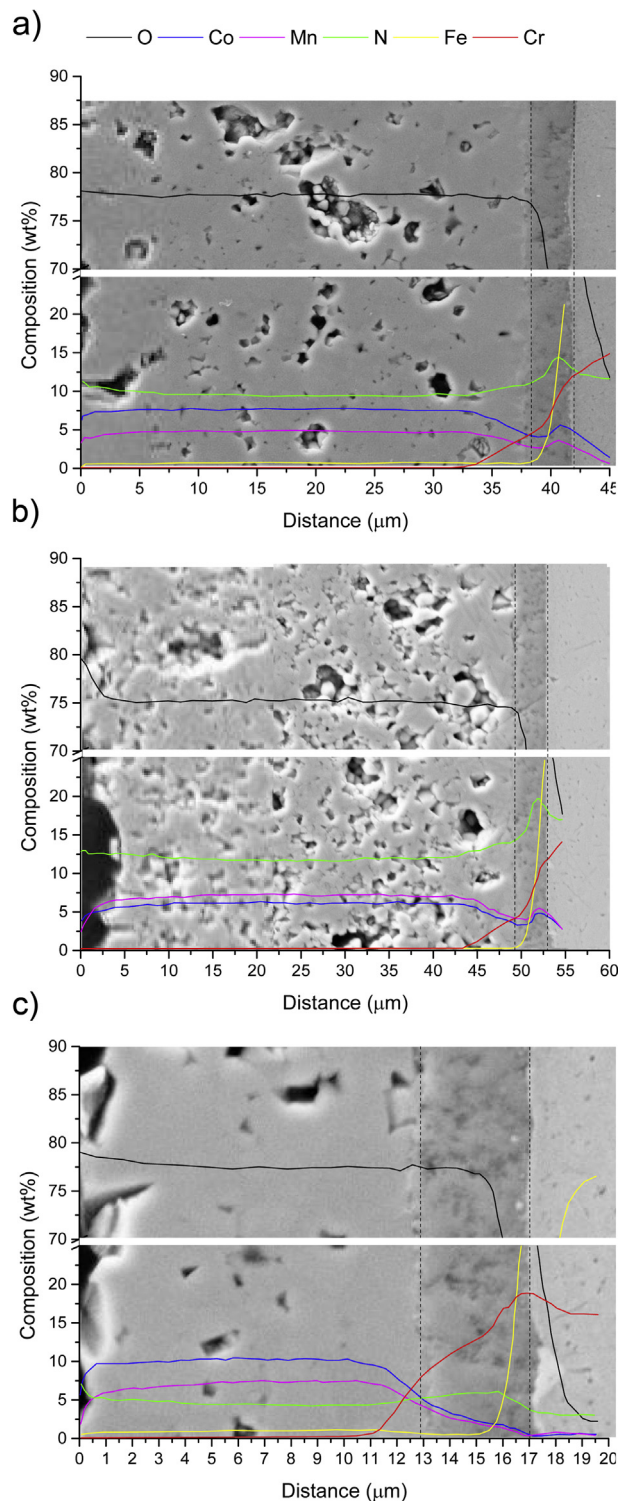

Fig. 9 – RF-GD-OES elemental analysis data from the oxidized a) TG1-MnCo$_{1.9}$Fe$_{0.1}$O$_4$ b) TG1-Mn$_{1.5}$Co$_{1.5}$O$_4$ and c) TG2-MnCo$_{1.9}$Fe$_{0.1}$O$_4$ coatings.

Cr-intensity started to increase near the oxide scales, which was in line with the EDS studies. This indicates that Cr migrated into the spinel coating forming Cr-containing spinel, either (Mn,Co,Fe,Cr)$_3$O$_4$ or (Mn,Co,Cr)$_3$O$_4$, depending on which coating material was used.

Area specific resistance behavior of the oxidized HVSPFS spinel coatings

Fig. 10 shows the area specific resistance behavior of the coatings during the 500 h oxidation cycle. The results present pure [substrate]$_{Crofer\ 22\ APU}$-[oxide scale]$_{Cr2O3}$-[coating]$_{Mn—Co-(Fe)\ spinel}$ contact, without contact paste. This means that contact points were formed between the same surface irregularities as observed in the cross-section analysis. The ASR slope with a huge angular value at the beginning of the test can be explained by the decrease of the contact resistance with the samples due to plastic deformation described by Dey et al. [34].

In later stages, the ASR values continued to decrease. Since it can be expected that the formation of the contact points dominated the ASR behavior at the beginning of the test, the authors consider that microstructural changes i.e., sintering and grain growth dominated the ASR behavior in the later phase. During sintering, material is transported by diffusion causing densification providing better contact between the deposited sub-micron- and nanoparticles and eventually crystallites grow to form larger grains [35], as confirmed by the XRD analyses.

The conduction mechanism in Mn containing spinels is widely agreed to be small polaron hopping [7,36] meaning that the electron is exited across the band gap from the valence band to the conduction band and therefore a hole is formed in the valence band (intrinsic semiconductor) [35]. Therefore, the single crystallites/grains are ideal for conduction, whereas the grain boundaries cause scattering due to the grain boundary phase. This grain boundary phase can be considered as an amorphous phase which most plausibly increases the resistivity of the coating material.

At the end of the 500 h test cycle the ASR values were still relatively high. The lowest ASR values of 46 mOhm cm^2 and 61 mOhm cm^2 were obtained with TG2-MnCo$_{1.9}$Fe$_{0.1}$O$_4$ and TG1-MnCo$_{1.9}$Fe$_{0.1}$O$_4$, respectively. The coating thickness had a direct influence on the ASR values, as seen with the differences between the iron doped coatings. The highest ASR value was obtained with the TG1-Mn$_{1.5}$Co$_{1.5}$O$_4$ coating, as at the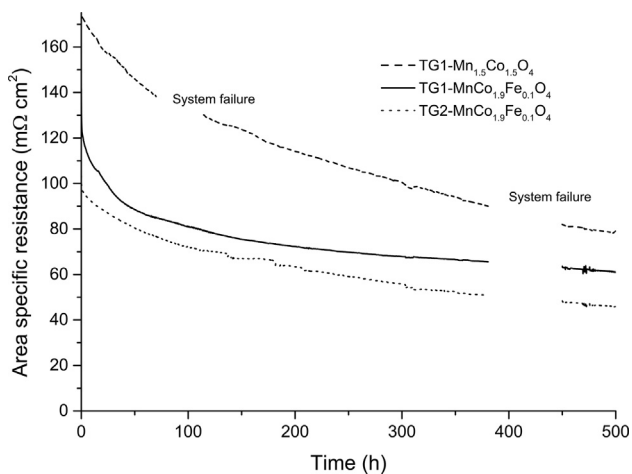 end of the test cycle the ASR reached 77 mOhm cm^2. As previously explained the surface roughness mainly affects the quality of the electrical contact. The contact pressure increases the plastic deformation of the contact irregularities, and in that regard the 4.50 kPa used in this study, is significantly less than the 0.064—0.074 MPa reported as optimum in Ref. [34].

Conclusions

High velocity solution precursor flame spray (HVSPFS) is a modification of the conventional dry powder high velocity oxy-fuel (HVOF) spraying processes, where the material feedstock is in the form of a liquid precursor. The MnCo$_{1.9}$Fe$_{0.1}$O$_4$ and Mn$_{1.5}$Co$_{1.5}$O$_4$ coatings were sprayed using nitrate-water based solution precursors. The as-sprayed coatings were oxidized at 850 °C for 500 h to simulate behavior in the SOFC stack.

The coatings were formed from nano- and sub-micron sized particles. The sub-micron sized particles, with a size range of 100—500 nm, were formed through the liquid-to-solid route from the atomized precursor droplets. Nanoparticles, with a size range of 10—20 nm were formed through the gas-to-solid route from vaporized precursors. The as-sprayed particles had single- or polycrystalline characteristics, with the average crystallite size from 4 to 8 nm.

The as-sprayed coatings had a strong tendency to sinter during the oxidation cycle, which was confirmed by microstructural changes and grain growth. Sintering was caused by the free energy associated with the surfaces of the exceptionally small particles and crystallite boundaries. The free energy was enhanced by the metastable phase structure and residual stresses formed during to the spray process.

Cr$_2$O$_3$ oxide scales were formed between the Crofer 22 APU substrates and the as-sprayed coatings. It can be expected that as-sprayed coatings contained oxygen on the particles' surfaces and/or oxygen diffused through the coating and eventually formed the Cr$_2$O$_3$ layer. However, the coatings effectively blocked migration of the Cr cations. Several quantitative analyses confirmed that Cr migrated a few microns into the spinel coatings, but did not migrate through the coatings. According to the results, Mn$_{1.5}$Co$_{1.5}$O$_4$ prevented migration of the Cr cations more effectively than MnCo$_{1.9}$Fe$_{0.1}$O$_4$.

The deformation of the contact surfaces and sintering of the microstructure, including grain growth, influenced the electrical properties of the spinel coatings. The area specific resistance values decreased notably at the beginning of the oxide cycle. This was caused by the deformation of the contact surfaces which increased the number of contact points, since direct coating—coating contact (without contact paste) was employed. During the later stages of the test, sintering improved the contact between deposited particles and grain growth decreased the number of less conductive grain boundaries. The decrease in the ASR values did not saturate during the 500 h oxidation cycle. However, acceptable values under 80 mOhm·cm^2 were obtained after the 500 h oxidation time.

According to the results, HVSPFS Mn$_{1.5}$Co$_{1.5}$O$_4$ coatings are suitable protective coatings for use on the ferritic stainless steels ICs employed in SOFCs. The Mn$_{1.5}$Co$_{1.5}$O$_4$ offered an

Fig. 10 — ASR values of the oxidized HVSPFS oxide spinel coatings.

excellent barrier against Cr migration, which can be considered the most important result for long term use.

Acknowledgments

REFERENCES

[1] Fergus J. Effect of cathode and electrolyte transport properties on chromium poisoning in solid oxide fuel cells. Int J Hydrogen Energy 2007;32:3664—71.

[2] Chen F, Sun E, Yamanis J, Hawkes J, Smeggil J, Warrier S, et al. Cr poisoning effect for solid oxide fuel cells. In: Mater. sci. technol. 2006 conf. exhib; 2006. p. 303—11.

[3] Kim JY, Canfield NL, Chick LA, Menhardt KD, Sprenkle VL. Chromium poisoning effect on various cathodes. In: Ceram. eng. sci. proceeding; 2005. p. 129—38.

[4] Miguel-Pérez V, Martínez-Amesti A, Nó ML, Larrañaga A, Arriortua MI. The effect of doping $(Mn,B)_3O_4$ materials as protective layers in different metallic interconnects for Solid Oxide Fuel Cells. J Power Sources 2013;243:419—30.

[5] Yang Z, Xia G, Li X, Stevenson J. $(Mn,Co)_3O_4$ spinel coatings on ferritic stainless steels for SOFC interconnect applications. Int J Hydrogen Energy 2007;32:3648—54.

[6] Kiefer T, Zahid M, Tietz F, Stöver D, Z H-R. Electrical conductivity and thermal expansion coefficients of spinel in the series $MnCo_{2-x}Fe_xO_4$ for application as a protective layer in SOFC. In: Linderoth S, Smith A, Bonanos N, Hagen A, Mikkelsen L, Kammer K, et al., editors. Proceeding 26th riso int. symp. mater. sci. solid state electrochmistry, Roskilde; 2005. p. 261—6.

[7] Liu Y, Fergus JW, Wang K, Dela Cruz C. Crystal structure, chemical stabilities and electrical conductivity of fe-doped manganese cobalt spinel oxides for sofc interconnect coatings. J Electrochem Soc 2013;160:F1316—21.

[8] Shaigan N, Qu W, Ivey DG, Chen W. A review of recent progress in coatings, surface modifications and alloy developments for solid oxide fuel cell ferritic stainless steel interconnects. J Power Sources 2010;195:1529—42.

[9] Wu J, Liu X. Recent development of sofc metallic interconnect. J Mater Sci Technol 2010;26:293—305.

[10] Pawlowski L. The science and engineering of thermal spray coatings. 2nd ed. Chichester: John Wiley & Sons; 1995.

[11] Puranen J, Lagerbom J, Hyvärinen L, Kylmälahti M, Himanen O, Pihlatie M, et al. The structure and properties of plasma sprayed iron oxide doped manganese cobalt oxide spinel coatings for sofc metallic interconnectors. J Therm Spray Technol 2010;20:154—9.

[12] Puranen J, Lagerbom J, Hyvärinen L, Mäntylä T, Levänen E, Kylmälahti M, et al. Formation and structure of plasma sprayed manganese-cobalt spinel coatings on preheated metallic interconnector plates. Surf Coatings Technol 2010;205:1029—33.

[13] Puranen J, Laakso J, Kylmälahti M, Vuoristo P. characterization of high-velocity solution precursor flame-sprayed manganese cobalt oxide spinel coatings for metallic sofc interconnectors. J Therm Spray Technol 2013;22:622—30.

[14] Thomann O, Pihlatie M, Rautanen M, Himanen O, Lagerbom J, Mäkinen M, et al. development and application of hvof sprayed spinel protective coating for sofc interconnects. J Therm Spray Technol 2013;22:631—9.

[15] Vargas MJG, Zahid M, Tietz F, Aslanides A. Use of sofc metallic interconnect coated with spinel protective layers using the APS technology. ECS Trans 2007;7:2399—405.

[16] Puranen J, Pihlatie M, Lagerbom J, Bolelli G, Laakso J, Hyvärinen L, et al. Post-mortem evaluation of oxidized atmospheric plasma sprayed Mn—Co—Fe oxide spinel coatings on SOFC interconnectors. Int J Hydrogen Energy 2014;39:17284—94.

[17] Puranen J, Pihlatie M, Lagerbom J, Salminen T, Laakso J, Hyvärinen L, et al. Influence of powder composition and manufacturing method on electrical and chromium barrier properties of atmospheric plasma sprayed spinel coatings prepared from $MnCo_2O_4$ and Mn_2CoO_4 + Co powders on Crofer 22 APU interconnectors. Int J Hydrogen Energy 2014;39:17246—57.

[18] Puranen J, Laakso J, Hyvärinen L, Kylmälahti M, Vuoristo P. Influence of spray parameters and characteristics of solutions on microstructure and phase composition of solution precursor atmospheric plasma sprayed (SPPS) Mn-Co spinel coating. In: Lima RS, Agarwal A, Hyland MM, Lau Y-C, Li C-J, McDonald A, et al., editors. Therm. Spray 2012 Proc. Int. Therm. Spray Conf. Houston: ASM international; 2012. p. 810—5. ASM Int.

[19] Nissinen T, Leskelä M, Gasik M, Lamminen J. Decomposition of mixed Mn and Co nitrates supported on carbon. Thermochim Acta 2005;427:155—61.

[20] Basu S, Cetegen BM. Modeling of liquid ceramic precursor droplets in a high velocity oxy-fuel flame jet. Acta Mater 2008;56:2750—9.

[21] Cetegen BM, Basu S. Review of modeling of liquid precursor droplets and particles injected into plasmas and high-velocity oxy-fuel (HVOF) flame jets for thermal spray deposition applications. J Therm Spray Technol 2009;18:769—93.

[22] Basu S, Jordan EH, Cetegen BM. Fluid mechanics and heat transfer of liquid precursor droplets injected into high-temperature plasmas. J Therm Spray Technol 2007;17:60—72.

[23] Chen D, Jordan EH, Gell M. Effect of solution concentration on splat formation and coating microstructure using the solution precursor plasma spray process. Surf Coatings Technol 2008;202:2132—8.

[24] Maury-Ramirez A, Nikkanen J-P, Honkanen M, Demeestere K, Levänen E, De Belie N. TiO_2 coatings synthesized by liquid flame spray and low temperature sol—gel technologies on autoclaved aerated concrete for air-purifying purposes. Mater Charact 2014;87:74—85.

[25] Nikkanen J-P, Heinonen S, Saarivirta EH, Honkanen M, Levänen E. Photocatalytically active titanium dioxide nanopowders: synthesis, photoactivity and magnetic separation. IOP Conf Ser Mater Sci Eng 2013;47:012066.

[26] Tikkanen J. Liquid flame spray development and its applications. Tampere University of Technology; 1999.

[27] Silwerstein RM, Webster FX. Spectrometric identification of organic compunds. 6th ed. John Wiley & Sons; 1997.

[28] Reed JS. Principles of ceramics processing. 2nd ed. Toronto: Johan Wiley & Sons; 1995.

[29] Mayo MJ. Processing of nanocrystalline ceramics from ultrafine particles. Int Mater Rev 1996;41:85–115.

[30] Jamin C, Rasp T, Kraft T, Guillon O. Constrained sintering of alumina stripe patterns on rigid substrates: effect of stripe geometry. J Eur Ceram Soc 2013;33:3221–30.

[31] Shannon RD. Revised effective ionic radii and systematic studies of interatomie distances in halides and chaleogenides. Acta Crystallogr Sect A 1976;32:751–67.

[32] Naka S, Inagaki M, Tanaka T. On the formation of solid solution in $Co_{3-x}Mn_xO_4$ system. J Mater Sci 1972;7:441–4.

[33] Persson ÅH, Mikkelsen L, Hendriksen PV, Somers MAJ. Interaction mechanisms between slurry coatings and solid oxide fuel cell interconnect alloys during high temperature oxidation. J Alloys Compd 2012;521:16–29.

[34] Dey T, Singdeo D, Bose M, Basu RN, Ghosh PC. Study of contact resistance at the electrode–interconnect interfaces in planar type Solid Oxide Fuel Cells. J Power Sources 2013;233:290–8.

[35] Barsoum M. Fundamentals of ceramics. McGraw-Hill Companies, Inc; 1997.

[36] Lu Z, Zhu J, Andrew Payzant E, Paranthaman MP. Electrical conductivity of the manganese chromite spinel solid solution. J Am Ceram Soc 2005;88:1050–3.